

School of Applied Science
Department of Applied Physics

Radiometric Processing of Multitemporal Sequences of
Satellite Imagery for Surface Reflectance Retrievals in
Change Detection Studies

Luigi John Renzullo

This thesis is presented for the degree of
Doctor of Philosophy
of
Curtin University of Technology

February 2004

Declaration

This thesis contains no material which has been accepted for the award of any other degree or diploma in any university.

To the best of my knowledge and belief this thesis contains no material previously published by any other person except where due acknowledgment has been made.

Signature:

Date:

26/2/04

Abstract

A relative, like-value image normalisation (LVIN) procedure was investigated as a means of estimating surface reflectances from sequences of Landsat TM and ETM+ imagery, and standardising image data for change detection studies when there are uncertainties in sensor calibration and atmospheric parameters over time. The basis of the LVIN procedure is that for an N -date sequence, the digital numbers (DN s) of $N-1$ *overpass* images can be mapped to the reflectance values of a *reference* image for a set of pseudo-invariant targets (PITs) common to all images in the sequence. The robust M-estimator was employed to provide the transformation function that achieved the mapping. The investigation also showed that in some instances the LVIN procedure could incorporate the modelled Path DN —the modelled DN for a target of zero surface reflectance.

A lack of surface validation data was a limitation in the investigation. However, a qualitative evaluation of the LVIN procedure was possible by examining the pre- and post-normalisation image histograms. In a comparison with the results of the 6S radiative transfer code, it was observed that when both overpass and reference images were acquired with the same sensor, the LVIN procedure appeared to correct for atmospheric effects; and when overpass and reference images were with different sensors, the LVIN procedure also corrected for between-sensor differences. Moreover, it was demonstrated for the more “temporally-invariant” PITs that the procedure retrieved surface reflectances that were on average within ± 0.02 reflectance units.

The ability of the LVIN procedure to standardise sequences of image data was further demonstrated in the study of vegetation change. The normalised difference vegetation index (NDVI) was calculated from LVIN estimates of surface reflectance for a selection of sites around the township of Mt. Barker, Western Australia. NDVI data had characteristics consistent with data that have been corrected for atmospheric effects.

A modification to the LVIN procedure was also proposed based on an investigation of some empirically-derived vegetation reflectance relationships. Research into the robustness of the relationships for a greater range of vegetation types is recommended.

Dedication

Questa tesi è dedicata alla mia cara Mamma, per ringraziarla per tutto l'amore e i sacrifici che ha profuso durante i miei studi.

Acknowledgements

My doctoral studies would not have been possible were it not for the financial support, academic guidance, and professional development provided by Curtin University of Technology and the Commonwealth Scientific and Industrial Research Organisation (CSIRO).

I am indebted to Curtin for the supervision of A/Prof. Merv Lynch and Dr. Brendan McGann. Their words of encouragement and constructive comments throughout the course of my studies were inspiring and greatly appreciated. My thanks are also extended to the staff and fellow students in Department of Applied Physics for making the university environment a fascinating and enjoyable place to be. Finally, I acknowledge the University for the Curtin University Postgraduate Scholarship that sustained me for 3.5 years.

To my comrades in the Remote Sensing and Satellite Research Group at Curtin, I wish to extend my heartfelt thanks for making my time in the group happy and memorable. Reflecting on our experiences together, my thoughts are best summed up as:

Pain and ache, boat journeys, marches, hunger and fatigue seemed to belong to the limbo of forgotten things, and there remained only the perfect contentment that comes of work accomplished. — Sir E. Shackleton, South.

I am grateful to the CSIRO Division of Mathematical and Information Sciences for the scholarship supplement and the opportunity to work in a professional environment. It was an honour to have the wisdom of Drs. Norm Campbell and Peter Caccetta to help shape my thesis topic. I am indebted to the Division for the many opportunities provided both during and after my studies.

Finally, I will be forever thankful to my dearest friends and to my family for their patience, for their love and support, and above all, for their faith in me when mine had run dry.

Table of Contents

Abstract	i
Dedication	ii
Acknowledgements	iii
List of Symbols and Acronyms	xvii
1 Introduction	1
1.1 Research Aim	2
1.2 Thesis Scope and Structure	3
2 Atmospheric Physics and Radiative Transfer	5
2.1 The Solar Environment	5
2.1.1 Solar Irradiance	5
2.1.2 Spectral Variations in Solar Irradiance	6
2.1.3 The Earth-Sun Distance	8
2.2 The Terrestrial Atmosphere	9
2.2.1 Atmospheric Pressure and Temperature	10
2.2.2 Water in the Atmosphere	13
2.2.3 Atmospheric Ozone	17
2.2.4 Other Gases	21
2.2.5 Atmospheric Aerosols	21
2.3 Radiative Transfer in the Terrestrial Environment	24
2.3.1 Radiance and Irradiance	24
2.3.2 The Absorbing and Scattering Atmospheres	25
2.3.3 Optical Thickness	26
2.3.4 Diffuse Reflection and Transmission	33

2.3.5	The Radiative Transfer Equation	34
2.4	Chapter Summary	42
3	Satellite Image Data and Processing	45
3.1	Satellite Image Data	45
3.1.1	A Brief History of the Landsat Satellites	46
3.1.2	Orbital Characteristics	47
3.1.3	Multispectral Image Acquisition	47
3.1.4	Image Data and Radiance Values	54
3.1.5	Scene Identification via the WRS	56
3.2	Modelling the At-Sensor Signal	57
3.2.1	Homogeneous Targets	58
3.2.2	Inhomogeneous Targets	62
3.2.3	Bidirectional Reflectance Distribution Function	64
3.2.4	Modelling Software: 6S	68
3.3	Issues in Multitemporal Analysis	70
3.3.1	Geometric Correction and Co-registration	71
3.3.2	Sensor Calibration	76
3.3.3	Atmospheric Effects in Satellite Imagery	82
3.3.4	Change Detection	92
3.4	Radiometric Processing of Multitemporal Sequences of Imagery	99
3.4.1	Unitemporal Methods	100
3.4.2	Multitemporal Methods	109
3.5	Chapter Summary	115
4	A Synthesis of Methods	118
4.1	A Like-value Method	119
4.1.1	A Simplified Radiative Transfer Equation	119
4.1.2	An Extension of the Like-value Procedure	121
4.2	Preliminary Data and Image Processing	126
4.2.1	Image Data	127
4.2.2	Scene Descriptions	128
4.2.3	Geometric Rectification	128

4.2.4	Ground-based Data for Hay	130
4.3	Image Normalisation Results	136
4.3.1	Reference Image Processing	136
4.3.2	Pseudo-Invariant Targets	145
4.3.3	Modelled Path DN	145
4.3.4	Like-Value Normalisation to Surface Reflectances	147
4.3.5	Retrieved Reflectances	153
4.3.6	Sensitivity to Uncertainty in Modelling Parameters	157
4.3.7	Discussion: The Like-value Image Normalisation Procedure	158
4.4	Application: Change in NDVI for Mt. Barker Vegetation	167
4.4.1	Some Spectral Vegetation Indices	167
4.4.2	Mt. Barker Vegetation Data	170
4.4.3	Discussion: Vegetation Change Detection	185
4.5	Some Empirical Vegetation Reflectance Relationships	186
4.5.1	Data and Processing	187
4.5.2	Using the Relationships in a LVIN Procedure	195
4.5.3	Discussion: Empirical Vegetation Reflectance Relationship	198
4.6	Chapter Summary	201
5	Conclusions	204
5.1	Image and Model Data	205
5.2	Addressing the Research Aim	207
5.3	Final Remarks	208
	References	209
A	Equation of State of Water Vapour and Other Useful Formulae	222
B	Ozone Absorption Coefficients for the Uardry MFRSR	224
C	Some radiosonde data for Western Australia, February 6, 2000	226
D	Effect of Variation in Elevation in the Reference Image for Mt. Barker	229
E	Overpass Like-value Image Normalisation Plots for Hay and Mt. Barker	233

F	Comparison of Free-Intercept and Constrained Regression Approaches	243
G	Pre- and Post-normalisation Image Histograms	249
H	Inter-band Correlation for Some Vegetation Targets	254
H.1	Spectroradiometer Measurements	254
H.2	Image Data	266
H.3	LVIN plots and the Kaufman Relationships	268

List of Figures

2.1	Variations in the solar constant illustrated in a composite from a number of space-borne missions.	7
2.2	Two data sets of the monochromatic solar irradiance at the top of the Earth's atmosphere.	8
2.3	A comparison of formulae for calculating the Earth-Sun distance	9
2.4	Atmospheric pressure variations with altitude	11
2.5	Atmospheric temperature variations with altitude	13
2.6	Water vapour profiles for the 6 model atmospheres used in 6S	15
2.7	Atmospheric ozone profiles for the six model atmospheres used in 6S. . . .	19
2.8	Graphical representation of scattering geometry, illustrating forward- (ψ_+) and back- (ψ_-) scattering angles	40
2.9	Scattering phase function for continental, urban and maritime aerosol types. The Rayleigh and two-term Henyey-Greenstein (TTHG) scattering phase functions are also displayed.	42
3.1	An illustration of the satellite and sensor view geometries that are involved in the production of images acquired with MSS, TM and ETM+ sensors .	48
3.2	Spectral response curves for the bands on the Landsat-5 MSS and TM, NOAA-11 AVHRR, and airborne MODIS	50
3.3	The normalised spectral response curves for Landsat-4 and -5 TM and Landsat-7 ETM+ sensors.	51
3.4	True- and false-colour composites of a Landsat-5 TM image	53
3.5	The WRS path/row designation for the same scene in (a) MSS and (b) TM imagery	56
3.6	The propagation of EM radiation from the Sun to the Earth and, finally, to the satellite sensor	59

3.7	Spherical albedo values calculated via the expression in Tanré et al. (1979) for different aerosol loadings.	62
3.8	An illustration of poor (a) and (b) good co-registration of two dates of TM imagery	74
3.9	Additive effects in satellite imagery due to intrinsic atmospheric reflectance	83
3.10	Simulated total atmospheric transmittance for mid-latitude summer con- ditions	85
3.11	Direct and diffuse transmittances due to scattering	86
3.12	Scattering transmittances simulated for a Landsat-5 TM image	87
3.13	Gaseous transmittances simulated for a Landsat-5 TM image	88
3.14	The effect of changes in target elevation on some gaseous transmittances for Landsat-5 TM bands.	91
3.15	Scatter plots illustrating the EL and REL procedures	101
3.16	Like-value image normalisation plot by Furby and Campbell (2001)	114
4.1	Image normalisation plots for the LVIN procedure (a.k.a. LVIN plots) described in Section 4.2.2 without (a) and with (b) modelled path DN . .	123
4.2	Location diagram of the two sequences of Landsat-5 TM and Landsat-7 ETM+ imagery used in the thesis	126
4.3	False-colour composites (RGB:5,4,2) of ETM+ images for (a) Hay, Janu- ary 7, 2000 and (b) Mt. Barker, February 6, 2000.	129
4.4	Spectrometer-acquired surface reflectances for some targets visited on the EOC field campaign	131
4.5	MFRSR measurements at the Uardry field site for March 27, 2000	133
4.6	Langley plots for the Uardry field site MFRSR data	133
4.7	Total, aerosol, molecular, and ozone optical thicknesses at the Uardry field site for March 27, 2000	134
4.8	Aerosol optical thicknesses from the Uardry data assuming different aerosol types	136
4.9	Scatter plots for the HEL procedure using ETM+ image data and surface reflectances	138

4.10	Comparisons of the pre- and post-correction surface reflectances for a couple of targets	140
4.11	Comparison of at-sensor and HEL-retrieved reflectances for the four targets visited on the EOC Uardry field campaign.	141
4.12	An illustration of the anti-correlation of the modelled path radiances and solar zenith angle	146
4.13	Like-value image normalisation plots for each band in the Hay ETM+ image acquired on January 7, 2000	149
4.14	Like-value normalisation plots for each band in the Mt. Barker TM image acquired on January 28, 1994	150
4.15	A comparison of free-intercept regression estimates of $X_{p\lambda}$ for bands 1–4 from Hay and Mt. Barker scenes	152
4.16	Plots of the retrieved ($\rho_{\text{corr}\lambda}$) and reference ($\rho_{s\lambda}$) reflectances for the most temporally-invariant PITs in the Mt. Barker sequence.	155
4.17	Pre- and post-normalisation histograms for the ETM+ image for Mt. Barker, February 11, 2002	156
4.18	Differences between <i>uncorrected</i> and <i>corrected</i> reflectances spectra for <i>E. globulus</i> plantations	172
4.19	NDVI histograms (based on corrected and uncorrected reflectances) for all the Mt.Barker images	174
4.20	An area of perennial vegetation. No significant loss or gain of vegetation is discernible in the time series of NDVI data.	178
4.21	The emergence of the Hambley blue gum (<i>E. globulus</i>) plantation, established in 1996.	179
4.22	The emergence of a large eucalypt plantation, established in 1991.	180
4.23	Loss of vegetation due to flooding.	181
4.24	Vegetation loss due to clearing	182
4.25	An illustration of vegetation loss and then recovery in the area of the Springwell blue gum (<i>E. globulus</i>) plantation, established in 1999.	183
4.26	Vegetation gain and loss for a small region of native vegetation.	184
4.27	Convolved Iris spectra (35 in total) of the McGillivray Oval grass acquired on January 19, 1994	188

4.28	Surface reflectances ρ_{s1} , ρ_{s2} , ρ_{s3} , and ρ_{s5} as functions of ρ_{s7} derived from McGillivray Oval grass spectra	191
4.29	Surface reflectances ρ_{s1} , ρ_{s2} , ρ_{s3} , and ρ_{s5} as functions of ρ_{s7} for the retrieved reflectances of 64 vegetated targets for all dates in the Mt. Barker sequence of TM and ETM+ imagery acquired over the period 1991–2002. The equations displayed are a summary of the results presented in Table 4.13. Also displayed in the dashed grey lines are the Kaufman relationships for bands 1 and 3.	194
4.30	Like-value image normalisation plots illustrating the empirical vegetation reflectance results for bands 1–3 and 5	197
B.1	The placement of the MFRSR bands over a simulated ozone and water vapour transmittance spectra	225
C.1	Diagram of Western Australia illustrating radiosonde launch sites	227
C.2	Pressure and temperature profiles recorded by Albany, Esperance, Kalgoorlie, and Perth radiosondes on February 6, 2000	228
D.1	Error $\rho_{s\lambda}$ for ETM+ bands 1 and 2 if $z = 200$ m is assumed when the true elevation $z = 0, 370$ or 900 m	230
D.2	Error $\rho_{s\lambda}$ for ETM+ bands 3 and 4 if $z = 200$ m is assumed when the true elevation $z = 0, 370$ or 900 m	231
D.3	Error $\rho_{s\lambda}$ for ETM+ bands 5 and 7 if $z = 200$ m is assumed when the true elevation $z = 0, 370$ or 900 m	232
E.1	Landsat-5 TM image for Hay acquired on July 22, 1999.	234
E.2	Landsat-5 TM image for Hay acquired on October 26, 1999.	235
E.3	Landsat-7 ETM+ image for Hay acquired on January 7, 2000.	236
E.4	Landsat-5 TM image for Mt. Barker acquired on January 20, 1991.	237
E.5	Landsat-5 TM image for Mt. Barker acquired on February 24, 1992.	238
E.6	Landsat-5 TM image for Mt. Barker acquired on January 28, 1994.	239
E.7	Landsat-5 TM image for Mt. Barker acquired on March 20, 1995.	240
E.8	Landsat-5 TM image for Mt. Barker acquired on January 7, 1998.	241
E.9	Landsat-7 ETM+ image for Mt. Barker acquired on February 11, 2002.	242

F.1	Relative difference between results calculated from free-intercept and constrained regression LVIN lines for all Hay images	244
F.2	Relative difference between results calculated from free-intercept and constrained regression LVIN lines for Mt. Barker Jan. 1991–Jan. 1994	246
F.3	Relative difference between results calculated from free-intercept and constrained regression LVIN lines for Mt. Barker Mar. 1995–Feb. 2002	248
G.1	Histograms of image data for Hay January 7, 2000.	250
G.2	Histograms of image data for Hay October 26, 1999.	250
G.3	Histograms of image data for Hay July 22, 1999.	251
G.4	Histograms of image data for Mt. Barker February 11, 2002.	251
G.5	Histograms of image data for Mt. Barker January 7, 1998.	252
G.6	Histograms of image data for Mt. Barker March 20, 1995.	252
G.7	Histograms of image data for Mt. Barker January 28, 1994.	253
G.8	Histograms of image data for Mt. Barker February 24, 1992.	253
H.1	The convolved Iris spectra (35 in total) of the McGillivray Oval grass acquired on January 19, 1994	255
H.2	The convolved Iris spectra (17 in total) of the McGillivray Oval grass acquired on February 18, 1994	256
H.3	The convolved Iris spectra (14 in total) of the McGillivray Oval grass acquired on March 30, 1994	257
H.4	The convolved Iris spectra (20 in total) of the McGillivray Oval grass acquired on April 27, 1994	258
H.5	The convolved Iris spectra (18 in total) of the McGillivray Oval grass acquired on May 27, 1994	259
H.6	The convolved Iris spectra (20 in total) of the McGillivray Oval grass acquired on July 28, 1994	260
H.7	The convolved Iris spectra (20 in total) of the McGillivray Oval grass acquired on September 6, 1994	261
H.8	The convolved Iris spectra (20 in total) of the McGillivray Oval grass acquired on October 11, 1994	262

H.9	The convolved Iris spectra (20 in total) of the McGillivray Oval grass acquired on December 6, 1994	263
H.10	The convolved Iris spectra (20 in total) of the McGillivray Oval grass acquired on January 6, 1995	264
H.11	The convolved Iris spectra (20 in total) of the McGillivray Oval grass acquired on February 7, 1995	265
H.12	Enlargements of the LVIN plots for bands 1, 2, 3 and 5 for the Mt. Barker TM imagery acquired on January 20, 1991. Twenty new data pairs corre- sponding to vegetated targets to which three vegetation reflectance rela- tionships (Table H.19) were applied are illustrated as red squares (Kauf- man), green triangles (Image-derived), and blue circles (Grass).	269
H.13	As in H.12 but for TM imagery acquired on February 24, 1992	270
H.14	As in H.12 but for TM imagery acquired on January 28, 1994	271
H.15	As in H.12 but for TM imagery acquired on March 20, 1995	272
H.16	As in H.12 but for TM imagery acquired on January 7, 1998	273
H.17	As in H.12 but for ETM+ imagery acquired on February 11, 2002	274

List of Tables

2.1	Radiosonde-derived scale height	12
2.2	Radiosonde-derived temperature lapse rate	14
2.3	Some precipitable water concentrations	16
3.1	A summary of Landsat satellite and sensor characteristics.	53
3.2	Responsivity g_λ [$\text{W}/(\text{m}^2 \text{ sr } \mu\text{m})/DN$] and zero-radiance bias $Q_{0\lambda}$ values for ETM+ band 1 (in high mode).	55
3.3	Radiometric scaling factors for converting a DN in a radiometrically cal- ibrated TM image into a radiance value [$\text{W}/(\text{m}^2 \text{ sr } \mu\text{m})$].	56
3.4	Exo-atmospheric Solar Irradiances for the TM and ETM+ images	58
3.5	6S simulated path radiances at 480 nm for a range of view angles and aerosol optical thickness	67
3.6	Average transmittance values due to O_2 , CO_2 , CH_4 , NO_2 , and N_2O for the Landsat-5 TM bands	89
3.7	Empirical vegetation reflectance relationships used to estimate $\tau_{M\lambda}$	107
4.1	Hay and Mt. Barker sequences image information	127
4.2	Total ($\tau_{\text{tot}\lambda}$), ozone ($\tau_{\text{O}_3\lambda}$), molecular ($\tau_{\text{R}\lambda}$) and aerosol ($\tau_{\text{M}\lambda}$) optical thickness values at the Uardry field site for March 27, 2000.	134
4.3	Scale height \bar{H} values derived from ABoM radiosonde pressure profiles acquired at four sites in Western Australia on February 6, 2000.	142
4.4	Lapse rates, δ , sea-level temperature, T_{z0} , and R^2 derived from radiosonde data acquired February 6, 2000	143
4.5	Estimates of precipitable water, $u_{\text{H}_2\text{O}}$, obtained from radiosonde profiles for the four locations in Figure C.1 on February 6, 2000.	144
4.6	Inputs to 6S for modelled path radiances	146

4.7	Mean absolute differences (MADs) calculated on the most temporally invariant targets in Hay scene	154
4.8	Percentage differences, relative to values used in Section 4.3.3, for $X_{p\lambda}$ modelled with uncertainty in some input parameters.	157
4.9	Dates and number of reflectance spectra acquired with a GER Iris Spectroradiometer.	187
4.10	The inter-band correlation of 35 convolved grass spectra	188
4.11	Estimates of slope and intercept from the regression of convolved grass spectra for bands 1, 2, 3 and 5 against band 7	190
4.12	Correlation matrix for the combined vegetation data (64 targets; 448 reflectances per band) for all dates of TM and ETM+ imagery in the Mt. Barker sequence over the years 1991–2002.	192
4.13	The estimates of slope and intercept from the regression of retrieved reflectances for vegetated targets in the Mt. Barker scene	193
4.14	A summary of the empirical vegetation reflectance relationships derived in this work	195
B.1	Ozone absorption coefficients $\alpha_{O3\lambda}$ (cm^{-1}) derived from MODTRAN4 ozone data for the 5 standard model profiles	225
D.1	The surface reflectance values, $\rho_{s\lambda}$, above which the error due to the assumption that $z = 200$ m, is less than 5% and 1%.	229
F.1	Comparison of the free-intercept and constrained regression results for the Hay overpass images.	243
F.2	Comparison of the free-intercept and constrained regression results for the Mt. Barker overpass images: 1991–1994.	245
F.3	Comparison of the free-intercept and constrained regression results for the Mt. Barker overpass images: 1995–2002.	247
H.1	Inter-band correlation of 35 convolved grass spectra for Jan. 1994	255
H.2	Inter-band correlation of 17 convolved grass spectra for Feb. 1994	256
H.3	Inter-band correlation of 14 convolved grass spectra for Mar. 1994	257
H.4	Inter-band correlation of 20 convolved grass spectra for Apr. 1994	258

H.5	Inter-band correlation of 18 convolved grass spectra for May 1994	259
H.6	Inter-band correlation of 20 convolved grass spectra for Jul. 1994	260
H.7	Inter-band correlation of 20 convolved grass spectra for Sep. 1994	261
H.8	Inter-band correlation of 20 convolved grass spectra for Oct. 1994	262
H.9	Inter-band correlation of 20 convolved grass spectra for Dec. 1994	263
H.10	Inter-band correlation of 20 convolved grass spectra for Jan. 1995	264
H.11	Inter-band correlation of 20 convolved grass spectra for Feb. 1995	265
H.12	Correlation matrix for vegetation targets January 20, 1991.	266
H.13	Correlation matrix for vegetation targets February 24, 1992.	266
H.14	Correlation matrix for vegetation targets January 28, 1994.	266
H.15	Correlation matrix for vegetation targets March 20, 1995.	267
H.16	Correlation matrix for vegetation targets January 7, 1998.	267
H.17	Correlation matrix for vegetation targets February 6, 2000.	267
H.18	Correlation matrix for vegetation targets February 11, 2002.	267
H.19	Empirical vegetation reflectance relationships of Kaufman et al. and those derived in this work	268

List of Symbols and Acronyms

$\alpha_{H_2O\lambda}$	Coefficient for water vapour transmittance
$\alpha_{O_3\lambda}$	Ozone absorption coefficient (cm^{-1})
$\beta_{H_2O\lambda}$	Exponent for water vapour transmittance
γ	Depolarisation ratio for dry air
δ	Temperature lapse rate (K/km)
δ_{atm}	Density of the atmosphere
Θ	Scattering angle
θ	Observer/sensor view zenith angle
θ_0	Solar zenith angle
$\kappa_{\text{tot}\lambda}$	Total extinction coefficient
λ	Wavelength (nm)
$\tau_{\text{tot}\lambda}$	Total atmospheric optical thickness
$\tau_{\text{abs}\lambda}$	Absorbing atmosphere optical thickness
$\tau_{\text{cal}\lambda}$	Retrieved (corrected) surface reflectances
$\tau_{\text{diff}\lambda}$	Scattering atmosphere optical thickness
$\tau_{\text{M}\lambda}$	Aerosol (Mie) optical thickness
$\tau_{\text{M}550\text{nm}}$	Aerosol optical thickness at 550 nm
$\tau_{\text{O}_3\lambda}$	Ozone optical thickness
$\tau_{\text{R}\lambda}$	Molecular (Rayleigh) optical thickness

$\rho_{\text{atm}\lambda}$	Intrinsic atmospheric reflectance
$\rho_{\text{corr}\lambda}$	Corrected reflectance or estimate of surface reflectance
ρ_{da}	Density of dry air (g/m^3)
$\rho_{H\lambda}$	Hemispherical reflectance, or albedo
$\rho_{R\lambda}$	Bidirectional Reflectance Factor (BRF)
$\rho_{s\lambda}$	Surface reflectance
$\rho_{\text{sat}\lambda}^*$	At-sensor (or image-derived) reflectance value
ρ_{wv}	Density of water vapour (g/cm^3)
ϕ	Observer/sensor view azimuth
ϕ_0	Solar azimuth direction
ψ_+	Forward scattering angle
ψ_-	Back scattering angle
$\omega_{0\lambda}$	Single scattering albedo
A	Ångström coefficient
A_λ	Image correction/normalisation coefficient (offset) for band λ
AFRI	Aerosol FRee vegetation Index
AOT(550 nm)	Aerosol optical thickness at 550 nm
ARVI	Atmospherically Resistant Vegetation Index
AU	Astronomical unit ($1.496 \times 10^{11}\text{m}$)
AVHRR	Advanced Very High Resolution Radiometer
B	Ångström exponent
B_λ	Image correction/normalisation coefficient (gain) for band λ

CSIRO Commonwealth Scientific and Industrial Research Organization

CAR CSIRO Atmospheric Research

CMIS CSIRO Mathematical and Information Sciences

CVA Canonical Variate Analysis

D Correction factor for Earth-Sun distance

DN Digital number (count)

DU Dobson unit (1000 DU = 1 atm-cm)

EL Empirical line

EM Electromagnetic

EOC Earth Observation Centre, CSIRO

ETM+ Enhanced Thematic Mapper Plus (Landsat-7 satellite sensor)

$F_0\lambda$ Solar spectral irradiance ($\text{W}/\text{m}^2/\text{nm}$) at 1AU

$F_{d\lambda}$ F_0 corrected for Earth-Sun distance

$F_{\text{surf}\lambda}^{\downarrow}$ Total downwards irradiance incident at the surface

$F_{\text{surf}\lambda}^{\uparrow}$ Total upwards irradiance from the surface

g_λ Detector element responsivity

\bar{H} Atmospheric pressure scale height

HEL Hybrid empirical line (of the EL and REL procedures)

$I_{\text{sol}\lambda}$ Attenuated solar irradiance

J_λ Source function

L_λ Radiance ($\text{W}/\text{m}^2/\text{sr}$)

L_λ^* The total radiance emerging from the TOA

$L_{p\lambda}$	Path radiance
$L_{s\lambda}$	Outward normal radiance from the Earth's surface
LVIN	Like-value image normalisation
m	Airmass
m_r	Mass mixing ratio (g/kg)
MAD	Mean absolute difference
MODIS	MODerate resolution Imaging Spectroradiometer
MFRSR	Multi-Filter Rotating Shadowband Radiometer
MSS	Multispectral Scanner
$n_{a\lambda}$	Refractive index of dry air
NDVI	Normalised Difference Vegetation Index
NDVI ^(CORR)	NDVI calculated using calibrated/corrected image data
NIR	Near-infrared region of the EM spectrum
path DN	A digital number corresponding to path radiance
P	Phase function
P_0	Standard pressure (= 1013.25 hPa)
$P_{M\lambda}$	Aerosol scattering phase function
P_R	Molecular scattering phase function
P_s	Surface or station-level pressure (hPa)
PIT	Pseudo-invariant target
$Q_{0\lambda}$	Zero-radiance bias for detector element
R	Bidirectional Reflectance Distribution Function (BRDF)

REL	Refined empirical line
RH	Relative humidity
RT	Radiative transfer
RTE	Radiative transfer equation
S	Diffuse reflectance function
s_λ	Spherical albedo
SAVI	Soil-Adjusted Vegetation Index
SWIR	Shortwave-infrared region of the EM spectrum
T	Diffuse transmission function
$T_{\text{abs}\lambda}$	Total transmittance through the absorbing atmosphere
$t_{\text{d}\lambda}$	Diffuse transmittance
$T_{H_2O\lambda}$	Transmittance of water vapour
$T_{O_3\lambda}$	Transmittance of ozone
T_0	Standard temperature (= 273.16 K)
T_s	Screen or station-level temperature (K)
$T_{\text{scat}\lambda}$	Total transmittance through the scattering atmosphere
TM	Thematic Mapper (Landsat 4 and 5 satellite sensor)
TOA	Top of the Earth's Atmosphere
TOMS	Total ozone mapping spectrometer
u_{H_2O}	Columnar water vapour concentration (g/cm ²)
u_{O_3}	Columnar ozone concentration (DU or atm-cm)
VIS	Visible region of the EM spectrum

$X_{p\lambda}$ Path DN (i.e. the DN corresponding to $\rho_s = 0$)

X_λ unprocessed image DN

X_λ^{Raw} raw image DN

z Elevation above sea level (m or km)

CHAPTER 1

Introduction

Space-based imaging of the Earth was born out of meteorological satellite studies in the late 1960s. Since then, the number of Earth-observing satellites has continued to grow. In fact, in the last decade alone, over 100 satellites have been placed in orbit for the purpose of monitoring the Earth’s land, oceans and atmosphere, spawning what has been referred to as *satellite constellations* (Asrar, 2002). This is a new paradigm that calls for an ensemble of space-based observations to provide an integrated view of the Earth system; strengthening the scientific understanding of the driving forces behind global change, and monitoring the planet’s “vital signs” (King and Herring, 2000).

An issue of critical importance, if space-based observations are to form an integrated set of global observations, is that of *sensor calibration*. Calibration, both within and between satellite systems, is important for maintaining data consistency through time and to facilitate comparisons between sets of remotely-sensed data. Left unaddressed, a lack of intra- and inter-system calibration has been likened to “apples-to-oranges” intercomparisons and analyses; it would be difficult to ascribe changes in the Earth system if data are themselves inconsistent (Barron et al., 1999).

When multiple dates of satellite imagery are used to analyse spatial and temporal patterns of change in the Earth’s surface properties, it is important that the atmospheric contributions to the at-sensor signal be removed (Kaufman, 1984). The processing of image data to achieve this *atmospheric correction* compensates for the atmospheric effects on solar radiation between the ground and the satellite sensor, so that changes in imagery observed through time may be ascribed to disturbances on the Earth’s surface and not the intervening atmosphere.

One of the longest serving campaigns of Earth-observing satellites has been the Landsat mission. Some 30 years since the launch of Landsat-1, 7 satellites and 3 sensors later, the Landsat mission continues to provide multispectral imagery of the Earth that have found applications in many diverse fields of research (Goward and Masek, 2001). The application for which long-term archives of Landsat imagery have been extensively

used is in the assessment of land cover change (Caccetta et al., 2000a,b; Richards and Furby, 2002).

A requirement for land cover change detection in multitemporal sequences of satellite imagery is that the data be processed into a consistent set of units, free of effects due changes in sensor calibration and atmospheric condition. This processing, however, may be hampered by uncertainties in sensor calibration and/or the parameters required to model the atmospheric effects. Radiometric processing of multitemporal sequences of Landsat TM and ETM+ images for the purposes of ensuring data consistency through time is the theme of this doctoral thesis.

1.1 Research Aim

The decision to express image data in a particular set of units (e.g. digital numbers, radiances, or reflectances) is often driven by the application for which the images are intended. Converting image data into surface reflectances has the advantage that these data are free of atmospheric effects, are corrected for seasonal and diurnal differences in solar position, and are independent of differences in sensor systems (Teillet et al., 2001); a desirable characteristic in multitemporal analysis. In order to estimate surface reflectances in imagery, most radiometric processing procedures rely on ground-based knowledge of surface reflectance and/or atmospheric properties; or they infer estimates of key atmospheric parameters from the imagery itself and neglect possible changes in sensor systems through time. Such procedures are not suitable for multitemporal analysis, particularly in retrospective studies when, more often than not, the required information (i.e. surface, atmospheric or sensor) is unknown.

When applications call for a comparative analysis of image data between dates, processing to an absolute scale is not always necessary. In these instances, images can be normalised to a common reference image (Hall et al., 1991; Furby and Campbell, 2001). Processing methods based on image-to-image normalisation are proposed to circumvent these uncertainties by adjusting each image in a multitemporal sequence to a common *reference* image. This gives each image the appearance that it was acquired under the same atmospheric condition, solar position, and with the same sensor as the reference. Surface reflectance retrievals are generally not possible with image normalisa-

tion procedures since, in the absence of *in situ* measurements, the reference image itself may be affected by the atmospheric effects.

This thesis investigates the possible use of image normalisation procedures to estimate surface reflectances in multitemporal sequences of satellite imagery. The motivation for the investigation is the suggestion made by both Hall et al. (1991) and Furby and Campbell (2001) that just such a relative, image-to-image procedure can in principle transform image data into surface reflectances, if the reference image itself is expressed in those units. Moreover, the thesis builds upon these authors' work by aiming to explicitly demonstrate that image normalisation can simultaneously correct for those factors that lead to observed change between images that are not due to modifications of the Earth's surface properties.

1.2 Thesis Scope and Structure

Before describing the factors that can hamper multitemporal analysis with satellite imagery, and methods for correcting their effects, it is important to understand how electromagnetic radiation emanating from the Sun interacts with the earth-atmosphere system, and is ultimately detected by the satellite sensor. This is achieved in Chapter 2 with descriptions of (i) the characteristics of solar radiation in the solar reflective region of the electromagnetic spectrum (i.e. 400–2500 nm), (ii) some physical properties of the Earth's atmosphere and its chemical constituents, and (iii) the mathematical formalisms that describe a simple model for the electromagnetic radiation emerging from the earth-atmosphere system. Formulae and definitions to be used in subsequent chapters are also presented in this chapter.

Chapter 3 narrows the focus of the thesis by presenting a brief overview of the characteristics of imagery acquired with multispectral sensors on the Landsat series of satellites, specifically the data for the solar reflective spectral bands. Continuing from the mathematical models describing the propagation of electromagnetic radiation in Chapter 2, a model for the at-sensor signal specific to the Landsat sensors is presented. The main factors affecting multitemporal analysis as they pertain to sequences of Landsat imagery are also given in this chapter. How these factors become manifest in the satellite imagery, as well as their impact on the mapping and monitoring of land cover change, is described.

This is followed by a review of radiometric processing procedures that seek to minimise their effect.

The theory and processing methodologies described in the preceding chapters are brought together in Chapter 4. In this chapter, the aim of the thesis is addressed with a description of the image normalisation procedure to be employed and the results of its application to two multitemporal sequences of Landsat imagery. Preliminary data processing along with a detailed discussion of the results, emphasising the normalisation procedure's ability to retrieve surface reflectances and correct for the aforementioned factors, is presented. The importance of image normalisation is demonstrated in an application to monitor vegetation change in one of the multitemporal sequences. Finally, the detail of preliminary investigations into a possible modification to the normalisation procedure ends the chapter.

The thesis ends with the conclusions drawn from the investigations and a statement of possible further work based on discussions given in Chapter 4.

CHAPTER 2

Atmospheric Physics and Radiative Transfer

This chapter describes the interaction of electromagnetic (EM) radiation emitted by the Sun with the atomic, molecular and particulate constituents in both the solar and terrestrial atmospheres. A simple yet accurate model representing the radiometric signal emerging from the earth-atmosphere system will be presented. Terms and expressions that will be used in subsequent chapters will also be defined.

2.1 The Solar Environment

Environmental conditions in the Sun's core are sufficient for nuclear fusion to produce the elements of the periodic table up to and including iron (Fe). Energy generated by nuclear fusion process generates convective forces that transports these elements through a convective layer ($\sim 10^5$ km thick) to an outer layers of the Sun known as the *photosphere*. The photosphere is a relatively thin layer of the solar atmosphere (a few hundred kilometres thick) from which nearly all the EM radiant output of the Sun is emitted. Fligge et al. (2001) state that 99% of the solar radiative output occurs within the wavelengths interval 300–10000 nm. It is the continuous absorption and emission of EM radiation by the elements in the photosphere that produces the light observed emanating from the Sun. The absorption characteristics of these elements, however, exhibit wavelength (or spectral) dependence, resulting in variations in the continuous spectrum of solar radiation emitted from the Sun (discussed in Section 2.1.2).

2.1.1 Solar Irradiance

The rate of energy transfer by EM radiation, the *radiant flux*, incident per unit area is termed the *radiant flux density* or *irradiance* with units watts per square metre (W/m^2). A quantity often used in remote sensing is that of irradiance per unit wavelength, and is termed the *spectral irradiance* (with units $\text{W}/\text{m}^2/\text{nm}$). Unless otherwise stated, the units of wavelength (λ) in this document are nm.

The total radiant flux from the Sun is approximately 3.84×10^{26} W, and since the mean Earth-Sun distance is 1.496×10^{11} m, the total solar irradiance, over all wavelengths, incident at the top of the Earth's atmosphere (TOA), at normal incidence to the Earth's surface is

$$F_0 = \frac{3.84 \times 10^{26}}{4\pi(1.496 \times 10^{11})^2} = 1370 \text{ W/m}^2.$$

While this quantity is known as the *solar constant*, space-borne observations, such as those from the Variability of Irradiance and Gravity Oscillation experiment (VIRGO) conducted aboard the Solar and Heliospheric Observatory (SOHO), reveal considerable variation of F_0 through time.

Figure 2.1 presents a 20-year time series of measurements of F_0 from a number of space-borne missions. The observed variations are due to localised events on the photosphere known as *sunspots*¹ and *faculae*². An increased number of these events occurs approximately every 11 years, a period known as the solar cycle.

2.1.2 Spectral Variations in Solar Irradiance

Instrumentation and measurement strategies designed to measure spectral variation in solar irradiance at the top of the Earth's atmosphere have been many and varied. They have included ground-based measurements, instruments mounted on high-altitude aircraft and balloons, and space-borne sensors (Arvesen et al., 1969; Neckel and Labs, 1984; Fligge et al., 2001).

The advantage of space-borne measurements is that they are free of the effects of the Earth's atmosphere which, depending on the wavelength of the radiation, can reduce the intensity of the measured radiation (more later). The high-altitude airborne campaign of Arvesen et al. (1969) provided a dataset of solar irradiance values measured at high resolution for wavelengths in the range 200–2500 nm. The NASA CV-990 aircraft conducted eleven research flights at altitudes between 11.6–12.5 km; the aircraft, therefore, was above 80% of the atmosphere (except the ozone layer) and, therefore, atmospheric effects were assumed to have marginal impact on the measurements. The solar irradi-

¹Sunspots are dark areas on the photosphere which are cooler than surrounding regions. They have lifetimes ranging from a few days to weeks and are accompanied by strong magnetic fields.

²Faculae are regions of the photosphere which are hotter than their surroundings. They often occur in conjunction with sunspots and also possess strong magnetic fields and similar lifetimes.

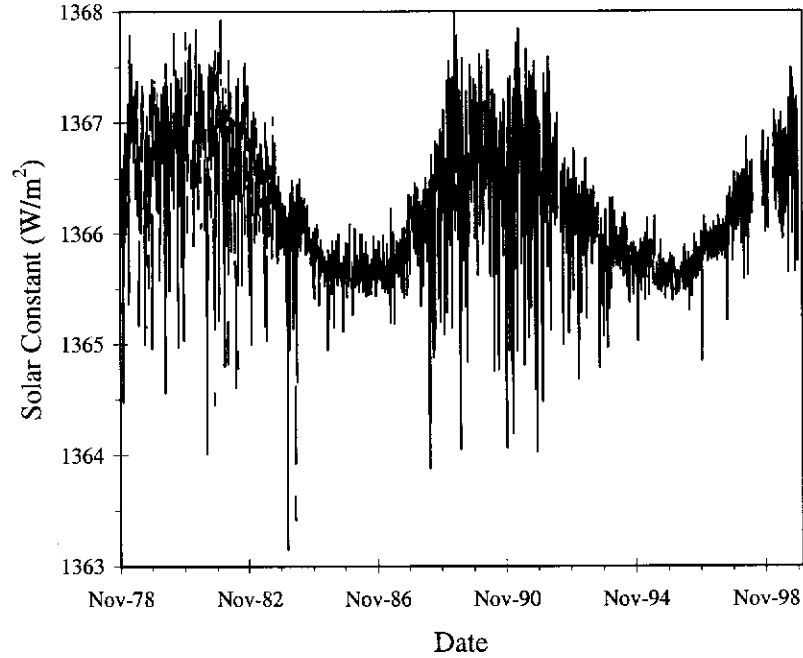


Figure 2.1: Variations in the solar constant illustrated in a composite from a number of space-borne missions.

ance data possess very high spectral resolution, and a precision of $\pm 1\%$ with an absolute accuracy around $\pm 3\%$ over most of the wavelength range.

The solar irradiance data given in Neckel and Labs (1984) represent corrections to the authors' earlier work. The solar irradiance measurements obtained were ground-based and circumvented the atmospheric problem described earlier by employing a *Langley* method of analysis (described in Section 2.3.3). The Langley method involves measuring the solar irradiance at a number of different Sun elevations and then extrapolating to zero airmass (Fligge et al., 2001). Using this approach, Neckel and Labs (1984) were able to obtain solar irradiance values at 1, 2 and 5 nm intervals (depending on the wavelength region) between 330–1248 nm with an absolute accuracy of the order of 1–2%.

Both the Arvesen et al. (1969) and Neckel and Labs (1984) datasets of monochromatic solar irradiance are displayed in Figure 2.2. It can be shown that the irradiance curve resembles that of a Planck's distribution for a blackbody at a temperature of 5777 K with a maximum occurring around 500 nm. This is consistent with Wien's displacement law, which states that the wavelength (λ_{\max}) corresponding to the peak in Planck's curve

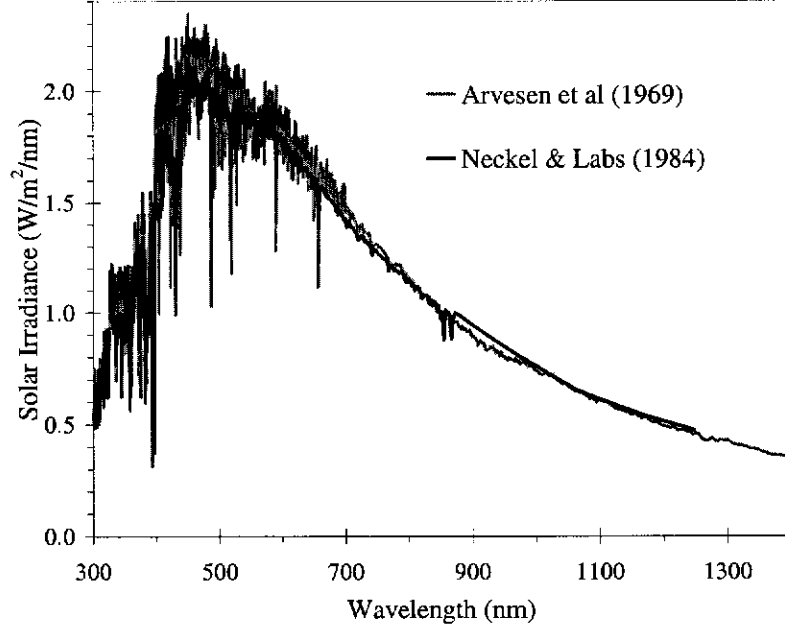


Figure 2.2: Two data sets of the monochromatic solar irradiance at the top of the Earth's atmosphere.

for a blackbody radiating at a temperature T are related as follows:

$$\lambda_{\max} T = 2.898 \times 10^6 \quad (\text{nm K}).$$

2.1.3 The Earth-Sun Distance

By far the largest source of variation in $F_{0\lambda}$ at the TOA is the orbit of the Earth around the Sun. The Sun is located at one of the foci of the Earth's orbit—an ellipse with eccentricity $e = 0.01673$, and the value of F_0 is expected to vary as the reciprocal of the Earth-Sun distance squared. The mean Earth-Sun distance is referred to as 1 Astronomical Unit (AU) and corresponds to a distance of 1.496×10^{11} m. Eckstein and Simpson (1991) defined the factor D (inversely proportional to the square of the Earth-Sun distance) to adjust F_0 for intra-annual variations in Earth-Sun distance, i.e.

$$D = [1 + e \cos(0.9863 \frac{\pi(J-3)}{180})]^2, \quad (2.1)$$

where J is the day of the year. A second expression was used by Vermote et al. (1997b), namely

$$D = \frac{1}{[1 - e \cos(0.9856 \frac{\pi(J-4)}{180})]^2}. \quad (2.2)$$

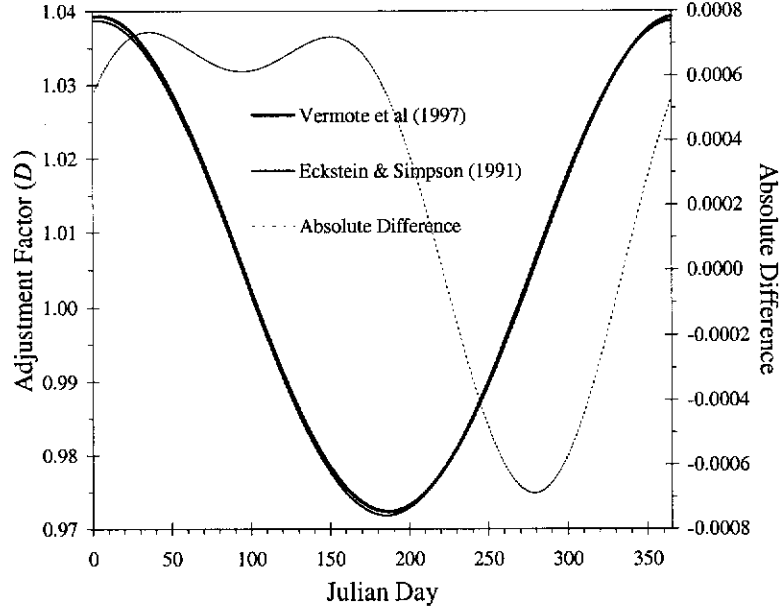


Figure 2.3: A comparison of two approaches for calculating the adjustment factor D applied to the solar intensity measurements based on the mean Earth-Sun distance.

In this thesis, the value of solar spectral irradiance corrected for Earth-Sun distance (i.e. time of year) is denoted $F_{d\lambda}$.

Figure 2.3 presents a time-series of D values calculated using the two expressions above. A discrepancy between expressions is observed at the maxima and minima of the time series, where the disagreement reaches 0.074% and 0.069% respectively. The maxima in Figure 2.3 correspond to the *perhelion* on January 3 (when the Earth is nearest the Sun) and the minima to *aphelion* on July 4 (where the Earth is furthest from the Sun). Using either expression for calculating D , it can be shown that solar intensity at perhelion and aphelion can differ by as much as 4% relative to the mean Earth-Sun distance (Mather (1999, p. 93) quotes a value of 3.5%).

2.2 The Terrestrial Atmosphere

Occupying the vast distance between the Sun and the Earth is a comparatively thin layer of gases and suspended particles that envelope the Earth, and collectively comprise the Earth's atmosphere. In Earth's case, 99% of the mass of the atmosphere is contained below 30 km. Up to about 100 km above sea level, the atmosphere can be stratified into

4 main layers. They are the *troposphere*, *stratosphere*, *mesosphere* and *thermosphere*. The following sections give brief discussions on some of the physical properties of these layers; their constituents, and measurements of their concentrations and distribution as they pertain to satellite-based remote sensing and the scope of this thesis.

2.2.1 Atmospheric Pressure and Temperature

Profiles of Atmospheric Pressure

Atmospheric pressure (P) is the weight of a column of air above a unit area and is expressed in *hectopascals* (hPa). The horizontal distributions of pressure are familiar to most in the form of synoptic charts on which isobars join regions of equal pressure. To analyse the spatial patterns of pressure it is important that the measurements (known as *station-level* values) are adjusted to a standard level. Usually the adjustment corrects for the station elevation and converts the pressure to a mean sea-level value.

The vertical distribution of atmospheric pressure is known as the pressure *profile*. As the density of the atmosphere decreases with altitude, so does the atmospheric pressure. Pressure profiles, for 6 standard atmospheric models available in the 6S software (Vermote et al., 1997b) are: mid-latitude summer (MLS) and winter (MLW), sub-arctic summer (SubS) and winter (SubW), tropical (TROP), and US 1962 (US62). These standard, model profiles are displayed in Figure 2.4.

One device that can measure changes in atmospheric pressure with altitude is a radiosonde. An example of a radiosonde-measured pressure profile is given in Figure 2.4. The data were acquired by a radiosonde released at 0900 hours from the Australian Bureau of Meteorology station at Wagga Wagga, New South Wales (station location E 147°27' S 35°10' and 220 m above sea level) on March 27, 2000. Absolute differences between radiosonde and model pressure profiles are also displayed. The radiosonde pressure profile closely resembles a mid-latitude summer profile up to 16 km, and then a tropical provides a closer up to an altitude of 25 km. A general convergence of pressure values as altitude increases is also observed.

As mentioned earlier, station-level pressure readings are typically converted to mean sea-level values so that spatial patterns of pressure can be observed without the influence of station elevation. If P_s denotes the station-level pressure (hPa) then the mean sea

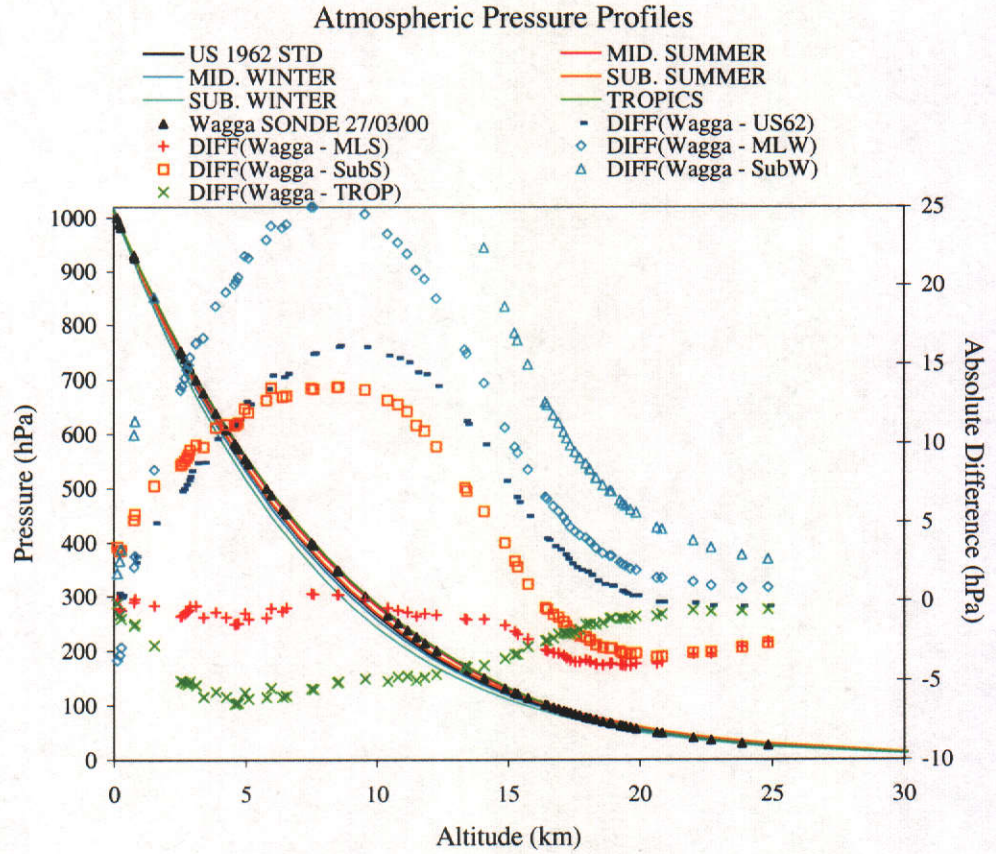


Figure 2.4: An illustration of atmospheric pressure variation with altitude. The solid lines represent model value of pressure for standard atmosphere models from 6S (Vermote et al. (1997)) and the triangles mark radiosonde pressure readings for Wagga Wagga, NSW March 27, 2000.

level pressure P_{msl} is calculated as,

$$P_{msl} = P_s \exp(z/\bar{H}), \quad (2.3)$$

where z is the station elevation above sea-level and \bar{H} is known as the *scale height*. The scale height can be estimated by (Wallace and Hobbs, 1977, p. 57) as:

$$\bar{H} = \frac{z_2 - z_1}{\ln(P_1/P_2)} \quad (2.4)$$

where P_1 and P_2 are pressure values at elevations z_1 and z_2 , respectively. Calculating a value of \bar{H} for the each level up to and including 10 km for the data displayed in Figure 2.4 and extrapolating to an elevation $z = 0$, gives the scale heights presented in Table

Table 2.1: Comparison of scale height \bar{H} values estimated from the Wagga Wagga radiosonde pressure profiles and those used in some standard atmospheric models.

Pressure Profile	\bar{H} (km)
Wagga Sonde	8.65
MLS	8.64
MLW	8.00
SubS	8.37
SubW	7.60
TROP	8.81
US62	8.35

2.1. The agreement between the Wagga Wagga radiosonde and mid-latitude summer scale heights is consistent with the conclusions drawn from Figure 2.4.

Profiles of Atmospheric Temperature

Atmospheric temperature (T) profiles exhibit a rather more complex behaviour with altitude. At the interface between atmospheric layers are regions where temperatures either remain constant (isothermal) or switch from an decreasing to increasing (or vice versa) trend. These regions can range from 2–10 km in thickness, and from the Earth’s surface to the TOA they are referred to as the *tropopause*, *stratopause* and *mesopause* respectively.

Radiosondes can also measure the vertical structure of temperature in the atmosphere. The Wagga Wagga radiosonde for March 27, 2000 and 6S model atmospheric temperature profiles are displayed in Figure 2.5. As with the pressure profile, there exists a great deal of similarity between the Wagga Wagga temperature profile and that of a mid-latitude summer model up to 13 km after which better agreement is observed with the tropical temperature profile.

In Figure 2.5 the sub-arctic winter temperature profile increases for the first kilometre. This event is known as a *temperature inversion* and is often observed on some hot summer nights or in locations where the Earth’s surface is cooler than the atmosphere directly above it. Generally, however, atmospheric temperature decreases linearly with altitude for the first 10-15 km. The rate of temperature decrease is known as the *lapse rate*, denote δ (K/km). A comparison of the lapse rates of the 6S model atmospheres

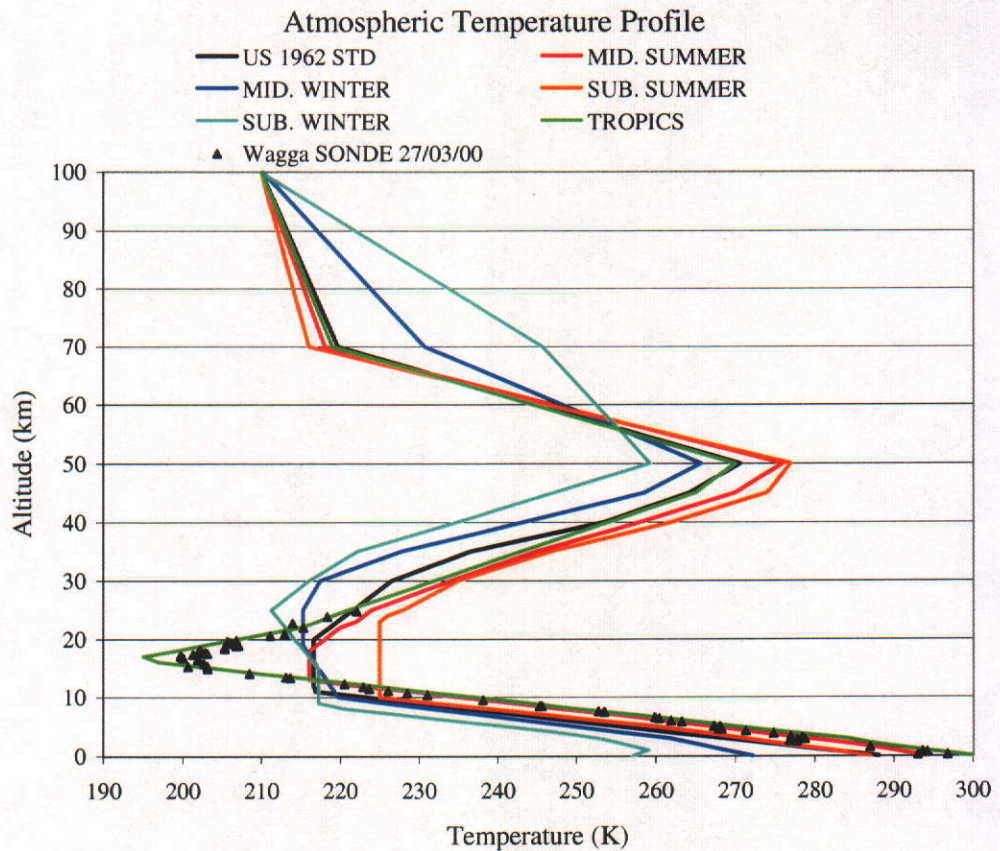


Figure 2.5: Atmospheric temperature profiles from the Wagga Wagga radiosonde (triangles) on March 27, 2000 and the 6 atmospheric models used in 6S.

with that derived from the Wagga Wagga radiosonde for March 27 2000 is given in Table 2.2. The agreement between radiosonde-derived lapse rate and that calculated for a mid-latitude summer is once again observed.

2.2.2 Water in the Atmosphere

Of all the constituents of the Earth's atmosphere, water is the only compound that can be present in all three phases (i.e., solid, liquid or gas). Clouds of liquid or solid water have a rather obvious impact on solar radiation in the visible region of the EM spectrum. A view of the Earth from space reveals that some clouds can completely obscure a view of the surface. Much of the incident solar radiation is reflected back into space, and it is only in certain wavelength regions, from the shortwave infrared through to the thermal infrared, that clouds may become transparent. The importance of water in its gaseous

Table 2.2: Comparison of atmospheric temperature lapse rates δ derived from the Wagga Wagga radiosonde and some standard atmospheric models.

Temperature Profile	δ (K/km)
Wagga Sonde	-5.94
MLS	-5.98
MLW	-5.41
SubS	-6.22
SubW	-4.88
TROP	-6.33
US62	-6.49

form, or *water vapour*, particularly its impact on the propagation of EM radiation, has been the focus of too many authors to mention here. These interactions may be modelled with software packages such as 6S (Vermote et al., 1997b) or MODTRAN4 (Anderson et al., 2000). Knowledge of the total amount of water vapour in the atmospheric column, also known as *precipitable water*, is required for accurate modelling.

Precipitable water at any given time may be estimated indirectly from satellite (King et al., 1992; Gao and Kaufman, 1999) or airborne (Roberts et al., 1997) measurements of reflected solar radiation, from surface measurements of temperature and water vapour pressure (Prata, 1996; Niemelä et al., 2001) and direct-beam solar spectra irradiance (Prata, 2000), or traditionally with profiling instrumentation such as radiosondes. For this thesis, estimating water vapour concentrations from radiosonde measurements alone shall be considered.

Estimating Precipitable Water Values

Total precipitable water u_{H_2O} is defined as the total mass of water vapour in the atmospheric column and has unit g/cm². Apart from measuring atmospheric pressure P and temperature T , radiosondes also measure a quantity known as the mass mixing ratio m_r (sometimes referred to as the specific humidity), with units g/kg, and represents the ratio of the density of water vapour to the density of air. That is,

$$m_r = \frac{\rho_{wv}}{\rho_{wv} + \rho_{da}} \quad (2.5)$$

where ρ_{wv} and ρ_{da} denote the density of water vapour and dry air respectively. Note that the above quantities are functions of altitude (z).

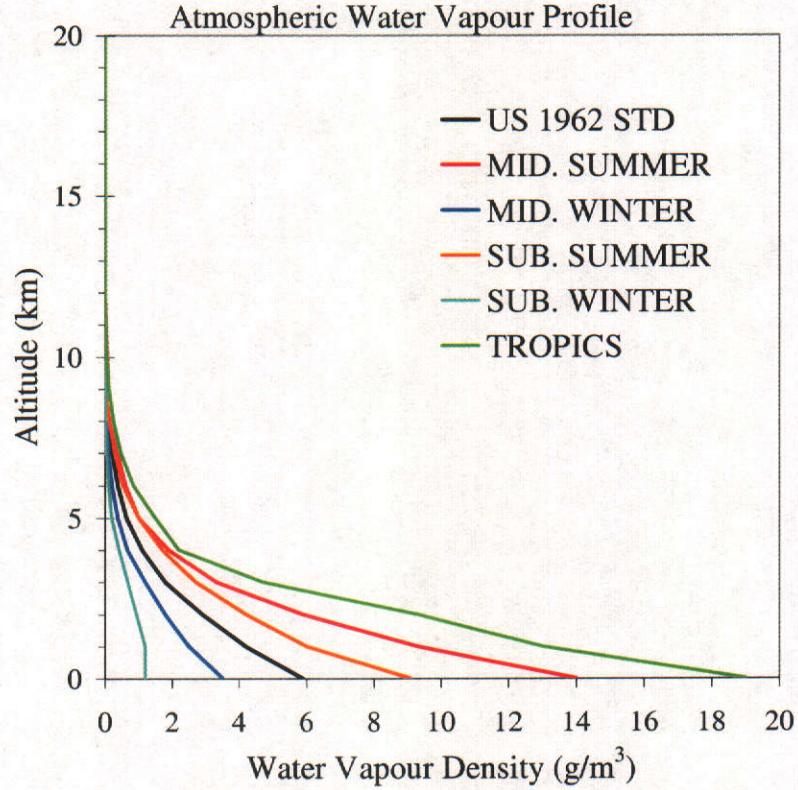


Figure 2.6: Water vapour density profiles for the six model atmospheres used in 6S.

To estimate u_{H_2O} , knowledge of the variation of ρ_{wv} and ρ_{da} with altitude is required. An illustration of the variation of water vapour density with elevation for the six model atmospheres used in 6S is given in Figure 2.6.

The density of dry air at an altitude z can be calculated using

$$\rho_{da}(z) = 1.292 \times 10^{-3} \left(\frac{273.16K}{T(z)} \right) \left(\frac{P(z)}{1013.25hPa} \right) \quad (2.6)$$

(refer to Eq. (A.4), Appendix A, p. 223). Rearranging Eq. (2.5) as

$$\rho_{wv}(z) = \frac{\rho_{da}(z)m_r}{1 - m_r}. \quad (2.7)$$

and using Eq. (2.6), an estimate of total precipitable water in the atmospheric column is calculated as,

$$u_{H_2O} = \int_{z_i}^{z_f} \rho_{wv}(z) dz, \quad (2.8)$$

where z_i and z_f are the initial and final altitudes at which radiosonde measurements were acquired. Applying this approach to the radiosonde data for the Wagga Wagga

Table 2.3: Some values of precipitable water for various bands Latitudes. (Summer conditions only)

Source	Precipitable Water (g/cm ²)		
	Tropical	Mid-Latitude	Sub-Arctic
Junge (1963)	4.1–3.5	3.5–2.1	2.1–1.3
6S Vermote et al. (1997b)	4.12	2.93	2.10
MODTRAN4 Anderson et al. (2000)	4.11	2.92	2.08

Bureau of Meteorology station gives the estimate of $u_{H_2O} = 1.83 \text{ g/cm}^2$. This method of calculating the total amount of precipitable water in the atmosphere will be regarded in this thesis as providing the best estimate. It will be referred to as the *column integrated* approach.

Water vapour pressure, e (with units hPa), represents the contribution that water vapour makes to the total atmospheric pressure. When a parcel of air contains the maximum amount of water for a given temperature, the air becomes saturated. The water vapour pressure associated with a saturated parcel of air is known as the *saturation water vapour pressure* and is denoted as e_s . Relative humidity, RH (measured as a percentage %), gives a measure of the amount of water vapour in the air compared to the maximum amount that can be held at a given temperature. It can be calculated using

$$RH = \frac{e}{e_s} \times 100,$$

and is another quantity that is measured by radiosondes. Appendix A contains formulae for calculating e from radiosonde measurements of P , T and RH .

Spatial Patterns of Precipitable Water

In applications that require estimates of precipitable water for modelling purposes, it is often sufficient to use values approximated from regional climate databases. Such databases consist of the long-term climatology from weather stations sparsely located around the globe. By splitting the globe up into broad bands of equal latitude, some examples of precipitable water values for the tropic, mid-latitude and sub-arctic regions are given in Table 2.3.

For more localised, and accurate, estimates of precipitable water, the column-integrated approach using radiosonde data is a preferable scenario. However, the spatial distribu-

tion of precipitable water estimates is limited to the number of radiosonde launch sites and their proximity to the geographic region of interest. Figure C.1 (Appendix C) gives the location of four radiosonde launch sites around Western Australia. Whilst they are quite far apart, for some studies the spatial resolution of the estimates of precipitable water obtained from the four radiosondes is adequate.

New satellite remote sensing technology (e.g. MODIS, see King et al. (1992)) enables accurate global mapping of precipitable water distribution at high spatial resolution on a daily basis. Some emerging technologies (e.g. GIFTS) promises radiosonde-quality soundings of atmospheric pressure, temperature and water vapour concentration at even higher spatial and temporal resolutions.

2.2.3 Atmospheric Ozone

In terms of abundance, ozone is a relatively minor constituent of the Earth's atmosphere. Yet its role in shielding the Earth's inhabitants from most of the harmful solar radiation is widely known. Particularly well known is the observed thinning of the ozone concentrations over the Antarctic regions in the southern hemisphere spring months. Ozone profiles exhibit a great deal of seasonal and geographical variation. Passive³ ground-based approaches using a statistical curve-fitting procedure for inferring ozone concentration from solar irradiance measurements (King and Byrne, 1976), or active airborne remote sensing techniques, such as LIDAR (Light Detection and Ranging) to measure ozone profiles (Browell, 1989, cited in Stephens (1994)), provide limited spatial information about the distribution of ozone around the globe. Space-borne remote sensing technologies, however, have provided ozone concentrations for almost the entire globe on a daily basis since the 1970s.

Since it is beyond the scope of this thesis to survey all the intricacies that a detailed study of ozone concentrations would entail, some of the profiles of ozone used by standard model atmospheres are briefly presented along with a discussion of widely used space-borne sensors designed to map the horizontal distribution of total ozone concentrations.

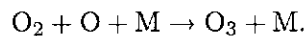
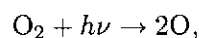
³Unlike *active* approaches for estimating atmospheric ozone concentrations, that involve the sensor/observer sending electromagnetic radiation into the atmosphere and measuring the return signal (echo), *passive* methods involve receiving EM from atmospheric constituents illuminated by an independent source, e.g. the Sun.

Some Model Profiles

Column-integrated (or total) ozone concentrations are measured in g/cm^2 , atmosphere-centimetres (atm-cm) or Dobson units (DU)⁴. In general, ozone concentrations peak in the stratosphere 15–30 km above the Earth’s atmosphere and reduce to zero at an altitude of around 50 km. Ozone concentrations of 4×10^{-5} – 6×10^{-5} g/m^3 can be observed in the troposphere up to about 8 km, as indicated in Figure 2.7, but ozone is by far a stratospheric gas. One of the objectives of the Stratospheric Aerosol and Gases Experiment (SAGE) I, II and III was to gather data concerning the spatial distribution of ozone by mapping vertical profiles from space-borne sensors employing a *limb-profiling*⁵ approach. Figure 2.7 presents six profiles for the model atmospheres used in 6S (Vermote et al., 1997b). The corresponding ozone concentrations for each profile are: US 1962 standard atmosphere, 344 DU; mid-latitude summer, 319 DU; mid-latitude winter, 395 DU; sub-arctic summer 345 DU; sub-arctic winter 480 DU; and tropical, 247 DU.

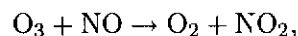
An explanation for the observed peak in ozone (O_3) concentration in Figure 2.7 is given by considering the following:

- Concentrations of oxygen gas (O_2) decrease with increasing altitude.
- Ozone is created when oxygen gas and atomic oxygen combine in the presence of sunlight (with energy $h\nu$) and a neutral third agent M (N_2 , for example). That is,



Reduced O_2 concentrations above 15–20 km mean that less ozone is created via the above process.

- Ozone is destroyed when it absorbs EM radiation of an appropriate energy level to lead to dissociation. That is,



⁴The Dobson unit represents the thickness (in mm) of the slab of ozone that results when the atmospheric column is brought to standard temperature and pressure and multiplied by a factor of 100. For example, a reading of 300 DU would correspond to a slab of ozone at STP of 3 mm. Also note that $1000 \text{ DU} = 1 \text{ atm-cm}$.

⁵When a space-borne sensor’s line-of-sight to the Sun is intercepted by the Earth’s atmosphere, a profile results from the Sun appearing to set behind the Earth.

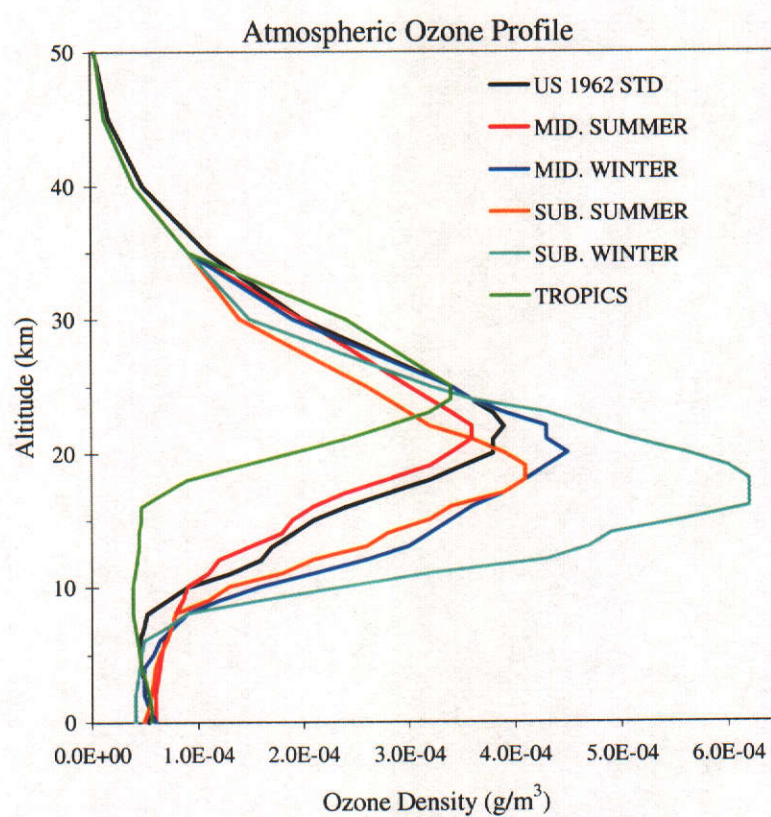
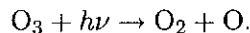


Figure 2.7: Atmospheric ozone profiles for the six model atmospheres used in 6S.



- A consequence of ozone destruction is that very little EM radiation of sufficient energy to lead to ozone creation penetrates to the lower levels of the atmosphere.

For further details on ozone creation and destruction, the reader is directed to Junge (1963).

The processes described above keep the concentration of ozone fairly constant, and it is only when an introduced agent, fulfilling the role of M, inhibits the formation of ozone (such as the infamous CFCs) that the equilibrium no longer exists. Clearly the rate of ozone destruction is at its peak when ozone is exposed to the solar radiation. At the subpolar latitudes in the winter months, very little solar exposure is present for dissociation to occur and consequently (Junge, 1963), ozone concentrations for the sub-arctic regions will, in comparison to other latitudes, be greater.

Mapping Total Ozone Concentrations from Space

Spatial distributions of total ozone concentration have been provided by space-borne sensors since 1978. The sensor used, the total ozone mapping spectrometer (TOMS), has been on board the Nimbus-7 (November 1978–1993), Meteor-3 (August 1991–November 1994), ADEOS (July 1996–June 1997) and Earth Probe (July 1996–) satellites.

TOMS provides an estimate of total ozone concentration by comparing the relative strength of the signal backscattered by the atmosphere for a small number (six for the Earth Probe TOMS) of wavelength bands located in the ultraviolet region of the EM spectrum known as the Hartley-Huggins bands (Stephens, 1994, p. 272). Further details are given in McPeters et al. (1998).

The TOMS provides high-quality estimates of ozone concentrations for spatial resolutions of $200 \times 200 \text{ km}^2$ (Nimbus-7 TOMS) down to $40 \times 40 \text{ km}^2$ resolution (Earth Probe TOMS). The Earth Probe TOMS, for example, achieves a $\pm 3\%$ absolute error, $\pm 2\%$ random error and a systematic error of at most $\pm 0.6\%$ resulting from a drift in sensor responsivity after the first 1.5 years of operation (McPeters et al., 1998). It has been shown that the TOMS estimates (from Nimbus-7 to Earth Probe) generally agree with measurements from ground-based stations to within 1% (McPeters et al., 1998).

Since mid-1995 the Global Ozone Monitoring Experiment (GOME) on the ERS-2

satellite (European Space Agency (ESA)) has provided daily estimates of ozone concentration and profile for any location on the globe. The instrument, which measures solar radiation reflected by the earth-atmosphere system over four channels in the wavelength range 240–790 nm, derives an estimate of total ozone concentration, employing differential absorption spectroscopy, with an absolute accuracy of $\sim 3\%$. A more recent instrument, on ESA’s ENVISAT (ENVironmental SATellite) and known as Global Ozone Monitoring by Occultation of Stars (GOMOS) seeks to estimate ozone, and some trace gas, profiles by maintaining line-of-sight to a set of stars sets through the atmosphere (Wehr et al., 2002).

2.2.4 Other Gases

Apart from water vapour (H_2O) and ozone (O_3), other gases that play an important role in influencing EM radiation in the wavelength regions between 400–2500 nm are (Vermote et al., 1997b; Vermote, 2002): oxygen (O_2); methane (CH_4); carbon dioxide (CO_2); carbon monoxide (CO); nitrous oxide (N_2O) and nitrogen dioxide (NO_2). Compared to the spatial distribution of atmospheric water vapour and ozone, these so called *other gases* are uniformly mixed and vary with altitude and temperature and pressure profiles in the fashion to be described in Section 2.3.3 (p. 28).

2.2.5 Atmospheric Aerosols

Aerosols are suspended particulates in the Earth’s atmosphere. The impact of aerosols on remotely sensed observations, solar radiation and climate variability has been discussed by many authors (examples are given the following). The varying spatial and temporal patterns of aerosol; their size and number distributions, different composition and absorption characteristics, make monitoring aerosol distributions and concentrations more elusive than the molecular counterparts—whose characteristics are relatively well understood. Much research, therefore, has been directed towards monitoring aerosol spatial distributions using both ground-based networks and remote sensing technologies. The following discussion considers only *passive* approaches to measuring aerosol properties. However *active* approaches such as Lidar have been used in monitoring aerosols, in particular their role as cloud condensation nuclei (CCN).

Aerosol Types and Sizes

The primary, or direct, sources of aerosols in the Earth's atmosphere are natural in origin. For example, aerosols can be windswept sand or dust from weathered or eroded surfaces, ash and soot from volcanic eruptions or forest fires, or sea spray resulting from the burst of bubbles and subsequent *jet drop* at the ocean surface (Twomey, 1977; d'Almeida et al., 1991). While some of the sources of natural aerosol may result from human activity, manmade sources of aerosol are typically due to pollutants and industrial emissions. An example of four aerosol types (or models) described by d'Almeida et al. (1991) are:

1. *Continental or rural aerosols*—described as those aerosols found in remote, pollution-free continental areas such as non-forested savannah and rural environments (clean-continental); or airborne particulates in regions slightly affected by industrial activity, traffic, and other anthropogenic activities (average-continental).
2. *Urban or industrial aerosols*—aerosols located in regions of high man-made pollution, from, for example, industrial power plants, residential sources or traffic.
3. *Desertic aerosols*—originating in arid or semi-arid regions of the world; these aerosols are mineral particles that, under favourable meteorological conditions, are transported into the atmosphere.
4. *Maritime aerosols*—burst bubbles at the ocean's surface, and the resulting jet drops occurring in the remote maritime environments, well away from coastal areas, are called clean-maritime aerosols. In the vicinity of polluted cities where continental airmasses encounter the marine environment (particularly near industrialised harbours or polluted regions) aerosols are termed marine-polluted.

For the scope of this thesis, the various aerosol types impact the form of *phase functions* and *single scattering albedo* (Section 2.3.5).

The characteristic difference between molecules and aerosols in the atmosphere is their respective size characterised by a radius, r . Molecules have a radius on the order of 0.1 nm, while aerosols can have a range of radii from 100–1000 nm. Aerosols are classed into three groups according to their radius. They are (i) *Aitken particles* ($r \leq 100$ nm); (ii) *large particles* ($100 < r \leq 1000$ nm); and *giant particles* (with $r > 1000$ nm).

Cloud droplets, however, which are considered a special subgroup of atmospheric aerosols (Twomey, 1977), can have radii from 10^4 nm (in clouds) to 1 mm (as rain drops). An understanding of the aerosol size and number distributions is not essential to the scope of this thesis and shall not be discussed here. The author acknowledges however, the importance of these parameters, particularly their impact on the form of the aerosol phase function (see Section 2.3.5).

Vertical Distribution of Aerosols

Aerosols generally reside in the troposphere; that is, below altitudes of around 12 km. Stratospheric aerosol concentrations are generally quite small except after volcanic eruptions which inject masses of sulphate (SO_4) particles into the stratosphere; in some cases increasing the concentrations by two orders of magnitude (Kaufman et al., 1997a; King et al., 1999). One of the objectives of SAGE I, II and III was to retrieve aerosol profiles by employing solar occultation (another name for limb-sounding). However, as Box and Box (2001) point out, the approach works well in the stratosphere but not the troposphere. Thus for the remainder of this thesis, unless stated otherwise, aerosols will be implied to mean tropospheric aerosols.

Monitoring Spatial Distributions of Aerosol

The significance of measuring atmospheric aerosol properties lies in their direct and indirect impact on the Earth's atmosphere. Aerosols directly affect the solar radiation budget by scattering and absorbing the solar irradiance as it propagates through the Earth's atmosphere. Measuring and monitoring aerosol properties has value in gaining an understanding of their impact on climate and the radiative budget, their role as condensation nuclei in cloud/haze formation (d'Almeida et al., 1991; King et al., 1992; Box and Box, 2001), and their effects on space- or air-borne measurements of surface reflectance (Kaufman, 1984; Fraser and Kaufman, 1985; Kaufman and Brakke, 1986). Kaufman et al. (1997b) state that a satellite-based approach to measuring the spatial distributions of aerosol concentrations has the potential of offering regional to global mapping on a monthly, weekly and even daily basis; providing the routine monitoring necessary to gain a fuller understanding of aerosol characteristics, their sources and sinks. The area of passive remote sensing of aerosol properties is reviewed in Kaufman et al.

(1997a), King et al. (1999), and Dubovik et al. (2002). A method for estimating aerosol concentrations with satellite-based observations will be described in Chapter 3.

Aerosol concentrations are also monitored with ground-based instruments. Networks of solar photometers measure atmospheric optical thickness (see Section 2.3.3), from which total (columnar) aerosol concentrations are derived. The Aerosol Robotic Network (Holben et al., 1998, AERONET) is one such network with solar photometers spread around the globe, the data from which has been used in studies of optical thickness (Formenti et al., 2002) and absorption and size distribution (Dubovik et al., 2002). Apart from providing important global-scale information on aerosols and their influence on climate, these ground-based instruments and methods (Section 2.3.3) provide crucial validation for space-borne measurements (Holben et al., 1998).

2.3 Radiative Transfer in the Terrestrial Environment

Section 2.1 described the sources of variation in the solar irradiance spectrum, prior to the solar radiation encountering the Earth’s atmosphere. Section 2.2 described some of the constituents of the terrestrial atmosphere—specifically molecules and aerosols with concentrations that vary considerably, both geographically and vertically; on temporal scales from minutes to decades. This section describes the interaction of the solar irradiance with the molecules and aerosols in the atmosphere and describes the mathematical formalisms that lead to a simplified version of the *radiative transfer equation*, which provides a quantitative model of the satellite-measured signal of emergent radiation from the earth-atmosphere system.

2.3.1 Radiance and Irradiance

Radiance denoted L_λ is the contribution of electromagnetic power incident on a unit area dA by a *cone of radiation* subtended by a solid angle $d\omega$ (in steradians, sr) at an angle θ to the surface normal. It has units $\text{W}/\text{m}^2/\text{sr}$ and is expressed mathematically as,

$$L_\lambda(\theta, \phi) = \cos(\theta) d\omega dA.$$

In spherical polar coordinates, $d\omega = \sin(\theta)d\theta d\phi$ where θ and ϕ are the *zenith*⁶ angle and *azimuth*⁷, respectively. If the radiance from the Sun incident at the TOA is denoted $L_{inc\lambda}$, then the solar *irradiance*⁸ is obtained by integrating over all possible zenith angles and azimuth directions, that is,

$$F_{d\lambda} = \int_0^{2\pi} \int_0^{\pi/2} L_{inc\lambda} \sin(\theta) \cos(\theta) d\theta d\phi. \quad (2.9)$$

Defining μ as the cosine of the zenith angle, let the above be rewritten as

$$F_{d\lambda} = \int_0^{2\pi} \int_0^1 L_{inc\lambda} \mu d\mu d\phi. \quad (2.10)$$

If a radiation field is termed *isotropic*, then at any point in the field the intensity of measured radiation is independent of the direction of observation (i.e., independent of θ and ϕ). In this case, Eq. (2.10) is evaluated to yield,

$$F_{d\lambda} = \pi L_{inc\lambda},$$

which can be rearranged to give the expression for radiance,

$$L_{inc\lambda} = \frac{F_{d\lambda}}{\pi}. \quad (2.11)$$

If the illuminating radiation is composed of parallel beams emanating from the direction (μ_0, ϕ_0) , then

$$L_{inc\lambda} = \frac{F_{d\lambda}}{\pi} \delta(\mu - \mu_0) \delta(\phi - \phi_0), \quad (2.12)$$

(Chandrasekhar, 1960, p. 22) which is equivalent to Eq. (2.11) when $\mu = \mu_0$ and $\phi = \phi_0$.

2.3.2 The Absorbing and Scattering Atmospheres

The two dominant mechanisms affecting the propagation of EM radiation of wavelengths between 400–2500 nm in the terrestrial atmosphere are *absorption* and *scattering*. In this thesis, absorption and scattering are treated as two separate events, although their combined effect is known as *extinction*.

Propagation of EM radiation through the atmosphere is often regarded as independent of azimuth direction, ϕ , and the intensity of radiation changes as a function of

⁶A zenith angle is a vector's angular deviation from an outward normal to the Earth's surface.

⁷Azimuth is the horizontal angular variation of a vector from a reference direction (usually in the direction of motion or true north).

⁸Solar irradiance, also known as total radiant flux per unit area—or radiant flux density—is denoted here as $F_{d\lambda}$, that is corrected for Earth-Sun distance, to distinguish it from solar irradiance at the mean Earth-Sun distance $F_{0\lambda}$ (see p. 8).

zenith angle, θ . Recall that θ represents the inclination of a vector in the direction of propagation with the outward normal to the Earth's surface, and that $\mu = \cos(\theta)$.

In the following discussion we shall refer to the absorbing atmosphere (mainly corresponding to the gases, although aerosol absorption, discussed later, is comparatively marginal) and the scattering atmosphere (the molecules and aerosols).

The degree with which molecules and aerosols absorb and scatter EM radiation is highly dependent on the particular wavelength region of the EM spectrum under consideration. To limit the problem, discussion here is restricted to wavelengths between 400–2500 nm.

2.3.3 Optical Thickness

A measure of the opacity or turbidity of the atmosphere for a given wavelength of EM radiation is the quantity called *optical thickness* (or often optical depth). From an altitude z above the Earth's surface to the top of the atmosphere, the total optical depth is calculated as,

$$\tau_{\text{tot}\lambda} = \int_z^{\infty} \kappa_{\text{tot}\lambda} \delta_{\text{atm}} dz,$$

where $\kappa_{\text{tot}\lambda}$ is the total extinction coefficient (which can be specified for each of the molecular species in the atmosphere) and δ_{atm} is the density of the intervening atmosphere between z and the top of the atmosphere. For the absorbing and scattering atmospheres we have respectively the absorbing and scattering optical thicknesses $\tau_{\text{abs}\lambda}$ and $\tau_{\text{diff}\lambda}$.

Absorbing Atmosphere

The absorbing gases in the atmosphere that most impact EM radiation in the wavelength region of interest are water vapour (H_2O), ozone (O_3) and, to a lesser extent, the other gases described in Section 2.2.4. For each of these gases, an optical thickness can be calculated given the concentration of the gases in the atmospheric column. The optical thickness of the absorbing atmosphere $\tau_{\text{abs}\lambda}$ is then a sum of the optical thickness for each species, that is

$$\tau_{\text{abs}\lambda} = \sum_{g=\text{H}_2\text{O}, \text{O}_3, \text{CO}_2, \text{CH}_4, \dots} \tau_{g\lambda},$$

and the transmittance through the absorbing atmosphere in the direction μ can be represented as the simple product of transmittance values for the individual gases, that

is

$$T_{\text{abs}\lambda}(\mu) = \prod_{g=\text{H}_2\text{O}, \text{O}_3, \text{CO}_2, \text{CH}_4, \dots} T_{g\lambda}, \quad (2.13)$$

where expressions for $T_{g\lambda}$ for some gases are presented below.

To EM radiation of certain wavelengths the absorbing atmosphere appears transparent ($\tau_{\text{abs}\lambda}$ is essentially zero) and the transmittance at these wavelengths is unity. Wavelength regions where $T_{\text{abs}\lambda} = 1$ are called *atmospheric windows*, and often satellite sensors that image or map features on the Earth's surface are designed to sense in these regions. Unfortunately at wavelengths beyond 1000 nm, signal levels decrease and satellite sensor bandwidths increase. Therefore, it is rare that sensor bands are entirely in the atmospheric windows and it is important to correct for the effects of gaseous absorption (discussed further in Section 3.3.3, p. 84).

Some Expressions for Direct Transmittance

A standard expression for calculating the direct transmittance of a beam of radiation at an angle θ off nadir through water vapour is the power law (Ouaidrari and Vermote, 1999; Prata, 2000),

$$T_{\text{H}_2\text{O}\lambda}(\mu) = \exp \left[-\alpha_{\text{H}_2\text{O}\lambda} (u_{\text{H}_2\text{O}} m)^{\beta_{\text{H}_2\text{O}\lambda}} \right], \quad (2.14)$$

where $u_{\text{H}_2\text{O}}$ is the column integrated value of precipitable water (see Section 2.2.2), $m = 1/\mu$, and $\alpha_{\text{H}_2\text{O}\lambda}$ and $\beta_{\text{H}_2\text{O}\lambda}$ are wavelength-dependent coefficients. Similarly, an expression for direct transmittance for ozone that is often used is the Beer-Lambert-Bouguer law⁹

$$T_{\text{O}_3\lambda}(\mu) = \exp[-\alpha_{\text{O}_3\lambda} u_{\text{O}_3} m] \quad (2.15)$$

where u_{O_3} is the total ozone concentration for the atmospheric column, and $\alpha_{\text{O}_3\lambda}$ is the wavelength-dependent ozone absorption coefficient (see for example Brion et al. (1998)).

For the other gases (OG) in the absorbing atmosphere, an expression often used for calculating the direct transmittance (Ouaidrari and Vermote, 1999) is,

$$T_{\text{OG}\lambda}(\mu) = \prod_{g=\text{O}_2, \text{CH}_4, \text{CO}_2, \dots} \exp \left[-\alpha_{g\lambda} \left(\frac{P_s}{P_0} m \right)^{\beta_{g\lambda}} \right],$$

⁹The Beer-Lambert-Bouguer law states that, the intensity of radiation that passes through a slab of medium with optical thickness τ , at an angle θ to normal incidence, is reduced by the factor $\exp(-\tau/\mu)$. Also recall that $\mu = \cos(\theta)$.

where P_s and P_0 are the surface and standard pressures ($= 1013.25$ hPa) respectively. Generally all gaseous absorption is dependent on pressure and temperature profiles (Vermote et al., 1997b). Broadening of the absorption features in gaseous transmittance spectra results from pressure-induced collisions (*Lorentz* broadening; dominating at high pressures) and thermal motion (*Doppler* broadening; dominating at high altitudes).

Scattering Atmosphere

One of the characteristics defining molecules and aerosols is their respective size or radii (see Section 2.2.5), and the way in which they scatter EM radiation is also related to their size. The branch of scattering theory that deals with EM radiation scattered by molecules (where the wavelengths are much larger than the physical dimensions of the scattering object) is called *Rayleigh scattering theory*; for aerosols (with comparable dimensions to the wavelengths of radiation) it is *Mie scattering theory*. As Twomey (1977) pointed out, Rayleigh scattering theory is a special case of the more encompassing Mie theory.

The optical thickness of the scattering atmosphere, denoted $\tau_{\text{diff}\lambda}$, is given as,

$$\tau_{\text{diff}\lambda} = \tau_{\text{R}\lambda} + \tau_{\text{M}\lambda},$$

where the $\tau_{\text{R}\lambda}$ and $\tau_{\text{M}\lambda}$ denote the molecular (or Rayleigh) optical thickness and aerosol (or Mie) optical thickness respectively. More on the mathematical forms for the optical thickness is given below.

Calculating Molecular Optical Thickness

Molecular optical thickness may be computed with the following expression:

$$\tau_{\text{R}\lambda} = \frac{8\pi^3(n_{a\lambda}^2 - 1)^2 N_c}{3\lambda^4 N_s^2} \left(\frac{6 + 3\gamma}{6 - 7\gamma} \right) \left(\frac{P_s}{1013.25} \right) \left(\frac{288.15}{T_s} \right). \quad (2.16)$$

Some of the terms in Eq. (2.16) require detailed explanations, the more obvious terms however are: λ denoting the wavelength in micrometers (μm); P_s and T_s , the surface pressure and temperature values (in hPa and K) respectively; the columnar number density N_c ($= 2.154 \times 10^{25} \text{ cm}^{-2}$ for standard conditions); and N_s which is the molecular number density ($= 2.547 \times 10^{19} \text{ cm}^{-3}$ for standard conditions).

The *refractive index* of dry air is denoted as $n_{a\lambda}$. The variation of refractive index with wavelength is expressed with the *dispersion equation* mentioned in Peck and Reeder

(1972) as,

$$(n_{a\lambda} - 1) \times 10^8 = 8342.13 + \frac{2406030}{130 - \lambda^{-2}} + \frac{15997}{38.9 - \lambda^{-2}}, \quad (2.17)$$

where wavelength (λ) is expressed in μm . Equation (2.17) is valid for dry air at standard pressure (1013.25 hPa) and 288.15 K, which explains the appearance of these values in Eq. (2.16). Peck and Reeder (1972) present the following dispersion equation which they observed to be a better fit to observational data than Eq. (2.17), particularly in the near-infrared regions 0.9–1.7 μm :

$$(n_{a\lambda} - 1) \times 10^8 = \frac{5791817}{238.0185 - \lambda^{-2}} + \frac{167909}{57.362 - \lambda^{-2}}. \quad (2.18)$$

Disagreement between the value of n_a calculated with (2.17) and (2.18) is very small, with the greatest discrepancy (observed in the region 800–2000 nm) on the order of $10^{-7}\%$. A value for the refractive index of dry air at 1013.25 hPa and 288.15 K at 590 nm is $n_{a\lambda} = 1.00028$.

The scattering of *natural light*¹⁰ by anisotropic molecules (e.g. N₂, O₂, CO₂) with random orientations was reviewed by Chandrasekhar (1960, p. 45-50) and Young (1981). When natural light is scattered by a molecule, the scattering event can be termed either *elastic*—where the scattered radiation observes no loss of energy; or *inelastic*—where the energy of the scattered radiation is different to the incident energy, and there has been a shift in the wavelength of radiation, i.e. *Raman-shifted*¹¹. A detailed explanation of the interaction of EM radiation at the atomic and molecular levels is given in Loudon (1983, Ch.8).

Anisotropic molecules alter the angular distribution of scattered light and increase the total scattering by the factor (in Eq. (2.16)),

$$\frac{6 + 3\gamma}{6 - 7\gamma},$$

where γ is termed the *depolarisation ratio* for dry air. Young (1980) gave a value for $\gamma = 0.0279$ that incorporates Raman-shift effects, which become prominent when molecules are strongly anisotropic (Young, 1980). Other authors have received criticism for using depolarisation ratios that do not take into account Raman effects; the error

¹⁰The term *natural light* is often used to refer to unpolarised light. Unpolarised light can be thought of as transverse waves with random orientation, i.e. no preferred direction of vibration.

¹¹The *Raman effect* is observed when light scattered from a molecule has a different wavelength to the incident light, and is said to be Raman-shifted. A change in wavelength results in a change of energy in the scattered beam since $E = hc/\lambda$.

resulting from the use of these incomplete values of γ in calculating molecular optical thickness, has been demonstrated to be around 4% (Young, 1980, 1981; Teillet, 1990).

Teillet (1990) reviewed various other expressions for calculating the molecular optical thickness and used Eq. (2.16) as a reference. One of these other expressions was that of Fröhlich and Shaw (1980),

$$\tau_{R\lambda} = \left(\frac{P_s}{1013.25} \right) (\alpha + \beta z) \lambda^{-(3.91+0.074\lambda+0.05/\lambda)}, \quad (2.19)$$

where λ is the wavelength in μm , P_s is the surface pressure (hPa), z is the elevation above sea level (in m), and α and β are seasonal- and latitudinal-specific coefficients given by the authors. Equation (2.19) is based on a least-squares curve fitting to values of τ_R calculated with Eq. (2.16) for a number of standard atmospheric profiles and incorporates Rayleigh scattering from water vapour.

Measuring Aerosol Optical Thickness

Spectral estimates of aerosol optical thickness can be obtained by subtracting molecular optical thickness and any absorption optical thickness values from the total optical thickness. This is expressed mathematically by numerous authors (e.g. Junge (1963, p. 143)) as,

$$\tau_{M\lambda} = \tau_{\text{tot}\lambda} - \tau_{R\lambda} - \tau_{\text{abs}\lambda} \quad (2.20)$$

Indeed, Eq. (2.20) is the basis behind many ground-based instruments designed to measure aerosol concentrations (refer to Section 2.2.5). Retrieving aerosol optical thickness from surface extinction measurements of solar irradiance will briefly be discussed in the following, while some methods for estimating aerosol optical thickness from space-borne measurements will be discussed in Chapter 3 (pp. 103–109).

The measurement of solar irradiance is known as *solar photometry*, and the instrument used to acquire these measurements is known as a *solar photometer*. Earth- or ground-based solar photometers measure the reduction in intensity of radiation along a direct beam from the Sun to the solar photometer. From these measurements, estimates of the atmospheric turbidity, or total optical thickness, may be inferred. The solar irradiance measured by a solar photometer at the Earth's surface assumes the form of the Beer-Lambert-Bouguer law,

$$I_{\text{sol}\lambda} = F_{0\lambda} \exp(-\tau_{\text{tot}\lambda}/\mu_0), \quad (2.21)$$

where $F_{0\lambda}$ is the solar irradiance at the TOA, $\tau_{\text{tot}\lambda}$ is the total atmospheric optical thickness and μ_0 is the cosine of the solar zenith angle θ_0 .

To retrieve atmospheric optical thickness values from the ground-based solar irradiance measurement, the *Langley* method (Harrison and Michalsky, 1994) of analysis, in which measurements of $I_{\text{sol}\lambda}$ are made for a number of different values of θ_0 , is often employed. In logarithmic form, Eq. (2.21) becomes,

$$\ln(I_{\text{sol}\lambda}) = \ln(F_{0\lambda}) - \tau_{\text{tot}\lambda}/\mu_0. \quad (2.22)$$

It can be seen from Eq. (2.22) that given different values of $I_{\text{sol}\lambda}$ acquired for different values of θ_0 , and assuming that the atmosphere does not change considerably over the time that measurements were made, an estimate of $\tau_{\text{tot}\lambda}$ can be retrieved from linear regression. The quantity $1/\mu_0$ is known as the *airmass*. Using the time series of irradiance measurements and Eq. (2.22) to extrapolate to zero airmass, an estimate of the solar constant $F_{0\lambda}$ for a given wavelength can be calculated; which may serve as a diagnostic check for the solar photometer.

The Multi-Filter Rotating Shadowband Radiometer (Harrison and Michalsky, 1994, MFRSR) is an example of a solar photometer that utilises the Langley method for estimating total atmospheric optical thickness. The MFRSR measures a time series of total-horizontal, diffuse-horizontal and direct-normal irradiance values at six narrow (~ 10 nm FWHM) bands between 400–960 nm, and one broadband silicon detector band. The total-horizontal irradiance, $I_{\text{total}\lambda}$, is the measurement made by the MFRSR of the entire sunlit hemisphere. A rotating arm holding a narrow metal strip occludes the Sun from the sensor to obtain the diffuse-horizontal irradiance, $I_{\text{diffuse}\lambda}$. The direct-normal contribution, $I_{\text{dirnorm}\lambda}$, is defined as the irradiance that is incident a surface normal to the direct beam. It is calculated by subtracting the diffuse-horizontal irradiance from the total-horizontal irradiance and dividing by the cosine of the solar zenith angle, i.e.

$$I_{\text{dirnorm}\lambda} = (I_{\text{total}\lambda} - I_{\text{diffuse}\lambda})/\mu_0.$$

For an MFRSR, the measured solar irradiance (Eq. (2.21)) $I_{\text{sol}\lambda} = I_{\text{dirnorm}\lambda}$. For some MFRSRs (Harrison and Michalsky, 1994; Holben et al., 1998; Prata, 2000), $I_{\text{sol}\lambda}$ data are stored as 1- or 2-minute averages. These instruments, therefore, acquire high temporal resolution time series of irradiance measurements (an example is given in Figure 4.5, p. 133).

To retrieve total atmospheric optical thickness estimates from MFRSR data, the time series of irradiance measurements is used and the Langley method of analysis is applied to each band—with the exception of the band around 933.2 nm because of the power law behaviour of water vapour attenuation at those wavelengths (e.g. Eq. (2.14, p. 27). An estimate of $\tau_{\text{tot}\lambda}$ is the slope of the line derived from linear regression of Eq. (2.22) using the morning (AM) or afternoon (PM) irradiance data (Figure 4.6, p. 133, provides an illustrative example). Moreover, since at small zenith angles (small airmasses) there is a greater likelihood of changes in atmospheric conditions affecting Langley analysis, and that at large zenith angles (large airmasses) atmospheric refraction plays a significant role in distorting irradiance measurements, it is suggested (Harrison and Michalsky, 1994; Formenti et al., 2002) regression should only include those data acquired for airmasses between 2–6. It is also recommended that a robust regression procedure be employed in estimating $\tau_{\text{tot}\lambda}$, since patches of cloud in the data translate into outliers in the regression analysis; and ordinary least squares estimates are very sensitive to outliers.

Atmospheric water vapour strongly attenuates the signal in the MFRSR 933.2-nm band. For the three other bands, it is atmospheric ozone that is the dominant absorbing gas. In fact, these three MFRSR bands are located in what is known as the *Chappuis band* (see Figure B.1, Appendix B), and Eq. (2.20) becomes,

$$\tau_{\text{M}\lambda} = \tau_{\text{tot}\lambda} - \tau_{\text{R}\lambda} - \tau_{\text{O}3\lambda}. \quad (2.23)$$

Spectral variation of $\tau_{\text{M}\lambda}$ is often assumed to follow a Ångström-type relationship. That is,

$$\tau_{\text{M}\lambda} = A\lambda^{-B}, \quad (2.24)$$

where A and B are the Ångström coefficient and exponent respectively. The aerosol optical thickness can be extrapolated to any wavelength region of interest, given estimates of A and B . Furthermore, if a value of aerosol optical thickness $\tau_{\text{M}\lambda_0}$ is known, or measured, at reference wavelength λ_0 , then Eq. (2.24) yields,

$$\tau_{\text{M}\lambda} = \tau_{\text{M}\lambda_0} \left(\frac{\lambda}{\lambda_0} \right)^{-B}. \quad (2.25)$$

Typical values of the Ångström exponent, B , for Mie scattering range from 1–1.8 (Junge, 1963; Twomey, 1977; Prata, 2000; Formenti et al., 2002).

2.3.4 Diffuse Reflection and Transmission

Initially, consideration is only given to propagation of the Sun's EM radiation through the Earth's scattering atmosphere and the resulting *diffuse radiation field*. Diffuse radiation is a result of natural light undergoing either one scattering event (*single scattering*) or many scattering events (*multiple scattering*). Note that the single scattering approximation is only valid for relatively clear atmospheres with low opacity (i.e. small $\tau_{\text{diff}\lambda}$).

Some Definitions and Assumptions

Fundamental to the treatment of the radiative transfer presented here, are the assumptions that the atmosphere can be stratified into horizontally homogeneous layers (hereafter referred to as a *plane-parallel* atmosphere), and that the scattering atmosphere is bound on two sides with optical thicknesses $\tau = 0$ and $\tau = \tau_{\text{diff}\lambda}$.

The direction of propagation of EM radiation incident at the TOA or Earth's surface from the Sun will be denoted by zenith angle, θ_0 , and azimuth, ϕ_0 . Similarly, the direction of EM radiation emerging from the Earth's surface-atmosphere system is denoted by zenith angle, θ , and azimuth ϕ . For consistency with the notation of most authors in the field, $\mu_0 = \cos(\theta_0)$ and $\mu = \cos(\theta)$. Finally, terms *inward* and *outward* are used to describe the propagation towards the surface of the Earth (the negative $(-)$ direction), and from the surface of the Earth to space (the positive $(+)$ direction) respectively.

Finally, for a plane-parallel, horizontally-homogeneous atmosphere of optical thickness $\tau_{\text{diff}\lambda}$, we denote the diffusely reflected radiance from the TOA as $L_\lambda(0; +\mu, \phi)$, and the radiance transmitted to the bottom of the atmosphere as $L_\lambda(\tau_{\text{diff}\lambda}; -\mu, \phi)$.

Reflection and Transmission Functions

The *reflection* and *transmission* functions are defined for a scattering atmosphere illuminated by solar irradiance, $F_{\text{d}\lambda}$, from the direction (μ_0, ϕ_0) as,

$$S(\tau_{\text{diff}\lambda}; \mu, \phi; \mu_0, \phi_0) = \frac{\pi L_\lambda(0; +\mu, \phi)}{F_{\text{d}\lambda} \mu_0} \quad (2.26)$$

and

$$T(\tau_{\text{diff}\lambda}; \mu, \phi; \mu_0, \phi_0) = \frac{\pi L_\lambda(\tau_{\text{diff}\lambda}; -\mu, \phi)}{F_{\text{d}\lambda} \mu_0}, \quad (2.27)$$

respectively. A *planetary albedo*, the fraction of solar radiation that is diffusely reflected back into space, is defined by integrating Eq. (2.26) over all possible (outward) zenith

and azimuth directions, that is,

$$s_{d\lambda}(\tau_{\text{diff}\lambda}; \mu_0) = \frac{1}{\pi} \int_0^{2\pi} \int_0^1 S(\tau_{\text{diff}\lambda}; \mu', \phi'; \mu_0, \phi_0) \mu' d\mu' d\phi', \quad (2.28)$$

which is assumed (in the above) to be independent of azimuth. The factor of $1/\pi$ ensures that the albedo has a value of at most 1. Similarly, the *diffuse transmittance* is defined as,

$$t_{d\lambda}(\tau_{\text{diff}\lambda}; \mu_0) = \frac{1}{\pi} \int_0^{2\pi} \int_0^1 T(\tau_{\text{diff}\lambda}; \mu', \phi'; \mu_0, \phi_0) \mu' d\mu' d\phi', \quad (2.29)$$

and gives a measure of the fraction of the radiation, incident from the direction (μ_0, ϕ_0) , that is diffusely transmitted through to the bottom of the scattering atmosphere.

An important property of the diffuse reflection and transmission functions is that they satisfy the Helmholtz' reciprocity principle, which states that S and T are unaltered when the direction of incidence and emergence are interchanged (Chandrasekhar, 1960, p. 172).

Finally, integrating Eq. (2.28) over all possible solar zenith angles gives the *spherical albedo*,

$$s_{\lambda}(\tau_{\text{diff}\lambda}) = \int_0^1 s_{d\lambda}(\tau_{\text{diff}\lambda}; \mu') d\mu', \quad (2.30)$$

which is defined as the probability that a photon that has been reflected by the Earth's surface, is then reflected by the atmosphere back towards the surface (which will occur over and over again).

2.3.5 The Radiative Transfer Equation

Modelling the Earth's scattering atmosphere as a plane-parallel homogeneous atmosphere with optical thickness τ illuminated by natural (unpolarised) light, the equation describing the diffuse radiation field propagating outwards in the direction (μ, ϕ) is written mathematically as,

$$\mu \frac{\partial L_{\lambda}(\tau; \mu, \phi)}{\partial \tau} = L_{\lambda}(\tau; \mu, \phi) - J_{\lambda}(\tau; \mu, \phi). \quad (2.31)$$

In the case of a scattering atmosphere with optical thickness $\tau_{\text{diff}\lambda}$, the formal solution of Eq. (2.31) (Chandrasekhar, 1960, p. 12) is,

$$\begin{aligned} L_{\lambda}(0; +\mu, \phi) &= L_{\lambda}(\tau_{\text{diff}\lambda}; +\mu, \phi) \exp(-\tau_{\text{diff}\lambda}/\mu) \\ &+ \int_0^{\tau_{\text{diff}\lambda}} \exp(-\tau'/\mu) J_{\lambda}(\tau'; +\mu, \phi) \frac{d\tau'}{\mu}, \quad \text{and} \end{aligned} \quad (2.32)$$

$$L_{\lambda}(\tau_{\text{diff}\lambda}; -\mu, \phi) = L_{\lambda}(0; -\mu, \phi) \exp(-\tau_{\text{diff}\lambda}/\mu) + \int_0^{\tau_{\text{diff}\lambda}} \exp[-(\tau_{\text{diff}\lambda} - \tau')/\mu] J_{\lambda}(\tau'; -\mu, \phi) \frac{d\tau'}{\mu}, \quad (2.33)$$

where Eqs. (2.32) and (2.33) represent the TOA outward emerging radiance and inward radiance at the Earth's surface respectively. Equation (2.31) is known as the *Radiative Transfer Equation* (RTE) and for a full treatment of the preceding and following discussions, the reader is referred to Chandrasekhar (1960).

The source function J_{λ} contains the mathematical description of the absorption, scattering and emission that needs to be included in the radiative transfer model. Thermal emission, for example, would be included in the RTE as additive contributions through the source function. For the scope of this thesis (400–2500 nm) however, thermal and other energy sources are negligible and J_{λ} will only consider absorption and scattering.

The RTE is an integro-differential equation because, as illustrated in Eq (2.34) below, J_{λ} contains a double integral. Whilst no analytic solution to Eqs. (2.31)–(2.33) exists, there are various approximations that can be made to recast the Eq. (2.31) into a solvable form. It is not the intention of this thesis to review the various approximation schemes. In the following section however, the simplest solution to the RTE is presented since it yields a sufficiently accurate model of the space-borne radiometric signal emerging from the earth-atmosphere system, which has found application in numerous authors' work. The approximation is based on the assumption that the scattering atmosphere is bound at the bottom by a *Lambertian surface*¹², and the RTE is recast as an equation in terms of surface reflectance (or albedo) $\rho_{s\lambda}$ and optical thickness $\tau_{\text{diff}\lambda}$.

Modelling TOA Emergent Radiances

Here a mathematical model for the EM radiation emerging from the top of the Earth's scattering atmosphere is presented. The formulation is based on the assumption that the scattering atmosphere of optical thickness $\tau = \tau_{\text{diff}\lambda}$ is bound at the bottom by a Lambertian surface with reflectance $\rho_{s\lambda}$. The radiance emerging from the TOA in the

¹²Radiation reflected by a Lambertian surface is isotropic (recall definition, p. 25) for any illumination direction, provided that the illumination is uniform across the surface.

direction (μ, ϕ) is given as,

$$L_{\lambda}^* = L_{\lambda}(0; +\mu, \phi) + \frac{1}{\pi} \int_0^{2\pi} \int_0^1 T(\tau_{\text{diff}\lambda}; \mu, \phi; \mu', \phi') L_{s\lambda} \mu' d\mu' d\phi' + L_{s\lambda} \exp(-\tau_{\text{diff}\lambda}/\mu), \quad (2.34)$$

where the first term on the right-hand side of the above represents the radiance reflected by the scattering atmosphere in the direction (μ, ϕ) and is termed the *path radiance*, later (p. 38) denoted $L_{p\lambda}$; the second term (the double integral) represents the radiance diffusely transmitted through the scattering atmosphere, with T defined on page 33, and contains the outward, surface-leaving radiance, $L_{s\lambda}$; and the final term on the right-hand side corresponds to the attenuation of the surface-leaving radiance via scattering out of the direct beam. The latter term is known as the *direct radiance* which obeys the Beer-Lambert-Bouguer law of extinction.

If it is assumed that the surface-leaving radiance, $L_{s\lambda}$, is isotropic (by the definition of a Lambertian surface) then integrating over the outward hemisphere—as in Eq. (2.10)—gives the total irradiance leaving the Earth's surface (sometimes referred to as exitance),

$$F_{\text{surf}\lambda}^{\uparrow} = \int_0^{2\pi} \int_0^1 L_{s\lambda} \mu d\mu d\phi = \pi L_{s\lambda}. \quad (2.35)$$

Furthermore, by using the definition of diffuse transmittance (Eq. (2.29), p. 34), Eq. (2.34) may be rewritten as,

$$L_{\lambda}^* = L_{\lambda}(0; +\mu, \phi) + L_{s\lambda} [\exp(-\tau_{\text{diff}\lambda}/\mu) + t_{d\lambda}(\tau_{\text{diff}\lambda}; \mu)] \quad (2.36)$$

There are three components to the solar irradiance that propagates through the Earth's scattering atmosphere to the Earth's surface: firstly, there is direct component representing the reduced intensity solar irradiance that results from scattering out of direct beam, namely,

$$F_{d\lambda} \mu_0 \exp(-\tau_{\text{diff}\lambda}/\mu_0); \quad (2.37)$$

secondly, there is the radiation that is diffusely transmitted to the surface which, using the expression for the diffuse transmittance Eq. (2.29), is written as,

$$F_{d\lambda} \mu_0 t_{d\lambda}(\tau_{\text{diff}\lambda}; \mu_0); \quad (2.38)$$

and finally, there is a component that results from the interaction of the outward radiance from the surface, $L_{s\lambda}$, that is reflected by the scattering atmosphere back towards the

surface. This final component is obtained by combining Eq. (2.10), for an isotropic radiation field, and the spherical albedo Eq. (2.30) yielding the expression,

$$\pi L_{s\lambda} s_{\lambda}(\tau_{d\lambda}). \quad (2.39)$$

Combining Eqs. (2.37), (2.38) and (2.39), the total irradiance at the Earth's surface is given as,

$$F_{\text{surf}\lambda}^{\downarrow} = F_{d\lambda}\mu_0 [\exp(-\tau_{\text{diff}\lambda}/\mu_0) + t_{d\lambda}(\mu_0)] + \pi L_{s\lambda} s_{\lambda}(\tau_{\text{diff}\lambda}). \quad (2.40)$$

For a Lambertian surface with reflectance $\rho_{s\lambda}$, the total outward irradiance leaving the Earth's surface is going to be some fraction of the total inward irradiance incident at the Earth's surface. In fact,

$$\frac{F_{\text{surf}\lambda}^{\uparrow}}{F_{\text{surf}\lambda}^{\downarrow}} = \rho_{s\lambda}.$$

Substituting Eqs. (2.35) and (2.40) into the above and rearranging in terms of $\rho_{s\lambda}$, gives the following expression for the surface-leaving radiance:

$$L_{s\lambda} = \frac{\rho_{s\lambda} F_{d\lambda}\mu_0 [\exp(-\tau_{\text{diff}\lambda}/\mu_0) + t_{d\lambda}(\mu_0)]}{\pi [1 - s_{\lambda}(\tau_{\text{diff}\lambda}) \rho_{s\lambda}]}. \quad (2.41)$$

To condense the notation in the above, the total transmittance through the scattering atmosphere, $T_{\text{scat}\lambda}$, in both the inward and outward directions is defined as,

$$T_{\text{scat}\lambda}(\mu_0) = \exp(-\tau_{\text{diff}\lambda}/\mu_0) + t_{d\lambda}(\mu_0) \quad \text{and} \quad (2.42)$$

$$T_{\text{scat}\lambda}(\mu) = \exp(-\tau_{\text{diff}\lambda}/\mu) + t_{d\lambda}(\mu), \quad (2.43)$$

respectively. Substituting the above into Eq. (2.41), and then Eq. (2.41) into Eq. (2.36) yields the following expression for the radiation emerging from the top of the scattering atmosphere:

$$L^* = L_{\lambda}(0; +\mu, \phi) + \frac{\rho_{s\lambda} F_{d\lambda}\mu_0 T_{\text{scat}\lambda}(\mu_0) T_{\text{scat}\lambda}(\mu)}{\pi [1 - s_{\lambda}(\tau_{\text{diff}\lambda}) \rho_{s\lambda}]}. \quad (2.44)$$

Note that Eq. (2.44) contains a geometric series in terms of spherical albedo, that is,

$$\frac{1}{1 - s_{\lambda}(\tau_{\text{diff}\lambda}) \rho_{s\lambda}} = \sum_{k=0}^{\infty} [s_{\lambda}(\tau_{\text{diff}\lambda}) \rho_{s\lambda}]^k.$$

This component has been interpreted (Tanré et al., 1979) as the fraction of radiation that has interacted with the surface and scattering atmosphere N times ($N \rightarrow \infty$) and is referred to as the *trapping mechanism* (Vermote et al., 1997b). For a relatively clear

atmosphere, where the value of $\tau_{\text{diff}\lambda}$ is small, the contribution due to the spherical albedo is also small; this is discussed further in Section 3.2.1 (p. 61).

Finally, a complete model of the emergent radiation at the TOA is obtained by incorporating the effect of gaseous absorption on the radiation along its downward and upwards path through the absorbing atmosphere. Thus, by incorporating the total transmittance through the absorbing atmosphere, Eq. (2.13, p. 27), in the downwards (μ_0) and upward (μ) direction yields,

$$L_{\lambda}^* = T_{\text{abs}\lambda}(\mu_0) T_{\text{abs}\lambda}(\mu) \left\{ L_{\lambda}(0; +\mu, \phi) + \frac{\rho_{\text{s}\lambda} F_{\text{d}\lambda} \mu_0 T_{\text{scat}\lambda}(\mu_0) T_{\text{scat}\lambda}(\mu)}{\pi [1 - s_{\lambda}(\tau_{\text{diff}\lambda}) \rho_{\text{s}\lambda}]} \right\}. \quad (2.45)$$

This equation is the simplification to the RTE that has been used in the work of numerous authors (Tanré et al., 1979; Fraser and Kaufman, 1985; Kaufman and Tanré, 1996a; Kaufman et al., 1997b; Liang et al., 1997; Vermote et al., 1997b; Ouaidrari and Vermote, 1999) in modelling the space-borne measurement of reflected solar radiation emerging from the earth-atmosphere system. It is important to note that Eq. (2.45) is an accurate model only if the assumptions on which it is derived are valid. When, for example, the bounding surface has non-Lambertian properties, then Eq. (2.45) must be modified to take this effect into account (discussed in Section 3.2).

Path Radiance and Scattering Phase Function

The path radiance, $L_{\lambda}(0; +\mu, \phi)$, in Eq. (2.45) is the component of the radiance emerging from the TOA that is independent of surface reflectance. There has been considerable interest in modelling the path radiance as it is a purely atmospheric signal from which one can infer various properties about the earth atmosphere (King et al., 1999, for example). The interest in path radiance in this thesis is in relation to its effect on space-borne observations and how one might compensate for it in satellite imagery (to be reviewed in Section 3.3.3, pp. 82–84). In the following, and hereafter, path radiance will be denoted $L_{\text{p}\lambda}$.

One of the key quantities in relation to the path radiance is the *scattering phase function*. It is a function of wavelength, inward and outward geometries, and physical properties of the scatterer (e.g. aerosol type). Chandrasekhar (1960, p. 146) used the

*single-scattering approximation*¹³, to define the scattering phase function, P , as,

$$P(\Theta) = \frac{\mu_0 + \mu}{\mu_0 \mu} S(\tau_{\text{diff}\lambda}; \mu, \phi; \mu_0, \phi_0),$$

which represents the angular distribution of scattered radiance as a function of *scattering angle* Θ . For notational convenience, the incident (μ_0, ϕ_0) and scattered directions (μ, ϕ) are replaced with the *forward scattering* ψ_+ ($0^\circ \leq \Theta \leq 90^\circ$) and *back scattering* ψ_- ($90^\circ < \Theta \leq 180^\circ$) angles, calculated (Eckstein and Simpson, 1991) as,

$$\cos(\psi_\pm) = \pm \mu \mu_0 - \sqrt{(1 - \mu^2)(1 - \mu_0^2)} \cos(\phi - \phi_0),$$

and are interpreted as follows:

ψ_+ : the angle between a vector from the target in the specular reflectance direction, and a vector from the target to the TOA in the direction (μ, ϕ) .

ψ_- : the angle between a Sun-target vector and a vector from the target to the TOA in the direction (μ, ϕ) .

Figure 2.8 illustrates the scattering geometry described above. The phase function can also be thought of as the probability that radiation coming from (μ_0, ϕ_0) will be scattered in the direction (μ, ϕ) .

The single-scattering approximation can be used to express the path radiance, $L_{p\lambda}$, described in the previous section as the contribution to the emergent radiance L^* at the TOA that has not encountered the Earth's surface, in terms of the phase function as (neglecting gaseous absorption),

$$L_{p\lambda} = \frac{F_{d\lambda} \mu_0 P(\Theta)}{4\pi(\mu_0 + \mu)} [1 - \exp(-\tau_{\text{diff}\lambda}(1/\mu_0 + 1/\mu))]. \quad (2.46)$$

If the scattering optical thickness is small, Eq. (2.46) can be simplified using

$$1 - e^{-\tau_{\text{diff}\lambda}(1/\mu_0 + 1/\mu)} \simeq \tau_{\text{diff}\lambda} \left(\frac{\mu_0 + \mu}{\mu_0 \mu} \right)$$

to

$$L_{p\lambda} = \frac{F_{d\lambda}}{4\pi\mu} P(\Theta) \tau_{\text{diff}\lambda}. \quad (2.47)$$

¹³Since the expressions for radiative transfer incorporating multiple scattering are very complex, the *single-scattering approximation* is employed in some applications where the assumption, that a photon is scattered only once along a given path, is valid.

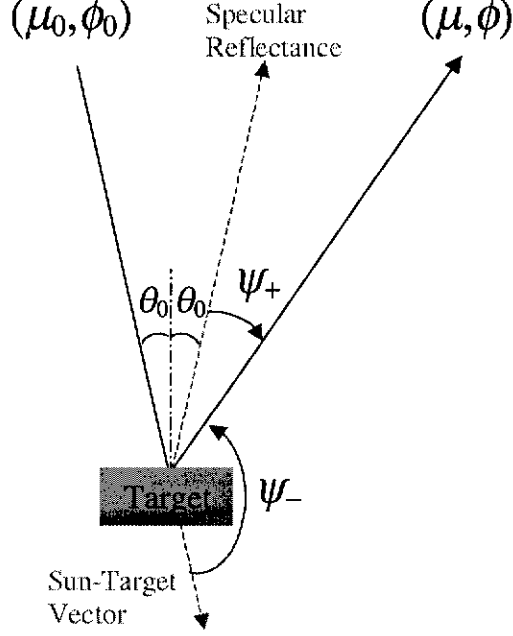


Figure 2.8: A graphical representation of the scattering geometry described in this section, illustrating forward- (ψ_+) and back- (ψ_-) scattering angles.

In a similar manner to the decoupling of the molecular and aerosol optical thicknesses in Section 2.3.3, the scattering phase function $P(\Theta)$ may be decoupled into molecular (Rayleigh), $P_R(\Theta)$, and aerosol (Mie), $P_{M\lambda}(\Theta)$, components. Note that, unlike its molecular counterpart, aerosol scattering phase functions exhibit a wavelength dependence (thus the λ subscript).

This decoupling allows Eq. (2.47) to be rewritten as,

$$L_{p\lambda} = \frac{F_{d\lambda}}{4\pi\mu} [P_R(\Theta)\tau_{R\lambda} + \omega_{0\lambda}P_{M\lambda}(\Theta)\tau_{M\lambda}], \quad (2.48)$$

where $\omega_{0\lambda}$ is called the *single scattering albedo*. The single scattering albedo is a quantitative measure of a particle's ability to absorb and/or scatter impinging radiation. Molecules in the scattering atmosphere are considered conservative and $\omega_{0\lambda} = 1$; they are purely scatterers. However, depending on the type considered (see Section 2.2.5), aerosols not only scatter light, but can also absorb a portion of the incident radiation; $\omega_{0\lambda} \leq 1$. If the particle was totally absorbing, $\omega_{0\lambda} = 0$. The single scattering albedo is a wavelength-dependent quantity that varies with aerosol type and relative humidity. d'Almeida et al. (1991) gives tabulated values of $\omega_{0\lambda}$ for a number of aerosol types for

wavelengths between 0.3–40 μm and for eight humidity classes.

Equation (2.48) is a model employed by some authors to represent the path radiance contribution in their atmospheric correction algorithms (Hill and Sturm, 1988; Miura et al., 2001) or in methods of retrieving aerosol (Mie) optical thickness from satellite observations (Kaufman et al., 1997b,a; King et al., 1999). It has been pointed out that the decoupling of the Rayleigh and Mie components of the path radiance is not valid for wavelength regions less than 450 nm and/or for large values of θ_0 or θ (Vermote et al., 1997b). The 6S software uses the successive orders of scattering (SOS) to estimate the path radiance which Vermote et al. (1997b) claim gives a highly accurate model value of $L_{p\lambda}$.

The basic form of the Rayleigh scattering phase function is,

$$P_R(\Theta) = \frac{3}{4}(1 + \cos^2(\Theta)).$$

Chandrasekhar (1960, p. 49) introduced the factor $\delta = \gamma/(2-\gamma)$ where the depolarisation ratio (see Section 2.3.3) γ is incorporated. The expression for the Rayleigh scattering phase function given by Chandrasekhar (1960, p. 49) is,

$$P_R(\Theta) = \frac{3}{4}\left(\frac{1-\delta}{1+2\delta}\right)(1 + \cos^2(\Theta)) + \left(\frac{3\delta}{1+2\delta}\right). \quad (2.49)$$

The aerosol scattering phase function, $P_{M\lambda}$, has a form dependent on the aerosol type considered. One of the requirements for accurate modelling of the path radiance is that the phase function and single scattering albedo are representative of the aerosol type for the area studied, since aerosol type varies with geographic location. Aerosol scattering phase functions are obtained using Mie theory under the assumption that aerosols are spherical particles. Figure 2.9 presents the scattering phase functions for a few different aerosol types over a range of scattering angles Θ . A molecular phase function is presented for comparison purposes. The maxima in aerosol scattering phase function for scattering angles less than 90° (relative to scattering angles greater than 90°) indicate that aerosols are predominately forward scatterers. In contrast the symmetric form of the molecular phase function indicates that molecules scatter equally in both the forward and backscattering directions.

An analytic expression for $P_{M\lambda}$ that Aranuvachapun (1983) demonstrated gave a satisfactory fit to realistic aerosol scattering phase functions for various types is referred

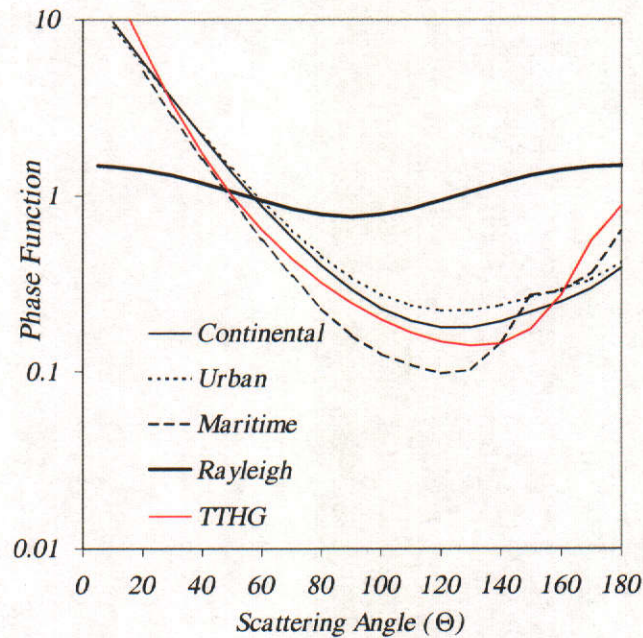


Figure 2.9: Scattering phase function for continental, urban and maritime aerosol types. The Rayleigh and two-term Henyey-Greenstein (TTHG) scattering phase functions are also displayed.

to as the *two-term Henyey-Greenstein scattering phase function*:

$$P_{M\lambda}(\Theta) = f_1 \frac{1 - g_1^2}{[1 + g_1^2 - 2g_1 \cos(\Theta)]^{3/2}} + (1 - f_1) \frac{1 - g_2^2}{[1 + g_2^2 - 2g_2 \cos(\Theta)]^{3/2}}, \quad (2.50)$$

where f_1 is a weighting factor applied to two single-term Henyey-Greenstein phase functions, and the so called *asymmetry parameters* g_1 and g_2 account for the large forward scattering peak that characterise aerosol scattering (see Twomey (1977, p. 214) for illustrations). An example given by Aranuvachapun (1983) using the parameters $f_1 = 0.9752$, $g_1 = 0.7281$ and $g_2 = -0.7638$ is presented in Figure 2.9.

2.4 Chapter Summary

- Spectral variations in the solar spectrum at the TOA are due to absorption by the elements in the solar atmosphere. There exist solar irradiance data spanning 400–2500 nm.
- The largest observed variation in the intensity of solar irradiance, F_0 , at the TOA is due to the Earth's elliptical orbit around the Sun. The scaling factor D adjusts

values of $F_{0\lambda}$ (based on mean Earth-Sun distance) for the time of the year and gives $F_{d\lambda}$.

- Vertical distributions (profiles) of pressure and temperature can be measured with radiosondes. There also exist model profiles of these quantities based on standard atmospheric conditions for given latitudes.
- Water vapour profiles can be derived from radiosonde data. These data can also be used to provide an estimate of the total-column integrated water vapour content (precipitable water, u_{H_2O}). Given an estimate of precipitable water, transmittance through the absorbing layer of the atmosphere due to water vapour can be estimated.
- Total ozone concentrations, u_{O_3} , have been measured around the globe by the TOMS since 1978. Model ozone profiles exist for given latitudes. From these models, ozone absorption coefficients α_{O_3} can be calculated and used with the estimate of u_{O_3} to calculate a transmittance through the absorbing layer of the atmosphere due to ozone.
- Total gaseous transmittance through the scattering layer $T_{abs\lambda}$ is dependent on wavelength, and obeys the Beer-Lambert-Bouguer law of extinction. It is also affected by pressure and temperature profiles.
- Aerosol spatial distributions vary considerably from location to location. There is much interest in space-borne technology to provide routine, large-area mapping of total aerosol concentration (or $\tau_{M\lambda}$) to gain a more thorough understanding of the impact of aerosols on climate. Ground-based solar photometers (e.g. MFRSR) can be used to estimate $\tau_{M\lambda}$.
- Aerosols have been categorised into various types (e.g. continental, urban, desertic and maritime), that are characterised by their specific phase function $P_{M\lambda}$ and single scattering albedo $\omega_{0\lambda}$.
- Scattering optical thickness $\tau_{diff\lambda}$ is the sum of aerosol (Mie) optical thickness, $\tau_{M\lambda}$, and molecular (Rayleigh) optical thickness, $\tau_{R\lambda}$.

- An expression exists for calculating Rayleigh optical thickness given surface pressure, P_s , and temperature, T_s , measurements. Much attention has focussed on complete representation of Rayleigh scattering and an accurate value of the depolarisation ratio γ .
- Total transmittance through the scattering atmosphere, $T_{\text{scat}\lambda}$, has a direct component, $(\exp(-\tau_{\text{diff}\lambda}))$, representing the reduced intensity by scattering out of the direct beam) and a diffuse component ($t_{\text{d}\lambda}$, representing the contribution from scattering events—single or multiple).
- The single-scattering approximation and the assumption that the atmosphere is bound at the bottom by a Lambertian surface, yields a simplified version of the radiative transfer equation that models the radiance emerging from the earth-atmosphere system L_λ^* as a function wavelength (λ), direction of incidence (μ_0, ϕ_0) and emergence (μ, ϕ), surface reflectance ($\rho_{s\lambda}$), gaseous absorption ($T_{\text{abs}\lambda}$) and scattering ($T_{\text{scat}\lambda}$).
- The path radiance $L_{\text{p}\lambda}$ is defined as the component L_λ^* that has not interacted with the surface. In the single-scattering approximation the path radiance is calculated from the incidence (μ_0, ϕ_0) and emergence (μ, ϕ) directions, the solar irradiance corrected for Earth-Sun distance ($F_{\text{d}\lambda}$), molecular ($\tau_{\text{R}\lambda}$) and aerosol ($\tau_{\text{M}\lambda}$) optical thicknesses, molecular scattering phase function (P_{R}), aerosol scattering phase function ($P_{\text{M}\lambda}$) and single scattering albedo ($\omega_0\lambda$).

CHAPTER 3

Satellite Image Data and Processing

For over forty years, humankind has been observing the Earth from the most unique of vantage points: Space. Data acquired with satellite-based remote sensing technologies have helped investigators monitor the Earth's atmosphere-hydrosphere-biosphere system: from the interactions of its various constituents; to the driving forces that lead to global change. The spectral, spatial and temporal characteristics of remotely-sensed data have and continue to contribute to an increased understanding of the workings of the planet.

This chapter begins with a brief overview of satellite-based remote sensing, with discussion limited to the imaging sensors on the Landsat series of Earth observing satellites. Image acquisition, data characteristics and radiometric processing specific to the multispectral sensors used in this thesis, are also described. Attention is then directed to modelling the satellite-measured signal and, in particular, describing those factors that contribute to observed changes in the image data that are not due to the Earth's surface properties alone. Some methods of change detection in satellite image sequences are presented and various radiometric processing methods for multitemporal studies are reviewed.

3.1 Satellite Image Data

Two satellite missions have continuously provided global observations of the Earth for the past 30 years: they are the Landsat and the US National Oceanic and Atmospheric Administration (NOAA) Polar Operational Environmental Satellite (POES) programmes. The sensors on these satellite platforms image the Earth at a range of spatial and temporal scales, and measure emergent radiations over a wide spectral range. To make a detailed comparison of all the image data characteristics acquired with all the sensors on both satellite platforms is beyond the scope of the thesis. Therefore, for the sake of brevity, discussion is limited in what follows to the image data used in this thesis;

namely that acquired with the *Thematic Mapper* (TM) sensors on the Landsat series of satellites. Reference is made to other platforms and sensors for comparison purposes only. It is stressed however that many of the concepts described in the following sections are not limited to the Landsat TM.

3.1.1 A Brief History of the Landsat Satellites

The Landsat satellite program began on July 23, 1972 with the launch of Landsat-1 (then called ERTS-1, for Earth Resource Technology Satellite 1). It was the first satellite to carry an imaging sensor known as the Multispectral Scanner (MSS). Four more Landsat satellites (numbered 2-5) carried the MSS. Landsat-4 and -5, launched in July 16, 1982 and March 1, 1984 respectively, also carried the Thematic Mapper (TM); the data from which offered higher spatial resolution (defined in Section 3.1.3) imagery than that provided by the MSS over a greater span of wavelengths. Landsat-6, which was due to be operational in late 1993, failed on launch. The latest in the Landsat series is the Landsat-7 satellite launched April 15, 1999 which carries the Enhanced Thematic Mapper Plus (ETM+). The orbital characteristics of the Landsat satellite, and the spatial and spectral coverage of their sensors are covered in the following sections.

Images acquired with the sensors on Landsat satellites were initially intended to service the needs of the US Geological Survey and Department of Agriculture (Mather, 1987, p. 49); the data are primarily used in mapping geology, crops, and pollution events (Goward and Masek, 2001). Since then the imagery has also been used to map and monitor dry-land salinity and native vegetation (Caccetta et al., 2000a,b), changes in urban environments (Ridd and Liu, 1998; Small, 2002), and general retrospective studies of land cover change (Graetz et al., 1992). All but Landsat-7 have been decommissioned; Landsat-5 was in operation for almost 14 years beyond its intended lifespan. The Landsat program will continue with Landsat-8 due to be launched in 2010. The technologies and data characteristics that have made MSS, TM and ETM+ imagery so valuable to such a wide community of users, has paved the way for the next generation of earth observation satellites (for example the Advanced Land Imager (ALI) on the Earth Observation (EO-1) satellite) ensuring the long-term continuity of image data of the Earth.

3.1.2 Orbital Characteristics

Each Landsat satellite was placed in a *sun-synchronous*¹ orbit, meaning that they crossed the equator (any given latitude for that matter) at the same *local* time every day. Landsat-1 to -3 crossed the equator on *descending node*² at 0930 hours local time (for any given longitude), Landsat-4 and -5 crossed at 0945 hours, and Landsat-7 ETM+ crosses at approximately 1000 hours. Finally the altitude of the orbits of Landsat-1 to -3 were nominally 919 km, whilst for Landsat-4, -5 and -7, orbits were 705 km.

The orbits of the Landsat satellites are also termed *near-polar*, that is they have *inclinations*³ between 98.2° – 99.1° , and were thus able to image most of the globe (from around 81° S to 81° N). Furthermore, the orbits were *retrograde*⁴ with periods of around 103 minutes (Landsat-1 to -3) and 98.9 minutes (Landsat-4, -5 and -7). This gave them a repeat coverage (over the same area on the surface) of 18 and 16 days respectively.

3.1.3 Multispectral Image Acquisition

The MSS, TM and ETM+ sensors contain an oscillating mirror that directs light emergent at the top of the Earth's atmosphere onto a number of fibre optic detector elements. As the mirror oscillates from one extreme to the other, the sensor essentially scans forwards (forward scan, see Figure 3.1) and backwards (reverse scan) across the satellite's track. The sensors are thus called *whisk-broom* scanners. The on-ground distance of a scan is approximately 185 km, a distance known as the *swath width*. The angle subtended by the satellite swath is often referred to as the *field of view* (FOV). The MSS had a FOV of 11.56° , the mirror oscillating $\pm 5.87^{\circ}$ off nadir. The FOV of the TM and ETM+ sensors on the other hand is approximately 15° because of the lower orbits of the Landsat-4, -5 and -7.

The orbital speed of these satellites in the along track direction is too high to feasibly scan one line at a time, so a number of detector elements are present to view the Earth simultaneously at equally spaced intervals along the track. For the MSS, six parallel detectors scanned six lines across the track, and data were acquired with each forward

¹If a Satellite's orbit of the Earth is such that its rate of precession matches the angular velocity of the Earth's motion around the Sun, then the orbit is called sun-synchronous.

²The north-south path.

³The angle that the orbital path makes relative to the equatorial plane.

⁴The longitudinal component of the satellite's path is from east to west.

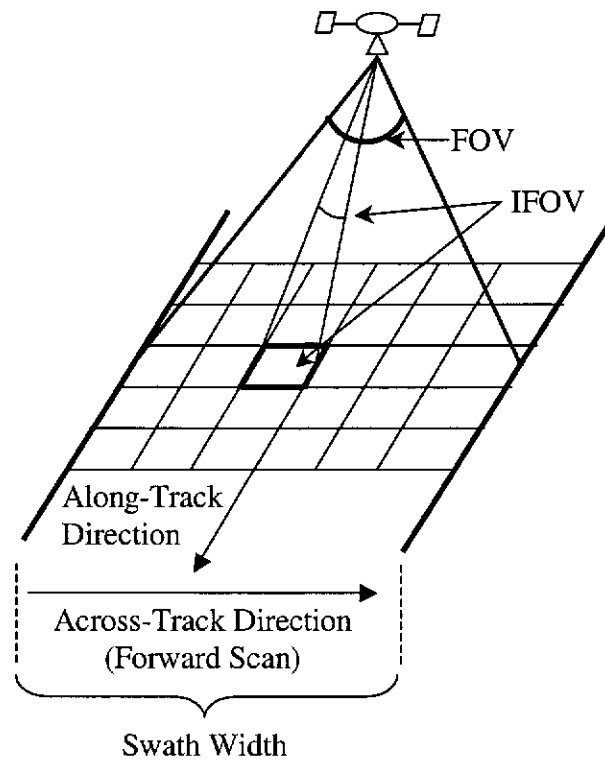


Figure 3.1: An illustration of the satellite and sensor view geometries that are involved in the production of the images acquired with MSS, TM and ETM+ sensors. The field of view (FOV) and instantaneous field of view (IFOV) are highlighted, as well as the along- and across-track directions.

scan only. Each scan line corresponds to an on-ground along-track distance of 79 m. At the beginning of each forward scan, each detector observed a region of the Earth's surface 474 m (6×79 m) along the track from the location of the previous scan.

For any one of the detectors in the MSS, signal integration time was about $9.96 \mu\text{s}$ (Mather, 1987). This produced 3300 samples across the 185 km swath. This meant that the interval of measurements across the satellite track was approximately 56 m. Therefore, each detector in the MSS integrates the electromagnetic radiation emergent from the Earth for a $79 \times 56 \text{ m}^2$ area on the ground. This area is given the name *instantaneous field of view* (IFOV) and corresponds to the on-ground dimensions of a *pixel* in the resultant image. The IFOV can also be specified as an angular width (Figure 3.1), and defines the spatial resolution of the image acquired.

Unlike the MSS, the TM and ETM+ have a staggered linear array of detectors designed to acquire measurements on both the forward and reverse scans. Each array has 16 detectors dedicated to measuring radiation in the solar reflective region of the EM spectrum (i.e. 400–2400 nm). These detectors have an IFOV of $30 \times 30 \text{ m}^2$, thus the resulting imagery has higher resolution than that of the MSS.

The sensors on the Landsat satellites were designed to measure EM radiation emergent from the top of the Earth's atmosphere in a discrete number of wavelength regions referred to as *bands*. There is one array of detector elements per band, and each band is characterised by a filter function, or *spectral response curve* (Figure 3.2), to perform a band-average of the continuous spectrum of EM radiation arriving at the sensor. The normalised spectral response curves for the TM and MSS on Landsat-5 are displayed in Figure 3.2. For comparison purposes, the response curves for some of the bands on the NOAA-11 Advanced Very High Resolution Radiometer (AVHRR) and the airborne Moderate Resolution Imaging Spectroradiometer (MODIS) are also displayed.

Figure 3.2 clearly demonstrates the obvious differences in relative spectral response between the MSS and TM sensors. There are also differences in the response curves for different versions of the same sensor, illustrated in Figure 3.3. The response curves for Landsat-4 and -5 TM are very close, however the ETM+ curves are significantly different. These differences can make images of comparable band numbers appear quite different, because the filters average the continuous spectrum of EM radiation which is affected by gaseous absorption in the atmosphere (more in Section 3.3.3, pp. 84–90).

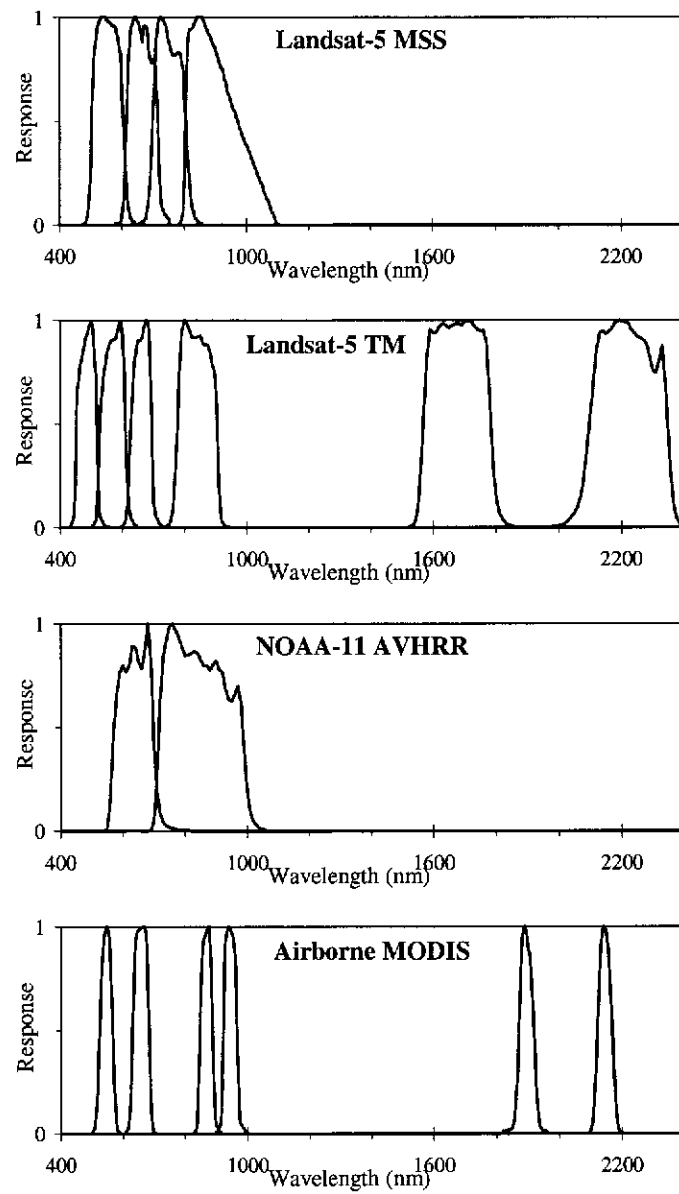


Figure 3.2: Normalised spectral response curves (or filter functions) for the bands on the Landsat-5 MSS and TM, NOAA-11 AVHRR, and airborne MODIS.

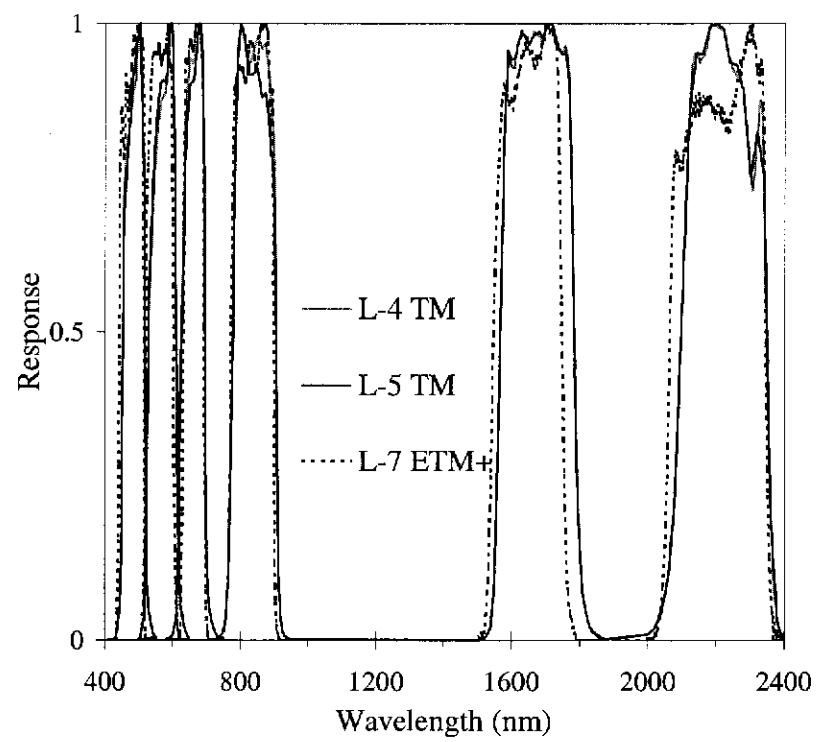


Figure 3.3: The normalised spectral response curves for Landsat-4 and -5 TM and Landsat-7 ETM+ sensors.

Multispectral Vs. Hyperspectral

Images acquired with the MSS, TM and ETM+ sensors are termed *multispectral*, as are AVHRR and MODIS, and are distinguishable by a relatively small number of spectral bands. In contrast, *hyperspectral* images are comprised of a large number (typically > 100) of contiguous, narrow spectral bands. The large number of bands in hyperspectral imagery means that, for each target on the Earth's surface, the solar reflected radiation is resolved into a quasi-continuous spectrum of radiation, which is why hyperspectral remote sensing is often referred to as *imaging spectroscopy*. The advantages offered by hyperspectral sensors, that their multispectral counterparts cannot, are very much dependent on the problem the individual researcher seeks to address with remotely sensed data (the reader is directed to Goetz et al. (1985) for some examples). For the objectives of this thesis, it is reasonable to limit attention to multispectral image data and processing. And while many of the concepts to be discussed in the following are also applicable to hyperspectral imagery, the nature of hyperspectral data raises many more issues that need to be taken into considerations (see, for example, Richards and Jia (1999, pp. 313–335)).

The MSS had in total 4 bands; two sensing the visible (500–700 nm), known as bands 4 and 5, and two the near infrared (700–1100 nm), named 6 and 7 (Figure 3.2). The MSS on Landsat-3 had a fifth, thermal band that was only active for a short while after launch. The TM and ETM+ sensors (Figures 3.2 and 3.3) on the other hand have 7 bands; three sensing the visible (450–690 nm), known as bands 1, 2 and 3; one in the near infrared (750–900 nm), known as band 4; two in the short-wave infrared (1550–2350 nm), known as bands 5 and 7; and one in the thermal infrared (10.4–12.5 μm), known as band 6. The ETM+ sensor on Landsat-7 has a panchromatic band (520–900 nm) known as Band 8, which has a higher spatial resolution than the other bands ($15 \times 15 \text{ m}^2$ pixels).

Figure 3.4 illustrates the RGB (red, green and blue) displays of a subset of a Landsat-5 TM image acquired over Geraldton, Western Australia on February 13, 1999. Figure 3.4(a) is known as a *true-colour* composite because the TM bands corresponding to the red, green and blue regions of the EM spectrum are displayed in RGB in the correct order. Figure 3.4(b) is called a *false-colour* composite as it displays TM bands 5, 4, and 2 in RGB. False-colour composites are useful in highlighting certain features in an image,

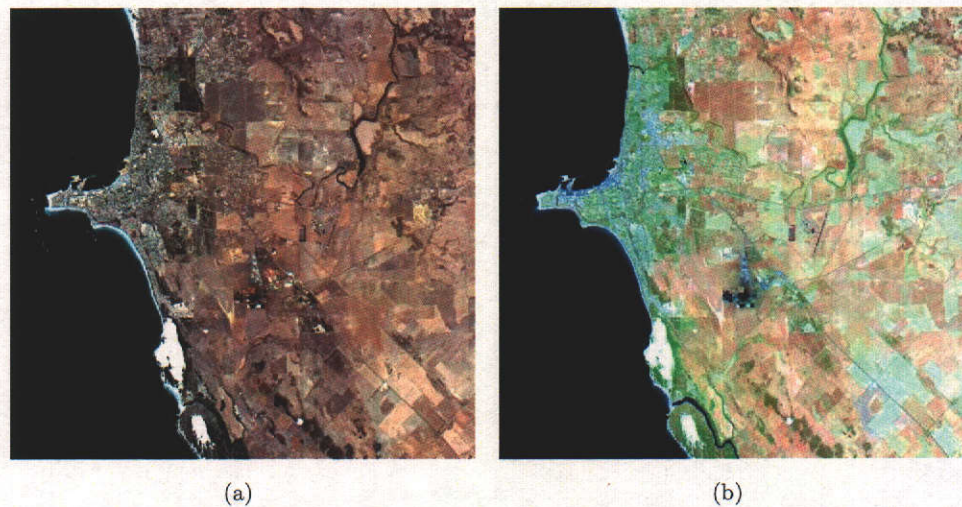


Figure 3.4: An example of a (a) true-colour (RGB:3,2,1) and (b) false-colour (RGB:5,4,2) composite of a subset of the Landsat-5 TM image for Geraldton, Western Australia.

Table 3.1: A summary of Landsat satellite and sensor characteristics.

	MSS	TM	ETM+
Satellite	Landsat-1 to -5	Landsat-4 & -5	Landsat-7
Bands	4, 5, 6 & 7 (8-thermal band Landsat-3 only)	1-5 & 7 (6-thermal band)	1-5 & 7 (6-thermal band, 8 panchromatic)
FOV	11.56° 185 km swath	15° 185 km swath	15° 185 km swath
IFOV	79 m (along-track) × 56 m (across-track)	30 × 30 m ²	30 × 30 m ²
Repeat Cycle	18 days (Landsat-1 to -3 only)	16 days	16 days
Equatorial Crossing	0930 hours	0945 hours	1000 hours

particularly if one knows the regions of the EM spectrum in which the feature strongly reflects solar radiation. For example, vegetation is known to reflect light strongly in the near infrared (bands 4 and 5) and green wavelengths (band 2) relative to other bands, thus the combination of these bands in RGB highlights vegetation as illustrated by the green areas in Figure 3.4(b).

3.1.4 Image Data and Radiance Values

A multispectral image emerges from the collation of successive scan lines along the track of the satellite's path. The arrangement of the pixels into a rectangular array provides a discretised view of the Earth from space. The inclination of the Landsat satellites' near-polar orbits has meant that most of the globe was imaged every 18 (MSS) or 16 (TM and ETM+) days. Landsat-1 to -3 completed 251 orbits before repeating the same path 18 days later, whilst Landsat-4, -5 and -7 completed 233 orbits in 16 days.

The EM signal received by the detectors is converted from an analogue signal into a *digital number* (DN). In the case of the MSS image data, the signal was quantised as a 6-bit integer, ranging from 0 (black), corresponding to no signal, to 63 (white) for detector saturation. These image data were transmitted to ground receiving stations where subsequent processing scaled the DN s for the first three bands (i.e. 4, 5 and 6) to 7-bit integers (0–127).

The TM and ETM+ image data have 8-bit (0–255) quantisation. For each spectral band λ , let X_λ denote the DN and L_λ^* the at-sensor radiance for a given pixel. The response for each of the 16 detectors in any given band is characterised by a *responsivity*, g_λ , also known as a *detector gain* with units $W/(m^2 \text{ sr } \mu m)/DN$, and a *zero-radiance bias* $Q_{0\lambda}$ (unitless). The so called *raw* DN s and the at-sensor radiances are thus related as,

$$X_\lambda^{Raw} = g_\lambda L_\lambda^* + Q_{0\lambda}. \quad (3.1)$$

More discussion on the link between image data and radiances, and the impact of changes in detector response is given in Section 3.3.2 (p. 76). Table 3.2 gives the current (as at November 12, 2002) values of detector responsivity and bias for ETM+ band 1. The values were obtained from the calibration parameter file (CPF) for the ETM+ sensor available from the website,

<http://landsat7.usgs.gov/cpf/default.html>.

The CPFs are archived and updated for ETM+ imagery acquired since launch to present.

Unlike the TM, the ETM+ sensor can acquire data in two modes: *low mode* can measure a greater range of radiances without saturating the sensor, the sensitivity however is lower; and *high mode*, where a smaller radiance range is measurable but the sensitivity

Table 3.2: Responsivity g_λ [$\text{W}/(\text{m}^2 \text{ sr } \mu\text{m})/\text{DN}$] and zero-radiance bias $Q_{0\lambda}$ values for ETM+ band 1 (in high mode).

Detector	1	2	3	4	5	6	7	8
g_λ	1.228	1.227	1.215	1.227	1.216	1.226	1.223	1.223
$Q_{0\lambda}$	14.86	14.80	15.13	15.00	15.14	15.08	15.23	15.09
	9	10	11	12	13	14	15	16
g_λ	1.229	1.232	1.222	1.219	1.223	1.224	1.228	1.239
$Q_{0\lambda}$	14.94	14.93	15.07	15.09	15.08	15.15	14.99	15.08

is increased. The data in Table 3.2 correspond to the high mode setting. For the ETM+ imagery used in this thesis, the data were acquired with high setting for most bands. The exception was band 4, which was set to low mode.

The DN s are then transmitted to a receiving station where, depending on the level of image product required, subsequent on-ground processing may be performed. Australia has a receiving station for Landsat data at Alice Springs, Northern Territory, from which image data is maintained and distributed by the Australian Centre for Remote Sensing (ACRES); part of Australia's national mapping agency, AUSLIG. The processing performed by ACRES to achieve the different level of image products conforms to that used by the Canada Centre for Remote Sensing (CCRS) and the standard format family as defined by the Landsat Ground Stations Operators' Working Group (LGSOWG) Technical Working Group (LTWG), and described in detail in ACRES (1999) for TM images.

For radiometrically calibrated TM image products, one can convert the DN , X_λ , into a radiance value, L_λ^* [$\text{W}/(\text{m}^2 \text{ sr } \mu\text{m})$], by applying the *radiometric scaling factors* in Table 3.3 as,

$$L_\lambda^* = L_{\min\lambda} + \left(\frac{L_{\max\lambda} - L_{\min\lambda}}{255} \right) X_\lambda, \quad (3.2)$$

where $L_{\min\lambda}$ and $L_{\max\lambda}$ are given for each band in Table 3.3 and correspond to the minimum and maximum radiance values for a $DN = 0$ and 255 respectively (Markham and Barker, 1986). The radiometric scaling factors are temporally-invariant (Teillet and Fedosejevs, 1995; Teillet, 2002), unlike the sensor's responsivity which can change through time (Section 3.3.2). These scaling factors are also available in the ancillary files provided with the image data storage media. Similar radiometric scaling factors are available for ETM+ image products, either from the CPFs or in ancillary files.

Table 3.3: Radiometric scaling factors for converting a DN in a radiometrically calibrated TM image into a radiance value $[W/(m^2 \text{ sr } \mu m)]$.

Band	$L_{\max\lambda}$	$L_{\min\lambda}$
1	152.1	-1.5
2	296.8	-2.8
3	204.3	-1.2
4	206.2	-1.5
5	27.19	-0.37
7	14.38	-0.15

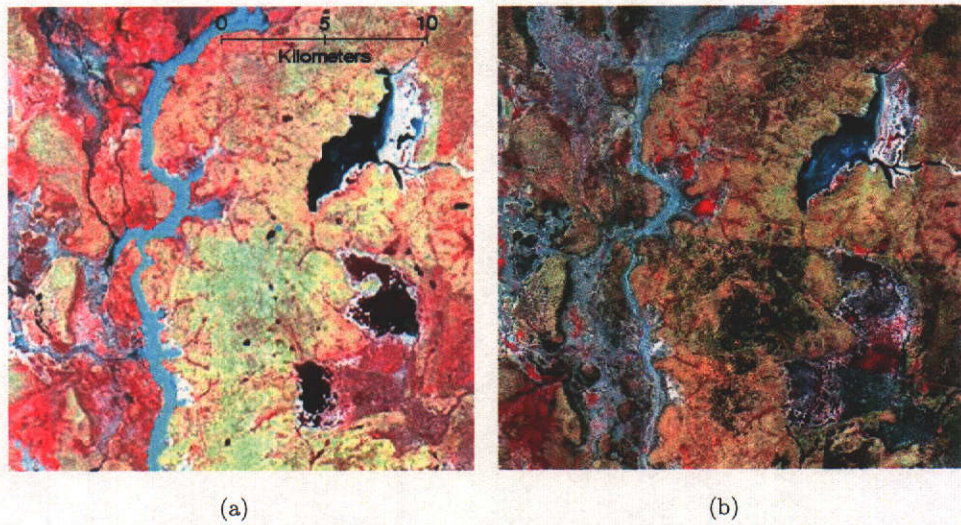


Figure 3.5: False-colour composites of (a) a Landsat-1 MSS image (RGB:7,5,4) acquired on February 2, 1974, and (b) a Landsat-5 TM image (RGB:4,3,2) acquired on September 25, 1988, with WRS path/row designations (99/80) and (93/80), respectively.

3.1.5 Scene Identification via the WRS

In this thesis, the area of the Earth's surface contained in an entire multispectral image is termed a *scene*. A scene in a Landsat image is referred to by its designated *path* and *row* number (path/row), as defined by the Worldwide Referencing System (WRS). Path numbers correspond to the satellite orbits (recall 251 for MSS images (Landsat-1 to -3) and 233 for MSS (Landsat-4 and 5), TM and ETM+ images), which increase sequentially from east to west. Row numbers refer to the latitudinal centre line of the scene. Row numbers increase sequentially from north to south.

Since the orbital characteristics of the first three Landsat satellites differ from those

of the last three, the path designations for a particular scene will be different when comparing old imagery to more recently acquired ones. The row designations have remained the same for all Landsat satellites. Figure 3.5 shows two image subsets of the same area on the Queensland-New South Wales border acquired with (a) the MSS on Landsat-1 on February 2, 1974, and (b) the TM on Landsat-5 on September 25, 1988, respectively. Their respective path/row designations are (99/80) for Figure 3.5(a) and (93/80) for 3.5(b). The choice of bands for the false-colour composites in Figure 3.5 were based on comparable MSS and TM bands in Figure 3.2.

3.2 Modelling the At-Sensor Signal

Tanré et al. (1979, 1981, 1983) were among the first to provide a mathematical model for the radiance signal emerging from the top of the Earth's atmosphere in a context suitable for satellite-based imaging in the solar reflective region of the EM spectrum. The expressions presented were based on the uniformity of the underlying surface/target in the IFOV (i.e. pixel) of the satellite sensor. Two cases were presented: (i) the target is homogeneous with Lambertian reflectance properties; and (ii) the target is inhomogeneous with non-Lambertian reflectance properties. These two scenarios will be discussed briefly in the following sections.

The radiance L_λ^* for a pixel in a particular band is calculated as described in Section 3.1.4 (p. 55). A quantity known as *at-sensor reflectance*, denoted $\rho_{\text{sat}\lambda}^*$, is calculated for the same pixel as,

$$\rho_{\text{sat}\lambda}^* = \frac{\pi L_\lambda^*}{F_{\text{d}\lambda} \mu_0}, \quad (3.3)$$

where $F_{\text{d}\lambda}$ is the exo-atmospheric solar irradiance ($F_{0\lambda}$) corrected for Earth-Sun distance via the adjustment factor, (calculated using Eq. (2.2)), and μ_0 is the cosine of the solar zenith angle (θ_0). The exo-atmospheric solar irradiance for the TM and ETM+ bands (at an Earth-Sun distance of 1 AU) are often provided along with the radiometric scaling factors (see Section 3.1.4) and are given in Table 3.4.

The at-sensor reflectance (also known as image-derived or top-of-atmosphere reflectance or planetary albedo) is not to be mistaken as an estimate of a target's surface reflectance $\rho_{s\lambda}$, because as we shall see in the following sections, $\rho_{\text{sat}\lambda}^*$ is composed of an atmospheric component, as well as components due to surface and atmosphere-surface

Table 3.4: Exo-atmospheric Solar Irradiances, $F_{0\lambda}$, at 1 AU for the TM and ETM+ images.

Band	$F_{0\lambda}$	
	TM	ETM+
1	1957	1969
2	1829	1840
3	1557	1551
4	1047	1044
5	219.3	225.7
7	74.52	82.07

interactions. Two advantages of transforming image data into an at-sensor reflectance were mentioned by Teillet et al. (2001): firstly, the transformation corrects for the cosine effects arising from different solar zenith angles and different Earth-Sun distances between different dates; and secondly, scaling by the exo-atmospheric irradiance adjusts for differences between sensors (Figure 3.3 in Section 3.1.3), which may be significant in multi-sensor studies. In the following, at-sensor reflectance is calculated to be consistent with the models presented by Tanré et al. (1979).

3.2.1 Homogeneous Targets

In Section 2.3.5, Eq. (2.45) was derived as the mathematical expression for the radiance emerging from the TOA at a zenith angle θ ($\mu = \cos(\theta)$) for an area of the Earth's surface (target) which is homogeneous in composition and Lambertian in surface reflectance ($\rho_{s\lambda}$) properties. Ignoring the effects of gaseous absorption on radiation propagating from the Sun to the target, and from the target to the satellite sensor, and assuming $\tau_{\text{diff}\lambda} = \tau_{\text{R}\lambda} + \tau_{\text{M}\lambda}$, Eq. (2.45) can be written as,

$$L_{\lambda}^* = L_{\text{p}\lambda} + \frac{\rho_{s\lambda} F_{\text{d}\lambda} \mu_0 T_{\text{scat}\lambda}(\mu_0) T_{\text{scat}\lambda}(\mu)}{\pi [1 - s_{\lambda}(\tau_{\text{diff}\lambda}) \rho_{s\lambda}]}, \quad (3.4)$$

where the terms have been defined in Section 2.3.5. Combining Eqs. (3.3) and (3.4) yields the expression for the at-sensor reflectance for a homogeneous, Lambertian target (Tanré et al., 1979, 1981, 1983),

$$\rho_{\text{sat}\lambda}^* = \rho_{\text{atm}\lambda} + \frac{\rho_{s\lambda} T_{\text{scat}\lambda}(\mu_0) T_{\text{scat}\lambda}(\mu)}{[1 - s_{\lambda}(\tau_{\text{diff}\lambda}) \rho_{s\lambda}]}. \quad (3.5)$$

Each of the components in Eq. (3.5) are summarised in the following and illustrated in Figure 3.6.

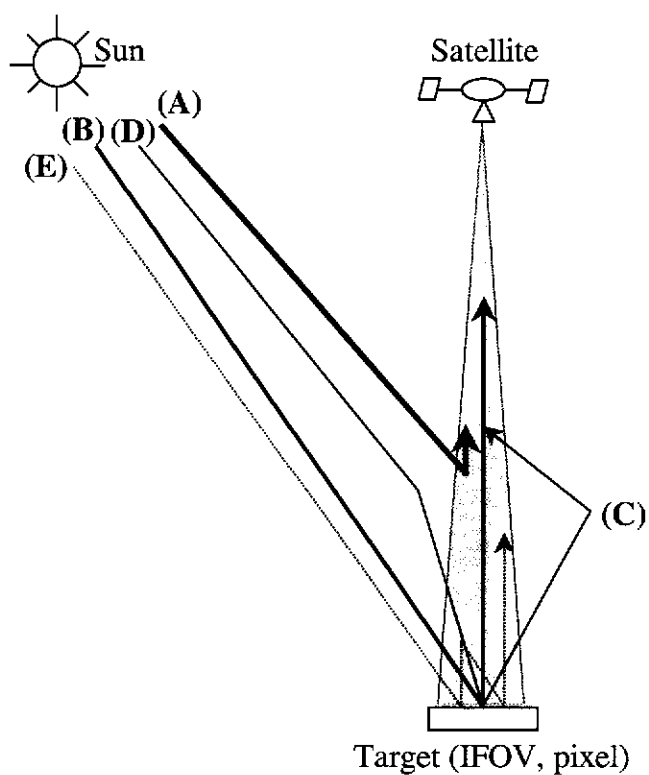


Figure 3.6: An illustration of the various paths that EM radiation may take as it propagates from the Sun towards the Earth's surface, and then into the IFOV of a satellite sensor.

Atmospheric Reflectance

The first term in Eq. (3.5), $\rho_{\text{atm}\lambda}$, is called the intrinsic *atmospheric reflectance*; a function of solar and sensor zenith angles, solar and sensor azimuths, and the optical thickness of the scattering layer. It incorporates the molecular and aerosol scattering phase functions (P_{R} and $P_{\text{M}\lambda}$), optical thicknesses ($\tau_{\text{R}\lambda}$ and $\tau_{\text{M}\lambda}$), aerosol single-scattering albedo ($\omega_{0\lambda}$), and scattering angle (Θ). In the single scattering approximation, it is written as,

$$\rho_{\text{atm}\lambda} = \frac{P_{\text{R}}(\Theta)\tau_{\text{R}\lambda} + \omega_{0\lambda}P_{\text{M}\lambda}(\Theta)\tau_{\text{M}\lambda}}{4\mu_0\mu}. \quad (3.6)$$

This is a purely atmospheric contribution to the at-sensor signal (Figure 3.6, path A), as it is that component of the radiation that has not interacted with the surface at all.

Diffuse/Direct Transmittance

The numerator on the right-hand side of Eq. (3.5) contains the information on the direct and diffuse transmittance of radiation interacting with the surface (assuming Lambertian reflectance) and received at the sensor. An itemised account of the possible paths is as follows:

- (i) the radiation is transmitted directly to the surface ($\exp(-\tau_{\text{diff}\lambda}/\mu_0)$), is reflected by the target ($\rho_{\text{s}\lambda}$) and transmitted directly to the sensor ($\exp(-\tau_{\text{diff}\lambda}/\mu)$) (Figure 3.6, path B), i.e.,

$$\exp(-\tau_{\text{diff}\lambda}/\mu_0)\rho_{\text{s}\lambda}\exp(-\tau_{\text{diff}\lambda}/\mu);$$

- (ii) the radiation is transmitted directly to the surface, is reflected, and diffusely transmitted to the sensor ($t_{\text{d}\lambda}(\mu)$) (Figure 3.6, path B–C), i.e.,

$$\exp(-\tau_{\text{diff}\lambda}/\mu_0)\rho_{\text{s}\lambda}t_{\text{d}\lambda}(\mu);$$

- (iii) the radiation is diffusely transmitted to the target, is reflected, and then directly transmitted to the sensor (Figure 3.6, path D), i.e.,

$$t_{\text{d}\lambda}(\mu_0)\rho_{\text{s}\lambda}\exp(-\tau_{\text{diff}\lambda}/\mu);$$

- (iv) the radiation is diffusely transmitted to the surface, reflected, and diffusely transmitted to the sensor (Figure 3.6, path D–C), i.e.,

$$t_{\text{d}\lambda}(\mu_0)\rho_{\text{s}\lambda}t_{\text{d}\lambda}(\mu).$$

The summation of all these possibilities results in the expression,

$$\rho_{s\lambda} [\exp(-\tau_{\text{diff}\lambda}/\mu_0) + t_{d\lambda}(\mu_0)] [\exp(-\tau_{\text{diff}\lambda}/\mu) + t_{d\lambda}(\mu)],$$

which, from the definition of Eqs. (2.42) and (2.43), becomes the expression in the numerator of Eq. (3.5). Tanré et al. (1981) refer to this as the *first-order* signal component.

Higher-Order Atmosphere-Ground Interactions

Second- and higher-order components (Tanré et al., 1981) are contained in the denominator of the right-hand side term of Eq. (3.5). Since the target's surface reflectance and the spherical albedo, s_λ , are quantities with values less than one, the term can be expressed as the geometric series,

$$\frac{1}{[1 - s_\lambda(\tau_{\text{diff}\lambda})\rho_{s\lambda}]} = 1 + s_\lambda\rho_{s\lambda} + (s_\lambda\rho_{s\lambda})^2 + \dots,$$

which is the component of radiation that is reflected by the target, then by the atmosphere, then by the target, and so on, until being received at the satellite sensor.

Tanré et al. (1979) employed the Eddington⁵ approximation to determined the following analytic expression to approximate the spherical albedo,

$$s_\lambda(\tau_{\text{diff}\lambda}) \simeq (0.92\tau_R + 0.33\tau_{M\lambda}) \exp(-\tau_{\text{diff}\lambda}).$$

This expression can be used to approximate the spherical albedo for a range of optical thicknesses and at a number of different wavelengths. Figure 3.7 illustrates the behaviour of s_λ with wavelength for a scattering atmosphere composed of (i) molecules only (thick line), (ii) molecules and aerosols with a visibility of 23 km (thin black line), and (iii) molecules and aerosols with a visibility of 5 km (dashed line). It is clear from Figure 3.7 that s_λ increases with increasing optical thickness (or decreasing visibility). It is therefore reasonable to expect that as $\tau_{M\lambda}$ increases, higher-order interactions become an increasingly significant contribution to the at-sensor signal. Generally, high-order contributions are on the order of a few percent (< 10%) of the first-order contributions.

⁵The Eddington method is used to approximate the integro-differential equation of radiative transfer (Section 2.3.5) as a pair of first-order ordinary differential equations (Joseph et al., 1976).

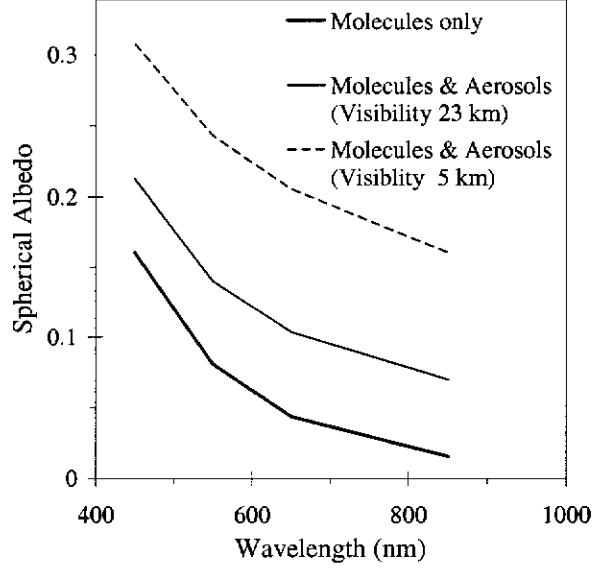


Figure 3.7: Spherical albedo values calculated via the expression in Tanré et al. (1979) for different aerosol loadings.

3.2.2 Inhomogeneous Targets

If the area on the Earth's surface contained in an image pixel is assumed now to be inhomogeneous, then the right-hand side of Eq. (3.5) is modified. Let there exist a small, uniform target in the sensor's IFOV, which (for argument's sake) is a circle (radius r), with reflectance $\rho_{s\lambda}$, and the reflectance of the target's surrounding environment is denoted $\rho_{e\lambda}$. If r is sufficiently small, the target's contribution to the diffuse radiation field detected by the satellite sensor will be negligible, and be primarily due to the surrounding environment. The possible paths radiation may take are:

- (i) the radiation can be directly or diffusely transmitted to the target and be reflected directly into the sensor's IFOV, i.e.,

$$\exp(-\tau_{\text{diff}\lambda}/\mu_0)\rho_{s\lambda}\exp(-\tau_{\text{diff}\lambda}/\mu) \quad \text{and} \quad t_{d\lambda}(\mu_0)\rho_{s\lambda}\exp(-\tau_{\text{diff}\lambda}/\mu); \quad \text{or}$$

- (ii) the radiation can be directly or diffusely transmitted to the environment surrounding the target, be reflected, and then diffusely transmitted to the sensor, i.e.,

$$\exp(-\tau_{\text{diff}\lambda}/\mu_0)\rho_{e\lambda}t_{d\lambda}(\mu) \quad \text{and} \quad t_{d\lambda}(\mu_0)\rho_{e\lambda}t_{d\lambda}(\mu).$$

The at-sensor reflectance is therefore modelled as (Tanré et al., 1981; Vermote et al., 1997b),

$$\rho_{\text{sat}\lambda}^* = \rho_{\text{atm}\lambda} + \left[\frac{\exp(-\tau_{\text{diff}\lambda}/\mu_0) + t_{\text{d}\lambda}(\mu_0)}{1 - s_{\lambda}(\tau_{\text{diff}\lambda})\rho_{\text{e}\lambda}} \right] [\rho_{\text{s}\lambda} \exp(-\tau_{\text{diff}\lambda}/\mu) + \rho_{\text{e}\lambda} t_{\text{d}\lambda}]. \quad (3.7)$$

It should be noted that including the environmental reflectance in the denominator of Eq. (3.7) is not strictly correct (that is, in the context of the original derivation of the trapping mechanism by Chandrasekhar (1960) and reviewed in Section 2.3.5). However, since the contribution of the higher-order interaction does not exceed 10–15% of that of the first-order term (Tanré et al., 1979, 1981), interchanging $\rho_{\text{e}\lambda}$ and $\rho_{\text{s}\lambda}$ is, in practice, inconsequential.

Using the analogy of a uniform target of radius r , it can be observed that as the radius increases, $\rho_{\text{e}\lambda} \rightarrow \rho_{\text{s}\lambda}$, Eq. (3.7) will become Eq. (3.5). Vermote et al. (1997b) defines the environmental reflectance as,

$$\rho_{\text{e}\lambda} = \frac{1}{2\pi} \int_0^{2\pi} \int_0^\infty \rho_{\text{s}\lambda}(r, \psi) \frac{df}{dr} dr d\psi,$$

where $f(r)$, known as the *environment function*, is the probability that radiation reflected at a point (r, ψ) (polar coordinates) from the target will be diffusely transmitted to the satellite sensor. From the discussion in the previous paragraph, it is clear that $f(0) = 0$ and $f(\infty) = 1$. Full details on the derivation of the above is given by Tanré et al. (1981).

The spatial average reflectance for the Earth's surface in the IFOV of a sensor can be defined as

$$\langle \rho_{\text{s}\lambda} \rangle = f(r)\rho_{\text{s}\lambda} + [1 - f(r)]\rho_{\text{b}\lambda}$$

where $\rho_{\text{b}\lambda}$ is the background reflectance, and $\langle \rho_{\text{s}\lambda} \rangle$ replaces $\rho_{\text{e}\lambda}$ in Eq. (3.7). For small r , the background reflectance dominates the average reflectance. This is a problem, particularly for small pixels, known as the *adjacency effect*, where the reflectance values of neighbouring pixels influence each others at-sensor signal. Furthermore the environment function $f(r)$ depends on molecular and aerosol phase functions and, through the diffuse transmittances, molecular and aerosol optical thicknesses (Vermote et al., 1997b) as well. Scattering due to molecules and aerosol dominate at the shorter wavelengths, thus environmental effects are most noticeable for spectral bands in the region < 1000 nm. It has also been shown that for larger wavelengths the single-scattering approximation of modelled at-sensor signal yields reasonable results, but for the shorter wavelength regions the

single-scattering model systematically underestimates the environmental effects (Tanré et al., 1981).

3.2.3 Bidirectional Reflectance Distribution Function

In the preceding sections it was assumed that the surface, whether homogeneous or inhomogeneous, in the IFOV of a sensor had Lambertian reflectance properties. Recall that a Lambertian target reflects radiance isotropically regardless of the direction of illumination, as long as it is illuminated uniformly across its surface. In reality, most targets exhibit a certain degree of non-Lambertian behaviour, and there typically exists a directional component in the reflected signal (that is, there will be variations in the reflected signal depending on illumination and view angles).

The *Bidirectional Reflectance Distribution Function* (BRDF) is used to specify the behaviour of surface scattering as a function of illumination and view geometry. It is a probability density function, denoted $R(\theta_0, \phi_0; \theta, \phi)$, that can be integrated over a solid angle to yield a probability that a photon will be scattered into a small solid angle around a particular view direction.

The radiance reflected by the target in the direction of a sensor (θ, ϕ) is defined as,

$$L_{\lambda}^*(\theta, \phi) = \int_0^{2\pi} \int_0^{\pi/2} R(\theta', \phi'; \theta, \phi) L_{\text{inc}\lambda}(\theta', \phi') \cos(\theta') \sin(\theta') d\theta' d\phi', \quad (3.8)$$

where $L_{\text{inc}\lambda}$ is the radiance of a direct beam illuminating the target. A *bidirectional reflectance factor* (BRF), ρ_R , is defined as the ratio of the reflected radiance to the radiance that would be reflected in the same view direction from a perfect isotropic (Lambertian) reflector under the same illumination conditions. Mathematically,

$$\rho_{R\lambda} = \frac{\int_0^{2\pi} \int_0^{\pi/2} R(\theta', \phi'; \theta, \phi) L_{\text{inc}\lambda}(\theta', \phi') \cos(\theta') \sin(\theta') d\theta' d\phi'}{\frac{1}{\pi} \int_0^{2\pi} \int_0^{\pi/2} L_{\text{inc}\lambda}(\theta', \phi') \cos(\theta') \sin(\theta') d\theta' d\phi'}. \quad (3.9)$$

Note that all the factors on the righthand side of Eq. (3.9) that are independent of angle will cancel upon substitution. Equation (3.9) thus becomes,

$$\rho_{R\lambda}(\theta_0, \phi_0; \theta, \phi) = \pi R(\theta_0, \phi_0; \theta, \phi).$$

The *hemispherical reflectance* or *albedo*, $\rho_{H\lambda}$, defined as the surface reflectance integrated over all viewing angles in the upward hemisphere, is

$$\rho_{H\lambda}(\theta_0, \phi_0) = \frac{1}{\pi} \int_0^{2\pi} \int_0^{\pi/2} \rho_{R\lambda}(\theta_0, \phi_0; \theta', \phi') \cos(\theta') \sin(\theta') d\theta' d\phi'. \quad (3.10)$$

The need to model a target's BRDF is particularly important in multitemporal image analysis because on different dates, changes in solar zenith angle and azimuth and—for some sensors more than others (AVHRR, see Cracknell (1997, p. 312))—the angle at which a target is viewed may lead to significant errors in reflectance estimation (Roujean et al., 1992). The various approaches to modelling target BRDF can be categorised as either physically-based, empirical or semi-empirical. Physically-based approaches are often computationally demanding as they involve modelling complex geometries of features on the target's surface (e.g. the orientation of leaves in a canopy), making them impractical for use in large-scale correction of satellite imagery. Of the other two categories, there are numerous other methods of which only the empirical approach of Walthall et al. (1985) and the semi-empirical approach of Roujean et al. (1992) shall be discussed here.

Walthall et al. (1985) observed that polar plots of simulated canopy BRFs for soybean plants, for a variety of solar (θ_0, ϕ_0) and view (θ, ϕ) geometries, resembled the family of curves of the limaçon of Pascal. Models producing the cardioid shape were tested on simulated data and shown to be very accurate ($< 0.3\%$ RMS error for $500 \text{ nm} \leq \lambda \leq 600 \text{ nm}$ and $< 3\%$ RMS error for $800 \text{ nm} \leq \lambda \leq 1100 \text{ nm}$). When the model was compared to field soil data (of different soil roughness), surprisingly good agreement (RMS error between 0.6 and 3.3%) was observed. Walthall et al. (1985) used the expression for BRF,

$$\rho_{\text{RL}} = a_1(\theta_0^2 + \theta^2) + a_2\theta_0^2\theta^2 + a_3\theta_0\theta \cos(\phi - \phi_0) + a_4,$$

where the coefficients a_1 to a_4 are estimated from statistical regression of a set of BRF measurements at different θ_0 , ϕ_0 , θ and ϕ values. For nadir-looking sensors such as the Landsat TM and ETM+, the expression of Walthall et al. (1985) reduces to,

$$\rho_{\text{RL}} = a_1\theta_0^2 + a_4,$$

which was used by Moran et al. (2001) to characterise the BRF, and assess the temporal stability, for some targets.

The approach of Roujean et al. (1992) to modelling the BRDF effects is based on the physical interaction of radiation with a heterogeneous surface. There are two components to the proposed model: Firstly, there is a *geometric* component, where a surface

is assumed to be comprised of a number of protrusions with a particular height and separation, and random orientation. The second is a *volume* component, that assumes a medium is homogeneous with randomly located scattering plane facets (e.g. a canopy). The proposed BRF model is written as,

$$\rho_{\text{RA}} = k_0 + k_{\text{geom}}f_{\text{geom}} + k_{\text{vol}}f_{\text{vol}} \quad (3.11)$$

where f_{geom} and f_{vol} are the geometric and volume scattering kernels, k_{geom} and k_{vol} are the geometric and volume scattering parameters, and k_0 is constant. Both f_{geom} and f_{vol} depend on the incident (θ_0, ϕ_0) and reflected (θ, ϕ) directions of the radiation. Coefficients k_{geom} and k_{vol} both relate to the sub-pixel surface (e.g. canopy) geometric and volume properties. Finally, k_0 is simply defined as the BRF when $\theta_0 = \theta = 0$.

The hemispherical reflectance is also calculated by Roujean et al. (1992) as,

$$\rho_{\text{H}\lambda} = k_0 + k_{\text{geom}}I_{\text{geom}} + k_{\text{vol}}I_{\text{vol}}$$

where I_{geom} and I_{vol} are integrals which may be accurately approximated by trigonometric functions that depend on solar zenith angle (θ_0) .

In their formulation, Roujean et al. (1992) also take into account the *hot spot* phenomenon, corresponding to the maximum in perceived target brightness when view and solar directions coincide.

Significance for Landsat TM and ETM+ Image Data

The Landsat TM and ETM+ sensors are widely regarded as nadir-viewing instruments, but at the extremes in the Earth scan, the sensor views range from $\pm 7.5^\circ$ off-nadir. This is small in comparison with other sensors (e.g. SeaWiFS, AVHRR, MODIS).

Table 3.5 presents 6S-modelled radiances at 480 nm for a range of view angles, θ_v , and aerosol optical thicknesses, τ_{M480nm} . The underlying surface is assumed to have zero surface reflectance, so the modelled radiances are in fact path radiances, L_{p480nm} . This wavelength region was chosen because of the relative dominance of the path contribution to the satellite-signal at 480 nm. Modelling error in Table 3.5 is interpreted as the percentage error incurred if a nadir (0°) view zenith angle is assumed when θ_v is the correct view angle. Clearly the table illustrates that if a pixel at the edge of a TM or ETM+ scan ($\pm 7.5^\circ$) is assumed to be viewed at nadir, the path radiance is underestimated by $< 5\%$; which is about the absolute accuracy of the TM and ETM+ sensors

Table 3.5: Simulated (6S) path radiances at 480 nm, L_{p480nm} [$W/(m^2sr\mu m)$], for a range of view zenith angles (θ_v) and aerosol optical thicknesses (τ_{M480nm}). The *Error* (%) is to be interpreted as the modelling error incurred for L_{p480nm} if $\theta = 0^\circ$ is assumed when $\theta = \theta_v$ is more appropriate.

θ_v	$\tau_{M480nm} = 0.06$		$\tau_{M480nm} = 0.12$		$\tau_{M480nm} = 0.23$	
	L_{p480nm}	% Error	L_{p480nm}	% Error	L_{p480nm}	% Error
0°	32.47	0	34.38	0	38.26	0
7.5°	34.02	-4.8	35.77	-4.3	39.90	-4.1
15°	35.99	-9.8	38.02	-9.5	42.10	-9.1
30°	41.26	-21.5	43.62	-21.1	48.27	-20.7
60°	63.43	-48.8	67.21	-48.8	74.33	-48.5

(Thome et al., 1993; ACRES, 1999; Teillet et al., 2001). For sensors like the AVHRR and MODIS (view angles $\sim 55^\circ$), these errors become unacceptably large, and the view geometry for pixels is far more significant.

The effect of solar and sensor viewing geometries on the estimate of a target's BRDF/BRF for TM and ETM+ imagery is not considered in this thesis. If it is assumed that the TM and ETM+ sensors are nadir instruments, then the Walthall model for BRF becomes dependent on the solar zenith angle and relative azimuth ($\phi - \phi_0$) only, as shown previously (p. 65). Danaher et al. (2001) and Wu et al. (2001), however, observed that there was systematic brightening of pixels near the western edge (backscattering direction) of imagery and a darkening of pixels near the eastern edge (the forward scattering direction), even after images were normalised for solar zenith angle and corrected for Earth-Sun distance. This causes problems for visual display when east-west neighbouring images are mosaiced (Wu et al., 2001).

Wu et al. (2001) investigated the use of 3 Walthall-type models to model the BRF for TM and ETM+ imagery. Based on the statistics of overlap regions they were able to correct for the east-west brightness differences that were a result of the $\pm 7.5^\circ$ change in view zenith angle. The method described remains a relative approach since overlap statistics are calculated using the at-sensor reflectance (Eq. (3.3), p. 57) which, as described in sections 3.2.1 and 3.2.2, are not the surface reflectances. The method does, in theory, normalise imagery for atmospheric effects, and has been successfully applied in the creation of a mosaic of the Australian continent; comprising 369 Landsat-7 ETM+ images (Wu et al., 2001).

3.2.4 Modelling Software: 6S

The computer code known as the *Simulation of the Satellite Signal in the Solar Spectrum* (5S) was developed by Tanré et al. (1986) to estimate the signal measured by a satellite sensor. The models used were those discussed in Sections 3.2.1 and 3.2.2, and users had the option of selecting a particular band for a number of satellite sensors, including for example NOAA-8 and -9 AVHRR, and Landsat-5 MSS and TM.

The 5S code was known to have some shortcomings. The issue of BRDF, for example, was not accounted for in the 5S code, thus targets are by default assumed to be Lambertian. Furthermore, some of the calculations were based on approximations and simplifications that limited the generality/accuracy of the software, particularly in relation to the diffuse (scattering) terms. Vermote et al. (1997b) commented that, '*the authors of 5S had to sacrifice the reality versus the practical use of simulation code*'. Nevertheless, 5S has been used by many researchers to calculate various terms in satellite image correction schemes (Caselles and López-García, 1989; Thome et al., 1993; Moran et al., 1995; Teillet and Fedosejevs, 1995), and as a means of assessing and comparing the accuracy of the results of correction strategies (Moran et al., 1992; Kaufman and Remer, 1994; Chavez, 1996).

Some ten years later, the *Second Simulation of the Satellite Signal in the Solar Spectrum* (6S) code was developed (Vermote et al., 1997b) which extended the generality of 5S and improved the accuracy of some of the computations. The 6S code is one of the more popular at-sensor signal modelling software packages and, like its predecessor 5S, has been used in many investigations where accurate models for path radiance, diffuse and direct transmittances, spherical albedo, surface-atmosphere interactions, and BRDF are required (Huete et al., 1997; Kaufman et al., 1997c; Zhao et al., 2001; Karnieli et al., 2001; Miura et al., 2001).

The interest in 6S for this thesis is that it serves to: provide the values required to illustrate some concepts discussed in the text (Chapter 2 and the next section for example); model the path radiance (or atmospheric reflectance) for the image normalisation procedure described in Chapter 4; and be used in the fashion described by Zhao et al. (2001) to estimate surface reflectances in imagery for comparisons with the image normalisation procedure described in Chapter 4.

The increased accuracy of 6S over its predecessor lies in the method utilised to model scattering effects. The code calculates the atmospheric reflectance, diffuse transmittance, spherical albedo and coupled absorption-scattering transmittance using the Successive Orders of Scattering (SOS) algorithm. This along with some other features of 6S are discussed briefly in the following.

Correction for Earth-Sun Distance

In 6S the Earth-Sun distance adjustment factor D is calculated via Eq. (2.2) after the code has calculated the day of the year, J , from the input values of day and month. The solar irradiance at the TOA, $F_{0\lambda}$ is multiplied by D to obtain the value $F_{d\lambda}$ that is referred to through this thesis.

Gaseous Absorption

Three additional atmospheric gases were added to the list considered in 5S. Gaseous absorption considered in 6S is due to ozone, O_3 ; oxygen, O_2 ; water vapour, H_2O ; carbon dioxide, CO_2 ; methane, CH_4 ; nitrous oxide, N_2O ; and carbon monoxide, CO . The methods used to calculate the transmittance through the absorbing atmosphere are the same as for 5S. However, 6S uses the parameters for the various gases from the HITRAN database at 10 cm^{-1} .

Atmospheric Reflectance

In 5S, as in Eq. (3.6, p. 60), the single scattering approximation allows the atmospheric reflectance to be written as a sum of molecular and aerosol contributions: the molecular contribution is calculated as per the first term of Eq. (3.6); the aerosol contribution is calculated using an approximation (Tanré et al., 1986, p. 91-93) in which the phase function, in the source term of the radiative transfer equation (RTE, Eq. 2.31), is approximated by two Legendre polynomials. Vermote et al. (1997b) has pointed out that this may not be true, particularly for short wavelengths ($< 450\text{ nm}$) and/or large solar or view zenith angles. So in 6S, the SOS algorithm is employed to calculate the atmospheric reflectance for a combined molecular-aerosol system.

In summary, the SOS algorithm is a numerical procedure used to solve the RTE in an iterative fashion. The full details of the implementation of the procedure in 6S

is given in Vermote et al. (1997a). Essentially, Eqs. (2.32) and (2.33) are solved for a discrete number of layers in the atmosphere. The iterative component arises when the initial solution, based on first-order scattering only, is fed back into the source function for each layer and repeated until convergence.

Diffuse Transmittance and Spherical Albedo

The diffuse reflectance S and transmission T functions were previously defined for a single scattering layer (Chapter 2, pp. 33–34). Since the SOS algorithm works on a discrete number of scattering layers in the atmosphere, these functions are more accurately modelled in 6S, particularly if one of the layers is at the level of the sensor. For space-borne observations the corresponding layer is the TOA, and these quantities are calculated in 6S with realistic mixing between aerosol and molecules (Vermote et al., 1997b).

Since functions T and S were used to define the diffuse transmittance (p. 34) and spherical albedo (p. 34), the 6S estimates of $t_{d\lambda}$ and s_λ are more accurately modelled than their 5S counterparts; calculated using the Zdunkowski approach and a semi-empirical formula (Tanré et al., 1986) respectively, which can have errors on the order of a few hundredths of a reflectance unit when solar or view angles are large, or when optical thicknesses are high (Vermote et al., 1997b).

3.3 Issues in Multitemporal Analysis

In Section 3.1.1, reference was made to a number of authors who have used satellite images beyond the limited areas of investigation for which the data were originally intended. Researchers have utilised repeated measurements of emergent radiation, for a given location on the Earth, available in multi-date sequences of satellite imagery to quantify change in some aspect of the Earth’s surface through time. The interpretation of the results from procedures applied to multiple satellite images of the same scene over time for the extraction of information, or enhancement of some aspect, is termed *multitemporal* analysis. This extends the spatial *mapping* of surface features (themata) in a satellite scene into temporal *monitoring*.

Multitemporal sequences of satellite imagery have been used in many diverse fields of study and application: from changes in atmospheric dynamics and composition; to

changes in sea surface temperature, ocean colour dynamics, and productivity. For land applications, however, there exists no more compelling demonstration of the usefulness of multitemporal image sequences than their application to the study of *land cover*⁶ change (Graetz et al., 1992). Sing (1989) provided some further examples of multitemporal analysis of land cover change, such as: assessing changes and shifts in cultivation; measuring rates of deforestation; monitoring changes in plant phenology and seasonal pasture production; disaster monitoring; crop stress; and day/night analysis of thermal emissions, to name a few.

There are a number of issues that must be considered when multitemporal sequences of satellite imagery are used to analyse land cover change. Left unaddressed these issues can hamper change detection efforts. How these issues are dealt with is largely dependent on the nature of the problem one seeks to investigate with the data. A review of some approaches designed to minimise the impact of the factors arising from these issues as well as the enhancement of image data is presented in Section 3.4. Attention focuses on the key issues that need to be considered in multitemporal analysis when Landsat TM and ETM+ images are used.

3.3.1 Geometric Correction and Co-registration

Jensen (1996, p. 124) provides a summary of some of the factors that lead to geometric distortion in imagery. One source of error is due to the FOV of the sensor and is known as *panoramic distortion*. Panoramic distortion is a result of the area of the Earth surface in the IFOV appearing larger at the beginning and end of each scan line than at nadir; resulting in bigger pixels at the edges of imagery than in the centre. This type of distortion is most noticeable for sensors with large FOV, such as AVHRR (FOV 112°) or MODIS (FOV 112°). For the TM and ETM+ sensors (FOV 15°), the panoramic distortion in pixel size is about 30 cm (approximately 1% of the pixel dimension) and can thus be ignored.

Other sources of geometric distortion due to the sensor system are corrected by on-ground processing prior to the data reaching the users (see Jensen (1996)). The geometric distortions of concern in multitemporal analysis, that are not due to the

⁶A generic term used to describe all possible landscapes. Landcover is defined by Graetz et al. (1992) as “the envelope of living organisms that exist on or in the terrestrial or oceanic surfaces, between the lithosphere and the atmosphere.”

sensor, are termed *planimetric distortions*, and relate to fixed features on the Earth's surface having different (x,y) positions between image pairs. The notation adopted here is that x represents the position number of a *pixel* (or cell) along a scan *line*, y , in an image. An image, therefore, is referred to as having M lines and N pixels per line (with $1 \leq x \leq N$ and $1 \leq y \leq M$).

Two approaches for correcting for planimetric distortions are image-to-map *rectification* and image-to-image *registration*. Rectification involves assigning to image coordinate, (x,y) a map coordinate (E,N) , where E and N are the *eastings* and *northings* of a particular map projection. Registration involves a translation and rotation of the image data so that two images of the same geographic area are positioned coincident with one another, so that the same feature of the Earth's surface has the same position in both images.

Rectification is desirable when one seeks to accurately estimate distances and areas, or when the image data are to be integrated with other geographic data, such as a geographic information system (GIS). In multitemporal analysis, it is crucial that images are accurately co-registered. However, the two processes are often combined in a hybrid co-registration scheme with the end result being an image sequence co-registered to the same map base.

Datum and Map Projection

It is well known that the shape of the Earth is not a sphere, but is better represented by a spheroid defined by certain major and minor axes. If at least one point on (or within) the spheroid can be linked to a point on (or within) the Earth (a point known as a *tie point*) then the spheroid defines a *datum*. Two datums commonly used in Australia are: the Australian Geodetic Datum AGD66, so called because it was fully defined in 1966, with a tie point located at Johnston's memorial (E 133°56', S 25°12') in the Simpson Desert, Australia; and the Geocentric Datum of Australia GDA94, with the tie point defined at the centre of mass of the Earth.

A *map projection* is a mathematical function to transform the 3-dimensional surface of the Earth into a 2-dimensional representation. There are numerous map projections, but one of the most used is that known as *transverse mercator*; a regular grid with the origin of the coordinate system located at the bottom-left corner of the grid. There are

a number of transverse mercator grids that cover the entire Earth, each one defining a *zone*. The Australian continent, for example, is covered by zones 48–58. The Australian Map Grid (AMG) and the Map Grid of Australia (MGA) are two examples of regular grids having transverse mercator projection, with distances measured in metres. The map grid for zone 50, AMG50 for example, has an origin off the southwest coast of Western Australia.

Image Co-registration

Accurate co-registration is essential for change detection studies, as poorly registered imagery can lead to the detection of false change and compromise the whole multitemporal effort (Sing, 1989; Furby and Campbell, 2001). Figure 3.8 illustrates the effect that poorly registered imagery have on multitemporal analysis. Displayed in both (a) and (b) are band 5 images for the same scene acquired on two different dates. The dark feature to the left of centre is an airport runway. The first date is displayed in the red, the second in green. Regions of no change between the two images are highlighted in shades of yellow. In Figure 3.8(a) the two images are clearly not registered very well as is evident by the green and red ghosting either side of the runway. Figure 3.8(b), on the other hand, illustrates better registration of the imagery and ghosting effects are significantly reduced. Ghosting, due to mis-registration, may lead to the detection of false change, particularly when change detection schemes are employed that involve pixel-wise operations.

Rectification involves selecting a number of *ground control points* (GCPs). GCPs are points on the Earth's surface, with known map coordinates, (E,N), that can be identified in imagery. A mathematical relationship between image coordinates (x,y) and the GCPs is determined via spatial interpolation and the image is transformed to the geometry of the map. The transformation assumes the form,

$$x = \sum_{k=0}^P \sum_{l=0}^Q a_{kl} E^k N^l, \quad (3.12)$$

$$y = \sum_{k=0}^R \sum_{l=0}^S b_{kl} E^k N^l \quad (3.13)$$

which is interpreted as mapping the image location (x,y) to map coordinate (E,N). The exponents P , Q , R and S are the orders of the polynomial in terms of eastings and nor-

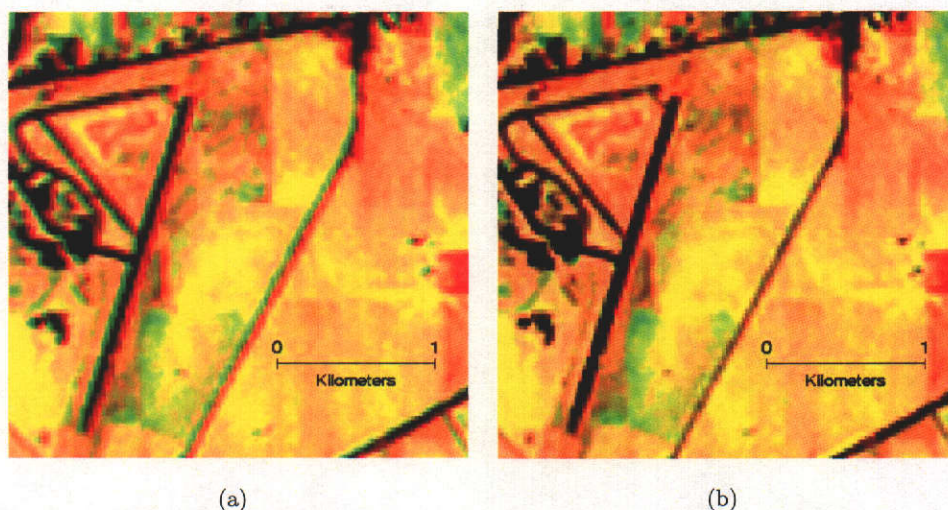


Figure 3.8: Illustration of poor (a) and (b) good co-registration of two dates of TM imagery (band 5). Shades of green and red indicate regions of false change.

things for line y and pixel x ; coefficients a_{kl} and b_{kl} can be determined via least-squares regression. Polynomials typically do not exceed third order, however the appropriate order can be determined via statistical significance testing (t -tests, for example) on the coefficients of the polynomials.

The number of GCPs used in the rectification process is not as important as the distribution of points throughout the scene. Typically around 100–200 GCPs are used in the rectification process (Furby, 2000), and a uniform distribution of points can minimise any bias that may lead to the type of mis-registration observed in Figure 3.8.

Registration, in its simplest form, is employed when it is not essential to assign the pixels in an image any geographic coordinates; for example, when one seeks to observe change between two images. In this situation, it is necessary however to ensure that the same fixed features in both images are accurately positioned. This is difficult when the images have different line and pixel numbers (encountered when subsets of image data are used). Therefore, one often finds that a combination of rectification and registration is employed, in which one image in the multitemporal sequence, referred to as the *rectification base image*, has been rectified to a map projection. All other images are then registered to the rectification base image.

In this combined approach, the GCPs that were used to rectify the base image are

also used to co-register the other *unregistered* images in the sequence. Each GCP must be linked to an image co-ordinate. This can be time consuming, particularly if the number of GCPs is large (> 100 say). Furby (2000) suggested an approach whereby the image coordinates for a small number of GCPs, 4 say, is determined by visual inspection. The approximate position of the remaining GCPs in the un-registered image is based on the original 4. The positions are further refined via a *cross-correlation feature matching* procedure between the rectification base image and un-registered image. The correlation is calculated for a neighbourhood of pixels (say 20×20 pixels) centred on the GCP for a spectral band with high contrast (TM band 5 for Summer scenes (Furby, 2000; Furby and Campbell, 2001)). A high correlation (around 1) indicates a good fit, whilst a low correlation (< 0.75) indicates a bad fit, and the corresponding GCPs are excluded from the rectification process. Mathematical relationships in the form of Eqs. (3.12) and (3.13) are then obtained between the un-registered pixel coordinates (x, y) and the GCPs in the base image (E, N) .

Resampling

Once expressions have been found that relate image coordinates to eastings and northings, the next task is to determine appropriate intensity values (DN) for the (E, N) coordinates in the rectified image. This is achieved by *resampling* the original, un-registered image. Three methods for resampling are described below.

Nearest neighbour resampling chooses the intensity of the pixel nearest the predicted position (\hat{x}, \hat{y}) from Eqs. (3.12) and (3.13). This method of resampling has the least impact on the radiometric quality of the data, since it involves copying an actual data value to the rectified image. Nearest neighbour resampling is criticised because edges appear in the rectified image in the direction of the sampling, however, it is the recommended procedure for multispectral images as it preserves between-band, or spectral, relationships.

Bilinear resampling performs a 2-dimensional interpolation of the four closest neighbours to the predicted (\hat{x}, \hat{y}) . The resulting rectified image will be smoother in appearance than that produced by nearest neighbour resampling, however between-band relationships may be compromised in the interpolation process.

Cubic convolution (also known as bicubic) also uses a neighbourhood of pixels (say,

16 pixels) to perform a 2-dimensional interpolation for the value at (\hat{x}, \hat{y}) , however the interpolating polynomial is a third-order polynomial (a cubic). The resulting image again appears smooth and thus the method suffers the same criticism as bilinear in regards to compromising between-band relationships and radiometric integrity of the original imagery.

3.3.2 Sensor Calibration

For many applications involving sequences of satellite imagery, the key issue is to ensure that a given sensor's response to a certain amount of radiance emerging from the earth-atmosphere system be the same at any time during the sensor's lifetime; changes in the satellite observations that are due to artefacts in the measurement system have the potential of being incorrectly attributed to changes in land use and land cover (Slater et al., 1987; Roderick et al., 1996; Thome et al., 1997; Dinguirard and Slater, 1999; Thome, 2001; Teillet et al., 2001). Of particular importance is a band's responsivity, g_λ , which (recall from Section 3.1.4, p. 54) relates the physical radiance received at the satellite sensor, L_λ^* , to the raw digital number (DN), X_λ , for that band.

Sensors on the Landsat series of satellites have achieved onboard in-flight calibration via an internal calibrator (IC) system. The ICs for Landsat-5 TM consists of 3 calibration lamps⁷, themselves calibrated pre-flight in a laboratory to a high degree of accuracy with integrating spheres (Markham and Barker, 1986; Thome et al., 1997). Detector pre-flight responsivities were determined from regression of the lamp responses against the pre-flight measured radiances, for eight different lamp states⁸. Onboard calibration of the detectors is achieved by routinely measuring lamp irradiances and the relating the values back to pre-launch radiance values. It has been noted, however, that the IC lamps have problems maintaining their pre-flight calibration in orbit as a result of the micro-gravity and vacuum conditions experienced in space (Slater et al., 2001). Consequently, the accuracy of the onboard in-flight calibration cannot be higher than the pre-flight calibration (Thome et al., 1997; Thome, 2001).

⁷The long-term characteristics of the IC lamps have been monitored by the group led by Dr. Dennis Helder from the South Dakota State University Image Processing Laboratory. Further details are available from the group's website <http://iplab2out.sdstate.edu/>. A description of the IC system for the Landsat-7 ETM+ sensor as well as other onboard approaches are found in Thome (2001).

⁸A lamp state is either on (= 1) or off (= 0). The 8 possible lamp states are (1 1 1), (1 1 0), (1 0 0), (0 0 0), (0 0 1), (0 1 1), (0 1 0) and (1 0 1), each producing a different irradiance level.

The onboard IC system permits TM and ETM+ sensor calibration to be monitored with high temporal frequency. Any changes in the detector responsivity are supposed to be monitored by the IC system and subsequently taken into account by the system that produces the radiometrically-calibrated image products. Differences between the 16 individual detectors are removed so that the radiance value is independent of detector number (Jensen, 1996, p. 108), and the end users need only concern themselves with applying the time-invariant radiometric scaling factors (Table 3.3, p. 56) to convert the *DNs* into radiance values (Teillet, 2002). It has been observed, however, that there have been changes to the Landsat-5 TM measurement system that were not captured by the IC (Thome et al., 1993, 1997). This finding has implications for the radiometrically-calibrated image products and the suitability of radiometric scaling factors in Table 3.3 for calculating accurate radiances. This, and the fact that onboard calibration is not as accurate as pre-flight, has led to a concerted effort in investigating alternatives to in-flight sensor calibration that are independent of onboard IC systems and pre-flight calibration.

Vicarious In-flight Calibration

Vicarious methods for calibrating satellite sensors are useful for monitoring a sensor's radiometric performance independently of onboard diagnostics (Dingirard and Slater, 1999). Two of the most often used methods for vicariously calibrating a satellite sensor were first proposed by Slater et al. (1987): these are the *reflectance-based* and *radiance-based* methods. The reflectance-based method requires measurements of surface reflectance, atmospheric optical thickness and meteorological measurements, and coincident satellite *raw* image *DNs* for a large, homogeneous target. These measurements are used in conjunction with radiative transfer code to model the at-sensor radiance. The radiance-based method attempts to mimic satellite observations by using spectrometer measurements of a surface target from an altitude above much of the scattering layer in the atmosphere. Radiative transfer code is used only to model residual scattering and absorption effects that may occur between the spectrometer and space. The raw image *DNs* for the target are divided by TOA radiance modelled with the reflectance- or radiance-based methods to yield estimates of sensor responsivity for each band (see Dingirard and Slater (1999) for more details). The key considerations of two field cam-

paigns that employed the reflectance-based method to monitor change in Landsat TM's responsivity are given below.

Surface reflectance measurements are often acquired with hand-held spectrometers whose spectral range matches that of the satellite sensor being investigated (e.g. TM/ETM+ between 400–2400 nm). It is also important to make a large number of ground-based measurements in the least amount of time, to ensure that there is as little change as possible in atmospheric condition and Sun angle from the time of image acquisition. Slater et al. (1987) described a “yoke” system to acquire numerous spectrometer measurements in which the instrument was suspended from a bar straddling the operator's shoulders and approximately 1 m to one side. Thome et al. (1993) described a “reflectomobile” in which the spectrometer is mounted on a trailer and towed across the target, reducing the acquisition time (compared to the yoke) by half.

It is recommended that the target be uniform and bright in surface reflectance, so that errors in modelling the scattering component of the satellite signal are reduced. The target should also be large enough such that a sufficient numbers of pixels may be used to estimate the target's average *DN*. The White Sands Missile Range test site in White Sands, New Mexico, has been used in numerous vicarious field campaigns (Slater et al., 1987; Thome et al., 1993; Thome, 2001) because it satisfies both criteria: the area is composed of gypsum sand dunes, which are quite bright, and contains relatively small amounts of vegetation; and the site where measurements were acquired is a rectangular, 480×120 m area corresponding to 16 rows of 4 pixels (64 pixels in total for each band) in a TM and ETM+ image. Thome (2001) gave further guidelines for selecting the ideal test site for a vicarious calibration field campaign. They include: the site elevation should be above 1 km, so uncertainty in aerosol characteristics has negligible influence on modelled radiance; and the site should be Lambertian in reflectance properties and flat terrain to minimise the impact of BRDF and shadowing.

In the vicarious calibration campaigns described by Slater et al. (1987), Thome et al. (1993) and Thome (2001), there were instruments measuring barometric pressure, and radiometers measuring solar extinction in a number of narrow bands. From these measurements, the researchers were able to infer estimates of molecular, aerosol, and ozone optical thicknesses, as well as columnar water vapour concentrations. These results, along with reasonable assumptions about the aerosol type, and the average surface re-

flectance for the test site were input to radiative transfer modelling code to yield an estimate of the at-sensor radiance. Finally, the average *DN* values for the test site were divided by the modelled at-sensor radiance to yield an estimate of the responsivity for each band.

Thome et al. (1993) utilised the reflectance-based method to estimate the Landsat-5 TM responsivity from image data acquired over the White Sands test site for 8 dates between July 1984 and August 1992. Data were also collected and processed for 2 additional dates (October 1993 and 1994) for the same test site, the results of which were published by Thome et al. (1997). The reflectance-based observations of Thome et al. (1993, 1997) demonstrated that there was a clear change in Landsat-5 TM responsivity during the sensor's lifetime that was much larger for bands 1–3 than the other bands. Apart from the last observation in the sequence, the responsivities for bands 4 and 7 appeared to have changed the least during the sensor's lifetime.

A comparison of the vicarious results with those determined via the onboard IC system, revealed good agreement in the behaviour of bands 1 and 2 responsivities; the vicariously-derived responsivities being slightly less than the IC-derived values. The IC system detailed an upwards-increasing trend in bands 2–4 responsivities that was not evident in the vicarious results. The IC responsivities for bands 5 and 7 had an erratic temporal behaviour with an apparently linear upwards trend; a behaviour not observed in the reflectance-based results because of the comparatively small number of field campaigns. The limited number of vicarious observations, however, indicated marginal differences relative to the pre-flight responsivities for bands 4, 5 and 7.

The onboard IC system reported an exponential decay in responsivity with time for bands 1–4 (the primary focal plane bands) that was attributed to outgassing of the spectral bandpass filters; the scatter of points for these bands were attributed to temperature effects and variations in the alignment between the detectors and the IC system (Thome et al., 1997). The erratic behaviour observed in the band 5 and 7 responsivities time series was attributed to interference due to the build up of frost on the window of the cold focal plane.

It is clear from the findings of Thome et al. (1993, 1997) that there were artefacts in the TM measurement system that lead to changes in responsivity that were not monitored by the IC system. In this regard, the usefulness of vicarious calibration has been

demonstrated; the only disadvantage is the relative infrequency with which vicarious calibration field campaigns are conducted (Thome et al., 1997). Nevertheless, the combined results of the onboard and vicarious calibrations indicated absolute radiometric accuracy of the TM sensor is around 5% for bands 1–4 and slightly higher in bands 5 and 7 ($< 10\%$). Finally, Thome et al. (1993) claims the most important finding of their investigations was the disagreement between the responsivities observed with the reflectance-based method and the gain factors for the Level 1 image products for the same image date. The observed responsivities were around 20% less than those in the Level 1 image product for the VIS bands, and disagreement for the other bands was at most 7%; further justification for the vicarious approach to monitoring sensor calibration.

A reflectance-based vicarious calibration campaign was conducted to monitor the Landsat-7 ETM+ sensor calibration (Thome, 2001). The image data were acquired for 4 dates within the first 198 days of the Landsat 7 mission. Using the same approach as that described above for the White Sands test site, Thome (2001) applied the reflectance-based method to data acquired for an additional two sites: a dry lake bed known as Railroad Valley Playa, Nevada; and Roach Lake Playa, California. It was observed that the reflectance-based responsivities for all dates agreed to within 3.5% of each other, and to with 7% of pre-launch values. From these finding Thome (2001) concluded that the ETM+ sensor calibration has remained stable.

Cross-calibration with Tandem Configuration

Teillet et al. (2001) took advantage of a rare situation in which the Landsat-5 TM and Landsat-7 ETM+ were in tandem orbit, that is with very similar orbital characteristics, and used the acquired imagery to calibrate one sensor with respect to the other. Only a summary of the cross-calibration methodology described by Teillet et al. (2001) is presented in the following.

The two test sites used in the investigations of Teillet et al. (2001) were the dry lake bed of Railway Valley Playa, Nevada, and a grassland site in Niobrara, Nebraska. Even though the TM and ETM+ images for both sites were acquired in relatively quick succession (~ 10 – 30 minutes apart), the data were converted into at-sensor reflectances to (i) minimise the impact of the slight difference in solar position, and (ii) compensate for differences in exo-atmospheric irradiances for the different TM and ETM+ band

responses. Using the link between at-sensor reflectance and raw image DN (via Eqs. (3.1) and (3.3)), Teillet et al. (2001) showed that the TM responsivity may be represented as a linear function of the ETM+ responsivity. For each test site, data pairs were constructed from bias-corrected DN s from both TM and ETM+ images. A straight line fit to these data pairs provided a value of slope M that, when applied to the ETM+ responsivity, gave an estimate of the TM responsivity for each spectral band.

The investigations of Teillet et al. (2001) demonstrated, once again, that there have been changes to the TM responsivity throughout the sensor's lifetime. Not only were the findings consistent with those of the vicarious calibration campaigns (Thome et al., 1993, 1997), but the amounts by which the responsivity in VIS bands decreased were of the same magnitude. It was concluded that using pre-flight calibration coefficients on image data for the VIS bands would lead to significant errors in at-sensor radiance calculations, as well as anything derived from radiances such as surface reflectances. The tandem cross-calibration responsivity for band 4 supported the observations of Thome et al. (1997) that no significant change has occurred in that band throughout the sensor's lifetime. Bands 5 and 7 also showed little change relative to pre-flight (around 1 and 2% in absolute value for band 5 and 7, respectively).

A Final Remark On Sensor Calibration

The impact that changes in sensor calibration can have on satellite imagery and derived image products in multitemporal analysis was demonstrated using AVHRR data by Roderick et al. (1996). Changes in sensor slope (related to the sensor's responsivity) from pre- to in-flight for the AVHRR throughout the sensors lifetime onboard NOAA-7, -9, and -11 are well documented (Cracknell, 1997, pp. 93–102). Of particular interest were the sensor slopes for bands 1 and 2, corresponding to the VIS and NIR respectively. From these bands, the normalised difference vegetation index (NDVI)⁹ is calculated; a popular index used by many investigators to monitor large-scale patterns of vegetation change and condition. Large errors of up to 0.07 NDVI units (i.e. approximately 10–40% of typical NDVI values for vegetated targets) are observed in the calculated index from

⁹An index calculated as the difference of reflectances in the NIR and red bands divided by the sum of reflectances for those same bands, was observed to be correlated with a number of canopy variables (see Tucker (1979) for example). Further details on the calculation of NDVI are presented in Section 4.4.1 on page 168.

differences in sensor slope alone (Roderick et al., 1996).

Roderick et al. (1996) constructed times series from 117 months of AVHRR-derived NDVI (spanning the lifetimes of AVHRRs on three NOAA satellites) for a large area over Western Australia. The data exhibited a strong seasonal component, which was removed using a 12-point moving average filter. This revealed three distinct trends: the first, corresponding to the data collected with the NOAA-7 AVHRR, was a flat, constant value around 0.07; the second, a linearly-increasing trend for the lifetime of NOAA-9 AVHRR; and the third was once again flat and constant in value, around 0.03, for the NOAA-11 AVHRR data. The errors in calculated NDVI that the observed trend introduced resembled (in regards to the shape of the curves) those simulated for NDVI that incorporated the changes in sensor slope reported by Kaufman and Holben (1993, cited in Roderick et al. (1996)). Removal of the trend resulted in a NDVI time series that was dominated by a seasonal component only (as expected).

The work of Roderick et al. (1996) is an example where techniques can be developed that correct image data for changes in sensor calibration independently of onboard or vicarious knowledge of sensor response. Roderick et al. (1996) noted that the described technique cannot be used to provide a calibration of the image data to an absolute scale, but for the application that their technique was intended (namely, using NDVI to monitor vegetation change), this is not essential. Such techniques achieve a *relative* calibration, and this is explained in further detail in Section 3.4.

3.3.3 Atmospheric Effects in Satellite Imagery

Atmospheric composition and properties vary on small and large spatial scales, and on temporal scales of the order of hours, days, months and years. In multitemporal analysis, therefore, it is a reasonable assumption to make that the atmospheric conditions on a given date will differ to those of other dates in the sequence. The atmospheric effects considered in this thesis are either *additive* or *multiplicative* in nature in regards to the measured at-sensor signal. Using simulated data provided by the 6S code, this section describes how these effects are manifest in satellite images.

Furthermore, to illustrate these effects, it is assumed in the examples presented that image data were acquired with the Landsat-5 TM sensor, with solar zenith angle and azimuth $\theta_0 = 36.19^\circ$ and $\phi_0 = 81.36^\circ$, respectively. Also note that in the figures

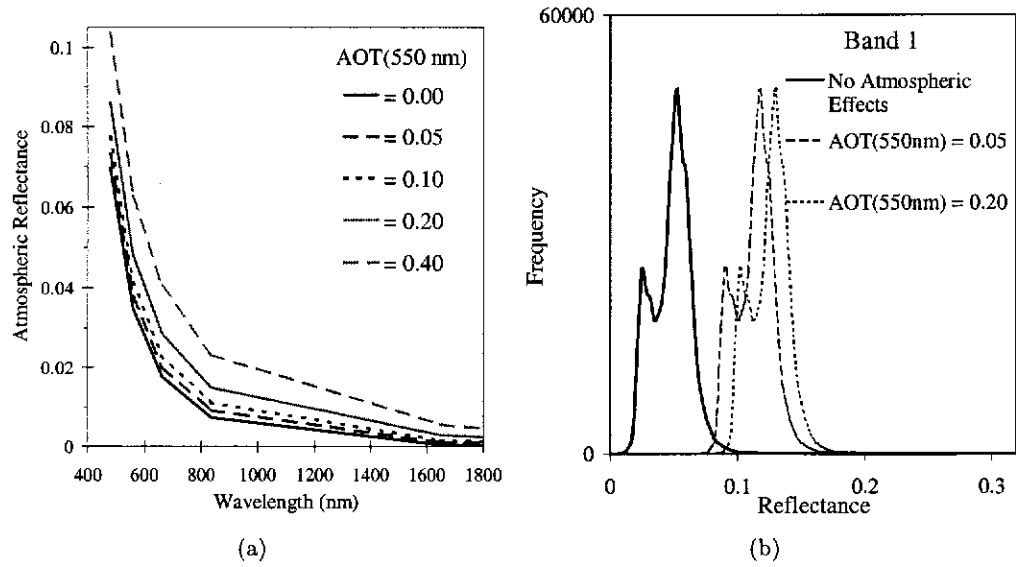


Figure 3.9: Additive effects in satellite imagery: (a) An illustration of the spectral behaviour of intrinsic atmospheric reflectance values, $\rho_{\text{atm}\lambda}$, for different aerosol optical thicknesses (AOT) at 550 nm; (b) The impact of the path effect on satellite image data for a subset of a Landsat-5 TM image ($\theta_0 = 36.19^\circ$ and $\phi_0 = 81.36^\circ$).

containing image histograms, the label “No Atmospheric Effects” is assigned to image data that have had all (if any) atmospheric effects removed.

Additive Effect

The additive contribution to the at-sensor signal, termed the *path effect*, is due to the intrinsic atmospheric reflectance, $\rho_{\text{atm}\lambda}$ (or path radiance, $L_{p\lambda}$). Recall from Eq. (3.6, p. 60) that in the single scattering approximation, the atmospheric reflectance is decomposed as separate contributions from molecules and aerosols. However, as was previously mentioned (p. 69), a more accurate formulation, encompassing a greater range of aerosol optical thickness and observation angles, deals with a combined molecule-aerosol system and the SOS algorithm (Vermote et al., 1997b). Finally, a more complete definition of the atmospheric reflectance incorporates any gaseous absorption that may occur along the path from the Sun to the satellite sensor (Figure 3.6, p. 59). The 6S code, therefore, was used to calculate the atmospheric reflectances presented in Figure 3.9.

In Figure 3.9(a), it can be seen that the path effect is most obvious in the VIS, and that $\rho_{\text{atm}\lambda}$ increases with increasing AOT. For wavelengths above 800 nm, the

atmospheric reflectance is observed to be less than 0.02 for $\tau_{M550nm} = 0 - 0.2$.

The implication for TM/ETM+ bands 1–3, is that the path effect introduces an offset in the image data (the offset decreasing in magnitude from bands 1 to 3). The offset has the effect of lightening the image data, which is illustrated in Figure 3.9(b) for band 1 data from a 512×512 subset of a Landsat-5 TM image.

If image data are free of atmospheric effects (Figure 3.9(b), histogram labelled “No Atmospheric Effects”), then the at-sensor reflectance (Eq. (3.3), p. 57) corresponds to the surface reflectance, that is $\rho_{sat\lambda}^* = \rho_{s\lambda}$. The path effect, however, results in a clear shift of the reflectance histogram to higher values. In Figure 3.9(b), molecular optical thickness is kept constant (as is gaseous transmittance) while the aerosol optical thickness takes on two values ($AOT(550\text{ nm}) = 0.05$ and 0.2), resulting in a histogram shift that increases with increased optical thickness. Therefore, the apparent (at-sensor) reflectance of a target, $\rho_{sat\lambda}^*$, becomes brighter; an effect most noticeable for dark (low reflectance) targets. In fact, if the target has a zero surface reflectance, then $\rho_{sat\lambda}^* = \rho_{atm\lambda}$.

Multiplicative Effects

The total atmospheric transmittance is a combination of scattering of the photons in and out of the direct beam by the molecules and aerosols, and absorption by atmospheric gases. The total atmospheric transmittance, simulated with MODTRAN4, for a mid-latitude summer model is displayed in Figure 3.10 for the solar reflective region of the EM spectrum. Also presented are the response curves for Landsat-5 TM bands 1–5 and 7, illustrating their placement in relation to some of the more prominent absorption features. The scattering effects on atmospheric transmittance exhibit a smooth wavelength dependence, impacting the VIS and NIR. Gaseous absorption occurs for a number of wavelengths throughout the solar reflective region; highlighted in Figure 3.10 are the gases contributing to some of the more prominent absorption features (from left to right: ozone (O_3), oxygen (O_2), water vapour (H_2O), carbon dioxide (CO_2) and methane (CH_4)).

Recall (pp. 60–61) that total scattering transmittance is defined as the sum of direct and diffuse transmittances through the scattering layer of the atmosphere. The 6S code was used to compute the direct and diffuse transmittances presented in Figure 3.11(a).

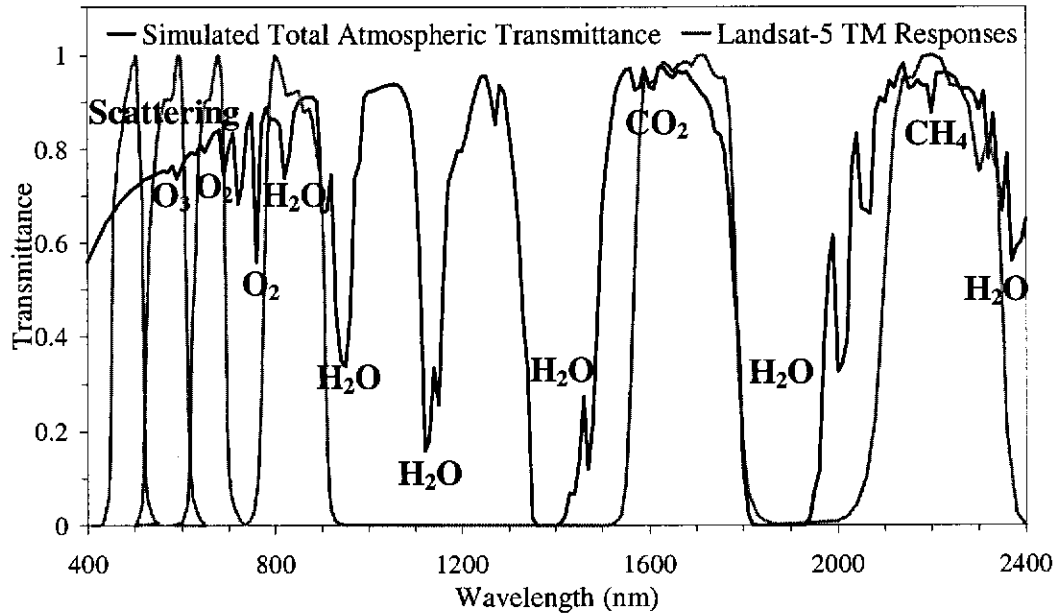


Figure 3.10: The simulated total atmospheric transmittance for a mid-latitude summer model (black line) and the Landsat-5 TM response curves (grey lines). Highlighted are some of the more prominent absorption features.

The direct (black lines) and diffuse (grey lines) transmittances in the figure correspond to a vertical path from sea level to TOA for different aerosol concentrations. The solid thick lines (black and grey) represent the transmittances for a scattering layer composed of molecules only (no aerosols). It is observed that increasing the aerosol optical thickness (while keeping molecular optical thickness constant) results in a decrease in direct transmittance but an increase in diffuse transmittance. This is because aerosols are predominately forward scatterers (Figure 2.9, p. 42); direct transmittance will decrease with an increase in AOT, since more photons are scattered away from a direct beam between the ground and the satellite sensor, and the diffuse transmittance increases as a result of more photons being scattered into the direct beam by the surrounding environment.

The decrease and increase in direct and diffuse transmittances is also observed when molecular and aerosol concentrations are kept constant, and only the view angle is increased (Figure 3.11(b)). For an $AOT(550\text{ nm}) = 0.05$ and view angles set at $\theta = 0^\circ$, 45° and 65° , it is clear that when the view angle increases, so too does the optical path length. Therefore, there is an increased likelihood for photons to be scattered away from

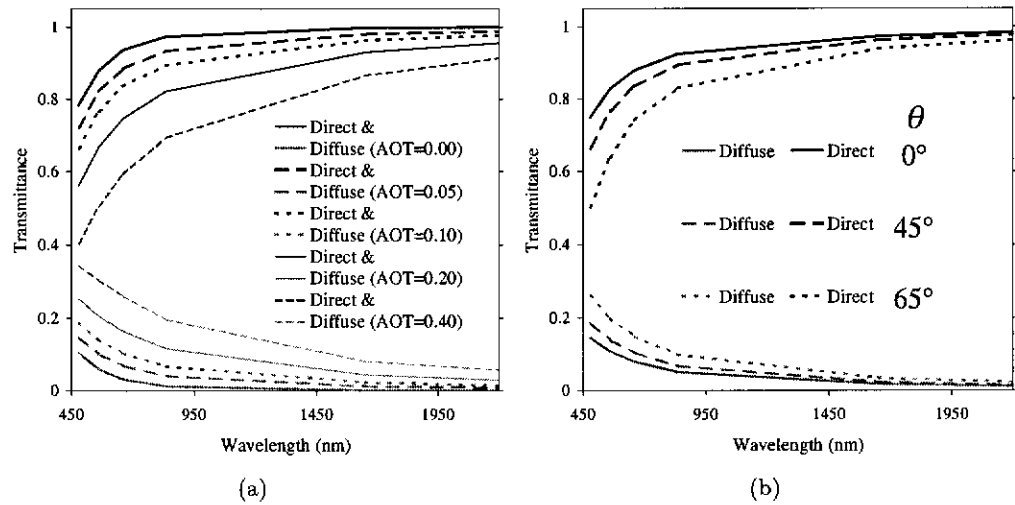


Figure 3.11: Direct (black lines) and diffuse (grey lines) transmittances due to molecular and aerosol scattering: subfigure (a) illustrating the spectral dependence for different aerosol optical thicknesses (AOT at 550 nm); subfigure (b) illustrating the direct and diffuse transmittance (AOT = 0.05) at different observation angles (θ).

and even into the direct beam.

The diffuse transmittance contribution to the total scattering transmittance is observed to be smaller than the direct transmittance. This is due to the relative contribution of the reflectance from a target's surrounding environment (pp. 62–64) being less than that of the target itself. As a result, the total scattering transmittance will always be closer to 1 than the direct transmittance alone. The combined effect of the direct and diffuse transmittances is a reduced intensity of the sensor-measured signal, illustrated for nadir view and $\theta_0 = 36.19^\circ$ $\phi_0 = 81.36^\circ$ in Figure 3.12(a) for three different aerosol optical thicknesses. It is clear from the figure that total scattering transmittance has most impact on the VIS bands. Figure 3.12(b) illustrates the effect of total scattering transmittance on Landsat-5 TM band 1 image data for two AOT values. Total scattering transmittance results in a reduced contrast in the image data, evident by the narrowing of the histogram. Furthermore, contrast appears to decrease when AOT increases, in direct correspondence with the observed behaviour of the total scattering transmittance. Note that the additive effect is not illustrated in Figure 3.12(b).

Of the atmospheric gases, water vapour plays an important role in the interaction with EM radiation (recall discussion, pp. 13–14). The large absorption features in

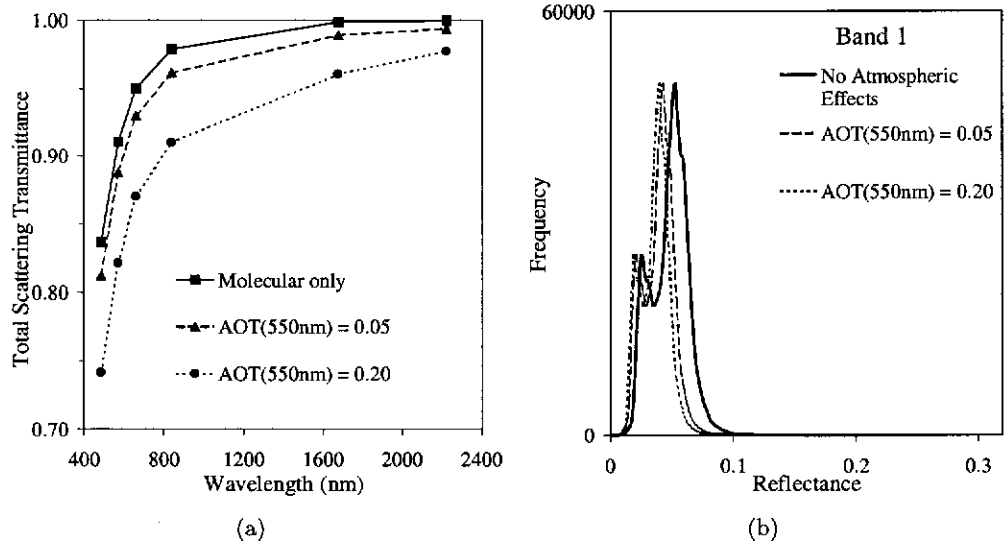


Figure 3.12: Total scattering transmittances simulated for Landsat-5 TM image data ($\theta_0 = 36.19^\circ$, $\theta_s = 81.36^\circ$): (a) the wavelength dependence for three different aerosol optical thicknesses (AOTs); (b) the reduced contrast in TM band 1 data due to scattering (no additive effects displayed here).

Figure 3.10 around 1400 and 1900 nm indicate that water vapour attenuates most (if not all) of the EM signal at, and around, those wavelengths. Although many satellite sensor spectral bands are designed to avoid, as much as possible, water vapour absorption features, most bands are nevertheless influenced by water vapour to some degree. For the TM and ETM+ sensors, water vapour absorption affects bands 2–5, and 7. It is expected from Figure 3.13(a), that water vapour absorption most significantly impacts TM band 5 (around 1650 nm), followed closely by band 4 and then band 7. The effect of this absorption on TM band 5 data is demonstrated in Figure 3.13(b) for two water vapour concentrations. Note that the effects of absorption by other gases is not presented in Figure 3.13(b).

Ozone absorption occurs for a range of wavelengths between 450–750 nm known as the *Chappuis band*. Ozone absorption, therefore, impacts TM and ETM+ bands 1–3. The maximum ozone absorption in the Chappuis band occurs around 600 nm, thus TM/ETM+ band 2 will be most significantly affected by ozone. This is observed in Figure 3.13(c) for a range of ozone concentrations (in Dobson units, DU). Figure 3.13(d) illustrates the effect of ozone absorption on Landsat-5 TM band 2 image data based on

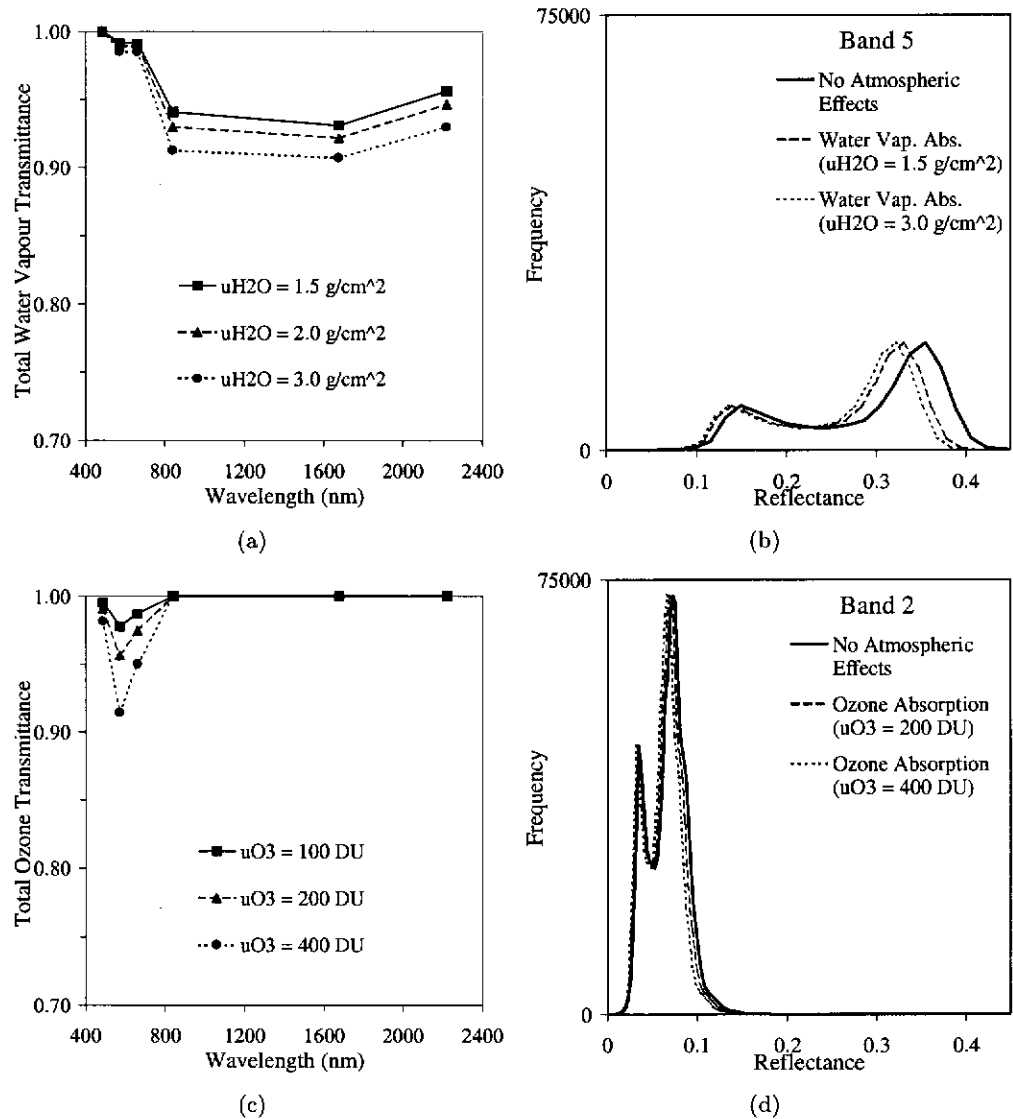


Figure 3.13: Water vapour and ozone transmittances simulated with 6S for Landsat-5 TM image data ($\theta_0 = 36.19^\circ$, $\theta_0 = 81.36^\circ$). Water vapour transmittance: (a) the wavelength dependence for three different water vapour concentrations; and (b) the reduced contrast in TM band 5 data due to water vapour absorption only. Ozone transmittance: (c) wavelength dependence for three different ozone concentrations; and (d) the reduced contrast in TM band 2 image data due to ozone absorption only (other gaseous absorption and additive effect not illustrated here).

two concentrations. Once again a reduction in contrast is observed. Note also that the path effect and absorption effects due to other gases are not illustrated.

The two ozone concentrations used in the simulations in Figure 3.13(d) represent the approximate minimum and maximum ozone concentrations typically observed in the mid-latitudes. The figure demonstrates that the change in the shape of the reduced-contrast histograms between $u_{O_3} = 200$ and 400 DU is relatively small. It may therefore be concluded that errors in ozone concentration estimates of the order of the absolute accuracy of some of the satellite observations (e.g. TOMS, p. 20) will have marginal impact on the modelling of ozone absorption for the TM/ETM+ VIS bands.

Apart from water vapour and ozone, the other atmospheric gases impacting the TM and ETM+ bands are: oxygen gas (O_2), carbon dioxide (CO_2), methane (CH_4), nitrogen dioxide (NO_2), and nitrous oxide (N_2O). The MODTRAN4 software, which uses the high-resolution transmission molecular absorption database (HITRAN), was used to simulate transmittance spectra for these gases, based on a vertical path from sea level to TOA, for 5 simulated atmospheres (i.e. mid-latitude summer and winter, sub-arctic summer and winter, and tropical atmospheres). The average transmittances (and corresponding standard deviations) of all simulated atmospheres are presented in Table 3.6.

Table 3.6: Average transmittance values due to oxygen (O_2), carbon dioxide (CO_2), methane (CH_4), nitrogen dioxide (NO_2) and nitrous oxide (N_2O) absorption for the Landsat-5 TM bands. The means and standard deviations (St. Dev) given are based on values from the 5 simulated atmospheres used in MODTRAN4. A blank cell means the corresponding band is unaffected by that particular gas.

		Landsat-5 TM Bands					
		1	2	3	4	5	7
O_2	Mean			0.989	0.997		
	St. Dev			8.5×10^{-5}	2.8×10^{-5}		
CO_2	Mean					0.993	0.992
	St. Dev					3.4×10^{-5}	2.6×10^{-4}
CH_4	Mean					0.995	0.969
	St. Dev					9.1×10^{-5}	5.1×10^{-4}
NO_2	Mean	0.998					
	St. Dev	9.5×10^{-5}					
N_2O	Mean						0.999
	St. Dev						5.7×10^{-5}

In Table 3.6, it can be seen that N_2O and NO_2 have the least impact on the TM bands, affecting bands 1 and 7 respectively, with transmittances around 0.999 and 0.998 respectively. Methane absorption in TM band 7 gives the lowest transmittance (0.97), while oxygen and carbon dioxide absorption resulted in transmittance values around 0.99. Other than water vapour and ozone, TM band 2 is unaffected by the presence of the “other” gases. Note that variations in the transmittance values are due to the differences in the atmospheric profiles used by MODTRAN4 to define the particular simulated atmospheres.

Finally, the total gaseous transmittance may be obtained using Eq. (2.13, p. 27) where the product of the individual transmittances for each gas in the absorption layer of the atmosphere is calculated.

Effects of Terrain Elevation

The additive and multiplicative effects described in the preceding examples have been computed for a fixed elevation and, therefore, atmospheric path length. There may be considerable variation in terrain elevation within a satellite scene, and one cannot expect that the path effect or the total transmittance will remain constant throughout the image. In fact, given stable atmospheric conditions, the physical properties of the atmosphere, such as the pressure and temperature profiles (Figures 2.4 and 2.5, pp. 11 and 13, respectively), and concentrations of various atmospheric constituents (e.g. Figure 2.7, p. 19) vary with altitude in the fashions described in Chapter 2. Simply stated, this is because there is less atmosphere above a target located on a mountain, for example, than there is at sea level.

To demonstrate the effect that variation in target elevation has on gaseous transmittance, 6S was used to compute the transmittances for Landsat-5 TM bands, for a mid-latitude summer atmosphere with $\theta_0 = 36.19^\circ$ and $\phi_0 = 81.36^\circ$, for a target located at a number of elevations. Transmittances were calculated for water vapour, ozone, methane, oxygen and carbon dioxide for elevations ranging from sea level to 32 km¹⁰ (where the target would be situated above 99% of the mass on the atmosphere). The results are displayed in Figure 3.14.

Generally, an increase in transmittance is observed for all gases in Figure 3.14 as the

¹⁰This is an unrealistic scenario since most terrestrial targets are located between 0–8 km.

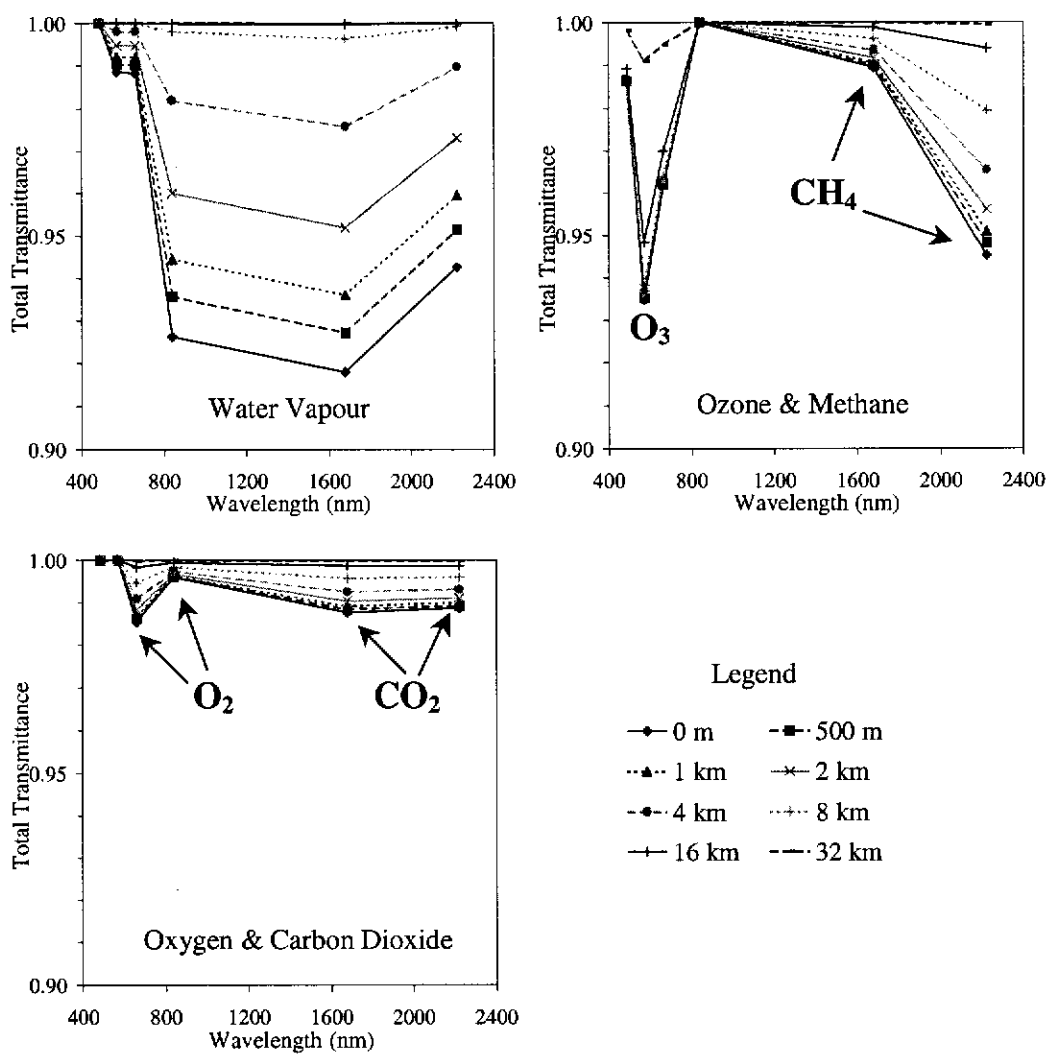


Figure 3.14: An illustration of the effect that changes in target elevation has on some gaseous transmittances for the Landsat-5 TM bands.

target elevation increases. For targets located within the first kilometre above sea level, transmittances for gases other than water vapour vary by $< 0.6\%$ (for water vapour, band 5 transmittances vary by $\sim 2\%$).

Clearly, water vapour transmittance is the most sensitive to changes in target elevation. This can be attributed to the rapid decrease in water vapour concentrations with increasing altitude (illustrated in Figure 2.6, p. 15). In fact, remotely-sensed estimates of precipitable water have been observed to be highly correlated with elevation (Roberts et al., 1997). The increase in transmittance between sea level and a 1-km elevation is equivalent to a decrease in column water vapour concentration of around 1.5 g/cm^2 . Generally, the higher the target elevation, the less precipitable water is present in the atmospheric column, and consequently the higher the transmittance.

In contrast, ozone transmittance appears to be the least sensitive to changes in elevation. In the figure, very little change in transmittance is observed for band 2 (i.e. the band most affected by ozone absorption) until the target elevation is 16 km. Recall from Chapter 2 (Figure 2.7, p. 19) that the peak in ozone concentration for a mid-latitude summer occurs around 22 km. Even at an elevation of 32 km, where most of the ozone concentration is below that altitude, the transmittance in TM band 2 is still 0.99. From this it can be concluded that, for most terrestrial targets, ozone transmittance is insensitive to target elevation.

3.3.4 Change Detection

Change detection studies often utilise multitemporal sequences of satellite imagery in an attempt to map and monitor physical modifications in land cover types, whether the cause be natural or anthropogenic. It is crucial that the topics discussed in the previous sections are taken into consideration prior to embarking on any change detection endeavour. Before describing methods for minimising the influence of those factors that may hamper change detection efforts (Section 3.4), this section describes some change detection techniques and the various shortcomings that may result if the issues raised in Sections 3.3.1, 3.3.2 and 3.3.3 are not addressed.

Change in surface features may be observed between any two (or more) multispectral images or processed higher-level image products, such as a classification or an image derived from spectral indices. Sing (1989) described two broad categories of change de-

tection techniques. The first category relates to those techniques based on the comparative analysis of independently produced images with simple image algebra. The second category are those techniques that simultaneously analyse multitemporal data with time series or multivariate statistical analyses. The following presents a review of some change detection techniques that fall into either one (or both) of these categories.

Image Arithmetic

Techniques that detect change by either differencing or ratioing two dates of satellite imagery (defined, for example, by Jensen (1996, pp. 266–269)) can be applied to each band in a multispectral image (pixel DN , X_λ , converted into at-sensor reflectances, $\rho_{\text{sat}\lambda}^*$, or retrieved surface reflectances $\rho_{s\lambda}$), a single band in a multispectral image, or the single image of a processed higher-level product (such as a vegetation index image). Change is observed for pixels in a difference image that have either a non-zero value (in the case of image differencing), or a value different to unity (in the case of image ratioing). Image differencing (or ratioing) is performed on a pixel-by-pixel basis, and whilst techniques incorporating such operations are sensitive to all those factors mentioned in the previous sections, the most significant errors arise because of mis-registration (see Figure 3.8, p. 74). Accurate co-registration of imagery is vital if the applied techniques are to yield any meaningful estimate of land cover change whatsoever. It is implied throughout the remainder of this chapter that the images described have been co-registered prior to any change detection technique being applied.

Upper and lower thresholds are applied to the difference (or ratio) image to compensate for possible uncertainty in atmospheric effects and/or sensor calibration. Change is attributed to pixels whose values fall outside the interval defined by the thresholds. Thresholds are often selected as integer multiples of the standard deviation about the mean difference value. The number of standard deviations can be determined interactively via visual inspection of the difference image. Sing (1989) stated that the threshold selection process is the most critical element of the image differencing and ratioing techniques. The subjective nature of the threshold selection, however, makes such techniques unattractive to many researchers, particularly since it requires some knowledge of the characteristics of the land cover which is often unknown.

Sing (1989) and Gong (1993) have both stated that change detected with single-band

differencing is dependent on the land cover type, and that different change information is contained in each spectral band. Furthermore, Gong (1993) pointed out that inappropriate placement of thresholds can fail to detect smaller, more subtle change between the two dates: too conservative (narrow interval) and an overestimate of potentially false change is detected; too liberal (wide interval) and the amount of change is underestimated. This has lead many researchers (examples are given in the following) to investigate alternative approaches to simple differencing (or ratioing) and to develop change detection techniques that in some way enhance the measure of change.

Multivariate Statistical Transformations

It is well known that there exists a certain degree of between-band interdependence in a multispectral image. Each pixel in a multispectral image may be thought of as a k -dimensional multivariate observation, where k is the number of spectral bands. A measure of this band interdependence is provided by the $k \times k$ *variance-covariance matrix*, denoted C .

Principal component analysis (PCA, see for example Richards and Jia (1999, pp. 133–148)) is a multivariate statistical technique that has been applied to multispectral imagery, to exploit the multivariate nature of the data. PCA produces uncorrelated (orthogonal) linearly-transformed components (i.e. the eigenvectors of C calculated from the original multispectral data) such that the first component accounts for the maximum portion of the total variance in a multivariate set of observations, with subsequent components accounting for decreasing amounts of variance. Gong (1993) applied PCA to the images resulting from a simple band-by-band difference of two images. The motivation for the approach was that the majority of the variance in a difference image is associated with change between the two dates, thus change information will be preserved in the first two or three principal components.

Fung and LeDrew (1987) used PCA to identify change between image pairs in a sequence of MSS images. Their approach was to concatenate the two images, forming a $2k \times n$ matrix (where n is the total number of pixels per band), and use PCA to provide the linear combination of the bands aligned in the direction of maximum data variance. Most of the variance in this framework is attributed to areas of no change, thus Fung and LeDrew (1987) observed that most of the change information was contained in the

minor components, since areas of land cover change occupy only minor portions of the entire image scene.

Once again, poor image registration, sensor calibration or atmospheric effects hamper the quality of the change highlighted with the above two approaches. Nielsen et al. (1998) have observed that errors in band-by-band differencing due to registration, atmospheric and sensor differences between image pairs are dramatically amplified when transformations, obtained via PCA, are applied to image data. Furthermore, they criticise the PCA approaches because images in the multitemporal sequence are required to have the same number of spectral bands if either the Fung and LeDrew (1987) and Gong (1993) approaches are employed.

Nielsen et al. (1998) proposed a scheme whereby change could be detected between two images with different numbers of spectral bands and even account for situations where the bands cover different regions of the EM spectrum. Their approach employed canonical variate analysis¹¹ (CVA, see for example Campbell and Atchley (1981)) to again obtain a linear transformation of the original data to maximise any deviation from no change between the two dates. The transformations were called multivariate alteration detection (MAD) transformation. Their investigations also focussed on the use of the minimum/maximum autocorrelation factor (MAF) transformation by Switzer and Green (1984) to smooth imagery prior to the application of the MAD transformation.

As with the PCA approaches, the MAD transformations are also affected by poor image co-registration as well as requiring that the images involved have the same number of pixels. Furthermore, the promise of the MAD approach of being applicable to images possessing different numbers of spectral bands, and spanning different wavelength regions, is unsubstantiated, but it is unlikely that the between-image correlation structure for given cover types is retained if different wavelength regions are considered.

Nielsen et al. (1998) applied their scheme to detect spatial patterns of change due to (i) urbanisation between two dates of Landsat MSS imagery for Queensland, Australia, and (ii) changes in sea surface temperature resulting from the El Niño-Southern Os-

¹¹The usual implementation of CVA in satellite studies is to maximise the spectral separation between two or more classes (defined in the following) in a satellite scene by computing linear combination of the original k bands in such a way that between-class differences are maximised relative to the within-class differences (Campbell and Atchley, 1981). These linear combinations are referred to as *spectral indices* (more in "Image Time Series" section below) and highlight features in an image corresponding to the particular class of interest.

cillation event between January 1982 and January 1983 with AVHRR image data over part of the California current system near Baja, California. They found that the MAD transformations produced more accurate results than the principal component analysis approach of Gong (1993). Furthermore, they claimed that the application of the combined MAF/MAD transformations removed any spatially incoherent noise and outliers in the imagery that may be attributed to poor image geometric registration. It was also noted that, since the linear gains and offsets that sensor calibration and atmospheric effects introduce in satellite imagery have an impact on the magnitude of the change measured, the image data should be properly intercalibrated.

Post-classification Analysis

This inter-band correlation may be observed for different land cover types, and is typically strongest within cover types than between them. Many researchers have utilised this fact to map different cover types with satellite imagery. The different land cover types are referred to as *classes*, or *themes* (e.g. vegetation, bare soil, water body), and a *classifier* allocates a particular *class label* to a pixel based on some prior information. When the classifier has processed every pixel in a multispectral image, the result is a map of the geographical distribution of a particular class (theme) referred to as a *classification* or *thematic map*.

Change detection via post-classification analysis is probably the easiest technique to describe. Change is detected in a multitemporal sequence of classifications if a pixel changes class between dates. Since each pixel in any given image is assigned one of discrete number of classes, it is a relatively simple and straightforward technique to automate. Furthermore, since the approach uses classifications, absolute accuracy of the multispectral image data is not essential. In fact, the only requirement is that the multispectral images in the sequence be normalised (more in Section 3.4). The main limitations to this method of change detection are the geometric co-registration of imagery and the accuracy of the classification.

The best known classifier is the *Maximum Likelihood* (ML, see for example Jensen (1996, pp. 229–231)) classifier. Since the ML classifier operates on a pixel-by-pixel basis, the resulting classification can sometimes appear quite ‘speckled’. One expects that neighbouring pixels most likely belong to the same class, and therefore a classi-

fication should preserve spatial continuity within classes. This is the basis for some proposed neighbourhood models (Besag, 1986; Kiiveri and Campbell, 1992; Campbell and Kiiveri, 1993, for example) that aid in maintaining the spatial cohesion expected in classifications. Kiiveri and Caccetta (1996) demonstrated that classifications resulting from procedures that incorporate spatial correlation in image data appear considerably smoother. Difficulty arises when there is a solitary pixel that actually corresponds to a certain class, yet because of its neighbours it is assigned to the class of its neighbours.

Kiiveri and Caccetta (1996, 1998) and Kiiveri et al. (2001) demonstrated how useful conditional (or causal) probability networks (CPNs) are at exploiting the temporal aspect to the change detection problem. The CPN classifier is applied to a sequence of classification, produced with the ML classifier for example, as input. The idea with the CPN approach is that if a pixel has a certain classification in one year, then if no change in land cover has occurred, the pixel will have the same classification the following year. Any uncertainty or error in pixel classification between image dates is compensated for via the temporal link in the CPN.

The result of the CPN classifier is the posterior probability for each pixel in an image belonging to a particular class; the resulting image is essentially a spatially-varying probability surface (Kiiveri et al., 2001). A threshold is applied to the probabilities (usually a value of 0.5): above the threshold, pixels are assigned to the particular class; below the threshold and the pixel is labelled as not belonging to that class. The CPN can also serve as a tool for integrating other data sources to aid in classification. The CPN approach has been utilised to map and monitor the spread of dry-land salinity and native vegetation in the southwest of Western Australia (Caccetta et al., 2000a,b).

Change detection by comparing classifications in a multitemporal sequence can only detect change in a discrete number of land cover types. The signal corresponding to these land cover types must be of sufficient strength and possess the appropriate spectral characteristics to be recognised by a classifier as belonging to a particular class. The *DN* for each band in multispectral images range from 0–255 (for TM/ETM+), and differences in these values between dates, due to vegetation stress for example, have the potential of confusing the classifier and subsequently lead to incorrect classification for a given pixel. For this reason, many researchers prefer to monitor the temporal behaviour of continuous variables, such as an image-derived vegetation index or surface reflectances.

The latter is only recommended if the image data are corrected for atmospheric effects and temporal change in sensor response; the topic of discussion in Section 3.4.

Image Time Series

Recall that spectral indices are linear combinations of the bands in a multispectral image that highlight the particular land cover feature of interest. Those spectral indices that highlight vegetated targets and are known as *vegetation indices*. These vegetation indices are attractive because they collapse the multivariate set of spectral observations into a single index that can be related to biophysical parameters of vegetation in the scene of interest (Roderick, 1994). As such, they can be used in investigations into vegetation cover and condition.

Roderick (1994) used satellite-derived vegetation indices to monitor the condition of vegetation from season to season, in various regions of Western Australia. The approach adopted was essentially to treat each pixel value in a normalised difference vegetation index (NDVI) image as a single observation in a time series, the length of which is dictated by the number of images in the sequence. Effectively there is a time series at each pixel location. He applied three standard time series techniques—Fourier transformations, autocorrelation, and classical decomposition¹²—to the NDVI time series and observed that, of the three methods investigated, the classical decomposition was the most effective at identifying inter-annual vegetation change.

Other vegetation indices, also derived from empirical observations of a variety of vegetation types, under a range of conditions, have been proposed that offer improved capabilities to the NDVI (discussed in Chapter 4, pp. 168–170). One such vegetation index is the soil-adjusted vegetation index (SAVI), proposed by Huete (1988), which enhances the vegetation signal and suppresses the soil component of the signal in satellite imagery over sparsely vegetated areas. Other authors have adopted a statistical approach based on CVA and image data from training sites to derive vegetation indices (Caccetta et al., 2000a; Behn et al., 2000; Furby, 2000).

In most cases an average value of the index, calculated for a neighbourhood of pixels,

¹²Classical decomposition is a term used here to describe the decomposition of a time series into its seasonal, trend and random parts. For example, the seasonal behaviour is removed from a time series by applying a 12-month, moving average filter. This leaves behind only the trend and random components of the time series.

is used to construct the time series rather than individual pixel values. This has the effect of minimising the impact of mis-registration. The other factors affecting change detection combine to introduce an offset and a gain that can affect the derived index. In the case of the indices derived using CVA, absolute accuracy of the image data is not important as long the images are normalised. As for the empirically-derived vegetation indices, sensor calibration, the atmospheric path effect and gaseous absorption, impact the spectral band and in turn modify the absolute accuracy of the vegetation indices calculated for different dates. If data are to be combined in a time series to monitor change, then they must be adjusted for these factors; methods that achieve this are discussed in the next section.

3.4 Radiometric Processing of Multitemporal Sequences of Imagery

Discussion in Section 3.3.2 focussed on sensor calibration and stressed the necessity of the routine monitoring of the radiometric performance of the satellite sensor (either via onboard systems, vicariously in field campaigns, via cross-calibration with other sensors, or in a combination of these approaches) to maintain a high level of consistency in image product throughout the sensor's lifetime. In Section 3.3.3 it was described how changes in atmospheric properties impact the satellite image data. Furthermore, Section 3.3.4 described how neglecting to address these two issues introduces errors that can hamper efforts in change detection. This section reviews some methods for minimising the impact of the factors that lead to observed change between images in a multitemporal sequence that are not due to modifications in land cover.

The radiometric processing of satellite image data to simultaneously compensate for changes in sensor calibration and atmospheric conditions through time, has been referred to as *image calibration* (Caccetta et al., 2000b; Wu et al., 2001; Furby and Campbell, 2001). This is not to be confused with sensor calibration, which converts the sensor-acquired signal (stored as a DN) into the physical units of radiance; or with atmospheric correction, which aims to remove the atmospheric effects from the radiances at the TOA (L_{λ}^*) and retrieve surface reflectances ($\rho_{s\lambda}$). In multitemporal analysis, the radiometric processing may be applied to an image in isolation of the other images in the sequence (*Unitemporal Methods*, Section 3.4.1), or in a relative, image-to-image fashion

where statistics derived for one image is used to transform the data in another image into similar units (*Multitemporal Methods*, Section 3.4.2). It is this author's belief that the latter approach to radiometric processing is more appropriately referred to as *image normalisation* and is the terminology adopted in this thesis.

3.4.1 Unitemporal Methods

The processing methods described in this section are applicable to single dates of satellite imagery. They can incorporate *in situ* measurements of surface reflectance and/or atmospheric parameters (e.g. optical thickness, pressure/temperature profiles, etc.), or they may derive the desired quantities from the image data itself. For multitemporal analysis, these methods may be applied to each image independently of the other images in the sequence.

Empirical Line Approaches

There are numerous processing procedures that aim to retrieve the surface reflected component from image DN for each pixel in a multispectral image. If a satellite overpass coincides with the acquisition of some ground-based surface reflectance measurements, $\rho_{s\lambda}$, for a number of targets within the scene, then these measurements along with the image data for the same targets, X_λ , can be used to obtain a transformation that, when applied to the whole satellite image, converts the image DN into a surface reflectance. Methods that transform satellite imagery in this fashion are known as *empirical line* (EL) procedures.

The traditional EL procedure can simultaneously correct for atmospheric effects and sensor calibration by mapping X_λ for a number (m say, where $m \geq 2$) of bright (high reflectance) and dark (low reflectance) pixels to the ground-based measurements of $\rho_{s\lambda}$ made for the same m targets. This mapping is achieved by fitting a straight line to data pairs formed from the image and ground data as illustrated in the scatter plot of Figure 3.15(a). Such a scatter plot is constructed for each spectral band and the estimates of intercept (a_λ) and slope (b_λ) of the line of best fit are rearranged to yield the *image correction coefficients*, $A_\lambda = -a_\lambda/b_\lambda$ and $B_\lambda = 1/b_\lambda$.

It is also desirable in the EL procedure that the surface target's area be greater than or equal to the spatial dimensions of an image pixel. A further requirement, often seen

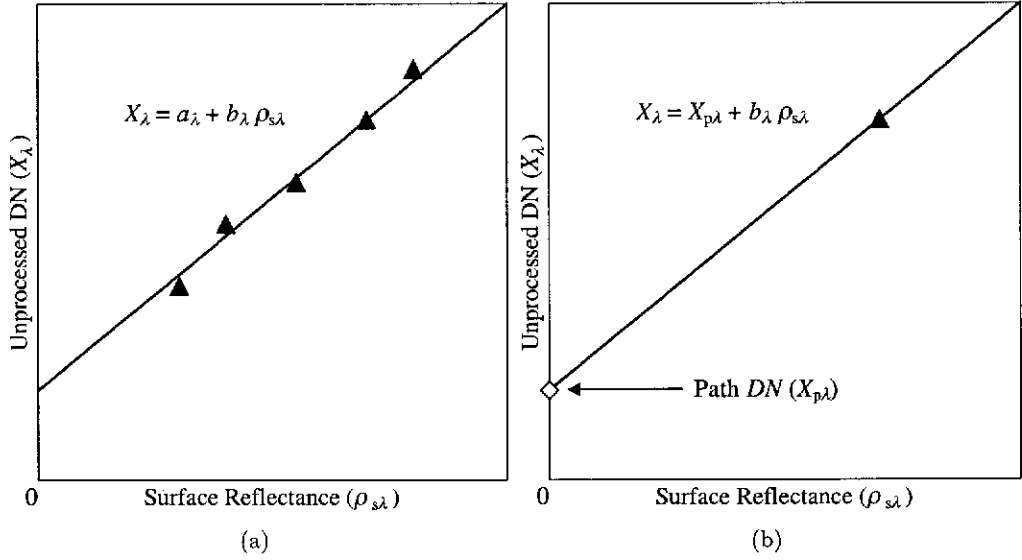


Figure 3.15: Scatter plots illustrating (a) the traditional empirical line (EL) procedure and (b) the refined empirical line (REL) procedure of Moran et al. (2001). Also displayed are the lines defined by either the slope, b_λ , and the intercept, that can either be statistically-derived, a_λ , or be the modelled path DN, $X_{p\lambda}$. Image correction coefficients are obtained from the estimated slope and intercept.

as a limitation of the EL approach, is that the selected target has spatially homogeneous surface reflectance properties. Most practical implementation of the EL procedure acquire a sufficient number of reflectance measurements over the extent of the target such that an average reflectance may be computed and used as a representative estimate of $\rho_{s\lambda}$ for that target.

Moran et al. (2001) proposed the refined empirical line (REL) procedure which differs from the EL approach described above firstly in regards to the surface target requirements, and secondly by incorporating the theoretically darkest pixel in an image into the straight line fitting. An example scatter plot used in the REL procedure is displayed in Figure 3.15(b). The REL procedure is a two-point regression between the surface-measured reflectance and image DN for one bright (high reflectance) target, and the modelled DN for a target with zero surface reflectance, denoted $X_{p\lambda}$, and referred to in this thesis as the *path DN*. The image correction coefficients in the REL procedure are given as $A_\lambda = -X_{p\lambda}/b_\lambda$ and $B_\lambda = 1/b_\lambda$.

In regards to the reflectance requirements for the bright target in the REL procedure, Moran et al. (2001) stated that:

1. the target should be bright;
2. the sensor resolution to target size ratio should be 1:8 (for the TM and ETM+ sensors this means that the target should have dimensions on the order of 240×240 m); and
3. the target's BRDF needs to be characterised. Moran et al. (2001) achieved this by adopting the empirical BRDF model of Walthall et al. (1985) which, for the TM and ETM+ sensors (p. 65), becomes a simple expression in terms of solar angle only.

Characterising the BRDF for a bright target in a scene of interest is suggested so that the REL approach can be applied to images where no coincident ground-based surface reflectance measurements have been acquired. The implication here is that the target's reflectance properties are temporally invariant and only change as a function of solar position and sensor viewing angles. Moran et al. (2001) emphasised the importance of the third requirement in the REL procedure by demonstrating that errors in surface reflectance estimation of around 10% may be incurred for changes in solar zenith angle up to 30° (i.e. $\Delta\theta_0 \sim 30^\circ$) if the target's BRDF is not well characterised.

Modelling the path DN requires knowledge of some atmospheric parameters for the date the imagery was acquired. Specifically, the parameters of particular importance in modelling $X_{p\lambda}$ are u_{O3} , u_{H2O} , $\tau_{R\lambda}$ and $\tau_{M\lambda}$, as well as (θ_0, ϕ_0) and (θ, ϕ) . From Figure 3.15(b) it can be seen that if $\rho_{s\lambda} = 0$ for a target and its surroundings, then

$$X_\lambda = X_{p\lambda},$$

and the sensor-measured signal is completely due to atmosphere effects. This is in fact the basis for many atmospheric correction procedures (see *Dark Target Approaches* section below).

The advantages of the REL method over the EL approach, Moran et al. (2001) claim, is that it is a relatively fast procedure to implement since the surface reflectance of only one bright target needs to be known. Most of the effort, they claim, is involved in characterising the target's BRDF. The task of atmospheric modelling (modelling the path DN) is comparatively easily if one is given measurements of optical thickness and employs atmospheric modelling software (e.g., 6S or MODTRAN). The image correction

coefficients determined via the EL or REL procedures define an equation that when applied to the DN s in an uncorrected satellite image converts the data into surface reflectances. The estimates of surface reflectance are given as,

$$\rho_{\text{corr}\lambda} = A_{\lambda} + B_{\lambda} X_{\lambda}, \quad (3.14)$$

where $\rho_{\text{corr}\lambda}$ are the *retrieved* (corrected) surface reflectances, and A_{λ} and B_{λ} have been defined previously. Using a comparison of the retrieved and measured (“true”) surface reflectances for a grassland site, Moran et al. (2001) showed that the REL procedure can estimate $\rho_{s\lambda}$ to within 0.01 reflectance units. Finally, Moran et al. (2001) showed that uncertainty in modelled path DN , due to limited knowledge in some of the atmospheric parameters, had little impact on retrieved reflectances for bright target (differences around 0.01 reflectance units for band 1 and less for other bands). It was noted, however, that the errors for dark targets should be higher since (as discussed in Section 3.3.3) additive effects due to atmospheric scattering are most noticeable for low reflectance targets.

Possible limiting factors for operational implementation of the REL procedure in multitemporal analysis are the required size of the bright target, the dependence on surface reflectance measurements, and the modelling of the path DN . There would be a handful of satellite image scenes that contained sufficiently bright targets with the desired 1:8 sensor-to-target area ratio, as well as the required ground-based reflectance and atmospheric measurements. Even fewer locations around the globe would exist where the required measurements were available for dates extending back through time (as required for retrospective studies of land cover change).

As a result, much research has focused on radiometric processing methodologies that are independent of ground-based measurements. The most popular techniques are those that derived estimates of the key atmospheric parameters from the imagery itself. Such methods are the topic of the next section.

Dark Target Approaches

A desirable feature of a radiometric processing procedure is if it allows the unknown atmospheric parameters to be inferred from the image data itself. These so called *image-based* procedures can be applied to any image in the multitemporal sequence, and for

any date, as they are not dependent on ground-based measurements of the desired atmospheric parameters. In the literature on these image-based procedures, attention focuses on their ability to correct for atmospheric effects; any changes in sensor calibration are assumed to be characterised and taken into account. To be consistent with the literature surveyed, the following discussion will also focus on image-based procedures for correcting atmospheric effects.

A common characteristic of many image-based procedures is that they exploit the darkest pixels in a scene because, as previously mentioned, the additive effects in imagery (i.e. the path effect, due solely to the atmosphere and having no surface contributions) are most obvious over low reflectance targets. Examples of the most often used dark targets are: water bodies, deep to minimise bottom reflectance and containing little, if any, suspended sediments; shadow areas resulting from terrain topography; and dense green vegetation. For these dark targets, the contribution to the sensor-measured signal is dominated by the path effect; the surface contribution is much smaller because of the lower surface reflectance. Thus, for a dark target,

$$X_\lambda \approx X_{p\lambda}, \quad L_\lambda^* \approx L_{p\lambda}, \quad \text{or} \quad \rho_{\text{sat}\lambda}^* \approx \rho_{\text{atm}\lambda}.$$

Surface reflectances for these targets belong to lower end of the image histogram (histogram minima), except in those image scenes that correspond to desert, arid or semiarid areas where few, if any, sufficiently dark targets can be found (Teillet and Fedosejevs, 1995).

The simplest image-based procedure for correcting the atmospheric path effect is the *dark-object subtraction* (DOS) procedure. The DOS procedure assumes that the at-sensor reflectance calculated for darkest pixels in a scene is a reasonable approximation for the atmospheric reflectance, that is $\rho_{\text{sat}\lambda}^* = \rho_{\text{atm}\lambda}$. By removing the estimate of $\rho_{\text{atm}\lambda}$ from the at-sensor reflectances calculated for the other pixels in an image, the DOS procedure effectively removes the path contribution to yield an estimate of surface reflectance. However, the path contribution is only one atmospheric effect observable in image data. The DOS procedure does not correct for the multiplicative effects of gaseous absorption, the direct and diffuse scattering transmittances (Section 3.3.3, p. 84), or the multiple surface-atmosphere interactions (Section 3.2, p. 61). In an evaluation of the retrievals from the DOS procedure and measured surface reflectances, Moran et al.

(1992) demonstrated unacceptably high errors were incurred as a result of neglecting the multiplicative effects; the DOS procedure gave results marginally different to no correction at all.

Chavez (1996) proposed an extension to the DOS procedure that incorporates a correction for the multiplicative atmospheric effects in imagery. The DOS procedure as described above was used to yield estimates of $L_{p\lambda}$. Furthermore, using gaseous transmittance values tabulated by Moran et al. (1992), Chavez (1996) derived empirically-based estimates of transmittance from the Sun to the target which, to first-order, were a reasonable approximation. Making the further assumptions that there was no diffuse contribution at the surface and that the total transmittance from target to sensor was unity, a simplified version of the RTE was inverted to yield estimates of surface reflectance. The procedure was evaluated against surface reflectance measurements, and it was observed that image-derived estimates were, on average, within 0.02 reflectance units of the *in situ* measurements. The numerous assumptions on which the procedure proposed by Chavez (1996) is based, however, suggest a limited range of applications and atmospheric conditions for which the procedure is suitable.

Other image-based procedures use estimates of path radiance (or atmospheric reflectance) from dark targets to infer estimates of specific atmospheric parameters. The parameter most often targeted is aerosol optical thickness, $\tau_{M\lambda}$, because, when compared to other atmospheric constituents, aerosols properties tend to be more elusive (Section 2.2.5, pp. 21–24). Recall (p. 40) that in the single-scattering approximation, the path radiance can be decomposed into molecular, $L_{p\lambda}^R$, and aerosol, $L_{p\lambda}^M$, components. That is,

$$L_{p\lambda} = L_{p\lambda}^R + L_{p\lambda}^M, \quad (3.15)$$

where

$$L_{p\lambda}^R = \frac{F_{d\lambda}}{4\pi\mu} P_R(\Theta) \tau_{R\lambda} \quad \text{and} \quad L_{p\lambda}^M = \frac{F_{d\lambda}}{4\pi\mu} \omega_{0\lambda} P_{M\lambda}(\Theta) \tau_{M\lambda}.$$

By subtracting the molecular component of path radiance (easily calculated using, for example, Eqs. (2.16) and (2.49), pp. 28 and 41, respectively) from the estimates of $L_{p\lambda}$ obtained from dark pixels, values of $\tau_{M\lambda}$ are obtained by rearranging the equation for $L_{p\lambda}^M$ given reasonable estimate of $P_{M\lambda}$ and $\omega_{0\lambda}$ based on the most suitable aerosol type. This is the adopted approach in the procedures proposed by Hill and Sturm (1988) and

Gilabert et al. (1994). In both procedures an estimate of $\tau_{M\lambda}$ (and the other atmospheric parameters which are estimated from model atmospheres) is assumed to be applicable over the entire image. The procedure described by Hill and Sturm (1988) obtains an estimate of $\tau_{M\lambda}$ for all bands in a multispectral image, whereas that of Gilabert et al. (1994) obtains an estimate for only two bands. The procedure of Gilabert et al. (1994) uses estimates of aerosol optical thickness obtained for TM (or ETM+) bands 1 and 3 to obtain the coefficient and exponent in the Ångström relationship (Eq. (2.24), p. 32) and the resulting formula provides estimates of aerosol optical thickness for the remaining bands.

Given an estimate of $\tau_{M\lambda}$ and model inputs for the other atmospheric parameters, the procedures above make use of some simplified RTE and models that approximate diffuse transmittance, spherical albedo, and environmental effects, such as those of Tanré et al. (1979, 1981, 1983), to retrieve estimates of surface reflectances from imagery. The retrieved reflectances were observed to be within 10–20% of ground-based measurements (Hill and Sturm, 1988; Gilabert et al., 1994).

Teillet and Fedosejevs (1995) used the 5S radiative transfer code to compute the modelled at-sensor reflectances for a given date of TM imagery based on typical values of some dark target surface reflectance and two or three different values of $\tau_{M\lambda}$. The idea here is that *true* values of $\tau_{M\lambda}$ can be estimated from the actual at-sensor reflectance (average value over all dark pixels) from the histogram minima and interpolation of the modelled at-sensor reflectances.

An Approach Based on Vegetated Targets

The previous section described how dark targets are utilised in many image-based atmospheric correction procedures to estimate aerosol optical thickness. The low surface reflectance of these targets means that the bulk of the contribution at the sensor is from the atmosphere, specifically the path radiance. For this reason, vegetated targets were sometimes not regarded as suitable dark targets because of the relatively high reflectance of vegetation in the NIR and green regions of the EM spectrum. In recent years, however, research has shown just how useful vegetated targets can be for estimating aerosol optical thickness. The success lies in the establishment of some *empirical vegetation reflectance relationships* which we shall briefly summarise here in the context of TM and

Table 3.7: Empirical vegetation reflectance relationships used to estimate aerosol optical thickness in Landsat TM and ETM+ bands 1–3.

Researchers	Relationship		
	Band 1	Band 2	Band 3
Kaufman et al. (1997c)	$\rho_{s1} = 0.25 \rho_{s7}$	—	$\rho_{s3} = 0.50 \rho_{s7}$
Ouaidrari and Vermote (1999)	$\rho_{s1} = 0.23 \rho_{s7}$	$\rho_{s2} = 0.67 \rho_{s7}$	$\rho_{s3} = 0.50 \rho_{s7}$
Karnieli et al. (2001)	$\rho_{s1} = 0.23 \rho_{s7}$	$\rho_{s2} = 0.31 \rho_{s7}$	$\rho_{s3} = 0.52 \rho_{s7}$

ETM+ sensors.

Many researchers (Kaufman et al., 1997c; Ouaidrari and Vermote, 1999; Karnieli et al., 2001) observed that for vegetated targets the surface reflectances in the TM/ETM+ VIS bands (bands 1–3) were highly correlated with surface reflectances in the SWIR band (band 7). One of the first demonstrations of this inter-band correlation was by Kaufman et al. (1997c) who used TM and Airborne Visible/Infrared Imaging Spectrometer (AVIRIS) measurements of selected targets. With data that had been corrected for atmospheric effects via *in situ* measurements of aerosol optical thickness and the 6S code, expressions relating surface reflectances in bands 1 and 3 to those in band 7 were established; these are given in Table 3.7. Ouaidrari and Vermote (1999) used atmospherically corrected TM data from three long-term ecological research (LTER) sites to establish the relationships for bands 1–3. Karnieli et al. (2001), on the other hand, used data from an ASD spectrometer mounted on a low-flying light aircraft to derive the relationships for bands 1–3 also given in Table 3.7.

Generally, agreement is observed across all three relationships for bands 1 and 3. Discrepancies, however, are observed in the relationships for band 2. The most likely reason why Kaufman et al. (1997c) did not establish a relationship for band 2 is because vegetation reflectance is higher in that band than in 1 or 3. In a communication with the author, Dr. Kaufman said that not only was high correlation needed to establish the relationships, but the reflectances have to be sufficiently low also. A high value of reflectance would increase the possibility of error in aerosol optical thickness estimation, particularly since retrievals are sensitive to uncertainty in single scattering albedo and phase function (e.g. Eq. (3.15)). With regards to the band 2 relationships by Ouaidrari and Vermote (1999) and Karnieli et al. (2001), no reason can be found in the literature surveyed that suggests why there is such a significant difference.

The empirical vegetation reflectance relationships of Kaufman et al. (1997c) have been used in operational procedures for estimating aerosol optical thickness with MODIS on the Terra satellite (Kaufman and Tanré, 1996b; Kaufman et al., 1997b). The fact that MODIS views the Earth at angles up to 55° off nadir, has lead researchers to assess the impact of angular variation on empirical vegetation reflectance relationships and the subsequent retrieval of aerosol optical thickness (Remer et al., 2001; Gatebe et al., 2001). For the TM and ETM+ sensors, which are essentially nadir-viewing instruments, the empirical vegetation reflectance relationships are unaffected by angular variation.

Liang et al. (1997) and Ouaidrari and Vermote (1999) employed the empirical vegetation reflectance relationships in procedures for correcting atmospheric effects in TM imagery. What these procedures offer that other dark-target methods do not is the opportunity to correct for spatially varying atmospheric optical thickness. The procedure described by Liang et al. (1997) operates on a user-defined *window* of dimensions $w \times w$ pixels (typical w values in the range 11–51); whereas that of Ouaidrari and Vermote (1999) partitions an image into a 4×4 array of *cells* in which the operations are performed. For each window, or cell, essentially the same algorithm is employed to estimate aerosol optical thickness (ignoring for the moment the band 2 processing of Ouaidrari and Vermote (1999)). The procedures may be summarised as follows:

1. Identify pixels corresponding to vegetated targets in a window/cell based on certain criteria (e.g. $\rho_{\text{sat}7}^* \leq 0.05$ and $\text{NDVI} > 0.01$). If vegetated target(s) found based on criteria, correct pixels for gaseous transmittance in band 7 and estimate ρ_{s7} ; go to [2]. If no vegetated target(s) satisfy the criteria, move to next window/cell and repeat [1].
2. Use the empirical vegetation reflectance relationships to obtain estimates for ρ_{s1} and ρ_{s3} for the vegetated target(s); go to [3].
3. Estimate aerosol optical thickness for band 1 and 3, i.e. τ_{M1} and τ_{M3} , from the at-sensor reflectances $\rho_{\text{sat}1}^*$ and $\rho_{\text{sat}3}^*$, the estimates ρ_{s1} and ρ_{s3} , and a simplified RTE using lookup tables for transmittances, solar irradiances, phase function etc.; go to [4].
4. Assuming aerosol optical thicknesses follow an Ångström relationship (Eq. (2.24),

p. 32), calculate the coefficient and exponent using τ_{M1} and τ_{M3} , and use the relationship to estimate τ_{M2} , τ_{M4} and τ_{M5} ; go to [5].

5. Input estimates of aerosol optical thicknesses and at-sensor reflectances into a simple RTE with lookup tables for transmittances, solar irradiances, phase function etc., and invert to retrieve surface reflectance $\rho_{s\lambda}$ for each pixel in a window/cell, and for band $\lambda = 1, \dots, 5$; move to next window/cell and go to [1].

The reader is directed to Liang et al. (1997) and Ouaidrari and Vermote (1999) for specific details of the algorithm, and to Kaufman et al. (1997b) for further comment on the appropriate vegetated target selection criteria. If a window or cell does not have any vegetated targets that satisfy the criteria, then the value of aerosol optical thickness from an adjacent window is used.

The limiting factor for the empirical vegetation reflectance relationship approach to aerosol optical thickness estimation or atmospheric correction is the need to have sufficiently dark vegetated targets. This is a problem for desert, arid, and even semiarid scenes where vegetation cover is sparse and soil/background dominates the reflectance signal.

3.4.2 Multitemporal Methods

The unitemporal radiometric processing methods of the previous section can be applied to each image in a multitemporal sequence in an attempt to obtain a consistent set of imagery through time. The methods requiring *in situ* measurements are limited to the scenes, and date, where the such data are available (a minority of locations around the globe). The Image-based procedures, whilst useful for correcting atmospheric effects, did not address the issue of uncertainty in sensor calibration through time.

In many change detection studies involving multitemporal sequences of satellite imagery (Section 3.3.4), the only requirement is that image data be normalised for the effects of atmosphere, solar position and sensor uncertainty. There are some methods that achieve this normalisation by selecting a common reference image against which all other images in the sequence are normalised. These relative, image-to-image *normalisation procedures* are a desirable alternative to the other methods when *in situ* data does not exist and when processing image data to an absolute scale is not essential (Hall et al.,

1991). A general description of the key aspects of some image normalisation procedures is given in the following.

Image Normalisation

In general, the process of image normalisation can be summarised as follows: Image *DN*s are extracted for a subset of pixels in both the reference image, $X_{\text{REF}\lambda}$, and the unprocessed image, X_λ ¹³. Based on this subset of pixels, a transformation is defined relating the *DN*s in the unprocessed image to values in the reference image. The transform is then applied to each pixel in the unprocessed image and the result is a processed, or normalised image ($X_{\text{corr}\lambda}$).

This procedure is applied to every image in the multitemporal sequence. If one can reasonably assume that any differences between images due to sensor calibration, solar position, and atmospheric effects introduce linear changes, the transformation takes the form of a straight line (Schott et al., 1988; Hall et al., 1991; Furby and Campbell, 2001). It is noted that the derived linear transformation is valid only if there is negligible within-image variability of atmospheric effects and there are no non-linear effects due to sensor calibration. The three key aspects of the image normalisation procedures that will be discussed in the following are: determining the subset of pixels; selecting an appropriate reference image; and finally the derivation of the linear transformation.

Pseudo-Invariant Target Selection

Common to all the image normalisation procedures in the following is the assumption that there are features common to all satellite image scenes that undergo negligible changes in reflectance over time. These features are known as *pseudo-invariant targets*¹⁴ (PITs) and correspond to objects on the Earth surface whose reflectance remains fairly constant through time. Typical PITs include: deep water bodies, such as ocean or lakes; urban features and asphalt surfaces, such as rooftops, large roads, or car parking lots;

¹³The procedure described by Caselles and López-García (1989) use the at-sensor reflectances, but since these values and *DN*s differ via a linear transformation, it is easy to show that the interpretation is not affected if X_λ is used instead of $\rho_{\text{sat}\lambda}$.

¹⁴The terminology *pseudo-invariant* features/targets was used by Schott et al. (1988) since very few targets on the Earth surface are truly invariant through time. Weathering, precipitation and seasonal changes in solar geometry, for example, change the reflectance characteristics of many surface features. In this thesis, the term pseudo-invariant target is used in reference to those features in a scene that are less likely to change through time than others.

other manmade features such as airport runways/tarmacs, quarries and gravel pits; and naturally occurring rocky outcrops, beach sand and soil (Schott et al., 1988; Caselles and López-García, 1989; Hall et al., 1991; Furby and Campbell, 2001).

Schott et al. (1988) described a procedure for PIT selection based on ratios of red and NIR bands (TM/ETM+ band 3 and 4, respectively) to identify water and urban features in imagery. The idea with the ratio approach is that vegetation tends to have a high ratio, whilst water and urban features ratios are somewhat lower. A threshold is applied to the ratio image such that only pixels with a ratio below the threshold are given a binary ON flag ($DN = 255$ say), and those pixels with ratios above the threshold are given a binary OFF flag ($DN = 0$). In a similar way, another ON/OFF image is created, this time identifying those pixels that correspond to vegetation and urban features. Vegetated and urban features have higher reflectance values in band 7 than water features and, therefore, an appropriately placed threshold can be used to create a binary ON/OFF image that highlights non-water targets. A combination of the two binary images via the logical AND operation finally results in a binary image that highlights only urban features; this, Schott et al. (1988), refer to as a *pseudo-invariant feature* (PIF) mask. For each band, image statistics (means and standard deviations) are calculated for pixels identified by the PIF mask, which are then to be used in the normalisation procedure they described (more later).

Hall et al. (1991) observed that in the non-vegetated extremes of the Kauth-Thomas (KT) tasselled cap transformation (Richards and Jia, 1999, pp. 148–152) greenness-brightness scattergram, there exist sets of pixels whose mean reflectance remains constant between dates. Two sets of invariant targets result from the procedure: a bright set and a dark set. The placement of the greenness and brightness thresholds determines the number of pixels contained in the dark and bright sets. Sampling errors may result if the thresholds are inappropriately placed: too generous and pixels may be included that are not invariant in reflectance through time (biasing the dark and bright target means); too narrow and there may be an insufficient number of pixels to accurately determine the transformation function. Hall et al. (1991) claim that if both dark and bright sets contain sufficient number of pixels, the procedure they describe is accurate to within ± 1 DN . The mean DN is calculated for pixels in the dark and bright sets, and these values are then used in the procedure they describe.

The procedures described by Caselles and López-García (1989) and Furby and Campbell (2001) adopt a manual approach for PIT selection. In the manual approach, targets are located from either ground knowledge, maps of the features in the area under investigation, or via visual inspection of the imagery. Caselles and López-García (1989) used 3 PITs in their investigations; one bright (sand) mid-range brightness (asphalt) and dark (clear water). If, however, for a particular date of imagery, one or more of these targets became unusable (e.g. obscured by cloud), then a new set of PITs needs to be chosen for that date. Furby and Campbell (2001) used robust regressions and argued that the resulting transformations were unaffected by change in up to half the PITs. Thus only one set of PITs was required for all images in the sequence, since outliers have negligible impact on the robust estimates of slope and intercept (i.e. the transformation function) alleviating the need for repeated visual inspection. The procedure described by Furby and Campbell (2001) recommend the use of 10-20 PITs.

Reference Image Selection

Reference images are often chosen on the basis that they, out of all the images in the sequence, have the largest dynamic range (Schott et al., 1988). The application of the multitemporal analysis also drives the choice of reference image: Mapping perennial vegetation in Western Australia, for example, required an expansion of the low range of *DN*s associated with native vegetation. Furby and Campbell (2001) found that images acquired in the Summer season (solar zenith at its minimum) served as the most suitable choice of reference image. Caselles and López-García (1989) also found that a Summer image was the best choice for the reference image because of the greater dynamic range of *DN*s.

Another reason to choose a particular date of imagery as a reference is because it may coincide with some *in situ* measurements of surface reflectance and/or atmospheric optical thickness. This point shall be referred to at the end of this section as it forms the basis for work presented in Chapter 4.

Normalisation Equations

Another fundamental assumption behind the normalisation procedures mentioned above is that an image *DN* is a linear function of surface reflectance. Mathematically, the *DN*s

in each band of a reference image, $X_{\text{REF}\lambda}$, and unprocessed image, X_λ , are related to the surface reflectance $\rho_{s\lambda}$ of a PIT as,

$$X_{\text{REF}\lambda} = a_\lambda^{\text{R}} + b_\lambda^{\text{R}} \rho_{s\lambda} \quad \text{and} \quad X_\lambda = a_\lambda^* + b_\lambda^* \rho_{s\lambda}, \quad (3.16)$$

where the a 's and b 's are the *unknown* offsets and gains containing information about the atmospheric effects, solar position, and sensor calibration for the given dates of imagery. After some rearrangement, it is straightforward to show that,

$$X_\lambda = a_\lambda + b_\lambda X_{\text{REF}\lambda}, \quad (3.17)$$

where $a_\lambda = (b_\lambda^{\text{R}} a_\lambda^* - b_\lambda^* a_\lambda^{\text{R}})/b_\lambda^{\text{R}}$ and $b_\lambda = b_\lambda^*/b_\lambda^{\text{R}}$.

Equation (3.17) provides a model by which the unprocessed DN s in a given image are related to the DN s in a reference image for each spectral band. Estimates of the intercept, a_λ , and slope, b_λ , in Eq. (3.17) are obtained by either using the statistics calculated for the PITs (Schott et al., 1988), or via linear regression of the mean DN from the dark and bright set of PITs (Hall et al., 1991), or the scatter plot of PIT DN s (Caselles and López-García, 1989; Furby and Campbell, 2001). To illustrate the latter, referred to here as the *like-value* approach, a typical scatter plot used in the procedure described by Furby and Campbell (2001) is given in Figure 3.16.

The number of points in the like-value scatter plot is typically higher than the number of PITs because targets are chosen whose dimensions extend beyond those of a single pixel to minimise the impact of mis-registration (Furby and Campbell, 2001). Consequently small neighbourhoods of pixels (around 2–4 pixels) are used to produce the scatter plots.

For each band, a normalisation plot is constructed from PIT data pairs with the reference DN s ($X_{\text{REF}\lambda}$) along the x -axis, and unprocessed DN s (X_λ) along the y -axis. The reason the axes are orientated as displayed in Figure 3.16 is to be consistent with Eq. (3.17) which treats $X_{\text{REF}\lambda}$ as the predictor variable and X_λ as the response variable.

Furby and Campbell (2001) recommend using a robust regression procedure since least-squares regression is sensitive to outliers in the scatter plot (Figure 3.16). The robust regression they used can treat up to half the total number of points in the scatter plots as outliers and discard them from the line fitting procedure. The scatter of points in like-value plots may be due to either the selected PITs not being as temporally invariant

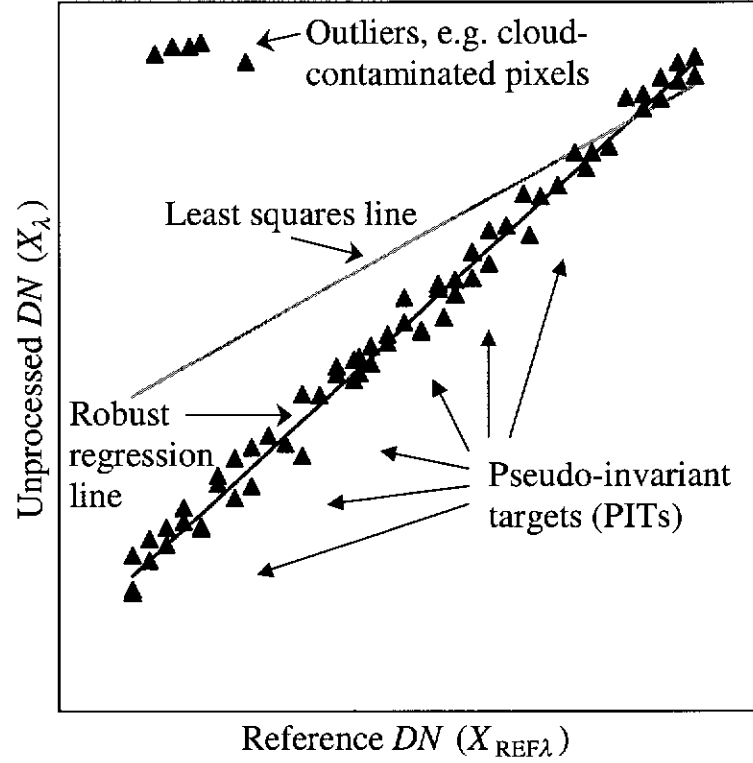


Figure 3.16: An illustration of ‘like-value’ scatter plot for the image normalisation procedure described by Furby and Campbell (2001).

as required, slight mis-registration between unprocessed and reference images, spatial heterogeneity of atmospheric properties, or cloud contaminated pixels.

Given regression estimates for a_λ and b_λ , the *image normalisation coefficients* are given as,

$$A_\lambda = -a_\lambda/b_\lambda \quad \text{and} \quad B_\lambda = 1/b_\lambda,$$

where A_λ and B_λ are referred to in this thesis as the image normalisation offset and gain respectively. Finally, these coefficients define the *image normalisation equation*, that is,

$$X_{\text{corr}\lambda} = A_\lambda + B_\lambda X_\lambda, \quad (3.18)$$

where $X_{\text{corr}\lambda}$ is the processed *DN* for the date of imagery under consideration. Equation (3.18) is ultimately applied to each pixel in an image to achieve the desired image normalisation.

Final Remarks on Image Normalisation

Furby and Campbell (2001) referred to their normalisation procedure as the *like-values* procedure, because after application of the procedure, the processed image will have *DN*s that are similar to those in the reference image. Similarly, Schott et al. (1988) referred to their procedure as *radiometric normalisation*. The fact that the reference image serves as a common normalisation source for the other images in the multitemporal sequence, led Hall et al. (1991) to call their procedure *radiometric rectification*, using the analogy of geometric rectification (p. 72). The images that result from the application of these normalisation procedures will appear as though they were acquired under the same atmospheric conditions, with the same solar position, and by same sensor (Schott et al., 1988).

Whilst the procedures above have been described in terms of image *DN*s, the units in which image data are expressed are immaterial to the processing. Therefore, if a reference image has been corrected for atmospheric effects, solar illumination, sensor view geometry, and sensor calibration, then image normalisation procedures can, in principle, be used to transform image data into surface reflectances or other units in the absolute scale (Hall et al., 1991; Furby and Campbell, 2001). A test for this would involve demonstrating that those factors mentioned above can be corrected for, and an estimate of surface reflectance can be retrieved, thus producing multitemporal sequences of imagery normalised to physical (reflectance) units that are consistent through time. This is the basis for the investigation presented in Chapter 4.

3.5 Chapter Summary

- Multispectral imagery acquired with thematic mapper (TM) and enhanced thematic mapper plus (ETM+) aboard the Landsat series of satellites have been used in many areas of multitemporal studies; the best known example is that of land cover change detection.
- The Landsat satellites carrying the TM and ETM+ sensors have a 16-day repeat coverage. Both sensors have a FOV = 15° (on-ground distance 185 km) and an IFOV of 30×30 m.

- The TM and ETM+ image data are composed of 6 spectral bands ($\lambda = 1-5$ and 7; 8-bit quantised grey-scale images) spanning the reflective region of the EM spectrum.
 - * For ‘raw’ TM and ETM+ images, the digital numbers, X_λ , are related to the at-sensor radiance, L_λ^* , via the detector responsivity, g_λ , and zero-radiance bias, $Q_{0\lambda}$.
 - * For radiometrically calibrated TM and ETM+ images X_λ is related to L_λ^* via radiometric scaling factors.
- Methods for detecting land cover change between dates of imagery in a multitemporal sequence are affected by the following factors:
 1. *Geometric co-registration* needs to be addressed otherwise mis-registration can cause pixel-by-pixel operations to detect false change.
 2. *Solar position*: may be corrected by scaling at-sensor radiance by TOA solar irradiance and the solar zenith angle to give the at-sensor reflectance, $\rho_{\text{sat}\lambda}^*$.
 3. *Sensor calibration*, e.g. changes in relative spectral response, between the various TM sensors and the ETM+ need to be taken into account. Also changes in detector responsivity for a given sensor that are not captured by the onboard calibration system need to be well-characterised.
 4. *Atmospheric effects*, in image data can be additive (due to scattering by molecules and aerosols; dominating the VIS bands and most noticeable over dark targets) and multiplicative (due to scattering and gaseous absorption; affecting all bands to certain degrees; reducing contrast in affected bands) in nature.
- Vicarious calibration campaigns aimed at addressing satellite sensor calibration are an accurate means of monitoring changes in sensor systems that are not detected by the onboard calibrators. They have the limitation, however, of being too infrequent for routine or operational use.
- Radiometric processing procedures for change detection studies involving satellite imagery aim at obtaining data that are consistent and comparable through time. Procedures can be categorised as unitemporal or multitemporal.

- * Unitemporal processing methods are often applied to images independently of the others in the sequence and may be dependent on ground-based measurements of surface or atmospheric properties. The required *in situ* measurements have limitations particularly in retrospective land cover change studies. Some, however, derive the desired quantities from the imagery itself. Those specifically referred to as atmospheric correction procedures do not address possible changes in sensor calibration through time.
- * Multitemporal processing methods are often based on image normalisation to a common reference image. These procedures simultaneously correct for differences in atmospheric condition, solar position, and sensor calibration between the unprocessed and reference images. Processed images will have the appearance that they were acquired under the same atmospheric conditions, with the same solar position, and by same sensor as the reference image.
- It has been noted that if the reference image has been corrected for the factors that can hamper change detection efforts, then in principle image normalisation procedures can transform image data into surface reflectances for each date in a multitemporal sequence.

CHAPTER 4

A Synthesis of Methods

This chapter focuses on the application of an image normalisation procedure to multi-temporal sequences of satellite imagery. Image normalisation has been described as a useful method (Hall et al., 1991) for standardising digital data in sets of imagery when inputs (such as sensor calibration coefficients and atmospheric parameters) required for other radiometric processing procedures are unavailable. The specific motivation for the work presented here stems from the following quote by Furby and Campbell (2001):

If we have a reference image that we can calibrate to reflectances (sic)¹, for example, by coincident ground reflectance measurements, the robust [like-value] procedure allows calibration of a sequence of images to that reference image and hence, to reflectance values.

Thus, it is the aim of this chapter to investigate an image-to-image normalisation procedure, to be described in Section 4.1, to permit comparisons of surface reflectances in multitemporal sequences of satellite imagery. Furthermore, by drawing on some of the theory and methods of Chapters 2 and 3, the results presented in Sections 4.2–4.3 address the notion that the normalised images produced have been corrected for sensor and atmospheric differences between image acquisition dates. Section 4.4 presents an application of the proposed procedure to a multitemporal sequence of images for the purposes of monitoring vegetation change through time; specifically investigating the impact of radiometric processing via the image normalisation procedure on time series of the derived vegetation index. The preliminary findings of a possible modification to the procedure, based on empirical reflectance relationships for vegetated targets, are given in Section 4.5. The chapter ends with Section 4.6 summarising the findings of this investigation.

¹Strictly speaking, one does not *calibrate* to reflectance units. In the context of this thesis, more appropriate terminology would be to normalise or standardise.

4.1 A Like-value Method

The image normalisation procedure to be described in this section differs from the relative, like-value “calibration” procedure described of Furby and Campbell (2001) in two respects: firstly, by incorporating the theoretically determined darkest pixel in an image, modelled with radiative transfer code and the radiometric scaling factors; and secondly, by using a calibrated, atmospherically-corrected reference image. The modelling component is proposed as means of applying the normalisation procedure to scenes where dark targets may be difficult to find. The resulting procedure has the potential to simultaneously correct for those factors that lead to a change in pixel DN that are not due to modifications in surface reflectance properties.

Applying the described procedure to two sequences of TM and ETM+ imagery, the following sections demonstrate that an image normalisation procedure may be used to correct for changes in sensor response, solar position and atmospheric effects over time, and result in a processed multitemporal sequence of satellite image data expressed as surface reflectances.

4.1.1 A Simplified Radiative Transfer Equation

Recall that the RTE (Eq. (3.4), p. 58) provides a model for the radiance emerging from the top of a plane-parallel atmosphere bounded at the bottom by a Lambertian surface. In the single scattering approximation, the radiance in each spectral band in the solar reflective region of the EM spectrum, λ , is modelled as,

$$L_{\lambda}^* = L_{p\lambda} + \frac{\rho_{s\lambda} F_{d\lambda} \mu_0 T_{\lambda}^{\downarrow\uparrow}}{\pi(1 - s_{\lambda} \rho_{s\lambda})}, \quad (4.1)$$

where L_{λ}^* is termed the at-sensor radiance; $L_{p\lambda}$ denotes the path radiance, that is, the contribution to the satellite signal from the atmosphere which is independent of surface reflectance $\rho_{s\lambda}$; $F_{d\lambda}$ is the exo-atmospheric solar irradiance adjusted for Earth-Sun distance; μ_0 is the cosine of the solar zenith angle θ_0 ; $T_{\lambda}^{\downarrow\uparrow}$ is the transmittance downwards and upwards through the atmosphere, combining extinction due to absorption by gases and scattering by molecules and aerosols along the direct Sun-target-sensor path, and diffuse scattering into the direct path; and s_{λ} is the spherical albedo, a function of molecular and aerosol optical thicknesses, representing the probability that a photon reflected by the target will be scattered back towards the target by the atmosphere above it.

The quantity in Eq. (4.1) of key importance in the assessment of land cover change is surface reflectance $\rho_{s\lambda}$. If a target's surface reflectance properties are temporally stable, then it is reasonable to attribute any observed change in at-sensor radiance (and thus, image data) through time for that same target to the other quantities in the equation. Radiometric processing procedures, therefore, aim to determine $\rho_{s\lambda}$ from Eq. (4.1) by taking into account sensor characteristics, atmospheric condition, solar illumination and viewing geometries.

Recall (Eq. 3.2, p. 55) that for each TM or ETM+ spectral band there exist radiometric scaling factors to convert the DN for any given pixel, X_λ , into an at-sensor radiance,

$$L_\lambda^* = O_\lambda + G_\lambda X_\lambda, \quad (4.2)$$

where, in the case of radiometrically-calibrated products (p. 55),

$$O_\lambda = L_{\min\lambda} \quad \text{and} \quad G_\lambda = \frac{L_{\max\lambda} - L_{\min\lambda}}{255}.$$

Note that the radiometric scaling factors differ between TM and ETM+ images and the level of image product acquired. They are designed to be temporally invariant (Teillet and Fedosejevs, 1995; Teillet, 2002), unlike the sensor calibration coefficients (related to sensor responsivity, g_λ , and zero radiance bias, $Q_{0\lambda}$) which can change over time. The internal calibrator (IC) systems onboard Landsat satellites monitor sensor responsivity through time and any changes are accounted for by the on-ground processing system in the production of radiometrically-calibrated image products. It has been noted (Thome et al., 1997; Teillet et al., 2001), however, that there have been changes to Landsat-5 TM responsivity through time that the ICs did not detect; potentially rendering the TM radiometric scaling factors obsolete. Changes in sensor responsivity, radiometric scaling factors, or on-ground processing are referred to collectively as *changes in sensor systems*.

A relationship between DN and surface reflectance is obtained by combining Eqs. (4.1) and (4.2) and expanding the term $\rho_{s\lambda}/(1 - s_\lambda\rho_{s\lambda})$ in a geometric series to give

$$X_\lambda = X_{p\lambda} + b_\lambda\rho_{s\lambda} + c_\lambda\rho_{s\lambda}^2 + d_\lambda\rho_{s\lambda}^3 + \dots \quad (4.3)$$

where $X_{p\lambda} = (L_{p\lambda} - O_\lambda)/G_\lambda$ is termed the *path DN* and corresponds to the digital number for a target with zero surface reflectance, $b_\lambda = F_{d\lambda}\mu_0 T_\lambda^{\uparrow}/G_\lambda\pi$, $c_\lambda = b_\lambda s_\lambda$ and

$d_\lambda = c_\lambda s_\lambda$. The relationship above clearly illustrates the additive and multiplicative components of the sensor output.

Many processing procedures that seek to determine surface reflectance from image data assume that a first-order approximation in $\rho_{s\lambda}$ is sufficient (Caselles and López-García, 1989; Moran et al., 2001). Using the fact that s_λ and $\rho_{s\lambda}$ are quantities less than one, it can be shown that for clear-sky conditions and typical solar-sensor geometries the quadratic and higher-order terms of Eq. (4.3) contribute at most $0.5DN$. The dependence of the spherical albedo on molecular and aerosol optical thicknesses, however, suggests that with increasing opacity, there is an associated increase in the contributions from a target's surroundings (due to the trapping mechanism) to the sensor-measured signal, in which case the higher-order terms in Eq. (4.3) become increasingly significant (Tanré et al., 1979).

Radiometric processing procedures that assume X_λ is a linear function of $\rho_{s\lambda}$ seek estimates of $X_{p\lambda}$ and b_λ for each band in a multispectral image. These coefficients are then rearranged to yield the coefficients A_λ and B_λ which in turn define the line,

$$\rho_{\text{corr}\lambda} = A_\lambda + B_\lambda X_\lambda, \quad (4.4)$$

where $A_\lambda = -X_{p\lambda}/b_\lambda$, $B_\lambda = 1/b_\lambda$ and $\rho_{\text{corr}\lambda}$ is an estimate of the surface reflectance for a pixel with DN X_λ . When the estimates of A_λ and B_λ are derived from image data and ground-based measurements of surface reflectance (e.g. p. 100) these coefficients are termed *image correction coefficients*. When the estimates of surface reflectance are obtained from a reference image and a processing procedure based on image normalisation is employed to derive A_λ and B_λ , the coefficients are termed *image normalisation coefficients*, and the line defines the *image normalisation line* (e.g., p. 114). The radiometric processing procedure described in the following section seeks to estimate these image normalisation coefficients for multitemporal sequences of TM and ETM+ imagery.

4.1.2 An Extension of the Like-value Procedure

The underlying basis for the image normalisation procedure described in the following, is that, in any image, there exists a subset of pixels corresponding to targets whose surface reflectance remains fairly constant over time (i.e. relative to other targets). If these so called pseudo-invariant targets (PITs) (Schott et al., 1988; Hall et al., 1991;

Furby and Campbell, 2001) are common to all images in a multitemporal sequence, then it is assumed that any change in pixel DN for these targets is due to differences in sensor systems and sensor view angle, solar position or atmospheric effects between image dates. Therefore after normalisation, the same target in every image is described as having *like-value* reflectances.

The *like-value image normalisation* (LVIN) procedure described here is so called because it involves normalising $N-1$ *overpass* (or unprocessed) images to a single *reference* (calibrated and atmospherically corrected) image in an N -date sequence. The LVIN procedure may be summarized as follows:

1. Co-register images, e.g. rectify to a common map base.
2. Select an appropriate reference image from the sequence.
3. Select a set of PITs common to all images.
4. For all overpass images, model the path DN ($X_{p\lambda}$) for each band.²
5. For each image, obtain image normalisation coefficients via regression of reference image reflectances against overpass image DN s for PIT data pairs.

For each band in a multispectral image, a *normalisation plot* in the fashion presented in Figure 4.1 is constructed. The items summarized above and their relationships to Figure 4.1 are discussed in further detail in the following.

Co-register Images

Accurate co-registration of the image sequence is of pivotal importance, since misregistration may lead to the detection of false change; compromising the whole premise of change detection studies. Registration of each image to a rectification base (an image with known map projection) is recommended. A cross-correlation feature matching procedure, for example, with a number (around 80) of good quality ground control points uniformly located throughout an image, may be used to register imagery with sub-pixel (< 30 m for TM and ETM+ images) accuracy (Furby, 2000).

²This step is optional and useful when too few or no dark PITs can be found in a satellite scene.

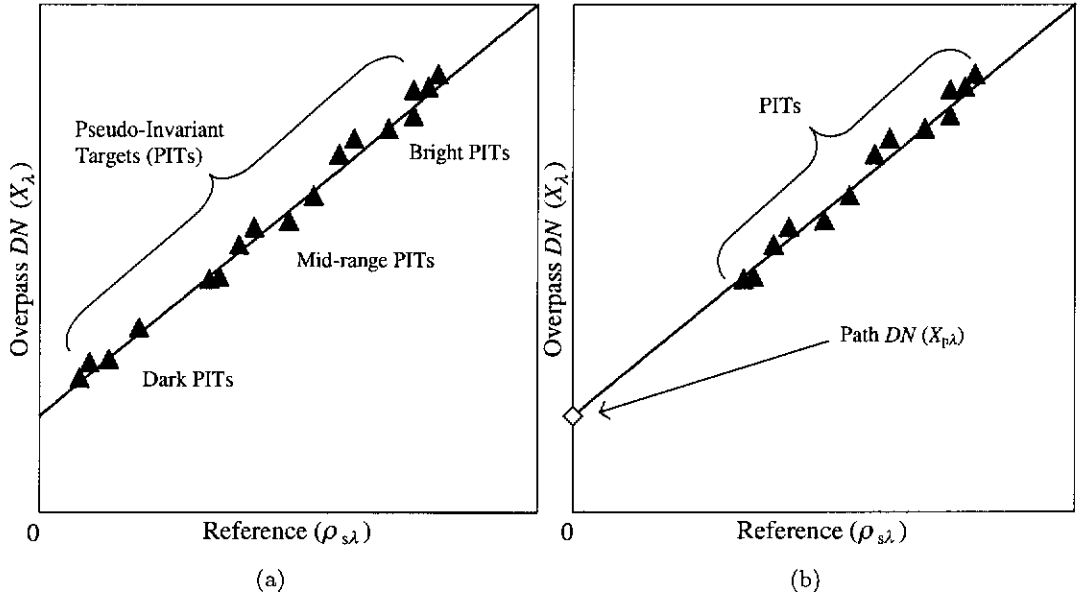


Figure 4.1: Image normalisation plots for the LVIN procedure (a.k.a. LVIN plots) described in Section 4.2.2 without (a) and with (b) modelled path DN .

Create Reference Image

One of the images in the sequence is chosen as the reference image against which all other images in the sequence will be normalised. Ideally, there would be at least one image acquired on a date with coincident ground-based measurements of $\rho_{s\lambda}$. Such an image would be the obvious choice of reference, and the image DN s can be converted to surface reflectances using the ground-based measurements in an empirical line or the refined empirical line procedure described by Moran et al. (2001).

It is more likely, however, that no coincident ground data exists for any date in the sequence. In this situation it has been suggested (Schott et al., 1988; Furby and Campbell, 2001) that the image with the greatest dynamic range of DN (typically a summer images because of the high solar elevation) be chosen as the reference. Converting the DN s in this image to at-satellite reflectances (which adjusts the data for solar elevation and Earth-Sun distance, but not atmospheric effects) is an effective way of making the image data dynamic ranges comparable (Wu et al., 2001). These data can be corrected for atmospheric effects to retrieve estimates of surface reflectance to within 6% of ground-based observations (Zhao et al., 2001) using standard model inputs

to atmospheric correction packages (e.g. 6S (Vermote et al., 1997b)), or to within 0.01–0.02 reflectance units using image-based techniques (Moran et al., 1992; Ouaidrari and Vermote, 1999).

Select a Set of PITs

Recall that PITs are those features in an image whose reflectance properties remain fairly constant over time compared to other features in an image. Examples of such features include deep water bodies, large areas of road or car park asphalt, rocky outcrops, bare ground and beach sand. Furby and Campbell (2001) suggest selecting a large number of PITs to cover the range of brightness values from dark (low reflectance), mid-range and bright (high reflectance) targets (Figure 4.1(a)). Potential PITs can be selected by visually inspecting the image data and/or using local knowledge of an area. This is generally the most time consuming aspect of the LVIN procedure. However, experience shows that a small number of PITs (typically around 10-20), spread uniformly over an image will, usually suffice. Furby and Campbell (2001) describe in greater detail the process of PIT selection.

Model Path DN

A knowledge of the path DN , $X_{p\lambda}$, is important in the LVIN procedure because, according to Eq. (4.3), it corresponds to a target where $\rho_{s\lambda} = 0$. The image normalisation procedure, therefore, will map digital numbers in an image equal to the path DN to a zero value of surface reflectance (Figure 4.1(b)). Image-derived estimates of path DN may be obtained from the imagery itself provided sufficiently dark targets can be found in the satellite scene, or there exists areas where terrain elevation casts shadows (refer to Section 3.4.1, p. 103).

If, on the other hand, a scene contains insufficiently dark targets or shadowed areas (i.e. where the assumption that target's reflectance is close to zero is invalid), one may resort to modelling the path DN . Modelled $X_{p\lambda}$ can be calculated from path radiance, $L_{p\lambda}$, modelled using radiative transfer (RT) code such as 6S, and the radiometric scaling factors (see Eq (4.3)). For accurate modelling of the path radiance, atmospheric data measured *in situ* is the preferred input to the RT code. If *in situ* data are not available, estimates of the required parameters (based on a simulated atmosphere or the regional

climatology for the time of year and the geographic location that the image was acquired) may be used.

Calculate Image Normalisation Coefficients

The final task in the LVIN procedure is to estimate the image normalisation offsets, A_λ , and gains, B_λ , and define the image normalisation equation (i.e. Eq. (4.4)),

$$\rho_{\text{corr}\lambda} = A_\lambda + B_\lambda X_\lambda,$$

where $\rho_{\text{corr}\lambda}$ is the estimate of surface reflectance for a target with an image DN value equal to X_λ . Two possible scenarios for obtaining estimates of A_λ and B_λ are given below.

For each of the M PITs, extract the set of X_λ from the overpass image and corresponding $\rho_{s\lambda}$ from the reference image and form the data pairs $\{(X_\lambda, \rho_{s\lambda})_i\}_{i=1}^M$ in Figure 4.1(a). A straight line fit to the data yields an intercept and slope that may be interpreted as estimates $\hat{X}_{p\lambda}$ and \hat{b}_λ of their respective counterparts in Eq. (4.3). It follows then that estimates of image normalisation coefficients are given for each band λ in an overpass image as $A_\lambda = -\hat{X}_{p\lambda}/\hat{b}_\lambda$ and $B_\lambda = 1/\hat{b}_\lambda$.

If, as a result of a lack of dark PITs, a modelled estimate of path DN is computed, the straight line fit may be constrained to pass through the point $(X_{p\lambda}, 0)$ and the slope of the line, \hat{b}_λ , determined by the mid-range and bright PIT data pairs as illustrated in Figure 4.1(b). The normalisation coefficients in this instance are given as $A_\lambda = -X_{p\lambda}/\hat{b}_\lambda$ and $B_\lambda = 1/\hat{b}_\lambda$.

The scatter of points in the LVIN plots is related to the PITs' temporal variability and departures from the assumed invariance. This may be due to the target not being as invariant in reflectance over time as desirable, changes in the spatial extents of the target and possible pixel mis-registration, or heterogeneous atmospheric properties over the extents of the scene (e.g. cloud contaminated pixels). Furby and Campbell (2001), therefore, recommend the use of a robust regression procedure to obtain the straight line fit to the data (see p. 113). A number of examples of robust regression procedures are given in Rousseeuw and Leroy (1987). Most robust regression procedures have a *breakdown point* of around 50%, which means that up to half the total number of data points may be spurious observations before the regression estimates are significantly

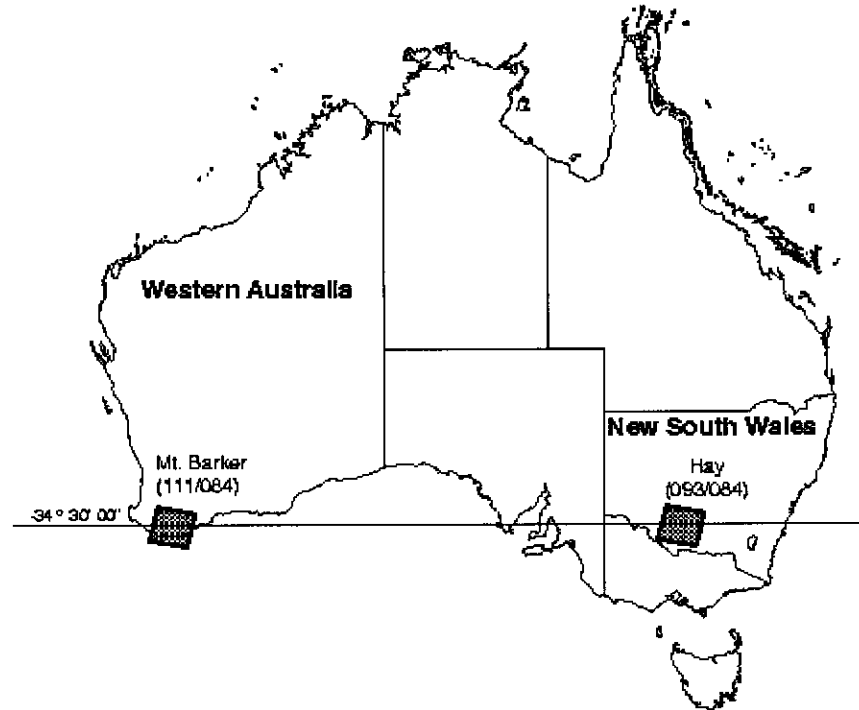


Figure 4.2: Geographic location of the two sequences of Landsat-5 TM and Landsat-7 ETM+ imagery used in the analysis presented in this chapter.

affected (In contrast, the least squares estimator has a breakdown point of 0%). In the context of the LVIN procedure, up to half of the PITs can have variable reflectance over time and still have negligible influence on the fitted line.

4.2 Preliminary Data and Image Processing

Two multitemporal sequences of Landsat-5 TM and Landsat-7 ETM+ images were used in the analysis presented here. The scene locations of both sequences on the Australian continent are highlighted in Figure 4.2. The first, known as the *Hay sequence*, corresponds to a relatively flat area of rural New South Wales, Australia (WRS Path 93 Row 84; scene centre \sim E 145°11', S 34°37'). The second, known as the *Mt. Barker sequence*, to the southwest coast of Western Australia (WRS Path 111 Row 84; scene centre \sim E 117°23', S 34°36') has significant variations in elevation throughout the scene. This section describes the image data and associated processing in preparation for the application of the like-value procedure.

4.2.1 Image Data

The acquisition dates for the TM and ETM+ images for both the Hay and Mt. Barker sequences are presented in Table 4.1. Most of the image data were acquired during the southern-hemisphere summer months, with the exception of Hay TM images for July 22 and October 26, 1999 which are winter and spring images respectively. Note that the Hay TM image for July 22, 1999 was acquired approximately 3 weeks after aphelion (Earth-Sun distance at its maximum) and has a very low sun elevation; consequently the image appears relatively dark.

Most of the TM data are level 4 bulk-corrected products with standard Canadian Centre for Remote Sensing (CCRS) formats. The author, however, acknowledges that there is no information or documentation that indicates the level of image product for the Mt. Barker image acquired on February 24, 1992. For the purposes of this thesis, it was assumed that it too was a level 4 bulk-corrected image. If this assumption is incorrect, then it is of interest to observe the impact that this uncertainty in radiometric scaling factors has on the LVIN procedure.

The ETM+ data have EOSAT Fast-L7 formatting and all bands were acquired with high gain settings, except band 4 for the Hay (January) and Mt. Barker (February) images which had low gain settings.

Table 4.1: The Hay and Mt. Barker sequences image dates and sensor information.

Date of Acquisition	Landsat Sensor	Earth-Sun Dist (AU)	Solar Zenith (θ_0)
Hay (93/84)			
July 22, 1999	TM	1.016	66.12
October 26, 1999	TM	0.994	37.75
January 7, 2000	ETM+	0.983	32.62
March 27, 2000	ETM+	0.997	49.24
Mt. Barker (111/84)			
January 20, 1991	TM	0.984	41.21
February 24, 1992	TM	0.989	46.86
January 28, 1994	TM	0.985	42.34
March 20, 1995	TM	0.995	53.66
January 7, 1998	TM	0.983	36.19
February 6, 2000	ETM+	0.986	37.84
February 11, 2002	ETM+	0.986	39.65

4.2.2 Scene Descriptions

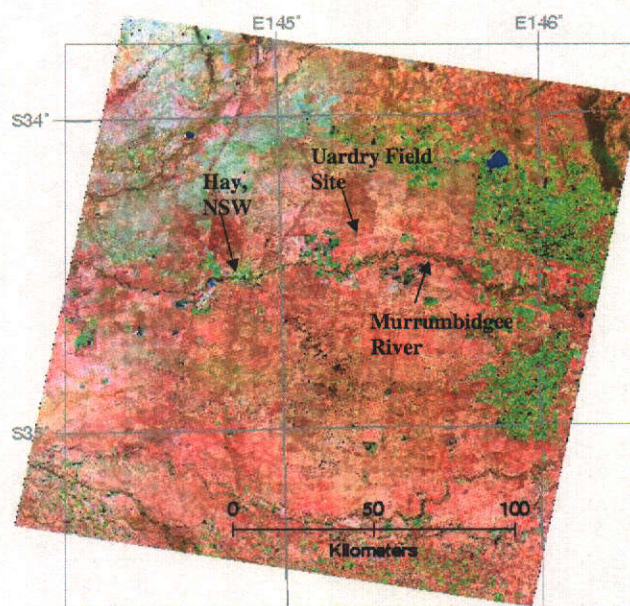
Hay images are characterized by the Murrumbidgee River running east–west across the scene and through the Hay townsite (Figure 4.3(a)). The area covered in each Hay image is relatively flat, with the typical terrain elevation ranging from 90–120 m above sea level. In fact, the scene contains the largest and most uniform plain on the Australian continent (Prata et al., 1997). Thus terrain illumination effects (e.g. shadowing) and changes in atmospheric properties due to elevation were considered negligible for the Hay sequence.

Mt. Barker images are characterized by the vast expanses of perennial native vegetation to the left and bottom of the imagery, and predominantly cleared land in the upper half of the scene (Figure 4.3(b)). The most discernible features in Mt. Barker images are the Stirling Ranges National Park to the top-right of the scene, and the Southern Ocean which bounds the bottom of the scene. Approximately ninety-five percent of the terrain in the Mt. Barker image is between 0–370 m above sea level.

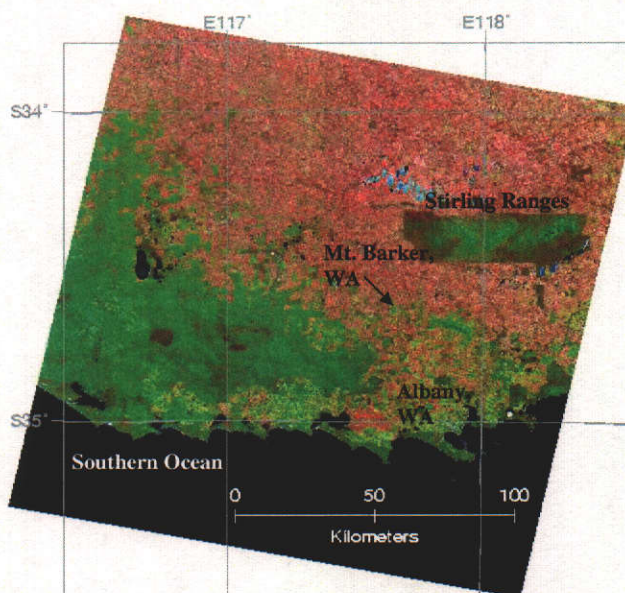
4.2.3 Geometric Rectification

For a given study region, all the images were rectified to common map base images. The Hay images were rectified to the base used in the Australian Greenhouse Office (AGO) project (Richards and Furby, 2002). The rectification base image has the map grid of Australia projection for zone 55 (MGA55), and uses the geocentric datum of Australia 1994 (GDA94). For Mt. Barker images, the rectification base was an image used in the Land Monitor project (Caccetta et al., 2000a), with the Australian map grid for zone 50 (AMG50) and the Australian geodetic datum 1966 (AGD66).

A cross-correlation feature matching procedure (Furby, 2000) was employed for a set of between 120–200 ground control points uniformly distributed throughout each scene. Nearest-neighbour resampling was used for the Hay sequence to preserve the radiometric integrity of the image data for subsequent comparison to ground-based spectrometer data. Cubic convolution resampling was used on Mt. Baker images. In both cases, rectification results were within an acceptable error level of ~ 30 m.



(a)



(b)

Figure 4.3: False-colour composites (RGB:5,4,2) of ETM+ images for (a) Hay, January 7, 2000 and (b) Mt. Barker, February 6, 2000.

4.2.4 Ground-based Data for Hay

On March 27, 2000 a field campaign was conducted by members of the CSIRO Earth Observation Centre (EOC) at the Uardry field site (Prata et al., 1997; Prata and Rutter, 2001) 60 km northeast of Hay. The date was chosen to coincide with the Landsat-7 overpass and the acquisition of the corresponding ETM+ image (Table 4.1). At the Uardry site, there is a 15-m tower (located at E 145°18', S 34°24', 110 m above sea level) from which surface albedo and meteorological data are continuously logged. Furthermore, a Multi-Filter Rotating Shadowband Radiometer (MFRSR) (Harrison and Michalsky, 1994; Yankee Environmental Systems, 1997) located at the site routinely records total atmospheric optical thickness. Since 1995 the Uardry site, maintained by the CSIRO Division of Atmospheric Research (CAR), has formed part of a Continental Integrated Ground Site Network (CIGSN) (Prata et al., 1997) and has subsequently been involved in a number of sensor calibration and validation programmes, such as those of the ATSR/ATSR-2 (Along-Track Scanning Radiometer on the Envisat satellite), MODIS on Terra and Hyperion on EO-1.

Surface Reflectance Measurements

Surface reflectance measurements were acquired on the EOC Uardry field campaign of March 27, 2000 for a number of targets around the field site with a variety of field spectrometers. Of interest in this work were the 4 targets for which data were acquired with either the Analytical Spectral Devices (ASD) FieldSpec or the Geophysical and Environmental Research (GER) Inc Iris Spectroradiometers³. These spectra, summarised in Figure 4.4, were for: a clay scald (denoted *Clay* measured with the Iris), approximately 500 m west of the Uardry tower; an area containing bare ground and dry grass (*Field*, acquired with the Iris) 50 m west of the Uardry tower; an area of ground below the tower (*Tower*, measured with an ASD from 15 m above the surface); and a grass target (*Grass*, measured with an ASD). These spectra were acquired from approximately thirty minutes prior to Landsat-7 overflight to two hours after the overpass time.

Within each target area, a number of spectrometer readings were acquired. These

³Relative radiometric calibration of the GER Iris is achieved by the sensor acquiring simultaneous measurements of the target and a spectralon (trademark of Labsphere Inc) plate; a highly reflective plate with near-Lambertian properties.

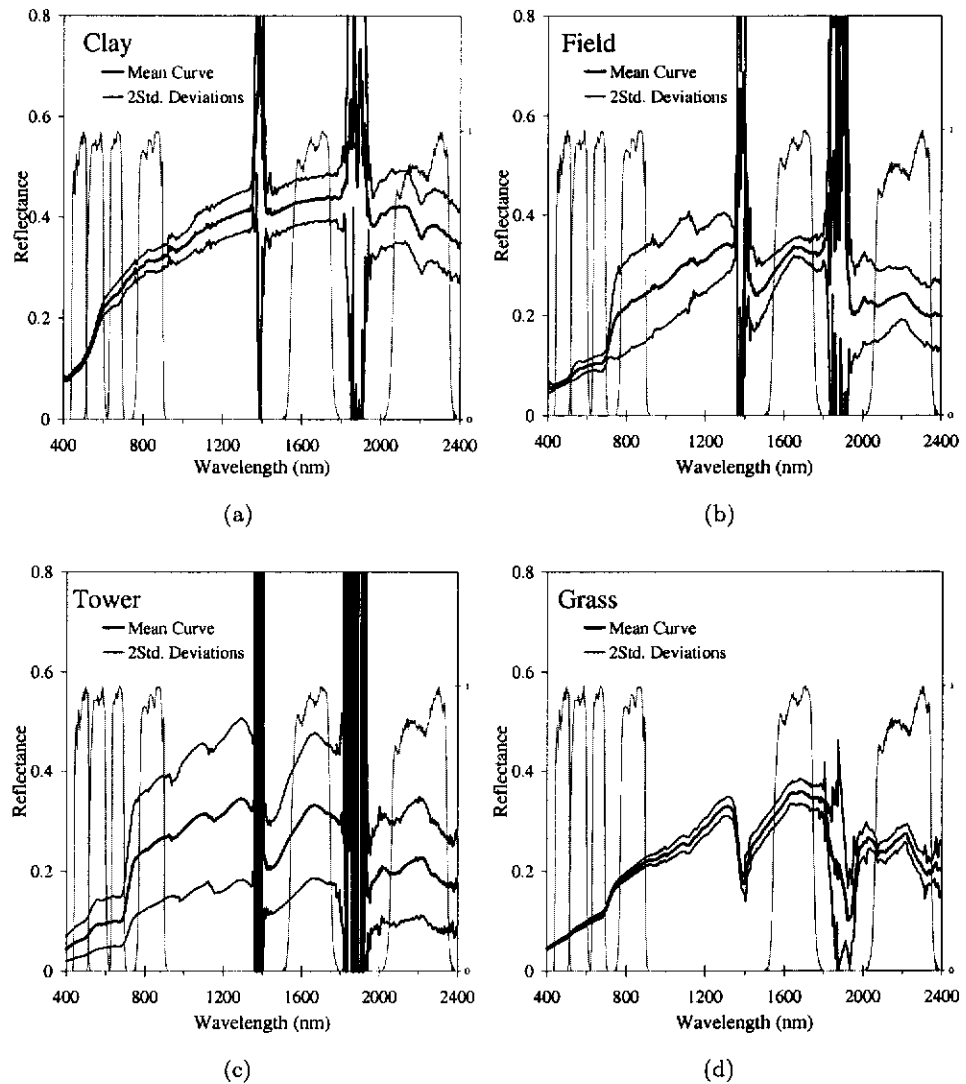


Figure 4.4: Spectrometer-acquired surface reflectances for (a) a clay scald; (b) an area of field (50 m west of tower); (c) the area below the tower; and (d) a grass patch acquired during the EOC calibration campaign of March 27, 2000 at the Uardry field site. The average reflectances for each target area are highlighted with thick dark lines, whilst the thin black lines mark two standard deviations about the mean curve. ETM+ response curves are illustrated in light grey.

readings were taken over an area extending beyond that of a single ETM+ pixel (i.e. $> 30 \times 30 \text{ m}^2$). For each target, the spectra were convolved with the ETM+ bands response functions (displayed in Figure 4.4 as light grey lines) to facilitate comparisons between ground-based and corresponding satellite image data.

Aerosol Optical Thickness

The time series of solar irradiance measurements for the MFRSR 416.6-nm band acquired at Uardry on the date of the EOC field campaign is given in Figure 4.5. The numerous ‘dips’ observed in the figure are due to cloud occluding the direct sunlight. For most of the afternoon the Uardry site was completely covered by cloud; evident in the data by the similarity between the total and diffuse irradiance measurements made around that time.

Patches of cloud were also observed in the morning. However there were sufficient data for the processing software (Dosband) to conduct Langley analysis (refer to Section 2.3.3, p. 31) on the morning direct-normal irradiance measurements and thus retrieve an estimate of $\tau_{\text{tot}\lambda}$ for each MFRSR band (Figure 4.6). The total optical thickness values measured are presented in Table 4.2.

On the day of the EOC field campaign, the TOMS instrument on the Earthprobe satellite (McPeters et al., 1998) retrieved a columnar ozone concentration over the Uardry site of $u_{O_3} = 255 \text{ DU}$. Using this estimate for the ozone concentration, and the ozone absorption coefficients ($\alpha_{O_3\lambda}$) in Table B.1 (Appendix B, pp. 224–225), ozone optical thicknesses, $\tau_{O_3\lambda}$, were calculated for each MFRSR band (see Table 4.2).

Screen-level temperature (T_s) and surface pressure (P_s) measurements, also acquired at the Uardry site around the time of Landsat-7 overpass, allowed the molecular optical thicknesses, $\tau_{R\lambda}$, to be calculated (using Eq. (2.16), p. 28) for each MFRSR band. The values obtained are also given in Table 4.2.

Finally, estimates of aerosol optical thickness, $\tau_{M\lambda}$, were obtained using Eq. (2.23, p. 32) and the values of $\tau_{\text{tot}\lambda}$, $\tau_{O_3\lambda}$ and $\tau_{R\lambda}$ described above. Figure 4.7(a) further illustrates the wavelength dependence of the optical thicknesses in Table 4.2. The estimate of aerosol optical thickness for the 615 nm band makes the curve depart from the expected, smooth wavelength dependence ($\sim \lambda^{-1}$). The estimates of molecular optical thickness, on the other hand, behave as expected ($\sim \lambda^{-4}$, Eq. (2.16)). So too does the estimate

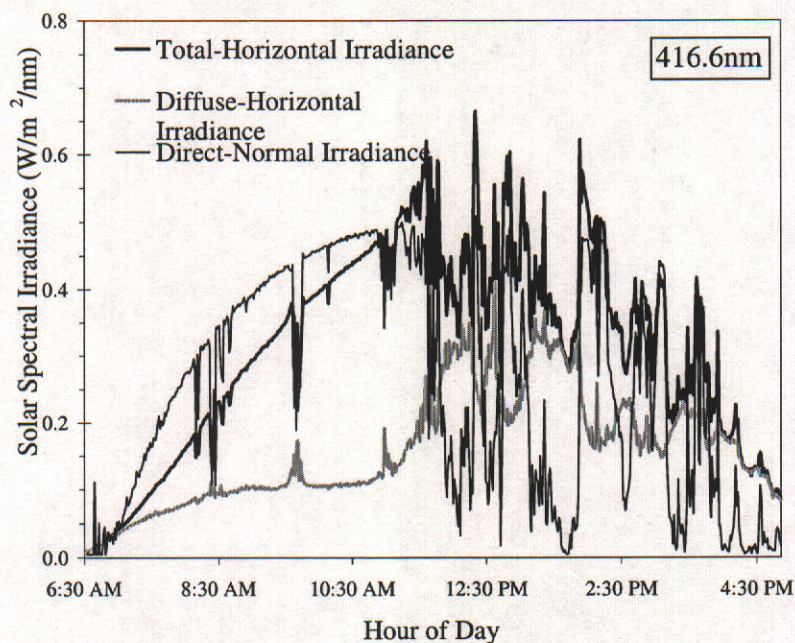


Figure 4.5: Time series of total-horizontal, diffuse-horizontal and direct-normal solar spectral irradiance measurements [$\text{W}/(\text{m}^2 \text{ nm})$] acquired for the 416.6 nm band with a multi-filter rotating shadowband radiometer (MFRSR) located at the Uardry field site on March 27, 2000.

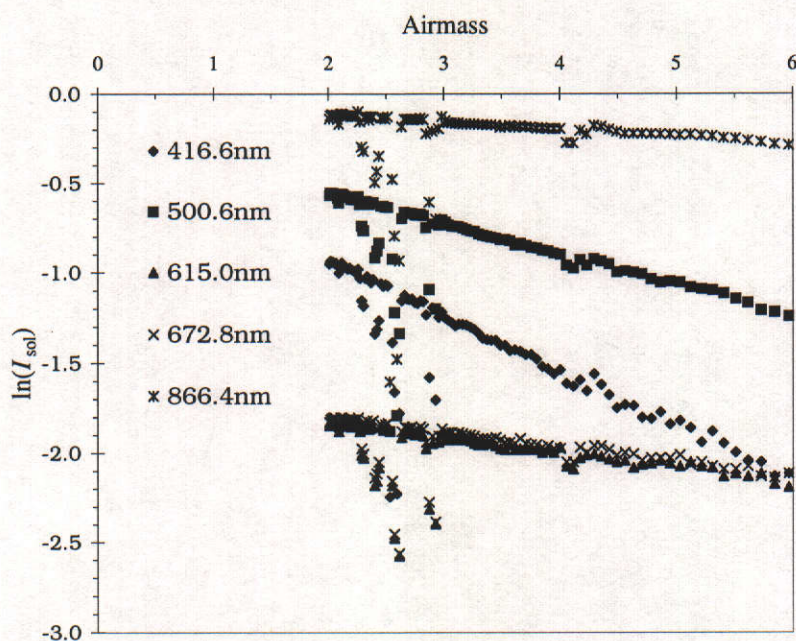


Figure 4.6: Langley plots of the morning (AM) MFRSR data acquired at the Uardry field site for March 27, 2000 for all the narrow bands except for 933.2 nm. The slope of the line gives an estimate of the total atmospheric optical depth $\tau_{\text{tot}\lambda}$.

Table 4.2: Total ($\tau_{\text{tot}\lambda}$), ozone ($\tau_{\text{O}_3\lambda}$), molecular ($\tau_{\text{R}\lambda}$) and aerosol ($\tau_{\text{M}\lambda}$) optical thickness values at the Uardry field site for March 27, 2000.

λ (nm)	$\tau_{\text{tot}\lambda}$	$\tau_{\text{O}_3\lambda}$	$\tau_{\text{R}\lambda}$	$\tau_{\text{M}\lambda}$
416.6	0.325	0.000	0.273	0.052
500.6	0.178	0.008	0.127	0.043
615.0	0.103	0.030	0.055	0.018
672.8	0.083	0.011	0.038	0.034
866.4	0.038	0.001	0.014	0.024

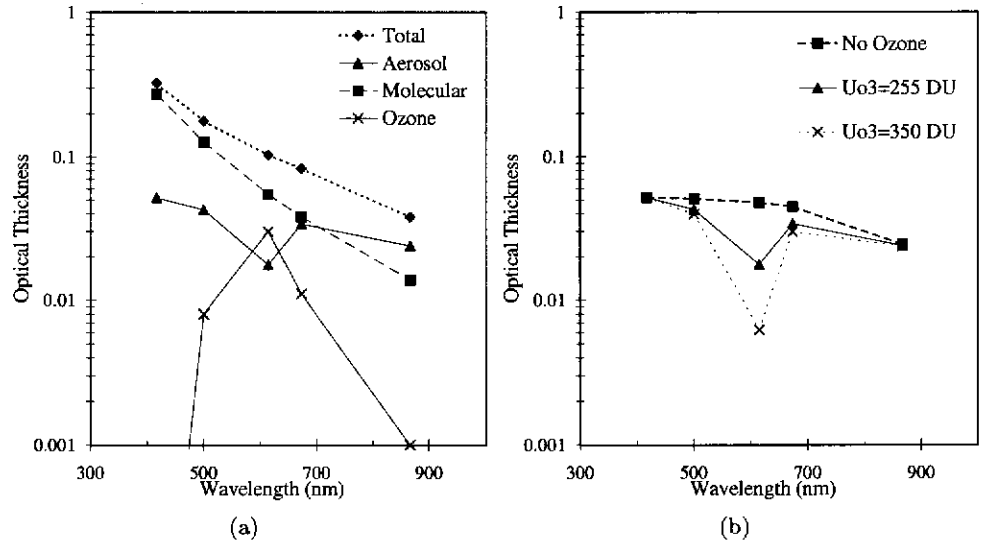


Figure 4.7: Optical thicknesses: (a) total, aerosol, molecular and ozone retrieved or calculated from measurements at the Uardry site; and (b) changes in estimates aerosol optical thickness for varying ozone concentrations.

of ozone; the 615 nm band is located in the Chappuis band where the value of $\tau_{\text{O}_3\lambda}$ is nearly a maximum (minimum transmittance; Figure B.1, p. 225) for a given ozone concentration.

It can be seen in Figure 4.7(b) that the value of $\tau_{\text{M}\lambda}$ in the 615 nm band is greatly affected by changes in ozone concentration. Recall that the TOMS estimate of ozone concentration at the Uardry site on the EOC field campaign was 255 DU. Increasing the concentration to 350 DU decreases the estimate of aerosol optical thickness in the 615 nm band by around 87%. As the ozone concentration decreases, the curve for $\tau_{\text{M}\lambda}$ begins flatten out and resemble the expected form of the wavelength dependence. In fact, the curves displayed in Figure 4.7(b) are similar to those used in King and Byrne (1976)

to illustrate their method for inferring columnar ozone concentrations from extinction measurements.

Estimates of $\tau_{M\lambda}$ can be used to establish an Ångström-type relationship. For the Uardry data, the low estimate of aerosol optical thickness at 615 nm will bias any linear fit to the data. This value was therefore excluded from the analysis, and the following relationship,

$$\tau_{M\lambda} = 26.91\lambda^{-1.03} \quad (4.5)$$

was obtained (see Figure 4.8). The relationship was used to yield an estimate of aerosol optical thickness at 550 nm, $\tau_{M550nm} = 0.04$. This is within the range determined in the long-term study by Prata and Rutter (2001) for the Uardry site, which shows that τ_{M550nm} ranges from 0.02–0.05 with an absolute error of ± 0.02 .

As to why the estimate of aerosol optical thickness is so much lower than the expected value in the 615-nm band, two possibilities may be considered: Firstly, the estimate of columnar ozone concentration for the date was too high; or secondly, there was a calibration or processing error in the corresponding MFRSR band on that date.

From Figure 4.7(b), one might (incorrectly) infer that an ozone concentration close to zero DU was present on the day—a physically unrealistic scenario. It is more likely, however, that the MFRSR underestimated the total optical thickness in the 615 nm band. Further investigation is required as to why the MFRSR (or the processing software) underestimated the aerosol optical thickness at 615 nm. For the purposes of this thesis, however, the estimate of obtained for τ_{M550nm} was satisfactory, particularly as it was within the range expected for the Uardry site (Prata and Rutter, 2001).

Aerosol Type

Using the estimate of τ_{M550nm} from the previous section, 6S was used to model the aerosol optical thickness values in the 6 ETM+ bands (in the region 400–2400 nm) for a variety of different aerosol types. These modelled values are displayed in Figure 4.8 for continental, urban, maritime and desertic aerosol types. Equation (4.5) is also displayed in the figure as the continuous line. A comparison of the MFRSR-derived and 6S-modelled values reveals best agreement with the continental aerosol type. It was therefore concluded that the aerosols present on the day of the EOC field campaign can best be characterised as

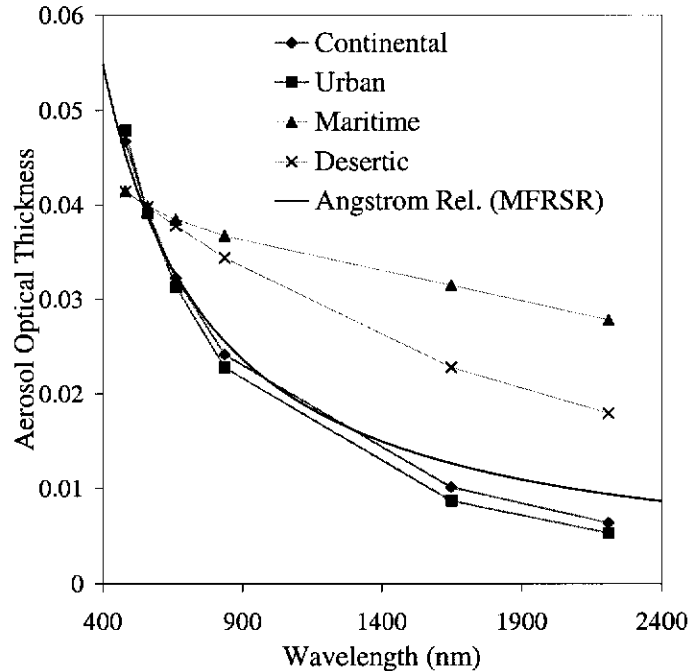


Figure 4.8: Aerosol optical thicknesses modelled using 6S for the ETM+ solar reflective bands (shapes connected with thin grey line) and using the Ångström relationship derived from MFRSR measurements on the day of the Uardry field campaign.

continental aerosols. This is again consistent with the findings of Prata and Rutter (2001) for the Uardry site.

4.3 Image Normalisation Results

In this section the LVIN procedure, described in Section 4.1.2, is applied to the Hay and Mt. Barker image sequences. For comparison purposes, the results of the application of the procedure with and without the use of modelled path DN s are presented. To distinguish between the two approaches, the terms *free-intercept* and *constrained* will refer to the LVIN procedure without (Figure 4.1(a)) and with (Figure 4.1(b)) the modelled path DN (Figure 4.1(b)) respectively.

4.3.1 Reference Image Processing

Once images in both multitemporal sequences had been co-registered, the next task was to choose/create appropriate reference images. In the following, the processing of the selected reference images for both the Hay and Mt. Barker sequences is presented.

Hay Reference Image

Recall (from Section 3.4.1, p. 100) that the empirical line (EL) procedure estimates the image correction coefficients from a straight-line fit to the $(X_\lambda, \rho_{s\lambda})$ data pairs for at least two targets in an image. Moran et al. (2001) described an approach where the surface reflectance measured for one bright target⁴ and the modelled path DN , $X_{p\lambda}$, are used to estimate surface reflectances in what they called the refined empirical line (REL) procedure (Section 3.4.1, p. 101). In this investigation, a procedure that incorporates the reflectance measurements of multiple targets as well as the modelled path DN was used to produce the reference image for the Hay sequence. It is referred to here as the *hybrid empirical line* (HEL) procedure and is described in the following.

The obvious choice for the Hay sequence reference image was that acquired by the ETM+ sensor on the date of the EOC Uardry field campaign on March 27, 2000. The ground-based spectrometer and atmospheric measurements acquired at the Uardry site were used along with the DN s extracted from the ETM+ image to construct the scatter plots in Figure 4.9. The figure shows: solid circles corresponding to the processed ground-based surface reflectance measurements; and hollow diamonds (on the y axis) to the path DN s modelled with 6S using atmospheric data acquired at the Uardry site (Section 4.2.4), and the ETM+ radiometric scaling factors from the image header file. The x coordinate of the solid points corresponds to the mean value for all spectra acquired at each target, with the x error bars extending to two standard deviations about the mean. Since the targets' size typically extended to beyond the dimensions of a single pixel, 3×3 neighbourhoods of pixels (centred on the recorded geoposition of the target) were extracted; the y coordinates of the data pairs in Figure 4.9 are the average DN for each target and the error bars are the two standard deviations limit about the mean.

For each HEL scatter plot, least squares regression provided the estimates of image correction lines that convert DN s into surface reflectances for each ETM+ band. The lines labelled *constrained* (dashed lines) correspond to the fit of the HEL procedure, as the regression is constrained to pass through the modelled path DN (shown as hollow diamonds on the y axis in Figure 4.9). For comparison purposes, the standard EL

⁴The REL procedure can, in principle, incorporate two or more bright targets. Moran et al. (2001), however, focused on the use of one bright target whose surface reflectance was well characterised.

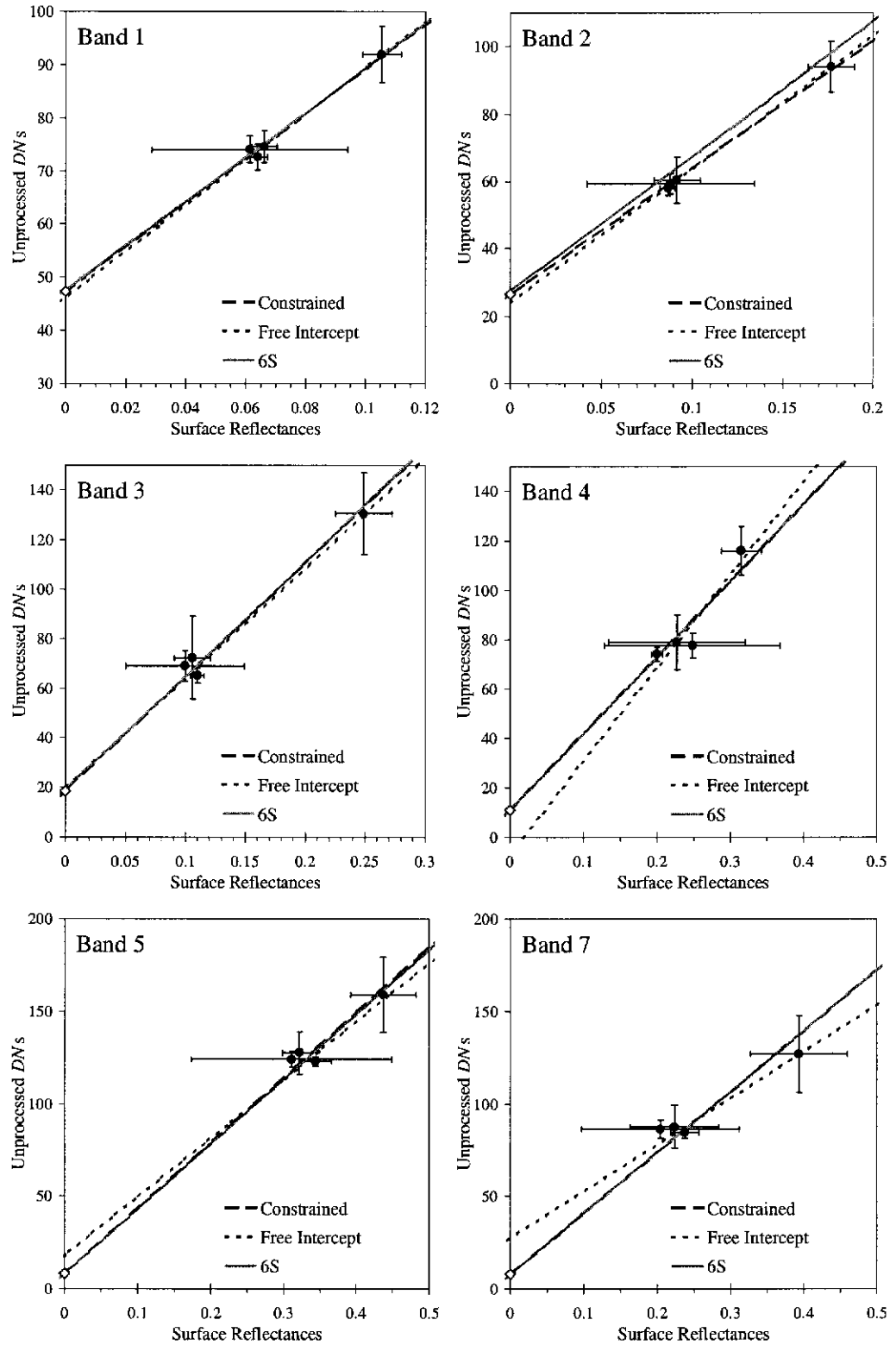


Figure 4.9: Scatter plots based on the ground-based and ETM+ image data acquired at the EOC field campaign on March 27, 2000. These data were used in a hybrid empirical line (HEL; dashed line) procedure to derive image correction coefficients used in the production of the Hay reference image. For comparison purposes, the EL (dotted) and 6S (light grey) correction lines are also displayed. Error bars denote the two standard deviation limits.

procedure provided image correction lines based on spectrometer data alone (i.e. no path DN) which are labelled *free-intercept* (dotted line in Figure 4.9), and 6S provided correction lines, labelled *6S* (light grey line in Figure 4.9), based on the Hay MFRSR estimates of AOT(550 nm), standard mid-latitude inputs for water vapour, temperature and pressure profiles. Excellent agreement was observed between the 6S and HEL correction lines for all bands (with the exception of band 2; however agreement was still within the 95% limits of the data) over most of the range of the image DN s.

The effect of having too small a number of surface reflectance measurements in the EL procedure is illustrated in Figure 4.9. The free-intercept approach would have resulted in significant errors in surface reflectance estimation, particularly for bands 4, 5 and 7 because of the limited number of points at the ‘dark’ end of the plots. Constraining the correction line to pass through the path DN was useful in tying down the regression for low reflectances.

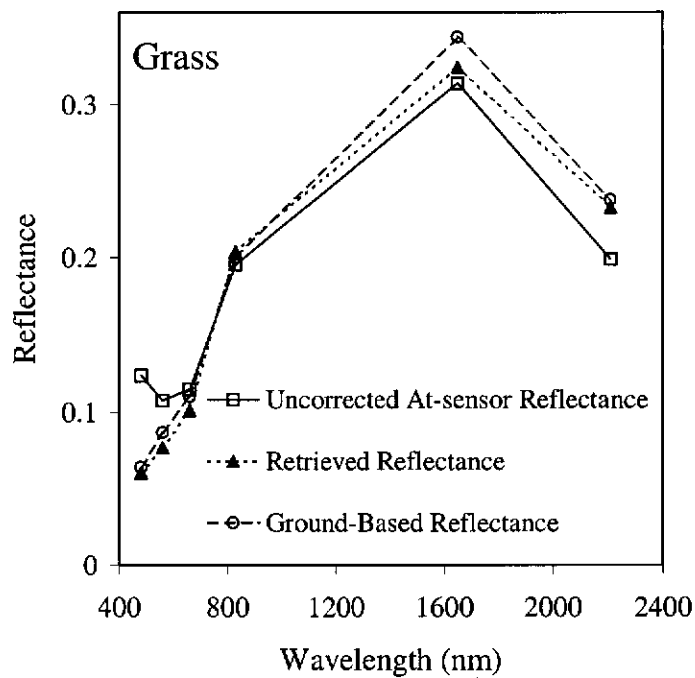
The slopes and intercepts of the HEL correction lines were used to estimate the image correction coefficients (in Eq. (4.4), p. 121) that produced the Hay reference image. The root mean squared (RMS) error (the standard deviation of the difference between retrieved value and ground-based measurement (Moran et al., 1992)) for the retrieved surface reflectances was 0.0098 (calculated on 28 points: 4 targets \times 7 bands), and the mean absolute differences⁵ (MADs) for bands 1–5 and 7 were 0.002, 0.009, 0.009, 0.017, 0.016 and 0.022 respectively. The increase in error for bands 4, 5 and 7 is due to increase scatter of the four targets about the line of best fit (Figure 4.9). The scatter overall may be mostly attributed to the calculated average ground-based reflectance measurements, which for 3 out of the 4 targets used had high variance (Figure 4.4).

Figure 4.10 displays the retrieved reflectances (triangles) resulting from the application of the HEL procedure to the image data for the (a) grass and (b) clay targets. One can clearly see that the retrieved reflectances are lower in value than the at-sensor reflectances (squares), and closer to the measured ground-based reflectances (circles), for bands 1, 2 and 3. Conversely, the retrieved reflectances for bands 4, 5 and 7 are higher

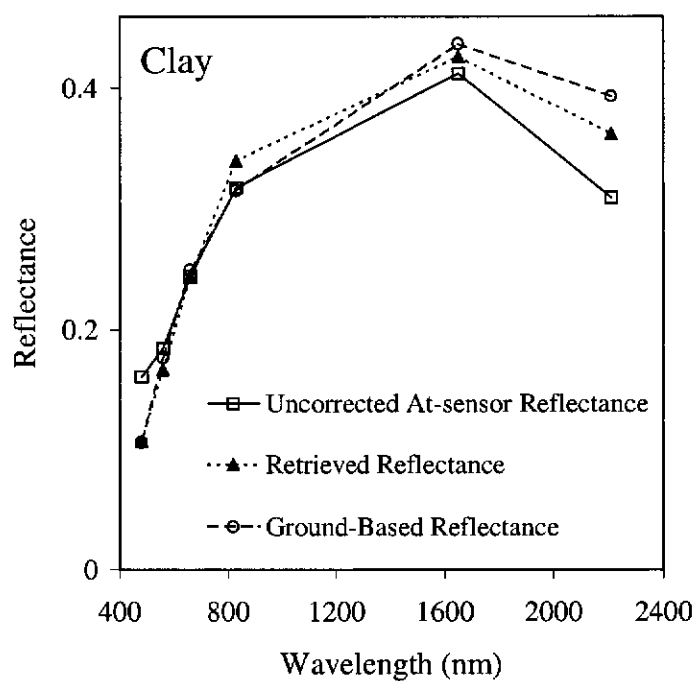
⁵For N points, the MAD is calculated as

$$MAD = \frac{1}{N} \sum_{i=1}^N |\rho_{corr\lambda} - \rho_{s\lambda}|_i$$

where $\rho_{corr\lambda}$ and $\rho_{s\lambda}$ are the estimated and reference surface reflectances respectively.



(a)



(b)

Figure 4.10: A comparison of the retrieved surface reflectance (using the HEL procedure; triangles) with the uncorrected at-sensor (squares) and ground-based (spectrometer data; circles) reflectances for the (a) grass and (b) clay targets measured during the EOC Uardry field campaign.

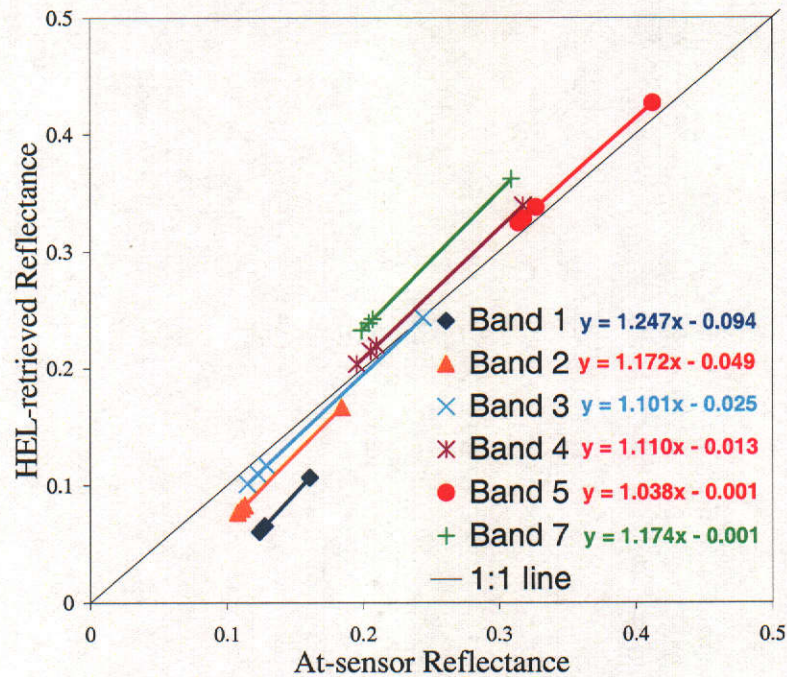


Figure 4.11: A comparison of the at-sensor and HEL-retrieved reflectances for the four targets visited on the EOC Uardry field campaign.

than the corresponding at-sensor reflectances. This behaviour is expressed in an alternative way in Figure 4.11. In this figure, the at-sensor and HEL-retrieved reflectances are plotted for each target measured during the EOC Uardry field campaign. The reflectances for bands 1, 2 and 3 fall below the 1:1 line whereas the reflectances for band 4, 5 and 7 fall above; supporting the observations made for Figure 4.10.

From the results presented in Figures 4.10 and 4.11, it appears that the HEL procedure has performed as expected of an atmospheric correction procedure. Specifically regarding the values of slope and intercept of the lines of best fit in Figure 4.11: the intercepts are indicative of the additive contributions of the atmosphere to the at-sensor signal (Section 3.3.3, p. 83), which the HEL procedure has been removed; whilst the slopes (all > 1) demonstrate the HEL procedure compensating for the multiplicative effects of gaseous absorption (Section 3.3.3, p. 84).

Mt. Barker Reference Image

The ETM+ image for Mt. Barker acquired on February 6, 2000 was selected as the most appropriate reference image for two reasons; namely the superior radiometric quality

of the ETM+ sensor over TM (Teillet et al., 2001), and greater dynamic range of that particular image data over other dates in the sequence. There were no surface reflectance measurements with which an EL procedure could be used to correct this image. There were, however, radiosonde and TOMS data to aid in the selection of the appropriate inputs to 6S and thus yield a correction equation for each band in the ETM+ image.

Radiosondes are routinely launched from Australian Bureau of Meteorology (ABoM) sites throughout Australia. Four sites were of interest in the production of the Mt. Barker reference image. Radiosondes from these sites were launched at 0900 hours local time on February 6, 2000; about an hour and a half prior to when the Landsat-7 ETM+ sensor acquired the image of the Mt. Barker scene (Table 4.1).

As there are no radiosonde launches from the Mt. Barker town site, radiosonde data from launch sites in the southwest of Western Australia were examined in an attempt to characterise the Mt. Barker area. Specifically, these were the radiosonde data from the Albany, Esperance, Kalgoorlie-Boulder and Perth airports (Figure C.1, Appendix C, p. 227). Equation (2.4, p. 11) was applied to successive pressure measurements up to an altitude of approximately 10 km for each radiosonde pressure profile. A line of best fit for these values was extrapolated to sea level to yield the values of \bar{H} presented in Table 4.3. The values of scale height compare quite closely to those of model atmospheric pressure profiles in Table 2.1 (p. 12); specifically for the mid-latitude summer or tropical pressure profiles. Examination of these radiosonde data with mid-latitude and tropical pressure profiles revealed that unexpectedly the best agreement occurs between the radiosonde data and the tropical profiles (Figure C.2(a)).

Temperature lapse rates, δ , calculated as the slopes of the lines of best fit for the first 10 kilometres of the radiosonde temperature measurements were obtained for each

Table 4.3: Scale height \bar{H} values derived from ABoM radiosonde pressure profiles acquired at four sites in Western Australia on February 6, 2000.

Pressure Profile	\bar{H} (km)
Albany	8.725
Perth	8.748
Esperance	8.573
Kalgoorlie	8.694

radiosonde and the results are given in Table 4.4. Also presented in the table are the sea-level temperature values T_{z0} which are the intercepts of the lines of best fit. A comparison of these lapse rates to those of the model atmospheric profiles given in Table 2.2 (p. 14) reveals good agreement with the mid-latitude summer profile. Examination of Figure C.2(b), however, shows better agreement with the tropical temperature profile, particularly for altitudes above 13 km.

The water vapour pressure was calculated at each altitude reached by the radiosondes from the measurements of temperature, pressure and relative humidity via expressions (A.6) and (A.7) in Appendix A (pp. 222–223). Finally, by rearranging Eq. (A.5), an estimate of the water vapour density at each altitude was obtained. After employing the column-integrated approach (Eq. (2.8), p. 15), an estimate of precipitable water, u_{H_2O} , was obtained for each location. These values are given in Table 4.5.

From the data in Tables 4.3, 4.4 and 4.5 it was concluded that, due to the similarity of the results, on the date of the ETM+ image acquisition for the Mt. Barker scene, stable meteorological conditions prevailed between the 4 described locations. Furthermore, in the absence of any higher-spatial resolution pressure, temperature and water vapour information, the radiosonde data for Albany was chosen as the best representation of the atmosphere in the Mt. Barker scene on February 6, 2000.

Estimates of total ozone concentration over the extent of the Mt. Barker image were obtained from the Earthprobe TOMS data. On average, the ozone concentration for February 6, 2000 was 263 DU (3 DU standard deviations).

Unfortunately, there were no *in situ* measurements of atmospheric optical thickness on the date of the ETM+ acquisition. An aerosol optical thickness $\tau_{M550nm} = 0.05$ and a continental aerosol type were assumed. The validity of these assumptions is discussed

Table 4.4: Temperature lapse rates, δ , sea-level temperature, T_{z0} , and regression correlation coefficient, R^2 , derived from radiosonde data for the four Western Australian launch sites on February 6, 2000.

Temperature Profile	δ (K/km)	T_{z0} (K)	R^2
Albany	-5.56	295.4	0.96
Perth	-5.97	299.2	0.98
Esperance	-5.32	293.0	0.93
Kalgoorlie	-5.72	296.9	0.94

Table 4.5: Estimates of precipitable water, u_{H_2O} , obtained from radiosonde profiles for the four locations in Figure C.1 on February 6, 2000.

Location	Albany	Esperance	Kalgoorlie	Perth
u_{H_2O} (g/cm ²)	1.28	1.35	1.08	1.16

later in Section 4.3.6.

Terrain elevation effects on the absorbing and scattering constituents of the atmosphere were discussed in Section 3.3.3 (p. 90). Even if the atmosphere's properties and constituents were uniform across an image (which was implied for Mt. Barker based on the preceding paragraphs), one would expect that the image correction coefficients would change from location to location as a result of elevation alone. For simplicity, however, the image correction coefficients derived for the Mt. Barker ETM+ image were based on one elevation. The errors this introduced are discussed in more detail in Appendix D and summarised briefly below.

Terrain elevation for the Mt. Barker scene ranges from sea level to over 900 m. A median elevation $z = 200$ m was used as input to 6S. It is reasonable to expect that this assumption may result in errors in surface reflectance estimation, especially for low reflectance values. For most of the terrain in the Mt. Barker reference image (between 20–370 m; Section 4.2.2), the error in assuming $z = 200$ m was less than 5% for $\rho_{s\lambda} \geq 0.04$, 0.02, 0.01, and 0.005 for bands 1–4, and better than 1% error for all reflectances in bands 5 and 7 (see Table D.1). For areas in the Stirling Range and Porongurup national parks (where $z \sim 900$ m, see Figure 4.3), the errors were somewhat larger. Since these elevations constitute a comparatively small portion of the Mt. Barker scene, they were considered inconsequential to the analysis that follows.

Finally, the 6S code was used to derive image correction coefficients to convert the ETM+ image DN s into surface reflectances in the manner described by Zhao et al. (2001). The information described above was used as the inputs to 6S. In summary, they were: a tropical pressure and temperature profile was used with $u_{H_2O} = 1.3$ g/cm², $u_{O_3} = 260$ DU, and it was assumed that the aerosols present were continental with $\tau_{M550nm} = 0.05$. The image correction coefficients were calculated for an elevation $z = 200$ m. The quality of a reference image produced in this fashion is far from ideal. There were no ground-based reflectance measurements with which to validate the reference.

The image, however, was useful for the comparative analysis to be described.

4.3.2 Pseudo-Invariant Targets

Visual inspection was the method employed for selecting the PITs to be used in the normalisation of the Hay image sequence. Images were displayed in true colour (RGB:3,2,1) and systematically searched for PITs, such as the examples on page 124. This method provided PITs in the Hay images such as bare ground, road intersections, white sand and car park asphalt. A single-pixel *DN* was extracted for each band from each of a set of 15 targets.

The PITs used for the Mt. Barker sequence were those used in the Land Monitor project (Caccetta et al., 2000a,b). Here 2×2 or 3×3 neighbourhoods of pixels were extracted for each of 30 PITs (totalling 120 pixels). Some of the sources of invariant targets were an asphalt surface of an airport runway, rocky outcrops, and the deep water in the Southern Ocean, which bounds the bottom of all Mt. Barker images.

4.3.3 Modelled Path *DN*

The Southern Ocean in the Mt. Barker scene provided a large number of suitably dark PITs for use in the LVIN procedure. Nevertheless, the modelled values of path *DN*s were computed for each image in the Mt. Barker sequence for comparison purposes.

Model path radiances were computed for each overpass image in both Hay and Mt. Barker sequences using 6S. The inputs to the software are summarised in Table 4.6. For Hay images these were a continental aerosol model with $\tau_{M550nm} = 0.035$, based on the observations of Prata and Rutter (2001) for the Uardry site, TOMS estimates of u_{O3} , and the appropriate choice of tropic, mid-latitude summer or winter atmospheric models for each date. The average value of aerosol optical thickness was chosen because of MFRSR calibration problems at the Uardry site on the dates of overpass image acquisition. Finally, the simulations were based on the elevation $z = 110$ m (range for a typical Hay scene is 90–130 m).

The aerosol type for all the Mt. Barker images was assumed to be continental, with $\tau_{M550nm} = 0.05$, and standard mid-latitude summer atmospheric temperature and pressure profiles were used. For the dates where TOMS data were available, these served as estimates of u_{O3} ; if they were not available, the standard 6S model values were used.

Table 4.6: Inputs used in 6S to model path radiances for each date of image acquisition in both Hay and Mt. Barker sequences. The inputs were: the day and month the image was acquired; the particular satellite sensor used; solar zenith angle (θ_0) and solar azimuth (ϕ_0); atmospheric water (u_{H_2O} in g/cm²) and ozone (u_{O_3} in cm-atm) content; aerosol type (AT), which in this study was assumed to be continental (Cont.); aerosol optical thickness at 550 nm (τ_{M550nm}); pressure and temperature profiles (Profiles), which in this study were assumed to correspond to standard mid-latitude summer (MLS) or winter (MLW) profiles; and mean target elevation (z).

Inputs	Hay Scene			Mt. Barker Scene					
Day	22	26	7	20	24	28	20	7	11
Month	7	10	1	1	2	1	3	1	2
Sensor	TM	TM	ETM+	TM	TM	TM	TM	TM	ETM+
θ_0	66.12	37.75	32.62	41.21	46.86	42.34	54.44	36.19	39.65
ϕ_0	40.02	62.20	78.05	81.99	69.53	79.94	62.16	81.36	69.31
u_{H_2O}	0.853	0.853	2.93	2.93	2.93	2.93	2.93	2.93	2.93
u_{O_3}	0.323	0.342	0.292	0.319	0.319	0.319	0.319	0.319	0.287
AT	Cont.	Cont.	Cont.	Cont.	Cont.	Cont.	Cont.	Cont.	Cont.
τ_{M550nm}	0.035	0.035	0.035	0.05	0.05	0.05	0.05	0.05	0.05
Profiles	MLW	MLW	MLS	MLS	MLS	MLS	MLS	MLS	MLS
z	110 m	110 m	110 m	200 m	200 m	200 m	200 m	200 m	200 m

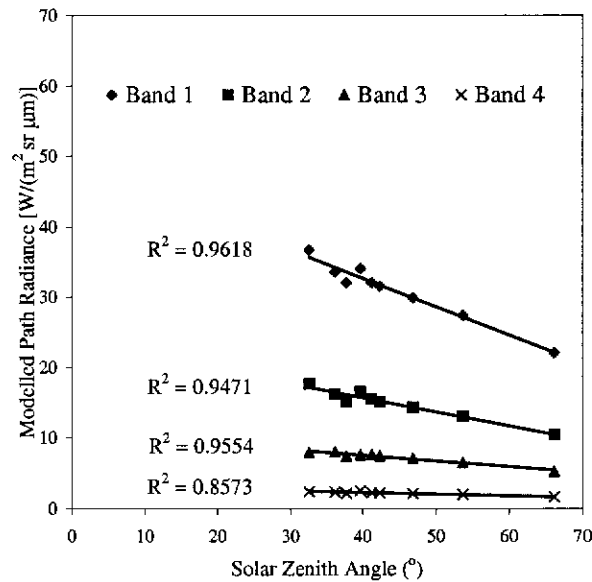


Figure 4.12: Variations in the modelled path radiance with solar zenith angle for the first 4 TM/ETM+ bands. Path radiances were modelled on the inputs to 6S, given in Table 4.6, for the dates that overpass images in both the Hay and Mt. Barker sequences were acquired.

Path radiances were modelled using 6S with a mean elevation for the Mt. Barker scene of $z = 200$ m.

Figure 4.12 illustrates the expected anti-correlation between the modelled path radiance and the solar zenith angle for each overpass image. Images will appear darker when the solar zenith angle is high as a consequence of the obliqueness of solar illumination ($\cos(\theta_0) \rightarrow 0$). The TM image for Hay acquired on July 22, 1999 is the darkest image in both sequences because of the high solar zenith angle (see Table 4.1); the corresponding value for $L_{p\lambda}$ is located at the bottom right of Figure 4.12. Points that deviate from the line are due to either a change in atmospheric profile used for the modelling (due to winter or summer dates of image acquisition), optical thickness or because of the ETM+ sensor acquires data slightly later in the day (smaller zenith angle) than the TM would if they acquired imagery on the same day. The path radiance corresponding to the ETM+ image for Hay on January 7, 2000 is the top left-most point whilst the TM image for Hay October 26, 1999 is the point that is consistently furthest from the line. Generally, the modelled path radiances behaved as expected.

Numerous assumptions have been made regarding the inputs to the modelled values. The error that these assumptions introduce to the modelled value of path radiance (and subsequently path DN) is addressed for the more significant parameters for the Hay and Mt. Barker scenes respectively in Section 4.3.6.

Finally these path radiances were converted to path DN using the radiometric scaling factors appropriate to the level of overpass image product. In the case of the Mt. Barker TM image for February 24, 1992, where the level of image product was not known, the radiometric scaling factors of Markham and Barker (1986) were used.

4.3.4 Like-Value Normalisation to Surface Reflectances

Normalisation (LVIN) plots were constructed for each band and for all overpass images using the unprocessed overpass DN , X_λ , and the surface reflectance, $\rho_{s\lambda}$, from the reference image for each PIT (Appendix E, pp. 233–242). Figures 4.13 and 4.14 show these LVIN plots for the Hay ETM+ image for January 7, 2000 and the Mt. Barker TM image for January 28, 1994 respectively. The black diamonds in each plot represent the

data pair $(X_\lambda, \rho_{s\lambda})$ for each pixel associated with a PIT⁶. The white diamonds on the y -axes represent the modelled path DN for the given band. Two lines were fitted to each plot: the first, known as the *free-intercept* line (solid black line), calculated on the PIT data pairs only; the second, is that which results from line of fit *constrained* to pass through the model $X_{p\lambda}$ (dashed line). The 95% confidence limits of the free-intercept lines are also displayed in the figure (in grey).

For the Hay and Mt. Barker sequences, the robust M-estimator⁷ was used to provide the free-intercept and constrained regression normalisation lines. The insensitivity of the M-estimator to outliers—relative to least squares—means that up to half the points in each LVIN plot may be discarded from the regression analysis. This means that if some of the PITs change in reflectance property between dates, or they are hidden by clouds on a given date, the image normalisation lines derived with the M-estimator will not be significantly biased. In all bands, and for most dates (with the exception of the Mt. Barker February 1992 TM image), the constrained regression lines were contained within the 95% confidence limits of the free-intercept regression lines.

For comparison, 6S correction lines (using the approach of Zhao et al. (2001)) were computed for each of the Hay overpass images (e.g. Figure 4.13, dotted lines). The 6S correction lines were determined using the available radiometric scaling factors of the respective sensors and modelled estimates of the atmospheric inputs. For the Hay ETM+ image for January 7 2000, the 6S correction line compared very well to the constrained regression line for all bands, however departed from linearity in the high reflectance range. The departure from linearity is a result of the 6S model giving a non-linear correction to the data that becomes more evident at high surface reflectances. For the TM images in the Hay sequence (Appendix E, Figures E.1–E.2) however, 6S and like-value lines differ significantly for bands 1–3; the slope of the 6S correction lines being much higher in value than the regression estimates, but the two slopes are in closer agreement for band 4.

The fact that the constrained regression lines were within the 95% confidence limits of the free-intercept lines was an interesting result. To compare the results of the free-

⁶The number of pixels per PIT for the Hay and Mt. Barker sequences is discussed in Section 4.3.2, p. 145.

⁷An improved robust M-estimator, available in the S-PLUS software (Venables and Ripley, 1999, pp. 171–174), was employed for this work. For further details on robust estimators in regression, the reader is directed to Rousseeuw and Leroy (1987).

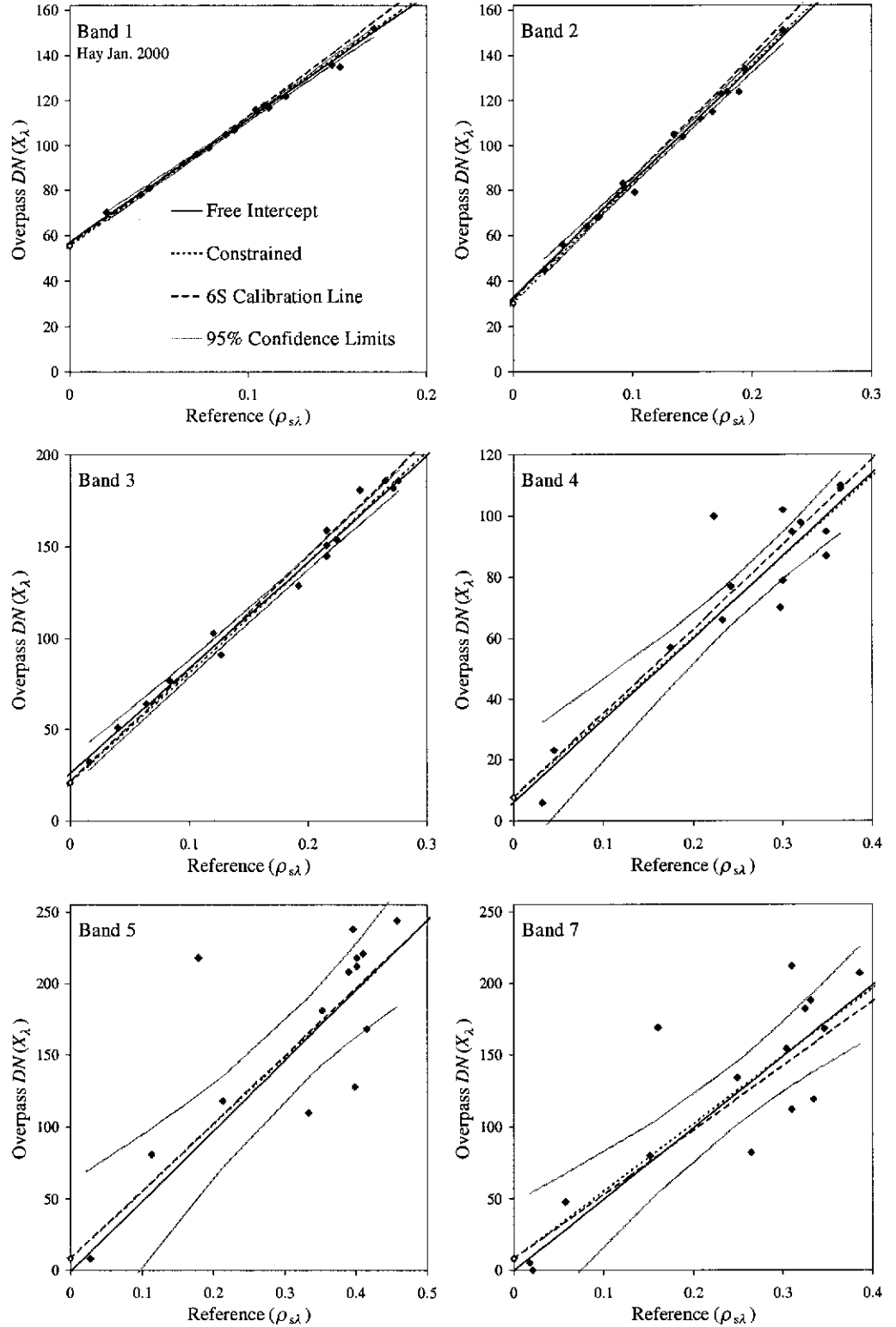


Figure 4.13: Like-value image normalisation plots for each band in the Hay ETM+ image acquired on January 7, 2000. Black diamonds represent the data pair $(X_\lambda, \rho_{s\lambda})$ for each pixel associated with a PIT, whilst the modelled path DN for each band is illustrated by a white diamond. The free-intercept and constrained regression lines are displayed as the solid and dashed lines respectively. The 95% confidence limits of the free-intercept regression line are also displayed in grey. The correction line provided by 6S based on atmospheric input is displayed (dotted line) for comparison purposes.

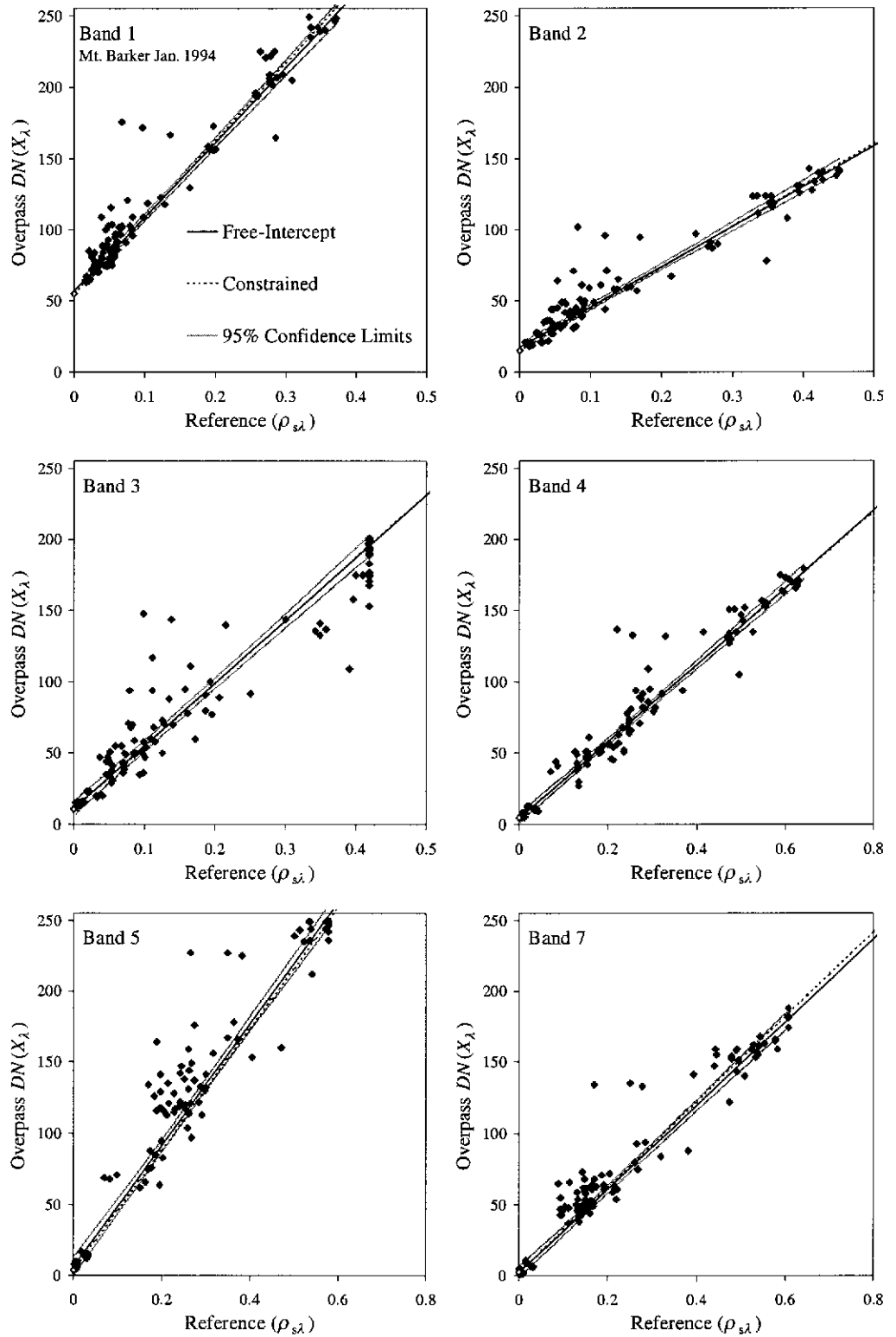
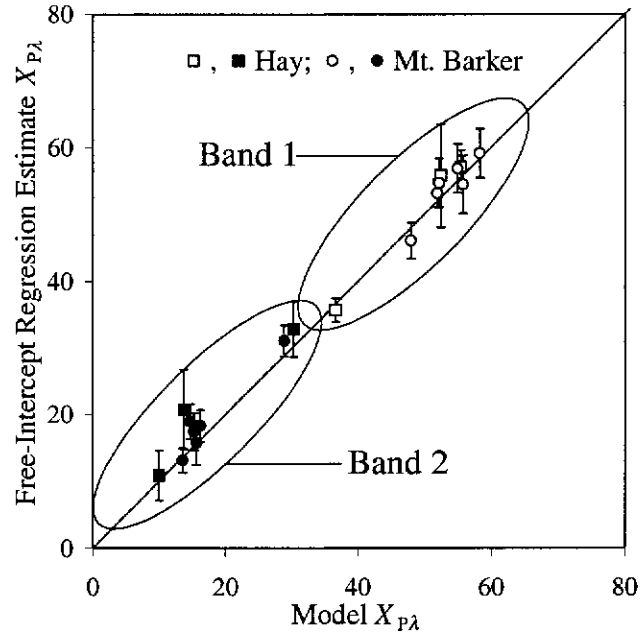


Figure 4.14: Like-value normalisation plots for each band in the Mt. Barker TM image acquired on January 28, 1994. Black diamonds represent the data pair $(X_\lambda, \rho_{s\lambda})$ for each pixel associated with a PIT, whilst the modelled path DN for each band is illustrated by a white diamond. The free-intercept and constrained regression lines are displayed as the solid and dashed lines respectively. The 95% confidence limits of the free-intercept regression line are also displayed in grey.

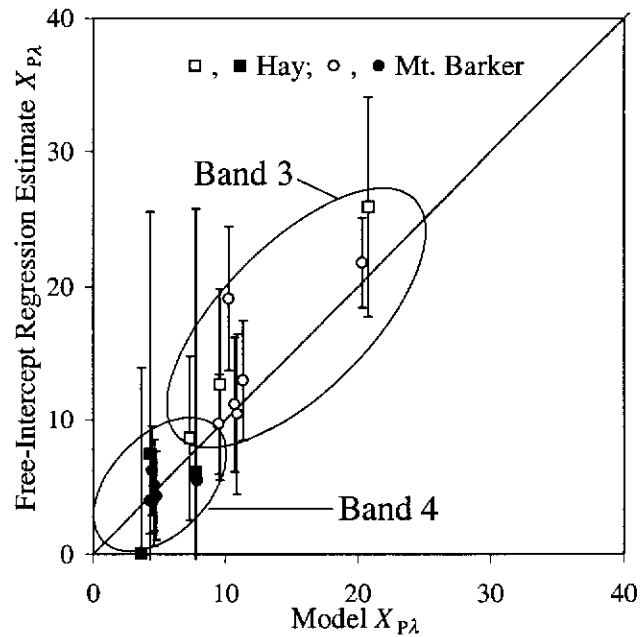
intercept and constrained approaches, both lines were used to retrieve reflectances for the PITs used in both multitemporal sequences. A straight line was fit to the retrieved reflectances, yielding a relationship between the free-intercept values and those obtained via the constrained approach (see Appendix F, pp. 243–248). Perfect agreement between the two approaches would have resulted in a slope of 1 and an intercept of 0 for each band. Instead, it was observed that the values for slope were between 0.91 and 1.24 for the Hay sequence (Table F.1), and between 0.96 and 1.14 for the Mt. Barker sequence (Tables F.2 and F.3). The intercept values for the Hay sequence were often above 0.01 in magnitude, and up to 0.03 three times; for the Mt. Barker sequence, however, the intercepts were more often < 0.01 in magnitude, and only increasing to 0.02 for the February 24 1992 TM data.

The discrepancy between the two approaches is illustrated in Figures F.1–F.3 (pp. 244–248) where the difference of free-intercept approach relative to the constrained approach is plotted (in %) for a range of reflectances. The discrepancies are observed to be most significant for low reflectances (i.e. $\rho_{\text{corr}\lambda} < 0.1$), with relative differences of more than 100% often observed. However, it can be seen that agreement between the two approaches is better than around 10% for reflectances above 0.1 for most of the range of the data, particularly in the VIS bands.

The disagreement between the two approaches is clearly a result of free-intercept normalisation line's estimate of y -intercept differing from the modelled value of path DN . To further investigate this discrepancy, the free-intercept regression lines were used to estimate $X_{p\lambda}$ for all bands in each overpass image. Figure 4.15 demonstrates that the modelled value of $X_{p\lambda}$ in all but one case (Mt. Barker 1992 image) lies within the 95% confidence interval of the regression estimate (error bars mark the $2 \times$ standard errors about the estimate). From this, it was concluded that there was no reason to reject the claim that the *true* normalisation line passes through the modelled path DN . Therefore, the constrained regression results were used to obtain image normalisation coefficients A_λ and B_λ for each band, and subsequently construct the normalisation line, $\rho_{\text{corr}\lambda}$, for each image (Eq. (4.4)).



(a)



(b)

Figure 4.15: A comparison of free-intercept regression estimates of $X_{p\lambda}$ for bands 1–4 from Hay and Mt. Barker scenes. The error bars mark the 95% confidence bounds ($2 \times$ standard error) about the free-intercept regression estimates.

4.3.5 Retrieved Reflectances

Image normalisation coefficients for the overpass images in the Hay and Mt. Barker sequences were derived from the constrained regression estimates of the LVIN lines. Unfortunately, there were no ground-based reflectance measurements with which the accuracy of the retrieved reflectances could be assessed; an all too frequently encountered problem when one attempts to analyse long-term series of archived data for indications of change in surface properties. Assuming, however, that for each scene there exists PITs that are reasonably invariant in reflectance property through time, the precision of the results was assessed in a comparison of the retrieved reflectances ($\rho_{\text{corr}\lambda}$) to the corresponding target in the reference image reflectances ($\rho_{s\lambda}$).

Table 4.7 presents the MADs (recall definition on page 139) calculated for the two most temporally-invariant bright, mid-range and dark PITs in each band of the images in the Hay sequence. Also displayed in brackets are the percentage errors relative to the reference reflectances. Generally errors in retrieved reflectances for bands 1–3 were within acceptable limits (Moran et al., 1992, with ± 0.02 reflectance units). For bands 4, 5 and 7, however, much poorer results were obtained; errors in reflectance retrievals were up to 30% for the bright PITs, and up to 86% for the dark PITs⁸. The poorer results for the infrared bands are primarily due to the increased scatter of points about the regression lines. The RMS error for all bands, across all dates for the targets in Table 4.7 was 0.063, whilst the RMS error calculated on bands 1–3 only was 0.011.

One can provide a physical explanation for the scatter observed in the LVIN plots for bands 4–7 by considering the data measured by the sensors in those bands. The respective bandwidths of bands 4, 5 and 7 are larger than the VIS bands (see Figure 3.3, p. 51) to compensate for the decreased signal level received by the TM and ETM+ sensors at the NIR-SWIR wavelengths. The bands, therefore, are more susceptible to spectral variations than their VIS counterparts. Furthermore these NIR-SWIR bands have a greater dynamic range than the VIS bands, which means that subtle variations in the spectrum—spectral variations in the surface reflectance properties or composition of the intervening atmosphere over time, for example—become more pronounced in these

⁸Moran et al. (1992) did not comment of the performance of the procedure they evaluated for bands 5 and 7, but band 4 was observed to perform the worst. Furby and Campbell (2001) also commented that the increased scatter in the NIR-SWIR bands affected the repeatability of their normalisation procedure.

Table 4.7: Mean absolute differences (with relative error in brackets) between retrieved and reference image reflectances, calculated for the most temporally invariant bright, mid-range and dark PITs (6 points = 3 dates \times 2 examples for each target) in the Hay overpass images.

Band	Targets		
	Bright	Mid-range	Dark
1	0.0054(3%)	0.0031(3%)	0.0034(10%)
2	0.0159(8%)	0.0066(4%)	0.0047(11%)
3	0.0142(6%)	0.0124(6%)	0.0060(15%)
4	0.0399(14%)	0.0301(10%)	0.0255(66%)
5	0.0868(30%)	0.0588(15%)	0.0200(81%)
7	0.0667(28%)	0.0401(13%)	0.0168(86%)

bands, leading to the observed scatter in the LVIN plots.

The software used to provide the M-estimates was also able to indicate which PITs were used to derive the ‘best’ normalisation line for images in the Mt. Barker sequences. Specifically, those PITs that were given a non-zero weighting for all bands in all the overpass images were deemed to be the most temporally invariant targets (see Figure 4.16). The reflectances retrieved for these PITs were used to calculate MADs. Across all dates, the MADs calculated for bands 1–5 and 7 were 0.006, 0.007, 0.009, 0.008, 0.008 and 0.010 respectively. The total RMS error, calculated on 1764 points (i.e. 6 dates \times 7 bands \times 42 pixels) was 0.012.

Figure 4.17 displays the pre- and post-normalisation histograms for a 2048×2048 subset of the ETM+ image for Mt. Barker February 11, 2002. The pre-normalisation reflectances are the at-sensor sensor reflectances (Eq. (3.3), p. 57), that is the radiances L_λ^* normalized by the factor $F_{d\lambda}\mu_0$. There are two post-normalisation histograms: the first corresponding to reflectances retrieved using *6S* and modelled atmospheric inputs; the second, labelled *LVIN*, corresponding to those reflectances retrieved via the LVIN procedure (the constrained regression approach). Similar histograms for the other overpass images used in this thesis are presented in Appendix G (pp. 249–253).

Figure 4.17 illustrates that after normalisation, there is a shift in histogram maxima to lower reflectances which is significant for bands 1 and 2, and slightly less for band 3. This observation is in support the notion that the additive effects of the atmosphere (dominated by scattering) have been removed. Also, the broadening of the post-normalisation histograms for bands 4, 5 and 7 appear to be in accordance with the

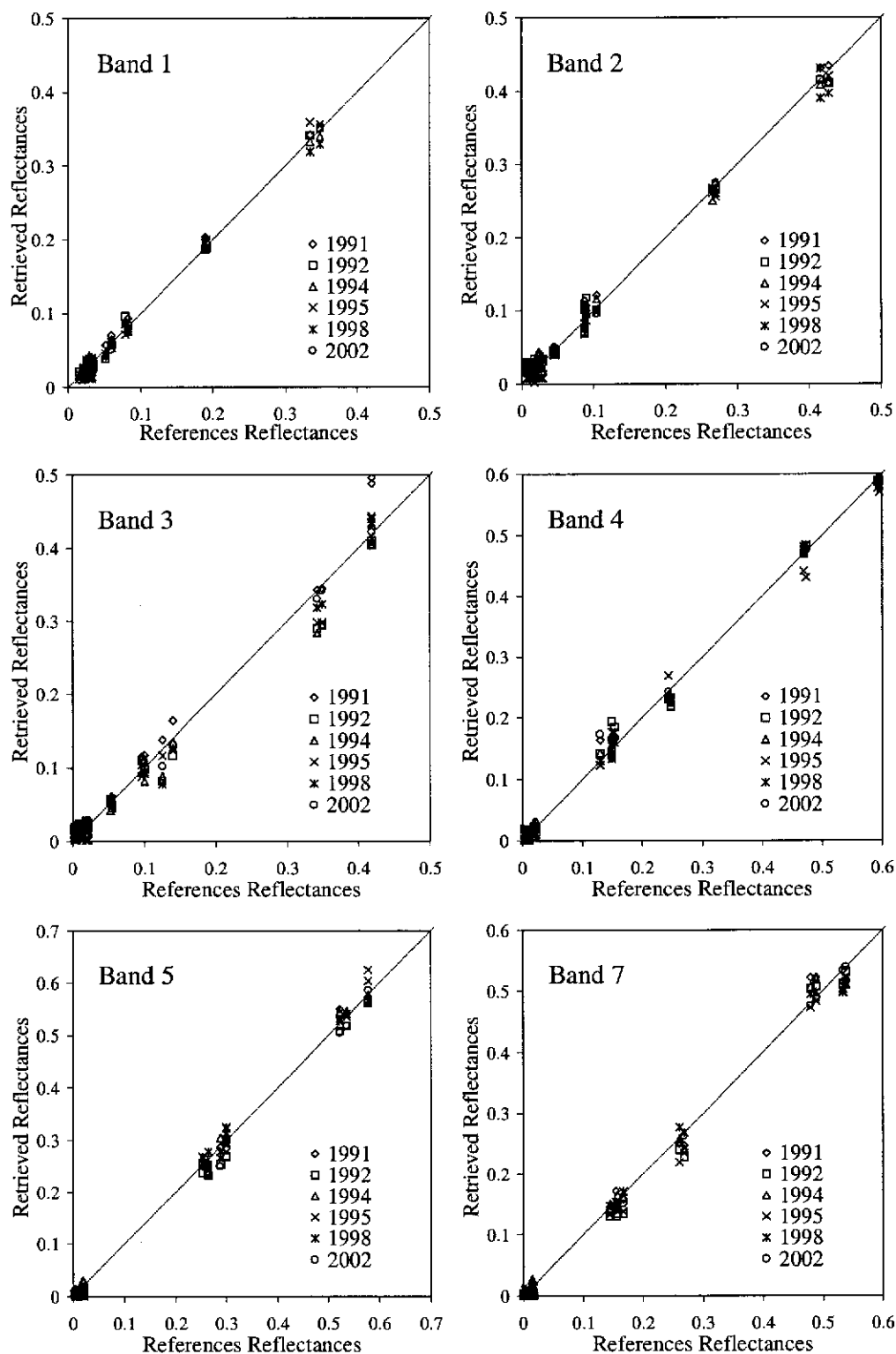


Figure 4.16: Plots of the retrieved ($\rho_{\text{corr}\lambda}$) and reference ($\rho_{s\lambda}$) reflectances for the most temporally-invariant PITs in the Mt. Barker sequence.

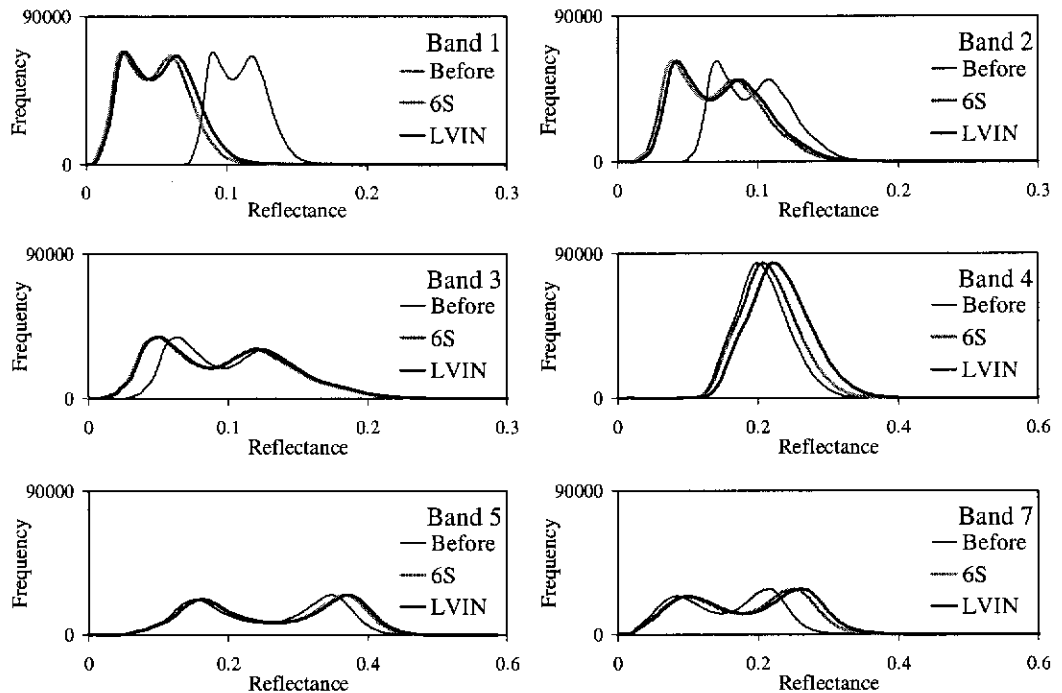


Figure 4.17: Pre- and post-normalisation histograms for the ETM+ image for Mt. Barker, February 11, 2002. The *Before* histograms represent the pre-normalisation reflectances, that is the at-sensor radiances normalised by exo-atmospheric solar irradiances. The *LVIN* histograms represent post-normalisation reflectances retrieved using the LVIN procedure. The histograms of 6S-retrieved reflectances are also displayed (*6S*, light grey lines).

compensation for the multiplicative effect, namely gaseous absorption, for these bands. Similar features are observed in the normalised ETM+ image for Hay acquired on January 7, 2000 (see Appendix G, Figure G.1). Both figures reveal excellent agreement between the LVIN procedure and 6S for the ETM+ image data.

Histograms for the TM overpass images in both Hay and Mt. Barker sequences are presented in Appendix G. Considering, for the moment, the reflectances retrieved using the LVIN procedure, a shift is once again observed in the histogram maxima to lower reflectances for bands 1–3. However, unlike the results for the same ETM+ bands (Figure 4.17), a broadening of the histograms is also observed for the VIS bands. This is most likely due to the LVIN procedure correcting not only for atmospheric effects, but also compensating for the differences in relative spectral responses between TM and ETM+ sensors Teillet et al. (2001). Once again, broadening is observed in the histograms of

Table 4.8: Percentage differences, relative to values used in Section 4.3.3, for $X_{p\lambda}$ modelled with uncertainty in some input parameters.

Changes in ...	Image Sequence	% difference in $X_{p\lambda}$					
		Band 1	2	3	4	5	7
τ_{M550nm}	Hay	± 5.2	± 7.1	± 9.3	± 9.2	± 6.5	± 2.0
Elevation (z)	Mt. Barker	± 1.7	± 1.4	± 1.2	± 0.6	± 0.1	± 0.0
Aerosol Type	Mt. Barker	0.9	0.4	-0.8	-3.4	-6.6	-5.6

bands 4, 5 and 7. Finally, LVIN and 6S histograms differ significantly, particularly in regards to the broadening observed in the VIS bands.

4.3.6 Sensitivity to Uncertainty in Modelling Parameters

Since the constrained LVIN procedure is dependent on modelled path DN , it is reasonable to inquire as to the impact of uncertainty in $X_{p\lambda}$ on the normalisation lines and subsequent surface reflectance estimates. Recall that the modelled path DN presented here were computed from the 6S estimates of path radiance, which were observed to be reasonably insensitive to uncertainty in water vapour, ozone and other gaseous concentrations, as well as to the choice of temperature and pressure profiles. It is also implied in the LVIN procedure that atmospheric properties within the image are spatially homogeneous and, therefore, the calculated values of path radiances are valid over the whole image.

The source of uncertainty with the greatest potential to significantly impact modelled $X_{p\lambda}$ for the Hay overpass images was the aerosol optical thickness. Using the TM image geometry for July 22, 1999 as the worst-case scenario image (because of the low sun elevation and therefore increased path length), the minimum and maximum values of τ_{M550nm} observed by Prata and Rutter (2001)—0.02 and 0.05 respectively—were input to 6S, and then the corresponding values $X_{p\lambda}^{(min)}$ and $X_{p\lambda}^{(max)}$ were calculated. The percentage differences relative to the case where the mid-range value was used (Section 4.3.3) are presented in Table 4.8.

Based on the percentage errors given in Table 4.8, the minimum and maximum path DN were calculated for all the overpass images in the Hay sequence. These values were then used to obtain new LVIN lines and the MADs for the retrieved reflectances were calculated for a relatively bright target ($\rho_{s1} \sim 0.15$) for the three overpass dates: for

bands 1–5 and 7 they were at most 0.0029, 0.0019, 0.0007, 0.0006, 0.0002 and 1×10^{-5} respectively. One can reasonably expect that for dark targets the MADs will be greater because of their proximity to the y -axis (Figure 4.1), where changes in y -intercept would have the most noticeable impact.

Apart from the obvious uncertainty in $\tau_{M\lambda}$ for Mt. Barker, variations in terrain elevation also have the potential to change path radiance values across the scene. Modelled $X_{p\lambda}^{(\min)}$ and $X_{p\lambda}^{(\max)}$ were computed for $z = 0$ m and $z = 370$ m respectively, using the solar-sensor geometry of the ETM+ image acquired over the Mt. Barker scene on February 6, 2000. The average percentage differences relative to the path DN used in Section 4.3.3 are given in Table 4.8. Finally, unlike the Hay scene for which, by virtue of its geographic location, one can reasonably assume the dominance of one aerosol type (in this case, continental), the Mt. Barker scene most likely contains a mix of different aerosols. Specifically, depending on the prevailing meteorological conditions at the time of image acquisition, any given Mt. Barker image most likely contains a mix of continental and maritime aerosols. The percentage difference given in Table 4.8 for aerosol type are to be interpreted as the error incurred if a continental aerosol type is used when a maritime aerosol would be more appropriate.

4.3.7 Discussion: The Like-value Image Normalisation Procedure

The following is a review of the results of the preceding sections, with particular emphasis on the application of the described LVIN procedure to the retrieval of surface reflectances. Some final comments are made with regards to the limitations and impact of the procedure, as well as some suggestions for potential improvements that may form the objective of future investigations.

Reference Images

Ground-based data from the EOC Uardry field campaign of March 27, 2000 and the coincident ETM+ imagery were used in a hybrid of the EL and REL procedures (called the HEL method, Section 4.3.1, pp. 137–141), to produce the reference image for the Hay sequence. The HEL procedure which, like the REL approach, constrained the correction line to pass through the modelled path DN , was found to be useful in *tying down* the regression for the low reflectances, particularly as there were so few surface

reflectance measurements (4 in total). The lack of uniformity in surface cover for the four targets visited contributed to the scatter of points in the HEL scatter plots. Greater consideration of the issues in surface target selection based on spatial homogeneity of cover types, target size and discernability in satellite imagery, and the range in brightness is recommended in future field campaigns if the HEL procedure is used to produce a reference image.

Furthermore, an independent set of reflectance measurements would have been desirable to assess the accuracy of the reflectances retrieved for the reference image. Instead, the accuracy of the resulting reference image could only be assessed by comparing the retrieved reflectances to the measurements of $\rho_{s\lambda}$ used in the HEL method (Figures 4.10 (a) and (b), p. 140).

Generally, however, the HEL procedure achieved the result expected of an atmospheric correction procedure (supported by the 6S results); namely, the removal of the additive path effect in the VIS bands, and the compensation for atmospheric absorption which is dominant in the NIR–SWIR bands. Further investigation of the sensitivity of the HEL procedure to uncertainty in the parameters required to model the path DN is recommended.

Radiosonde measurements were used to aid in selecting atmospheric model parameters suitable for the Mt. Barker ETM+ image acquired on February 6, 2000 (see Section 4.3.1, pp. 141–145 and Appendix C, pp. 226–228). From these data an estimate of precipitable water was calculated and input to 6S, along with tropical pressure and temperature profiles chosen as appropriate for the date that the image was acquired. There were no ground-based optical thickness measurements available for the Mt. Barker reference image. However, an estimate of columnar ozone concentration provided by the Earthprobe TOMS, and a value of $\tau_{M550nm} = 0.05$ with a continental aerosol model were used as input to 6S. The result was a correction line with which the Mt. Barker reference image was created. The accuracy of the reference image was limited to how representative the atmospheric inputs to 6S were of the actual atmospheric conditions at the time of image acquisition, and the degree of within-image atmospheric variability. Errors in surface reflectance retrievals due to difference in elevation alone were found to contribute around 5% over most of the range of reflectance values in the scene (Appendix D, pp. 229–229).

The methods employed in the production of the reference images above are far from perfect. Implicit in these approaches is the assumption that atmospheric properties (e.g. pressure, temperature, optical thicknesses, concentrations) are uniform throughout the scene. Were higher spatial resolution atmospheric data available, alternative approaches to reference image production would have been explored. The methods chosen in this thesis were considered the most appropriate for the limited amount of radiometric processing data available (either directly or vicariously), and it was felt that the results obtained were acceptable for the subsequent analysis.

Modelled Path DN

Path DN , $X_{p\lambda}$, were computed from the 6S-modelled path radiance, $L_{p\lambda}$, and the appropriate radiometric scaling factors for the image data under consideration (Section 4.3.3, pp. 145–147). It was noted that there was uncertainty with regards to the level of product for the Mt. Barker TM image acquired on February 24, 1992 (p. 127). Use of the incorrect scaling factors on an image is likely to have a rather obvious effect on the modelling component of the described LVIN procedure; the retrieved surface reflectances, particularly the low reflectances, will have a large error as a result of the normalisation line being constrained to pass through an incorrect path DN . An appreciation of how significant an impact this uncertainty has on the reflectances retrieved was gained in a comparison of the modelled path DN to the estimates provided by the free-intercept approach (discussed later).

There were two other potential sources of error in the modelled estimates of path radiances. The first, due to the model itself, was based on inherent assumption of the 6S code that the scattering layer in the atmosphere (from which the path radiance emanates) is above the water vapour absorption layer, and consequently uncertainty in water vapour concentration had no impact of the modelled path radiances. A more realistic model would allow for water vapour absorption to impact the path contribution to the at-sensor signal, since aerosols (dominant forward scatterers) also reside in the first few kilometres of the troposphere along with water vapour. The impact of water vapour absorption, therefore, would affect the values of $X_{p\lambda}$ for bands 2–5 and 7 (see for example Figure 3.13, p. 88).

The second source of error in modelled path radiance was due to the uncertainty in in-

put parameters to the 6S code. Estimates of ozone concentration provided by the TOMS instrument were used, where available, otherwise model atmosphere concentrations were used. The uncertainty due to absolute accuracy of the TOMS-derived estimates of u_{O_3} ($\sim 3\%$) has negligible effect on the values of $X_{p\lambda}$ ($< \pm 0.5 \text{ DN}$) for the VIS bands (which are most affected by ozone absorption). The choice of model pressure and temperature profiles, which have an impact on gaseous transmittance, were observed to have a similar negligible impact.

Sensitivity analysis was conducted on those input parameters that were believed to have a more significant impact on the error in modelled path DN for the overpass images (Section 4.3.6, pp. 157–158). These parameters were aerosol optical thickness, terrain elevation and aerosol type. As there were no *in situ* or remotely-sensed estimates of aerosol optical thickness, the inputs to 6S were $\tau_{M550nm} = 0.035$ for Hay images, and $\tau_{M550nm} = 0.05$ for Mt. Barker images. Based on the findings of Prata and Rutter (2001), the errors that result if a mid-range value for τ_{M550nm} was assumed (Table 4.8, p. 157) are observed to be most significant for band 3 ($\sim 9\%$); an error corresponding to about $\pm 1 \text{ DN}$ for the typical estimates of $X_{p\lambda}$ in that band. The error for band 1 was $\sim 5\%$, or $\pm 3 \text{ DN}$, for the typical values of $X_{p\lambda}$ in that band. Errors of this magnitude are small compared to the uncertainty in regression estimate of $X_{p\lambda}$ (Figure 4.15, p. 152). Furthermore, in a sensitivity test similar to that conducted by Moran et al. (2001), the impact of these errors on surface reflectance retrieval for a relatively bright target was shown to be very small ($MAD \sim 0.003$ for band 1).

Variations in terrain elevation were considered to have the potential for most significantly impacting Mt. Barker images, since 95% of terrain in the standard scene is between 20–370 m above sea level. The errors incurred if the elevation $z = 200 \text{ m}$ (the median value) was assumed for the whole scene introduced at most a $\pm 2\%$ error in band 1 (the error decreasing with increasing band number to $\sim 0\%$ in band 7). Since this error is smaller than that due to uncertainty in aerosol optical thickness (previous paragraph), it is speculated that terrain elevation has negligible impact on surface reflectance retrieval over most of the Mt. Barker scene; the exception being the remaining 5% of the scene, such as the Stirling Ranges where elevations $> 900 \text{ m}$ may be observed.

For Hay it was assumed that, because of the geographic location of the scene (Figure 4.2, p. 126), the dominant aerosol type present for all dates is best characterised as

continental. Furthermore, in the absence of any extreme events, such as large fires or an increase in industrial activity, this is a reasonable assumption to make. A continental aerosol type was also assumed for the Mt. Barker scene; even though one might reasonably expect that, because of the geographic location, a mix of aerosol (probably marine, urban and continental) would be more realistic. If a marine aerosol type was more appropriate, it was shown that modelled $X_{p\lambda}$ would underestimate the ‘true’ path DN by approximately 3, 7 and 6% for band 4, 5 and 7 respectively. These errors correspond to at most 0.3 DN for the typical values of path DN for these bands.

It was concluded from the above that, for the limited range of data in this work, modelled $X_{p\lambda}$ were relatively insensitive to uncertainty in atmospheric parameters. Once again, lack of validation data hampered efforts for a more thorough investigation of the uncertainty in model path DN .

Like-value Normalisation

Normalisation plots for the like-value procedure were constructed from the DN s of a set of PITs (Section 4.3.2, p. 145) and their corresponding reflectances from the reference image (Appendix E, Figures E.1–E.9, pp. 234–242). Systematic searches by visual inspection of the Hay imagery, displayed in RGB:3,2,1, provided 15 PITs. From these, single-pixel data ($\rho_{s\lambda}$, X_λ) were extracted; thus, Hay normalisation plots contained 15 data points. The 30 PITs used in Mt. Barker sequence, obtained through expert knowledge of the geographic location of suitable targets in the scene, were inherited from the Land Monitor project. Since neighbourhoods of pixels were used, Mt. Barker normalisation plots contained data points from 120 pixels.

For the data in the normalisation plots, departures from colinearity may be attributed to either: PIT misregistration, variability of atmospheric properties above each PIT, the PITs having non-Lambertian reflectance properties, or the PIT’s surface reflectance not being as temporally invariant as desired. For the Hay sequence data, the scatter of points about the calculated regression lines was observed to be greatest for bands 4, 5 and 7 compared to the VIS bands, and more in bands 5 and 7 than in band 4. This observation is consistent with the findings of findings of Schott et al. (1988), Hall et al. (1991), and Furby and Campbell (2001). Since the dynamic range of the image data is greatest in the band 4, 5 and 7 (see Histograms, Figures G.1–G.8), one can expect that

subtle variations in surface reflectance in these bands may be amplified relative to the VIS bands.

Robust regression is preferred (Furby and Campbell, 2001) to minimise the influence of PITs affected by the factors mentioned in the previous paragraph on the normalisation line. In this work, the robust M-estimator was employed to yield the estimates of intercept and slope (i.e., the normalisation offset and gain respectively) that defined the normalisation lines. The improved M-estimator in the S-PLUS software (Venables and Ripley, 1999) procedure begins with an estimate of the regression coefficients provided by the S-estimator (Furby and Campbell, 2001). If the test for bias fails, the original S estimates of slope and intercept are returned.

Surface Reflectance Retrievals

A comparative analysis (Appendix F, pp. 243–248) was conducted on surface reflectances retrieved using the LVIN procedure employing either the free-intercept regression or the constrained regression approaches (Section 4.1.2, pp. 121–126). Significant disagreement between the two approaches was observed, particularly for low reflectances ($< \sim 0.1$) which constitutes a large portion of the range of reflectances in VIS bands. The differences observed between the two approaches may be attributed to the free-intercept estimates of y -intercept differing from the modelled values of path DN . The scatter of normalisation data points impacts where the regression line meets the y -axis: if too few data points contribute to the regression line, significant discrepancy will be observed between modelled $X_{p\lambda}$ and y -intercept. In the analysis, the discrepancy was observed to be more prevalent in the Hay sequence than in the Mt. Barker sequence; most likely because of the comparatively small number of points in the Hay normalisation plots than in the Mt. Barker plots.

Nevertheless, the modelled path DN s were generally contained within the 95% confidence limits of the free-intercept regression estimates (Figure 4.15, p. 152). This finding implied that statistically there was no reason to reject the hypothesis that the *true* normalisation line passed through the modelled value. Constraining the regression fit to pass through the modelled path DN also has the advantage of circumventing the difficulties often associated with image-derived estimates of path radiance, particularly in areas where no (or too few) dark features exist.

The constrained regression application of the LVIN procedure was used to retrieve surface reflectances for each overpass image in both multitemporal sequences (even though the Mt. Barker sequence had sufficient numbers of dark PITs). A comparison of histograms of retrieved reflectances and those uncorrected, at-sensor reflectances for a subset of the ETM+ image data (see Figure G.1, p. 250 and Figure 4.17, p. 156) revealed that the LVIN procedure had an impact expected of an atmospheric correction procedure. When the overpass and reference images were acquired with the same sensor (in this case the ETM+), adjustments for any differences in the sensor's response through time were assumed to be small compared to the corrections required for solar position and atmospheric effects. In agreement with the at-sensor signal modelling, the additive contribution of the atmosphere (the path radiance) was removed (the amount removed decreased with increasing band number) from ETM+ bands 1–3; evident by the shift in histograms to lower reflectances post-normalisation. Furthermore, the reduction of intensity of sensor-measured signal due to gaseous absorption in band 4, 5 and 7 (and thus, compression of the dynamic range of data in these bands) has been removed; evident by the broadening of the histograms post-normalisation. It may therefore be concluded that the application of the LVIN procedure removes the influence of atmospheric effects from image data acquired with the same sensor as the reference. Furthermore, the agreement with the 6S correction results further supports this claim.

Similarly, a comparison of the pre- and post-normalisation histograms for the TM images in the Hay and Mt. Barker sequences, revealed not only a general shift towards a lower reflectance range post normalisation for bands 1–3, but a broadening of the histograms as well. From the comparison of histograms produced via the 6S and LVIN procedures (Figures G.2–G.8, pp. 250–253), it was observed that the LVIN procedure compensated for the differences in TM and ETM+ sensor responses.

The lack of validation data meant that only the precision of the procedure could be assessed in a comparison between the retrieved reflectances and those of the same targets in the reference images. Errors in retrieval are attributed to the scatter of the PITs about the normalisation line (the causes for the scatter were described earlier). Using the standards set by Moran et al. (1992) as a guide, the MADs and RMS errors were calculated for a subset of PITs in both sequences. For the Hay images, reflectance retrievals in bands 1–3 were very good (within < 0.016 reflectance units, corresponding to

15% for dark PITs) but considerably poorer in bands 4, 5 and 7 (errors up to 86% for dark PITs). The RMS error calculated for the first three bands was 0.011, whilst the value calculated across all bands was 0.063. The increased scatter in the infrared bands and the relatively small number of pixels (15 pixels) used in the Hay sequence normalisation, meant that only a small number of points fell on, or close to, the fitted lines. One can assert that increasing the number of pixels contributing to the regression process—by considering neighbourhoods rather than single pixel data—will greatly improve the MAD results in the infrared bands. This was observed in the MADs calculated for Mt. Barker (120 points) sequence. The MADs calculated were all < 0.01 across all bands, with an RMS error = 0.012 (Figure 4.16, p. 155). Overall, using the criteria of Moran et al. (1992) and Gilabert et al. (1994), retrieved reflectances were within the limits deemed acceptable for most practical applications.

Final Remarks on Limitations and Future Work

The two most often criticised assumptions on which the LVIN and similar image normalisation procedures are based are that: the estimated normalisation offsets and gains are applicable to the entire satellite scene; and a linear adjustment to the image's DN s is adequate for the retrieval of surface reflectances. On the former point, with the exception of localised haze events, smoke plumes, frontal systems or severe weather phenomena, spatial heterogeneity of atmospheric properties will contribute marginally to the scatter of points in LVIN plots when compared to variations in surface cover. On the latter point, there are a number of physical arguments proposed as to why a non-linear correction of image data is required. If the simplified RTE given in Eq. (4.1) represents a reasonable approximation of the at-sensor signal, then the very nature of the expression demands that the adjustment assumes a non-linear form. Also the linearity assumption becomes invalid for large field-of-view sensors because of the increased path length (and thus, optical thickness) at the large zenith angles. Many authors argue (Schott et al., 1988; Hall et al., 1991; Gilabert et al., 1994; Chavez, 1996; Roberts et al., 1997; Moran et al., 2001; Furby and Campbell, 2001) that when optical thicknesses are small (and/or the sensor field of view small), a linear fit (truncation of Eq. (4.3) to first order) is a sufficient approximation. In this investigation, the scatter of points in the LVIN plots would have obscured any non-linear behaviour of DN with $\rho_{s\lambda}$, thus no attempt was

made to investigate anything other than a linear fit to the normalisation data.

The LVIN procedure may breakdown when applied to image data with higher than 8-bit quantisation; for example, imagery such as AVHRR with 10-bit quantisation or the 16 bits for MODIS imagery. Subtle variations in surface reflectance (for the PITs) and uncertainty in model parameters may be amplified in the greater dynamic range of the data. An additional complicating factor relates to the pixel size of aforementioned sensors; very few targets with dimensions $\sim 250 \times 250 \text{ m}^2$ (let alone 1 km^2) possess reflectance properties that are temporally invariant.

Incorporating the model path DN into the LVIN procedure was suggested as a means of circumventing any difficulties associated with finding sufficiently dark PITs. The results in this chapter have focussed on a LVIN procedure that constrains the regression line to pass through the point $(0, X_{p\lambda})$. This was observed to be useful particularly when the scatter of points meant that the free-intercept approach would have incorrectly estimated the contribution of the path radiance. Future investigation may consider a scheme whereby, instead of constraining the fit to pass through the model path DN , the point is assigned a weighting factor based on the uncertainty of the calculated $X_{p\lambda}$. This approach would be desirable when there are dark targets present in a scene and, because of uncertainty in inputs to 6S (say), one wishes to down-weight the influence of the path DN and allow the image data to dominate the determination of the best fit line.

The suitability of radiometric processing procedures that rely on atmospheric model inputs are often debated since the required parameters are typically unknown and the selection of simulated atmospheric model values is clearly a less favourable alternative to *in situ* knowledge on the day concerned. It is noted, however, that current and future developments in remote sensing technologies may provide accurate estimates of some of the required input atmospheric data. Routine estimates of aerosol optical thickness and column water vapour concentration are provided by MODIS globally every 2 days; TOMS provides daily estimates of total ozone concentration; and the geostationary GIFTS promises radiosonde-quality soundings of atmospheric pressure, temperature and water vapour concentration at unparalleled spatial and temporal scales.

4.4 Application: Change in NDVI for Mt. Barker Vegetation

One of the most important applications of satellite remote sensing of the terrestrial environment has been the mapping and monitoring of vegetation cover. Of the variety of land cover types, vegetation plays many vital roles in the lives of the Earth's inhabitants: vegetation converts carbon dioxide into oxygen via the process of photosynthesis, and water vapour via transpiration; vegetation is consumed as a food source; vegetation is used as a home or shelter for many of the Earth's inhabitants; and vegetation is used in many products to service the needs of humankind, such as housing material, furniture, fuel for heating and combustion to generate energy. Consequently, there has been widespread interest in the capabilities of remote sensing technologies to provide assessments of inter-annual and longer-term vegetation change, resulting from either natural or anthropogenic causes. Specifically, much attention has focussed on the development of *spectral vegetation indices* (or just vegetation indices) derived from multispectral image data to enhance and highlight vegetated features within a satellite scene.

This section begins with a description of some vegetation indices. The impact of the LVIN procedure on calculated values of the popular normalised difference vegetation index (NDVI, more in Section 4.4.1) is presented. The section ends with some discussion on the effect of image normalisation, via the LVIN procedure, on vegetation change detection and monitoring.

4.4.1 Some Spectral Vegetation Indices

Tucker (1979) used ground-based spectral measurements of vegetated targets to investigate the correlation between a number of *vegetation indices*, derived from combinations of the spectral bands in the green, red and NIR regions of the EM spectrum, and six 'canopy variables' (namely, total wet and dry biomass, dry green and brown biomass, leaf water content, and total chlorophyll content). Two key findings of the investigations were that (i) indices based on a combinations of red and NIR bands were superior to the green-red band combinations in terms of their correlation with the six canopy variables; and (ii) indices using the red and NIR bands were sensitive to photosynthetically active vegetation, and thus chlorophyll content. These red-NIR band combinations are

also known as *greenness indices* since the higher chlorophyll content, the more green pigments in the plant and, consequently, the more red (and for that matter, blue) EM radiation is absorbed. They have also been used in the assessment of plant health; a plant under stress absorbs less red EM radiation when compared to a healthy plant because of the lower concentrations of chlorophyll present in the unhealthy plant. Furthermore, the NIR band is useful because no matter what the condition of the plant, it will reflect stronger in the NIR than in the VIS bands because of multiple scattering in leaf and canopy layers (Kumar et al., 2001).

A popular greenness index often used in satellite remote sensing is the *normalised difference vegetation index* (NDVI). The NDVI is related to the amount of chlorophyll present in leaves of (healthy⁹) vegetation. Furthermore, for healthy vegetation, NDVI can be related to the amount of vegetation in the IFOV of a satellite sensor. High NDVI values are associated with areas of higher projected leaf area, whilst lower values correspond to low leaf area. In other word, NDVI may be used as indicator of vegetation canopy density.

It is computed as the difference of the NIR and red band reflectances divided by the sum of reflectances for those same bands. For Landsat TM and ETM+ sensors, NDVI is calculated from the at-sensor reflectances as,

$$\text{NDVI} = \frac{\rho_{\text{sat4}}^* - \rho_{\text{sat3}}^*}{\rho_{\text{sat4}}^* + \rho_{\text{sat3}}^*}, \quad (4.6)$$

where ρ_{sat3}^* and ρ_{sat4}^* are obtained from TM and ETM+ bands 3 and 4 via Eq. (3.3, p. 57) and are not corrected for atmospheric effects. If the image data are corrected for changes in sensor calibration, solar position and atmospheric effects, then the NDVI may be calculated as,

$$\text{NDVI}^{(\text{CORR})} = \frac{\rho_{\text{corr4}} - \rho_{\text{corr3}}}{\rho_{\text{corr4}} + \rho_{\text{corr3}}}, \quad (4.7)$$

where ρ_{corr3} and ρ_{corr4} are estimated values of surface reflectance (from the LVIN procedure, for example). Other indices (based on the NDVI) have been proposed that are designed to enhance the vegetation component to the data whilst minimising the potential problems of using uncalibrated/uncorrected image data, and some of these are briefly described in the following.

⁹Low chlorophyll content in leaves is a symptom of a stressed, or unhealthy, plant. The lower chlorophyll content means less red light is absorbed; leading to a yellowing of the leaves—a condition known as chlorosis—and consequently a lower calculated value for NDVI.

Huete (1988) proposed the Soil-Adjusted Vegetation Index (SAVI) to minimise the impact of soil reflectance on the at-sensor signal when vegetation is sparse or the canopy cover is less dense. The expression used to calculate the SAVI differs from that of the NDVI by a constant C , introduced to account for first-order soil-vegetation interactions and the absorption of red and NIR radiation by the canopy (Huete, 1988). The SAVI is calculated as,

$$\text{SAVI} = (1 + C) \frac{\rho_{\text{sat}4}^* - \rho_{\text{sat}3}^*}{\rho_{\text{sat}4}^* + \rho_{\text{sat}3}^* + C}. \quad (4.8)$$

Recommended values of C range from 0.25, when vegetation densities are high, to 1, when vegetation densities are low. Most papers (Kaufman and Tanré, 1992; Miura et al., 2001; Karnieli et al., 2001, for example) choose $C = 0.5$, which is the suggested value for semi-vegetated areas.

Many authors have noted the importance of correcting for atmospheric effects in image-derived vegetation indices (Paltridge and Mitchell, 1990; Kaufman and Tanré, 1996b; Miura et al., 2001, to name a few). A vegetated target's actual surface reflectance (e.g. measured *in situ*) is typically low in the red band, i.e. $\rho_{\text{s}3} < 0.1$, but higher in the NIR, $\rho_{\text{s}4} > 0.15$ (Kaufman and Tanré, 1992). Path radiance, atmospheric scattering and absorption effects, however, modify the surface-reflected solar radiation and result in at-sensor reflectances for TM/ETM+ bands 3 and 4 such that, $\rho_{\text{sat}3}^* > \rho_{\text{s}3}$ and $\rho_{\text{sat}4}^* < \rho_{\text{s}4}$. For a given vegetated target, therefore, it follows that changes in molecular and aerosol optical thickness through time will impact calculated values of NDVI (i.e. Eq. (4.6)) for the target. Kaufman and Tanré (1992) noted that the NIR band will be more affected by uncertainty in aerosol phase function and single scattering albedo (i.e. aerosol type) rather than aerosol concentration (optical thickness). Furthermore, the fact that optical thicknesses (total, molecular and aerosol) all decrease in magnitude with increasing wavelength, atmospheric effects are more noticeable in the red band than the NIR.

Kaufman and Tanré (1992) proposed an Atmospherically Resistant Vegetation Index (ARVI) where *atmospherically resistant* refers to the ARVI's insensitivity to changes in atmospheric optical thickness when compared to the NDVI. In addition to the red and NIR bands, the ARVI incorporates the blue band (TM/ETM+ band 1) in a 'self-correcting' index, namely,

$$\text{ARVI} = \frac{\rho_{\text{sat}4}^* - \rho_{\text{sat}3}^* + \gamma(\rho_{\text{sat}3}^* - \rho_{\text{sat}1}^*)}{\rho_{\text{sat}4}^* + \rho_{\text{sat}3}^* - \gamma(\rho_{\text{sat}3}^* - \rho_{\text{sat}1}^*)}, \quad (4.9)$$

where $\rho_{\text{sat}1}^*$ is the at-sensor reflectance for the blue band and γ is a constant. Based on 5S simulations of several surface covers, and for a range of optical thicknesses, Kaufman and Tanré (1992) showed that a value of $\gamma = 1$ gave an ARVI that was 4 times less sensitive to atmospheric optical thickness than the NDVI. (Note that the ARVI becomes the NDVI when $\gamma = 0$.)

Another vegetation index that aims to be resistant to atmospheric effects, specifically the influence of aerosols, is the Aerosol Free vegetation Index (AFRI) developed by Karnieli et al. (2001). The AFRI utilises the fact that aerosols are essentially transparent to radiation in the SWIR band (TM/ETM+ band 7), and the empirical vegetation reflectance result (Table 3.7, p. 107),

$$\rho_{\text{s}3} \approx 0.5 \rho_{\text{sat}7}^*,$$

where $\rho_{\text{sat}7}^*$ is the at-sensor reflectance in the TM/ETM+ band 7, which is assumed to be free of aerosol effects. In the case of TM or ETM+ image data, the AFRI is calculated by substituting the above expression into Eq. (4.6) to yield,

$$\text{AFRI} = \frac{\rho_{\text{sat}4}^* - 0.5\rho_{\text{sat}7}^*}{\rho_{\text{sat}4}^* + 0.5\rho_{\text{sat}7}^*}. \quad (4.10)$$

4.4.2 Mt. Barker Vegetation Data

The application of vegetation indices to satellite image data to monitor vegetation through time will be demonstrated using the Mt. Barker sequence (Table 4.1, p. 127). This multitemporal sequence was chosen because of the author's familiarity with much of the clearing of native vegetation and establishment of new plantations in the region through his involvement with the Land Monitor project (Caccetta et al., 2000a,b).

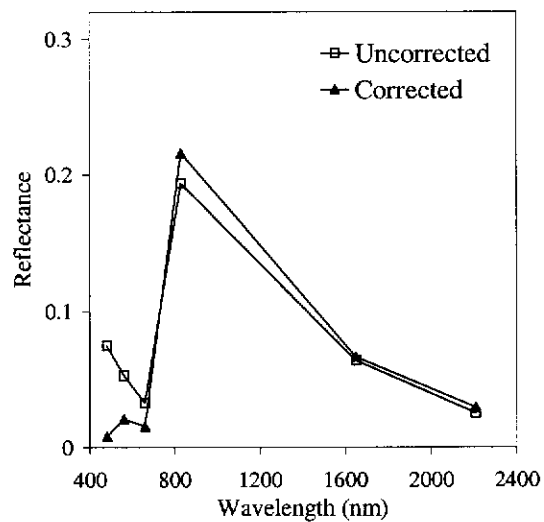
In this section, and in the following figures, reference will be made to *uncorrected* and *corrected* image data. Uncorrected reflectances refer to image data that has been converted into at-sensor reflectances; these data have not been corrected for atmospheric effects or between-sensor differences. Corrected reflectances correspond to image data that have been processed with the LVIN procedure to yield estimates of surface reflectance. Terminology for the NDVI, therefore, will be *uncorrected NDVI*, corresponding to those computed from uncorrected reflectances (Eq. (4.6)), and *corrected NDVI*, computed from corrected reflectances (Eq. (4.7)).

Corrected Vs. Uncorrected Image Data

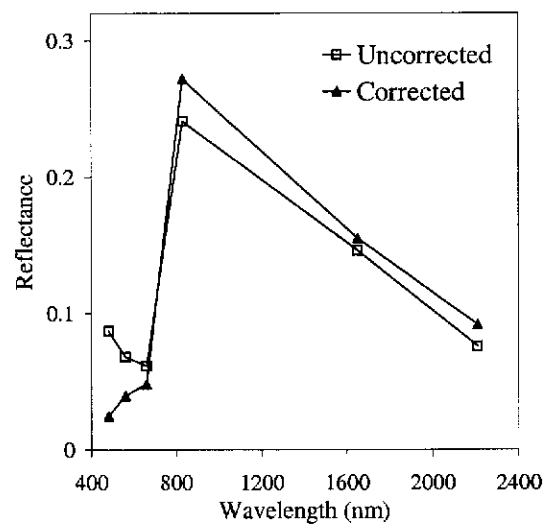
Figure 4.18 illustrates the difference between corrected and uncorrected reflectances for two vegetated pixels in the ETM+ image for Mt. Barker, February 11, 2002. It is clear from the comparison of uncorrected and corrected data, that atmospheric effects (i.e. the additive effects in the VIS bands and the multiplicative effects of atmospheric absorption in the NIR-SWIR bands) have been removed by the LVIN procedure. To describe the difference in general shape of the two corrected reflectance spectra, it is important to first understand some of the characteristics of the vegetation under investigation.

Both Figures 4.18 (a) and (b) display the reflectance spectra for a pixel located in two different Blue Gum (*eucalyptus globulus*) plantations. Figure 4.18(a) is a blue gum pixel in a plantation known as the Hambley Tree Farm, 2 km east of the Mt. Barker townsite on Oatland Road, established in 1996 by Integrated Tree Cropping Inc. Figure 4.18(b) is a pixel from a large (1107 ha) plantation of blue gums known as the Springwell Tree Farm, 20 km southeast of the Mt. Barker townsite, established in 1999 by Timbercorp Inc. Blue gums are extensively planted throughout the Mt. Barker scene (in fact, in many parts of southwest Western Australia) and are used for wood chips, pulpwood and salinity control (Marcar et al., 1995).

On the date that the ETM+ image was acquired (February 11, 2002) the Hambley plantation was about 6 years old, and the blue gums were nearing full maturity: that is, approximately 12 m tall; having compact crowns 4–5 metres in diameter; their branches retained to half the trunk height; and with drooping sickle-shaped leaves, a dark glossy green in colour. Juvenile blue gums, on the other hand, have ovate, greyish-blue leaves, covered with a powdery white substance. Common practice in many tree farms is to plant the blue gums in rows separated by about 3–4 metres. Thus, at the time that the ETM+ image was acquired, the blue gums in the Springwell plantation were about 3 years old: approximately 5 m tall; and, since canopy closure occurs between 2–4 years, a considerable amount of the at-sensor signal may be attributed to the sand on which the plantation is located. The difference between the two corrected reflectance spectra, may therefore be attributed to the difference in age of the two plantations and the implications for land cover and leaf and canopy reflectance. Specifically, the lighter-coloured leaves in the younger blue gums explains why the VIS reflectances are higher in Figure 4.18(b)



(a)



(b)

Figure 4.18: The difference between *uncorrected* and *corrected* reflectances illustrated with blue gum (*E. globulus*) spectra from (a) a 6-yearold plantation and (b) a 3-yearold plantation.

than in (a), and the influence of the sand explains why the reflectance in the red and NIR-SWIR bands are higher in (b) than in (a).

Figure 4.18 also illustrates that the difference between the NIR reflectances and those of the red band has increased after the LVIN procedure was applied. This suggests that NDVI calculated using corrected reflectances (Eq. (4.7)) will be higher than those calculated from uncorrected reflectances (Eq. (4.6)) for the same target. In fact, from Figures 4.18(a) and (b) the uncorrected NDVI are 0.70 and 0.59 respectively, whereas the corrected NDVI for the same figures are 0.86 and 0.70 respectively.

Equations (4.6) and (4.7) were applied to a 2048×2048 subset of the Mt. Barker scene. Histograms of the corrected and uncorrected NDVI for each date in the sequence are presented in Figure 4.19. As expected, the histograms generally move toward the higher NDVI range after image data are converted to surface reflectances. A broadening of the histograms is also observable; a result due to the multiplicative correction of the NIR reflectances by the LVIN procedure. The observed behaviour in the histograms is consistent with the observations of Kaufman and Tanré (1996b).

The maxima observed at the low NDVI end of the histogram are attributed to the non-vegetated pixels in the image. Note that considerably more greenery is present in the Mt. Barker 2000 and 2002 images. This is due to grasses sprouting as a result of an un-seasonally wet summer (2000) and recent rainfall events (2002) for the area. The histograms for these dates are consequently flatter because the peaks corresponding to the non-vegetated pixels are heavily suppressed compared to the histograms for the other dates in the sequence.

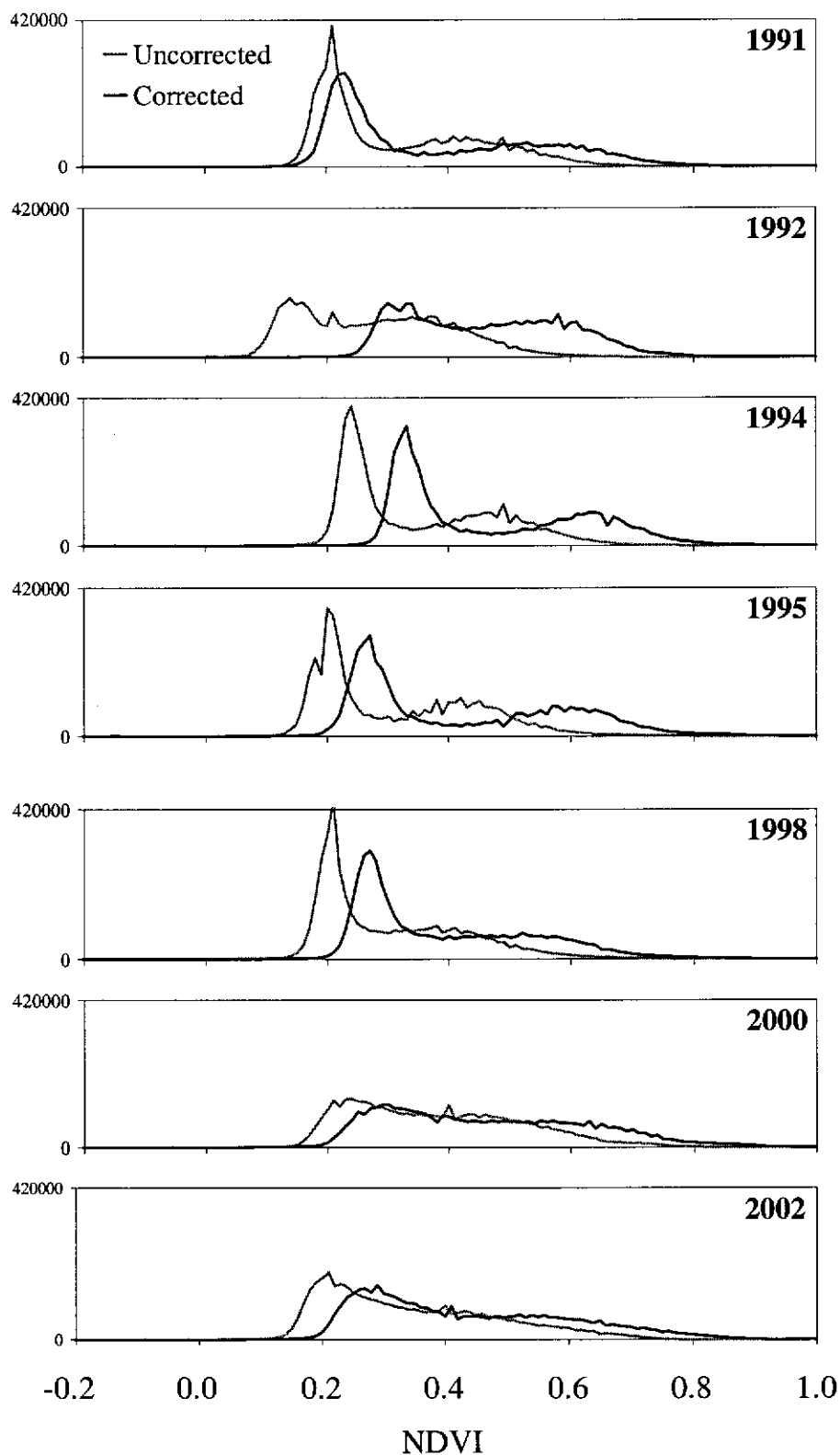


Figure 4.19: NDVI histograms for a 2048 × 2048 subset of Mt. Barker scene over all dates in the sequence. The terms uncorrected and corrected NDVI are defined in Section 4.4.2.

NDVI Time Series

The following addresses how the NDVI may be used to monitor change in vegetation through time, and describes the differences that result from the use of uncorrected and corrected NDVI.

NDVI time series were constructed for selected areas within the Mt. Barker scene where there have been observable changes in vegetation cover for some of the dates in the sequence. The vegetation change considered were related to surface cover, such as: vegetation loss, as a result of clearing or through natural occurrences such as flooding or fire; vegetation gain through either re-vegetation (i.e. the establishment of new plantations) or recovery after vegetation loss; and a combination of loss and recovery.

The Figures 4.20–4.24 are constructed as follows: At the top of each figure there are 3 small subsets of the imagery, displayed in RGB:5,4,2, for dates at the start (1991), middle (1995), and end (2002) of the Mt. Barker sequence. There is an NDVI time series at the bottom of the page constructed from the mean uncorrected and corrected NDVI values (calculated via Eqs. (4.6) and (4.7) respectively) for a neighbourhood of pixels, highlighted in the RGB imagery as red polygons. The error bars in the time series mark 2 standard deviations about the mean NDVI value. Recall, also, that the ETM+ image acquired in 2000 was chosen as the reference image and was processed to surface reflectances differently from the other dates in the sequence.

To begin, an area where no detectable vegetation change has occurred for any date in the Mt. Barker sequence (supported by the Land Monitor project) is presented in Figure 4.20. The area displayed by red polygon, centred on (E 117°39', S 34°38'), is perennial vegetation on the outskirts of the Mt. Barker townsite. The uncorrected NDVI for the TM February 24, 1992 image is observed to be out of alignment (underestimated) with the other dates in the sequence. This disagreement was not observed in the corrected NDVI series, which reveals a consistently high NDVI value (average of 0.73) through time with each date within 2 standard deviations of each other.

The location of the Hambley blue gum plantation is displayed in Figure 4.21. The red polygon is centred on (E 117°42', S 34°38'). It can be observed that prior to the plantation's establishment in 1996 the NDVI values are low, indicating that no significant vegetation is present until after that date. The Figure illustrates a relatively recent

example of vegetation gain. The time series shows a transition from a non-vegetated area, then the highly probable presence of vegetation in 1998, and finally the emergence of vegetation of sufficient density that it was detectable in the imagery for 2000–2002. Once again the uncorrected NDVI is shown to give an erroneously low value for the 1992 imagery which once corrected is more consistent with the time series between 1991 and 1994. The dip in the both NDVI time series around 1995 may be attributable to plantation management practices, where the area is cleared or plowed of grasses and shrubs prior to planting.

It is important to note that vegetation must attain a certain level of canopy density in order to be detected in a TM/ETM+ pixel. There is, therefore, a temporal lag from when vegetation is planted (or begins to re-grow) to when it is observed in satellite imagery. As the vegetation matures, the canopies become fuller and the calculated NDVI value increases. When canopies have attained certain density, NDVI values calculated through time will begin to level off, or *saturate*, independent of any increase in biomass of the understorey (Tucker, 1979).

Figure 4.22 is another illustration of vegetation gain. The red polygon, centred on (E 117°59', S 34°43'), is within an area which is a large eucalypt plantation, 3 km east of the Porongurup National Park (south of the Stirling Range National Park). This plantation was established after the acquisition of the TM image in 1991; very probably the same year because the time series of calculated NDVI shows significant vegetation growth for the area by 1992. From the 1995 image through to the last date of the sequence, the NDVI remains stable (around 0.85 for the corrected NDVI). This quite rapid NDVI saturation is consistent with the observations made for Figure 4.21.

Vegetation loss is illustrated in Figure 4.23. In this instance, vegetation was lost due to flooding. In fact, the dark blue area around the red polygon (E 117°43', S 34°27') is a swamp, just west of the Stirling Ranges, which is known to be subject to intermittent flooding (similar flooding is observed in the 2000 data). Water targets have low, often negative, NDVI values (negative if uncorrected NDVI is calculated).

Figure 4.24 illustrates vegetation loss due to clearing. The area investigated (enclosed in a red polygon) is centred on (E 117°52', S 34°45'). The time series reveals that clearing occurred in 1994 after the acquisition of the imagery. Note that in NDVI time series clearing events are characterised by a sharp transition from high to low NDVI values.

In both the plots of vegetation loss, the uncorrected NDVI for 1992 appears to be lower than the NDVI of its neighbours in the series. This has been adjusted in the corrected NDVI data.

Figures 4.25 and 4.26 are examples of regions in the Mt. Barker scene which have undergone a combination of vegetation gain and loss throughout the time series. Figure 4.25 corresponds to the location of the Springwell blue gum plantation, established in 1999. What is observed is an area of native vegetation which was cleared sometime after the acquisition of the image in 1992 (but prior to 1995), and then the emergence and maturation of the blue gum plantation over the period 1998-2002. The plantation was obviously not of sufficient vegetation density (for reasons explained on page 171) to have reached its maximum NDVI value (i.e. saturated) in the 2000 image data. Figure 4.26 illustrates vegetation gain and then a loss after the 2000 image was acquired. The area displayed is a small patch of native vegetation south of the Mt. Barker townsite. The large error bars (relative to the other time series) are a result of the variety of different cover types (and therefore reflectances) in the area of native vegetation.

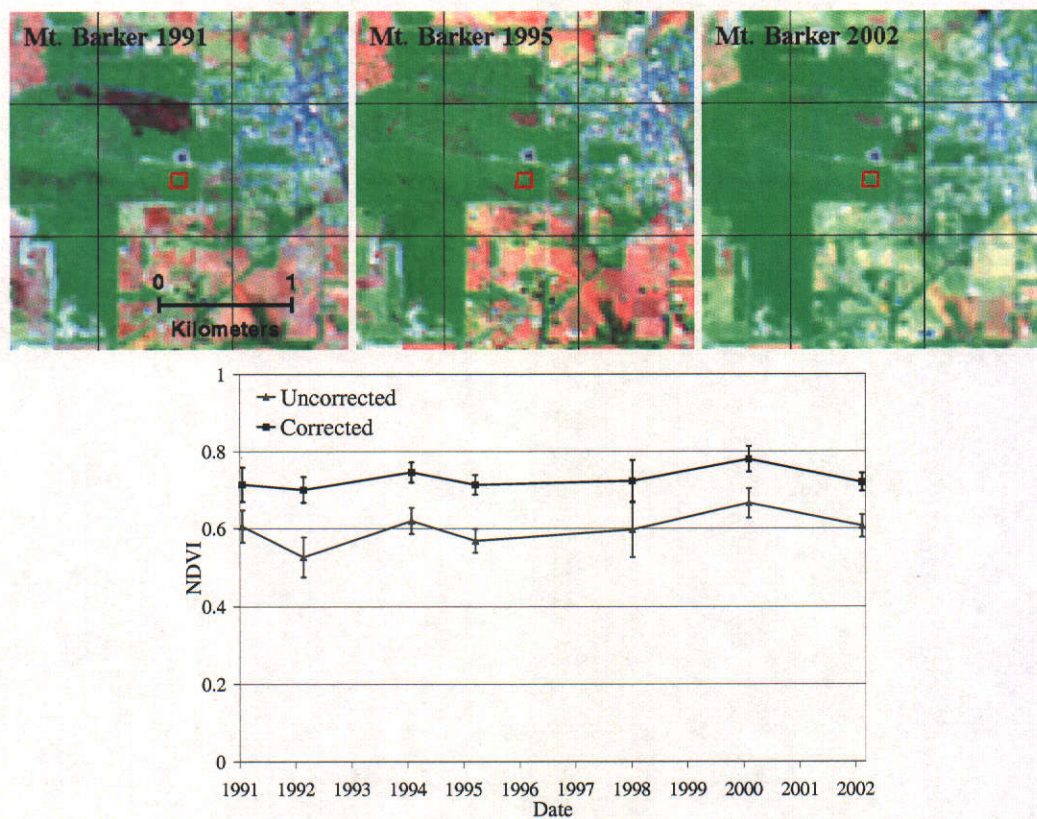


Figure 4.20: Imagery for an area of perennial vegetation in the Mt. Barker scene for three selected years from 1991–2002. The time series of corrected NDVI (black line) calculated for the region highlighted by the red polygon (centred on E 117°39', S 34°38') shows no significant loss or gain of vegetation, whereas the uncorrected NDVI series (grey line) shows variation.

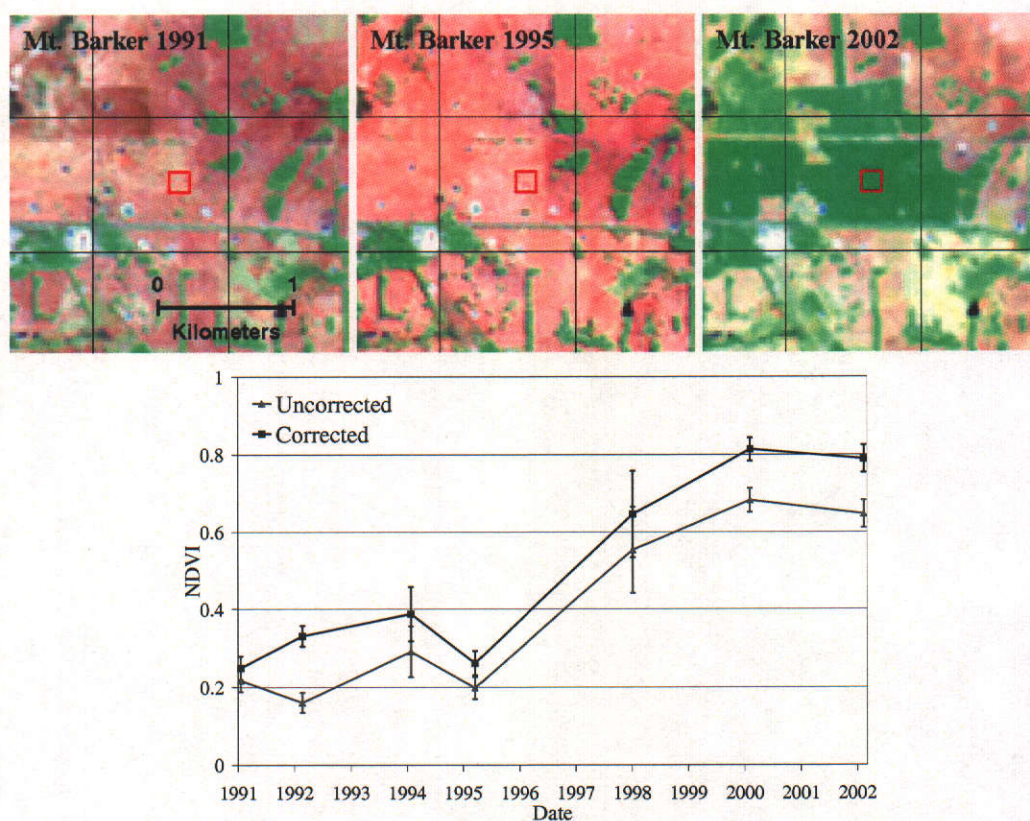


Figure 4.21: Imagery illustrating the emergence of the Hambley blue gum (*E. globulus*) plantation, established in 1996. Corrected and uncorrected NDVI time series show an increasing NDVI value from 1995–1998 to the eventual saturation of NDVI from 2000–2002 for the area highlighted by the red polygon (E 117°42', S 34°38').

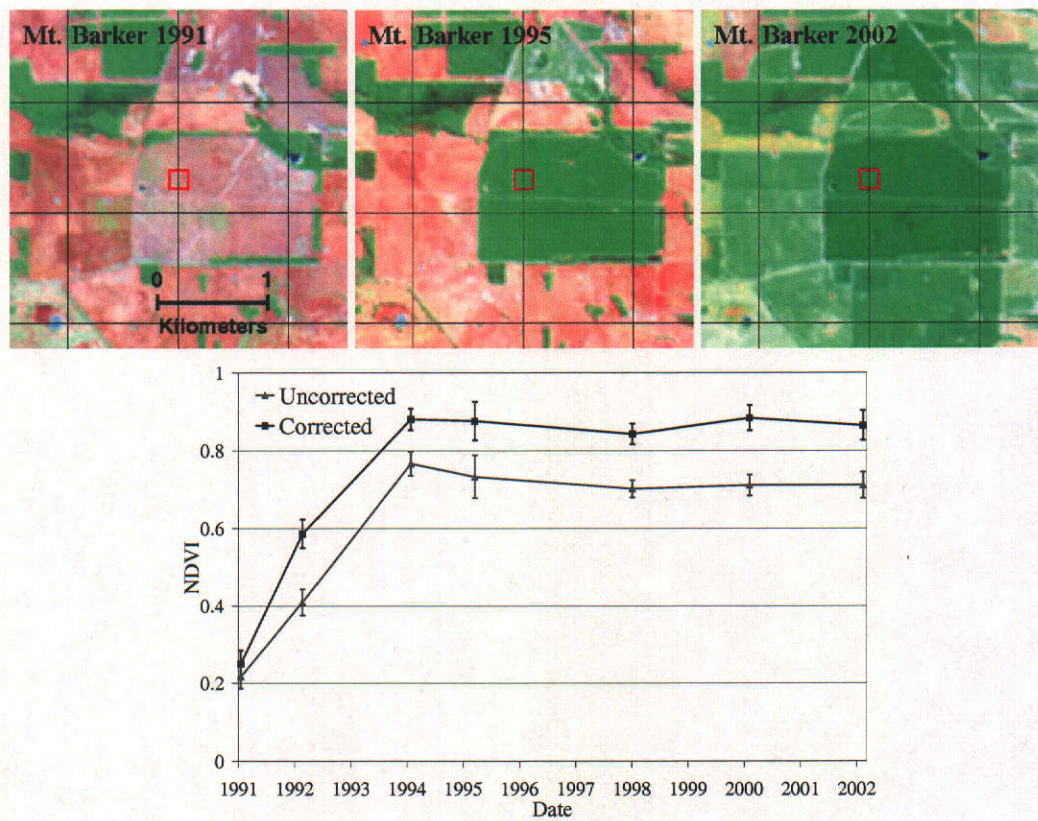


Figure 4.22: Imagery illustrating the emergence of a large eucalypt plantation. NDVI values, calculated from uncorrected and corrected reflectances for the area highlighted by the red polygon (centred on E 117°59', S 34°43'), increase after the plantations was established in 1991 and saturate from 1994–2002.

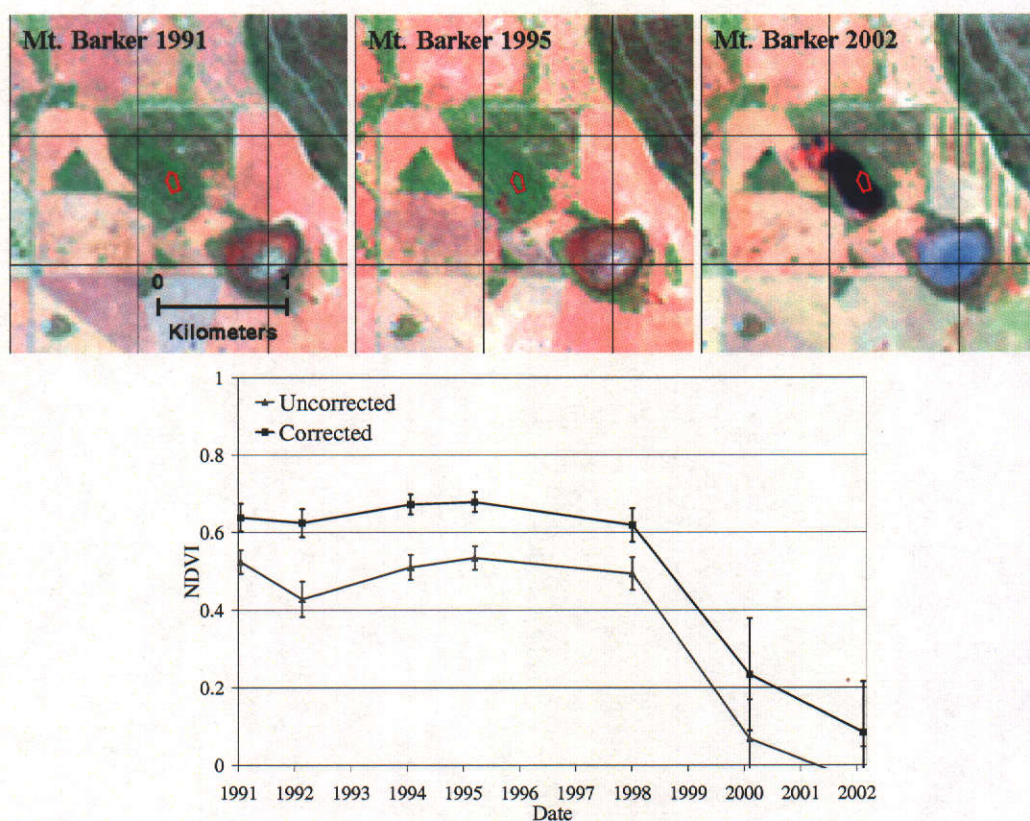


Figure 4.23: Imagery illustrating a loss of vegetation due to flooding. The dark-blue area surrounding the red polygon (centred on E 117°43', S 34°27') is known to be subject to intermittent flooding. NDVI values for this area, in both the corrected and uncorrected series, suggest that there is a certain amount of vegetation present between 1991-1998, but NDVI values decrease in 2000 and reach a minimum in 2002—a negative value in the uncorrected series. Also, the NDVI value in the uncorrected series for 1992 is brought into alignment with neighbouring dates in the corrected series.

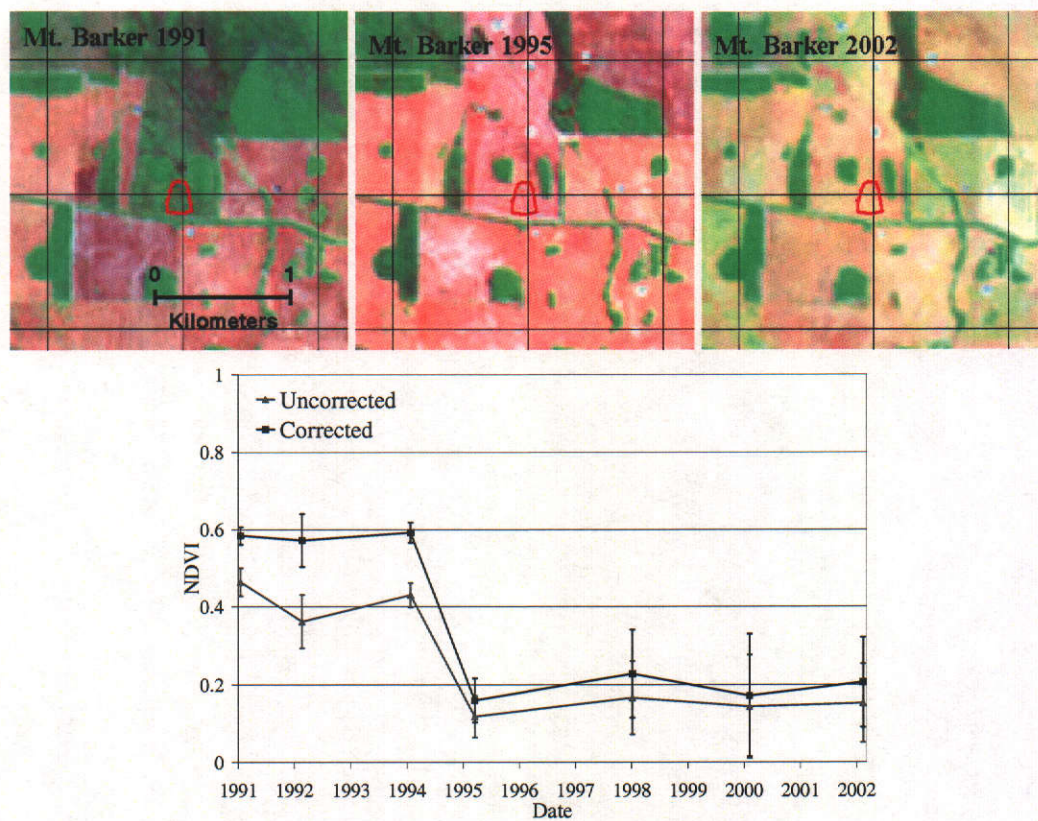


Figure 4.24: Imagery illustrating vegetation loss due to clearing. In both corrected and uncorrected NDVI time series, the loss of vegetation is evident for the area highlighted by the red polygon (centred on E 117°52', S 34°45') by a sharp transition from high NDVI values from 1991–1994 to low NDVI values from 1995–2002. The uncorrected NDVI value for 1992 is brought into alignment with its neighbouring dates in the corrected NDVI.

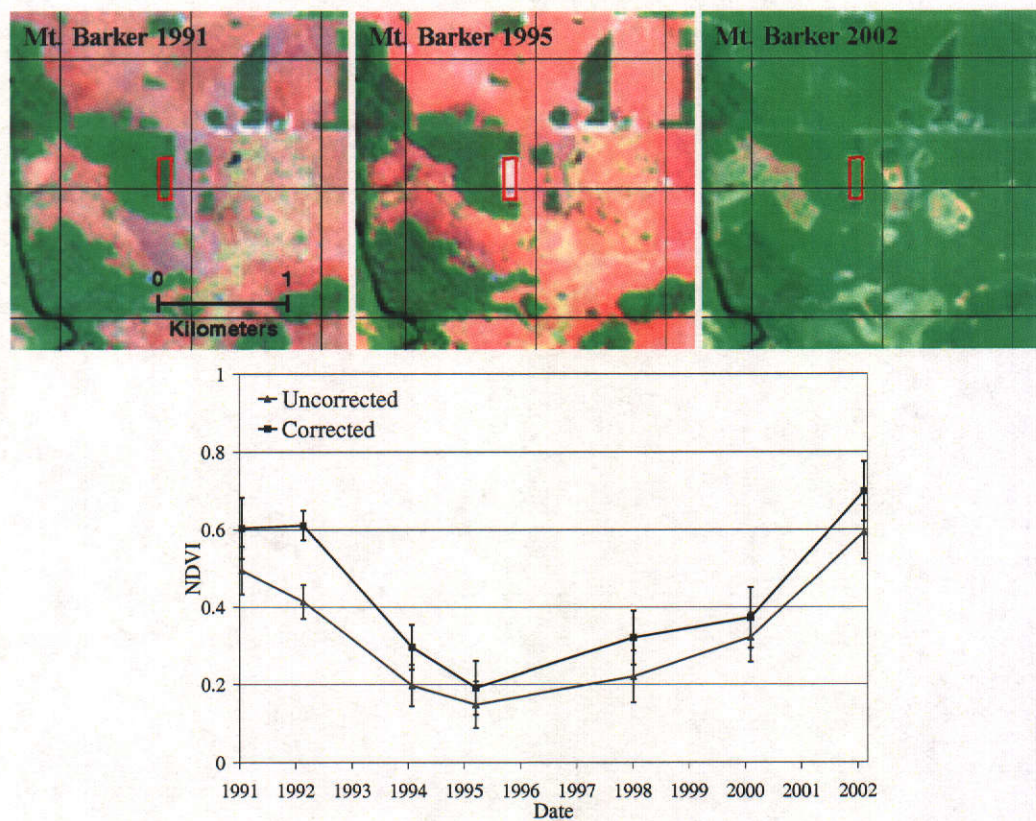


Figure 4.25: Imagery illustrating vegetation loss and then recovery in the area of the Springwell blue gum (*E. globulus*) plantation. The red rectangle (E 118°04', S 34°44') highlights some native vegetation that was cleared after the 1992 image was acquired and then was replanted with blue gums in 1999. The uncorrected NDVI value from 1992 is brought into agreement with the 1991 value in the corrected NDVI series.

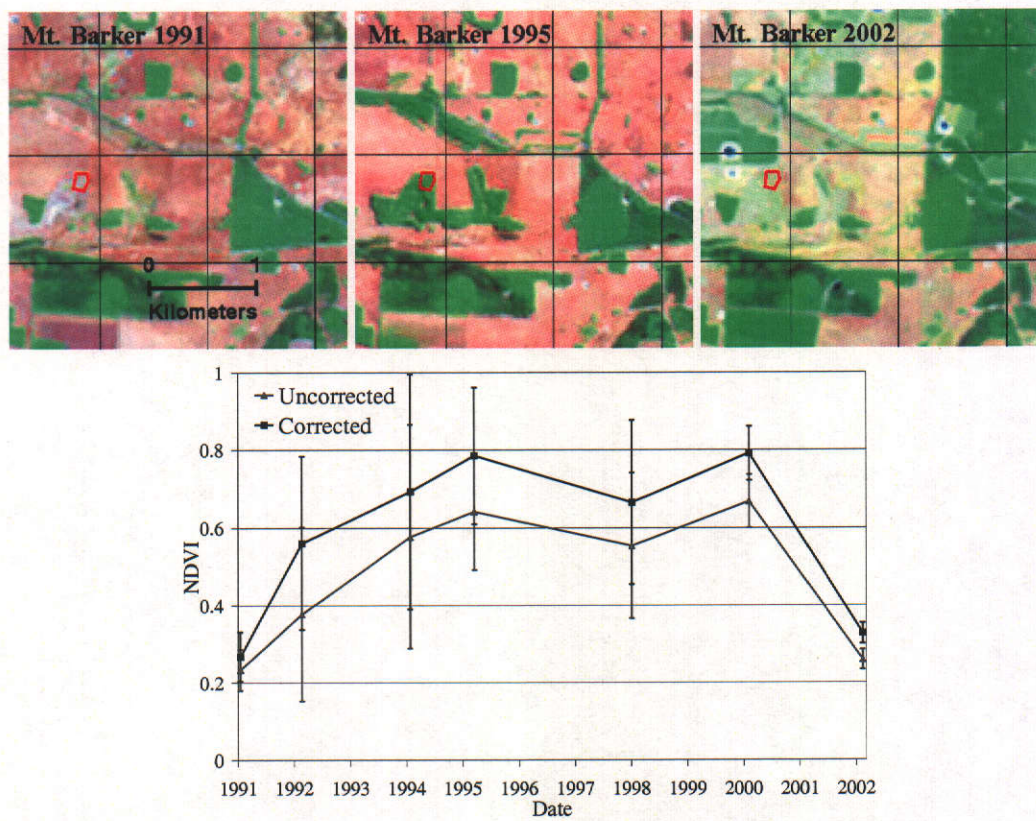


Figure 4.26: Vegetation gain and loss for a small region of native vegetation. The large error bars on the NDVI values in both uncorrected and corrected time series is due to the highly variable ground cover in the area highlighted by the red polygon (centred on E 117°35', S 34°45').

4.4.3 Discussion: Vegetation Change Detection

It was the aim of Section 4.4 to investigate the impact of the LVIN procedure on the calculation of NDVI and the implications for vegetation monitoring with time series data. The Mt. Barker sequence of images was used for the investigation because of the author's familiarity with areas of vegetation in the region. An examination of the reflectance spectra (both the uncorrected, at-sensor reflectance and that derived via the LVIN procedure) for two pixels corresponding to an old and a new blue gum plantation (Figure 4.18, p. 172), demonstrated that the LVIN procedure removed the atmosphere's additive effect on reflectances in the red band (band 3) described by Kaufman and Tanré (1992), and compensated for the dominance of atmospheric absorption in the NIR band (band 4). The increased difference between NIR and red bands meant that the resulting NDVI were generally higher in value than those calculated using uncorrected data. Moreover, an increase in the dynamic range of the NDVI was observed as a result of the multiplicative correction of reflectances in the NIR band (Figure 4.19, p. 174).

NDVI time series were constructed from the uncorrected and corrected NDVI for selected regions of vegetation change within the Mt. Barker scene (pp. 175–184). The time series were a simple but effective means of visualising vegetation change: Vegetation loss was represented by a sharp transition from high to low NDVI value; whereas vegetation recovery, or gain, was observed to be a slower transition from low to high value of NDVI, because vegetation must attain a certain level of canopy density before it is detected in the image data.

The most obvious difference between the uncorrected and corrected time series was that the corrected time series was, as expected, always higher than the uncorrected series. It was observed, however, that the uncorrected NDVI values for the TM image acquired on February 28, 1992 were consistently lower than its neighbouring values, particularly when there was no observed change in vegetation across the three consecutive image dates (e.g. Figure 4.20). The fact that uncorrected NDVI values are calculated with at-sensor reflectances, one must consider the possibility that there was an error in the choice of radiometric scaling factors or the solar/sensor geometry information for the 1992 image. This explanation, while tentative and in need of further investigation, may potentially account for the observed disagreement between free-intercept estimates and

modelled values of path DN described in Section 4.3.4 (see page 151 and Figure 4.15, p. 152). Nevertheless, it was observed in the corrected NDVI time series that the LVIN procedure adjusted for the underestimate of the index in the 1992 data.

4.5 Some Empirical Vegetation Reflectance Relationships

Sections 4.1–4.3 explored the use of modelled estimates of path DN in the LVIN procedure. The path DN is the digital number of the theoretically darkest pixel in an image since it corresponds to a target with a surface reflectance of zero. There are a number of assumptions¹⁰ one can make when calculating the path DN for a scene that, under certain circumstances (see pp. 160–162), may make it an undesirable component of the LVIN procedure. There is, therefore, an interest in exploring image-based approaches of relating image DN to surface reflectances. To this end, an approach based on the empirically-derived reflectance relationships of Kaufman et al. (Section 3.4.1, pp. 106–109) for vegetated targets will be considered in this section.

The empirical vegetation reflectance relationships have found application in mapping aerosol concentrations with MODIS imagery and correcting atmospheric effects in Landsat TM and ETM+ imagery. Recall that the expressions derived by Kaufman et al. (1997c) relate the reflectances observed in the SWIR bands (TM/ETM+ band 7) to those in the VIS (TM/ETM+ bands 1 and 3) for vegetated targets were,

$$\rho_{s1} = 0.25 \rho_{s7}, \text{ and} \quad (4.11)$$

$$\rho_{s3} = 0.50 \rho_{s7}. \quad (4.12)$$

It is the aim of Section 4.5 to investigate the use of the above relationships (hereafter, the *Kaufman relationships*) in a LVIN procedure as alternative to modelling the path DN (i.e. Step 4 of the described LVIN procedure, page 122) when satellite scenes are lacking in terms of dark pseudo-invariant targets. To begin, Section 4.5.1 will describe the results of testing the Kaufman relationships; firstly with ground-based spectrometer data for a vegetated target, and then with corrected Mt. Barker images of the previous section. Then in Section 4.5.2 a description of how the Kaufman relationships may be incorporated into a LVIN procedure is provided.

¹⁰Assumptions are made when there are uncertainties in, for example, the use of radiometric scaling factors, sensor calibration, or some of the atmospheric parameters required to model path radiance.

4.5.1 Data and Processing

Table 4.9: Dates and number of grass reflectance spectra acquired with a GER Iris spectroradiometer on the McGillivray oval (E 115°47', S 31°57'), Western Australia.

Date	Num. of Spectra	Date	Num. of Spectra
January 19, 1994	35	September 6, 1994	20
February 18, 1994	17	October 11, 1994	20
March 30, 1994	14	December 6, 1994	20
April 27, 1994	20	January 6, 1995	20
May 27, 1994	18	February 7, 1995	20
July 28, 1994	20	Total = 224	

Spectrometer Measurements

Palmer (1995) describes a CSIRO Mathematical and Information Sciences (CMIS) field campaign where a GER Iris spectroradiometer¹¹ acquired ground-based reflectance measurements of grass on the McGillivray football oval (E 115°47', S 31°57') in Floreat, Western Australia. Table 4.9 gives the dates of the CMIS field campaign. On each date, a spectroradiometer reading was performed at various locations around the oval in an attempt to obtain an area mean reflectance. The number of spectra in Table 4.9 is, therefore, equal to the number of locations visited. For this investigation, the spectra acquired were convolved with the Landsat-5 TM and Landsat-7 ETM+ response curves (e.g. Figure 4.27; the spectra for the other dates are displayed in Figures H.1–H.11, Appendix H, pp. 254–265). The resulting spectra, whether processed with the TM or ETM+ response curves, showed very little differences.

The inter-band correlation of the convolved data (both the TM and ETM+ convolved spectra) was assessed by computing correlation matrices for each date. As an illustrative example, the correlation matrix for the January 1994 spectra is given in Table 4.10. Differences in the correlation matrix between TM- and ETM+-convolved data were marginal. However, it was observed for all dates that band 4 data showed little correlation with any of the other bands. High inter-band correlation was observed between the VIS bands (bands 1–3), as well as between bands 5 and 7. In the interests of establishing Kaufman-type relationships, attention was restricted to the correlation

¹¹The same GER Iris spectroradiometer used on the EOC field campaign in Hay (see p. 130).

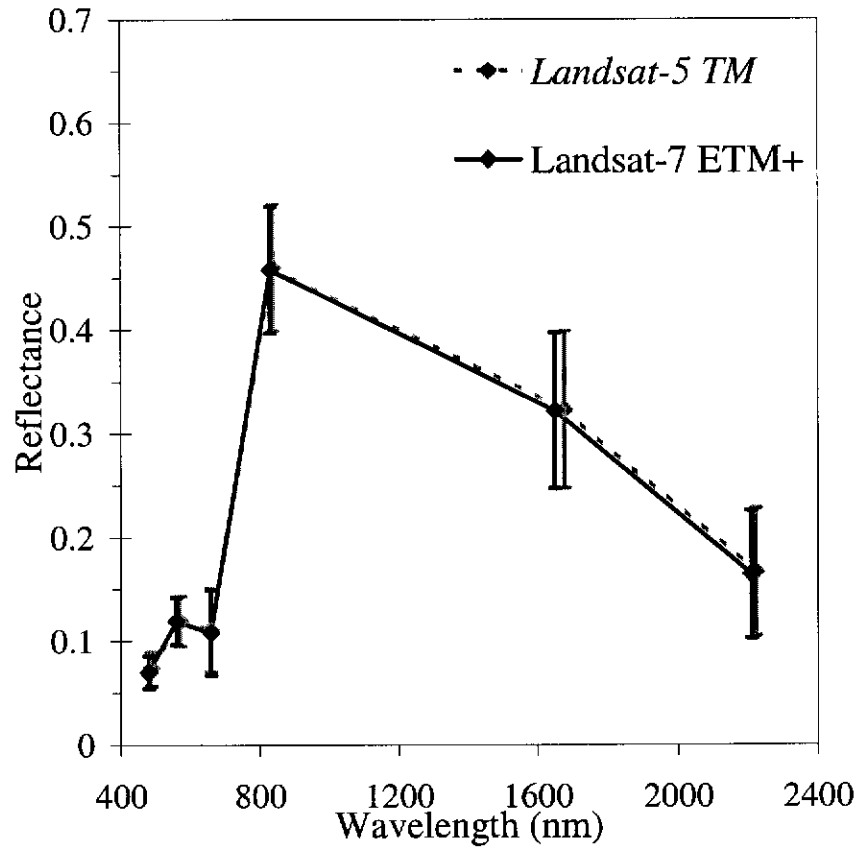


Figure 4.27: The convolved Iris spectra (35 in total) of the McGillivray Oval grass acquired on January 19, 1994: Grey diamonds correspond to the mean value of spectra convolved with the Landsat-5 TM response curves; black diamonds correspond to the mean value of spectra convolved with the Landsat-7 ETM+ response curves. Error bars mark $2\times$ standard deviations about the mean value.

Table 4.10: The inter-band correlation of 35 convolved grass spectra for January 1994. Presented are the Iris spectra convolved with Landsat-5 TM response curves (in italics, lower triangle), and the spectra convolved with the Landsat-7 ETM+ response curves (upper triangle).

	1	2	3	4	5	7
1	1.000	0.927	0.944	-0.248	0.895	0.889
2	<i>0.945</i>	1.000	0.874	-0.121	0.795	0.807
3	<i>0.951</i>	<i>0.906</i>	1.000	-0.301	0.889	0.923
4	<i>-0.236</i>	<i>-0.137</i>	<i>-0.287</i>	1.000	-0.372	-0.455
5	<i>0.891</i>	<i>0.814</i>	<i>0.889</i>	<i>-0.369</i>	1.000	0.969
7	<i>0.889</i>	<i>0.830</i>	<i>0.921</i>	<i>-0.447</i>	<i>0.971</i>	1.000

of bands 1–5 with band 7.

The spectra from dates in which band 7 exhibited correlations of 0.8 or better with bands 1, 3 and 5, and 0.6 or better with band 2, were combined. This meant that only spectra from 6 of the 11 dates (namely January, March, May, July, and September 1994, and February 1995) could be used. The resulting data set contained 127 values per band. Least-squares regression was employed to provide the estimates of the slopes and intercepts required to define the relationships. The results are presented in Table 4.11. It can be seen that the estimates of slopes and intercepts for the relationships of both TM- and ETM+-convolved spectra are very similar; that is, within 0.01 units of each other in value. Taking the average of the TM and ETM+ estimates for slope and intercept resulted in the following relationships for the ground-based spectra of McGillivray oval grass,

$$\rho_{s1} = 0.03 + 0.25 \rho_{s7}, \quad (4.13)$$

$$\rho_{s2} = 0.06 + 0.29 \rho_{s7}, \quad (4.14)$$

$$\rho_{s3} = 0.02 + 0.54 \rho_{s7}, \text{ and} \quad (4.15)$$

$$\rho_{s5} = 0.14 + 1.09 \rho_{s7}. \quad (4.16)$$

The results in Table 4.11 are displayed graphically in Figure 4.28. Also illustrated in the figure are the Kaufman relationships (see Eqs. 4.11 and 4.12) for band 1 and band 3 (in grey). The expression for ρ_{s1} and ρ_{s3} as functions ρ_{s7} from this analysis and the Kaufman relationships compare very closely in the estimates of slope; certainly if one considers the standard errors given in Table 4.11 and those of Kaufman et al. (1997c, Table 1). The most notable differences between the Kaufman relationships and the relationships derived in this research from the grass spectra above, are the offsets (i.e. the intercepts). Kaufman et al. (1997c) describes how their relationships were based on atmospherically corrected TM and AVIRIS images over a number of test sites. The offsets obtained in their investigations range between -0.011 and 0.022 for band 1, and between -0.014 and 0.025 for band 3. The offsets they observed, however, were attributed to residual atmospheric effects in the imagery used and, since they were on average around 0.005 , could be ignored. Similarly, offsets in the relationships observed by other authors (Gatebe et al., 2001; Karnieli et al., 2001) have been ignored because they were attributed

Table 4.11: The estimates of slope and intercept from the regression of the convolved grass spectra (127 in total) for bands 1, 2, 3 and 5 against band 7. Also presented in the table are the regression correlation coefficients (R^2), and the calculated standard errors (Std. Error) and t -values for the estimated parameters.

TM				ETM+		
	Slope	Intercept	R^2	Slope	Intercept	R^2
Band 1						
	0.249	0.029	0.763	0.244	0.027	0.771
Std. Error	0.013	0.002		0.012	0.002	
t -value	19.6	11.8		20.0	11.9	
Band 2						
	0.302	0.063	0.627	0.279	0.067	0.596
Std. Error	0.021	0.004		0.021	0.004	
t -value	14.1	15.5		13.3	17.0	
Band 3						
	0.532	0.017	0.806	0.541	0.014	0.813
Std. Error	0.024	0.005		0.024	0.004	
t -value	22.2	3.6		22.7	3.1	
Band 5						
	1.095	0.142	0.916	1.086	0.146	0.913
Std. Error	0.030	0.006		0.031	0.006	
t -value	35.9	24.6		34.9	24.9	

to the same atmospheric effects. Karnieli et al. (2001), for example, using ground-based spectra (ASD spectrometer measurements) found that $\rho_{s2} = 0.05 + 0.33 \rho_{s7}$, which is comparable to expression Eq. (4.14), yet the offset was still considered negligible.

The t -values were computed in the regression analysis of the convolved grass spectra (Table 4.11). The t -value for a 95% level of significance on 120 degrees of freedom (i.e. the number of points minus the two parameters estimated) is $t_{95\%} = 1.66$. The t -values calculated for all parameters were considerably more than $t_{95\%}$; thus the calculated offsets are statistically significant and, as far as the grass spectra are concerned, cannot be ignored. However, as was pointed out by Gatebe et al. (2001), for a vegetated target with $\rho_{s7} = 0$, one expects that ρ_{s1} and ρ_{s3} also to be equal to zero. The question then arises: Where does the offset in the grass spectra analysis come from? Potential reasons why significant and relatively large offsets were observed in the analysis will be addressed Section 4.5.3.

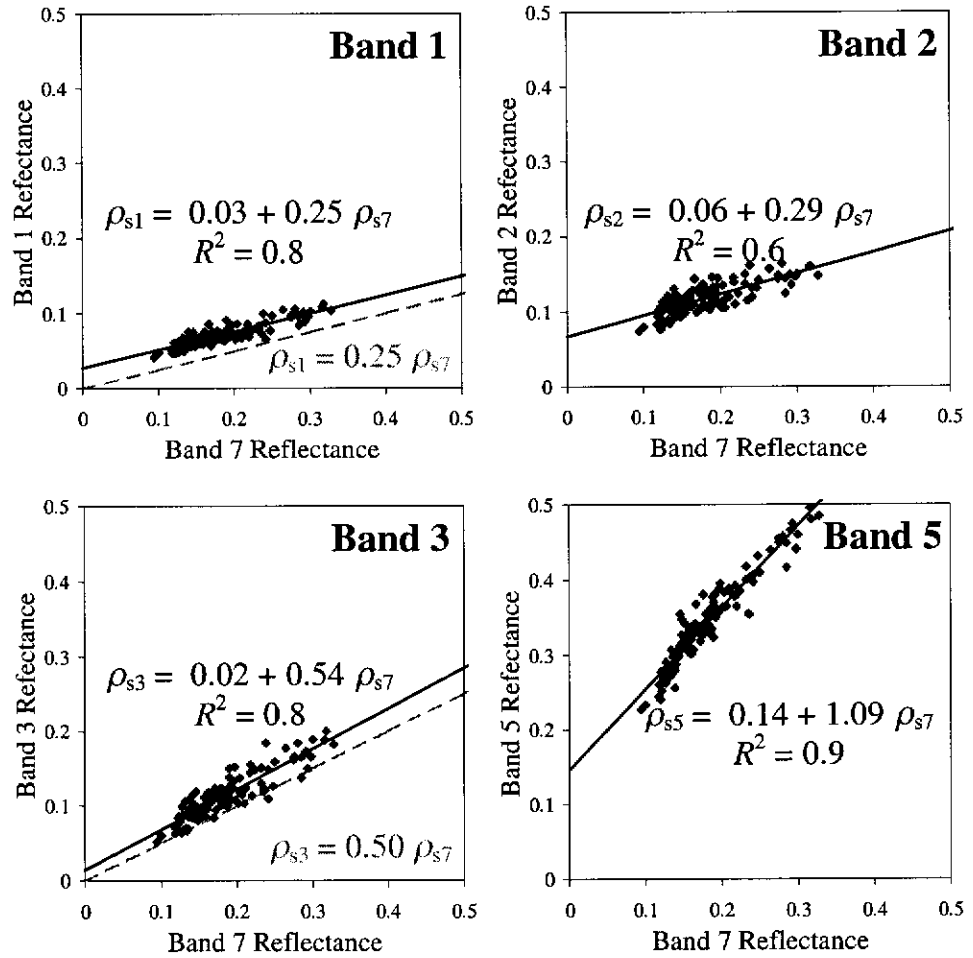


Figure 4.28: Surface reflectances ρ_{s1} , ρ_{s2} , ρ_{s3} , and ρ_{s5} as functions of ρ_{s7} derived from McGillivray Oval grass spectra. The equations displayed are a summary of the results presented in Table 4.11. Also displayed in the dashed grey lines for bands 1 and 3 are the corresponding Kaufman relationships (Eqs. 4.11 and 4.12).

Table 4.12: Correlation matrix for the combined vegetation data (64 targets; 448 reflectances per band) for all dates of TM and ETM+ imagery in the Mt. Barker sequence over the years 1991–2002.

	1	2	3	4	5	7
1	1.000	0.844	0.912	-0.032	0.829	0.838
2		1.000	0.925	0.196	0.703	0.654
3			1.000	-0.001	0.837	0.817
4				1.000	-0.035	-0.207
5					1.000	0.942
7						1.000

Image Vegetation Data

Kaufman et al. (1997c) derived their empirical vegetation reflectance relationships using TM and AVIRIS imagery that had been atmospherically corrected, using measurements of atmospheric optical thickness acquired *in situ*, and converted into surface reflectances. The vegetation targets chosen in their investigations were dark (reflectances < 0.1 – 0.15 in band 7) and corresponded to regions of dense native vegetation (Kaufman and Remer, 1994; Kaufman et al., 1997c).

Recall from previous sections (Section 4.4, for example) that the Mt. Barker scene contains an abundance of densely vegetated areas (i.e. nature reserves, perennial native vegetation, and large plantations). For this investigation the aim was to establish image-derived Kaufman-type relationships from the retrieved surface reflectances in the corrected Mt. Barker imagery.

Sample vegetation spectra were extracted for each date in the Mt. Barker sequence for regions where vegetation remained stable throughout the entire temporal sequence (see for example Figure 4.20, p. 178). In total 64 targets were identified; the vegetation spectra were chosen such that $\rho_{s7} < 0.15$. From these data an inter-band correlation matrix was calculated for each date using the 64-point data (given in Appendix H, pp. 266–267). As with the grass spectra, high correlations (> 0.85) were observed between bands 1–3 and 5, and band 7. Finally, the data for all dates in the TM-ETM+ sequence between 1991 and 2002 were combined to form a larger dataset of 448 points (64 targets \times 7 dates). The correlation matrix for the combined dataset is given in Table 4.12.

Once again, the intention was to determine expressions for ρ_{s1} , ρ_{s2} , ρ_{s3} and ρ_{s5} as linear functions of ρ_{s7} from the vegetation data. Plots of the reflectances for these

Table 4.13: The estimates of slope and intercept from the regression analysis of the combined data set of atmospherically corrected vegetation reflectances (Mt. Barker image sequence) for bands 1, 2, 3 and 5 against band 7. Also presented are the regression correlation coefficients (R^2), and the calculated standard errors (Std. Error) and t -values for the estimated parameters.

	Slope	Intercept	R^2
Band 1	0.285	0.005	0.702
Std. Error	0.009	0.001	
t -value	32.4	9.03	
Band 2	0.262	0.021	0.488
Std. Error	0.014	0.001	
t -value	18.3	22.8	
Band 3	0.416	0.013	0.806
Std. Error	0.014	0.001	
t -value	29.9	14.8	
Band 5	1.284	0.052	0.887
Std. Error	0.022	0.001	
t -value	59.1	38.3	

bands against the reflectances in band 7 are given in Figure 4.29. The results of the least-squares regression for these data are given in Table 4.13.

A comparison of the relationships derived above with the Kaufman relationships for bands 1 and 3 reveals close agreement (i.e., within the range of slope and intercepts estimated by Kaufman et al. (1997c) and others (Remer et al., 2001; Gatebe et al., 2001)). The offsets observed in the relationships above are smaller than those observed in the McGillivray Oval grass analysis of the previous subsection, and are similarly statistically significant (see t -values in Table 4.13; for 446 degrees of freedom $t_{95\%} = 1.645$). To two decimal places, the relationships derived from the Mt. Barker sequence vegetation spectra are summarised as:

$$\rho_{s1} = 0.00 + 0.28 \rho_{s7}, \quad (4.17)$$

$$\rho_{s2} = 0.02 + 0.26 \rho_{s7}, \quad (4.18)$$

$$\rho_{s3} = 0.01 + 0.42 \rho_{s7}, \text{ and} \quad (4.19)$$

$$\rho_{s5} = 0.05 + 1.28 \rho_{s7}. \quad (4.20)$$

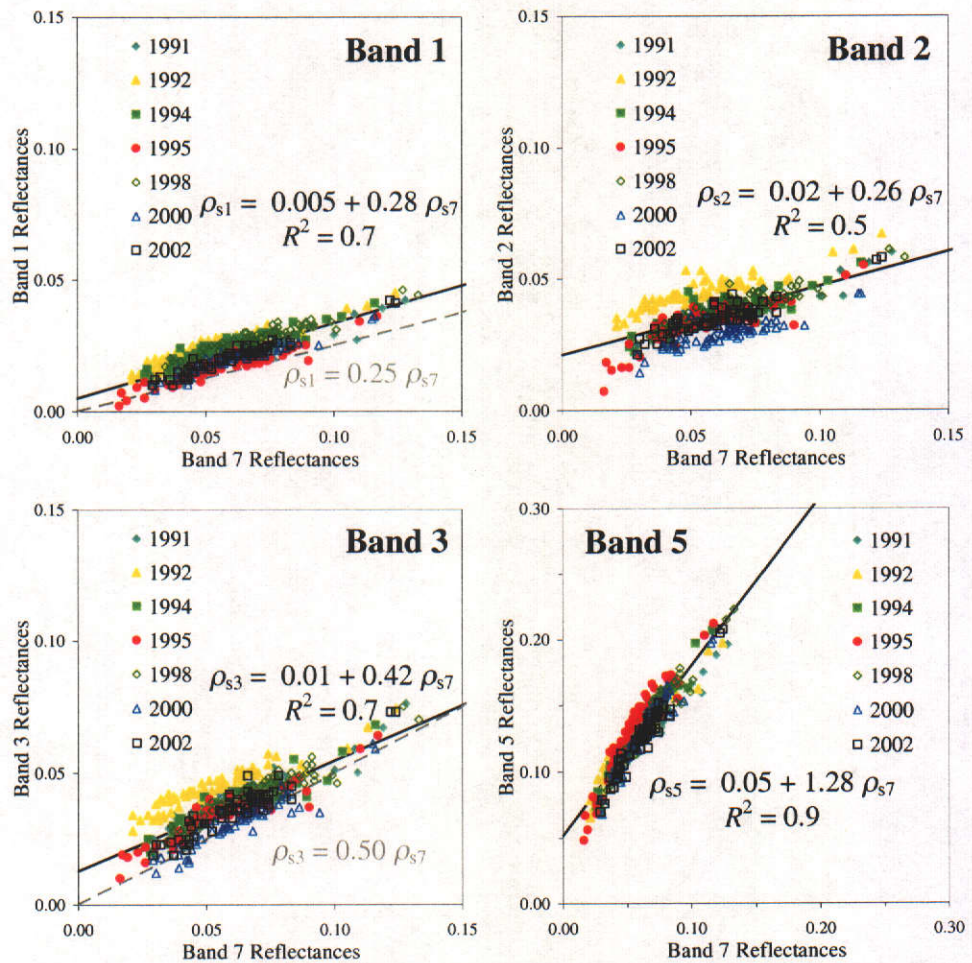


Figure 4.29: Surface reflectances ρ_{s1} , ρ_{s2} , ρ_{s3} , and ρ_{s5} as functions of ρ_{s7} for the retrieved reflectances of 64 vegetated targets for all dates in the Mt. Barker sequence of TM and ETM+ imagery acquired over the period 1991–2002. The equations displayed are a summary of the results presented in Table 4.13. Also displayed in the dashed grey lines are the Kaufman relationships for bands 1 and 3.

Table 4.14: A summary of the empirical vegetation reflectance relationships of Kaufman et al. (Kaufman) and the relationships derived in this work using retrieved reflectance for vegetation in Mt. Barker sequence (Image-derived) and McGillivray Oval grass spectra (Grass Spectra).

	Kaufman	Image-derived	Grass Spectra
Band 1	$\rho_{s1} = 0.25 \rho_{s7}$	$\rho_{s1} = 0.005 + 0.28 \rho_{s7}$	$\rho_{s1} = 0.03 + 0.25 \rho_{s7}$
Band 2		$\rho_{s2} = 0.02 + 0.26 \rho_{s7}$	$\rho_{s2} = 0.06 + 0.29 \rho_{s7}$
Band 3	$\rho_{s3} = 0.50 \rho_{s7}$	$\rho_{s3} = 0.01 + 0.42 \rho_{s7}$	$\rho_{s3} = 0.02 + 0.54 \rho_{s7}$
Band 5		$\rho_{s5} = 0.05 + 1.28 \rho_{s7}$	$\rho_{s5} = 0.14 + 1.09 \rho_{s7}$

4.5.2 Using the Relationships in a LVIN Procedure

Recall that it was the aim of Section 4.5 to investigate the potential use of the empirical vegetation relationships in the LVIN procedure as an alternative to modelling the path DN with radiative transfer code. Here a comparison is made between the various relationships presented previously. For simplicity, they shall be referred to as: *Kaufman* corresponding to the expressions of Kaufman et al. (1997c); *Image-derived* for the relationships derived from vegetation targets in the Mt. Barker sequence of normalised TM and ETM+ images; and *Grass spectra*, corresponding to the relationships based on the McGillivray Oval grass spectra. The expressions for each of these relationships are given in Table 4.14.

The proposal is to remove Step 4 (pp. 121–126) of the LVIN procedure and replace the modelled estimate of path DN with an estimate derived from the imagery itself. The Kaufman relationships may be used to attribute a surface reflectance to a DN value for a vegetated target in an uncorrected image. This approach may be incorporated into the LVIN procedure as follows:

Identify pixels in the image corresponding to dense vegetation. For these pixels:

1. Assume that band 7 DN are only affected by gaseous absorption through the atmosphere and calculate the at-sensor reflectance ρ_{sat7}^* . That is,

$$\rho_{sat7}^* = T_7^{\downarrow\uparrow} \rho_{s7}$$

where $T_7^{\downarrow\uparrow}$ is the total atmospheric gaseous transmittance from Sun to target, and from target to sensor for band 7. The transmittance may be approximated using standard atmospheric inputs to RT code such as MODTRAN or 6S. Perform

a simple atmospheric correction on the band 7 data by rearranging the above expression to yield ρ_{s7} . The aim should be to select 10–20 targets with $\rho_{s7} < 0.15$.

2. Calculate surface reflectances ρ_{sk} for $k = 1, 2, 3$ or 5 using empirical vegetation reflectance relationships, namely

$$\rho_{sk} = a_k + b_k \rho_{s7},$$

where a_k and b_k are the intercept (offset) and slope of one of the expressions in Table 4.14 (note that for the Kaufman relationships, $k = 1$ or 3).

3. Extract the (uncorrected) DN for the k th band, X_k , and form the data pair (ρ_{sk}, X_k) ; where ρ_{sk} is estimated from the previous item.
4. Incorporate (ρ_{sk}, X_k) into the LVIN plot for the k th band and proceed with the free-intercept approach to the LVIN procedure—the output will be a sequence of images normalized to like-value reflectances.

Note that since there is no empirical vegetation reflectance relationship for ρ_{s4} , the above approach will not work for band 4. Possible methods for addressing this problem are suggested in Section 4.5.3.

To make a comparison between the three empirical vegetation reflectance relationships, and to demonstrate their application in the proposed ‘new’ LVIN procedure, the Mt. Barker sequence of images was once again employed. The sequence is ideal for the comparison because of the sufficient number of dark pixels in the normalisation plots (mainly extracted from the Southern Ocean). Thus the normalisation plots for the overpass images in Mt. Barker sequence (Appendix E; Figures E.4–E.9, pp. 237–242) and the free-intercept regression LVIN line (with the 95% confidence limits) were used in the comparison.

Twenty new vegetation targets were identified in the Mt. Barker imagery. The pixel DN for these targets were processed as described above, and surface reflectances were calculated via the Kaufman, grass spectra and image-derived relationships. The data pairs (ρ_{sk}, X_k) , $k = 1, 2, 3$, and 5 , were made for each vegetated target and superimposed over the normalisation plots for each overpass date in the Mt. Barker sequence (see Appendix H; Figures H.12–H.17, pp. 269–274). An enlargement of the normalisation plots for the Mt. Barker January 20, 1991 image is displayed in Figure 4.30.

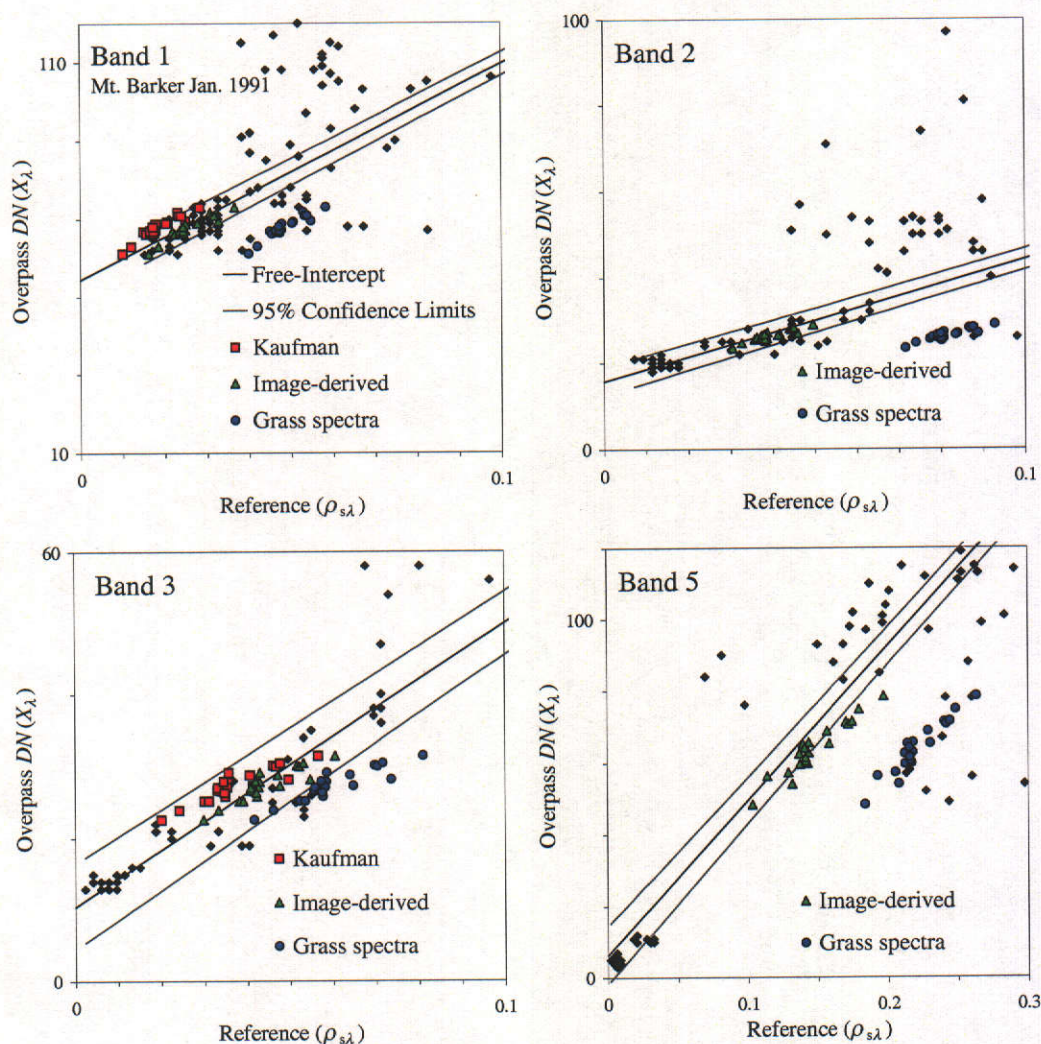


Figure 4.30: An enlargement of the LVIN plots for bands 1, 2, 3 and 5, from the Mt. Barker image for January 20, 1991. The black diamonds are the pixel DN s for the PITs in the LVIN plots; Figure E.4. The black lines are the free-intercept LVIN lines with 95% confidence limits delineated in grey. Also illustrated are the data for the 20 vegetation targets to which the empirical vegetation relationships have been applied: namely, those derived by Kaufman et al. (Kaufman, red squares), and the two sets of relationships derived in this work (Image-derived, green triangles; and Grass spectra, blue circles), defined in Table 4.14.

It was observed that the data pairs constructed for the Kaufman and Image-derived relationships were closest in value (i.e. for bands 1 and 3). Furthermore, the points derived from the Kaufman relationships (red squares) were generally lower in surface reflectance than those from the other two relationships and were therefore the left-most data pairs in the normalisation plots for bands 1 and 3. The points produced with the Grass spectra relationships (blue circles) had much higher estimates of surface reflectance and were the right-most points in the plots. Since values for slope in the Kaufman and Grass spectra relationships are very close, it is clear that the differences observed are due to the intercepts (the large offset) used in the Grass spectra relationships.

For most of the normalisation plots, the Image-derived relationships (green triangles) gave data pairs that consistently fell within the 95% confidence limits of the free-intercept LVIN line; with the exception the 1992 band 3 normalisation plot where none of the points produced using either of the relationships was contained within the limits. The Kaufman relationships were the next best at producing points that were within the 95% confidence limits. The Grass spectra, however, only produced a few points (between 1–5) that were within the confidence limits, if any at all.

4.5.3 Discussion: Empirical Vegetation Reflectance Relationship

Ground-based spectra and image-derived reflectances for some vegetation targets were used to construct Kaufman-type empirical vegetation reflectance relationships with the aim of potentially being used in a LVIN procedure. The expressions obtained relate the surface reflectances for TM/ETM+ bands 1, 2, 3 and 5, to band 7 reflectances for vegetated targets. For bands 1 and 3, the expressions obtained in this work were consistent with previous work (Kaufman et al., 1997c; Gatebe et al., 2001), and similarly for band 2 (Karnieli et al., 2001). The main difference between this work and that of others was that the calculated intercepts (offsets in the relationships) were statistically significant and, as far as the data were concerned, could not be considered negligible.

An alternative to the path *DN* modelling component of the LVIN procedure was described that incorporates the empirically-derived vegetation reflectance relationships. Essentially, the relationships are used to estimate surface reflectances for vegetated targets within an image which would then be used with the corresponding pixel *DN* to form data pairs. These vegetated data pairs are then used in the normalisation plots to

influence the regression line in the low reflectance region. Of the three empirical relationships investigated (i.e. Kaufman, Grass spectra and Image-derived, p. 195), closest agreement was observed between data pairs produced with the Kaufman and Image-derived relationships. This was because the values of slope in both sets of relationships were similar, and the offsets in the Image-derived relationships were smaller than those in the Grass spectra relationships.

Using the Mt. Barker normalisation plots as a guide, it was generally observed that the Kaufman and Image-derived relationships gave vegetation data pairs that were within the 95% confidence limits of the free-intercept regression LVIN line. The one instance for which all three relationships gave points outside these limits was for band 3 in the 1992 image. Recall from previous sections that the Mt. Barker 1992 image has twice before provided results that were against the general trends (i.e. modelled and free-intercept estimates of path DN , p. 151; uncorrected NDVI times, p. 185). It was speculated previously that problems with this date may be due to uncertainty in the radiometric scaling factors for the 1992 image data. If this is the case, the fact that the scaling factors are used to yield at-sensor reflectances for band 7 means that the use of the incorrect coefficients may result in errors in surface reflectance estimation for that band; in turn affecting ρ_{s3} estimation, thus explaining the observed disagreement with the general behaviour.

The Image-derived relationships computed in this work have the added advantage that they provide estimates of surface reflectance in two extra bands (bands 2 and 5) for which the Kaufman relationships did not. Also, the fact that the Image-derived relationship consistently provided vegetation data pairs that were within the 95% confidence limits of the free-intercept LVIN line, implies that the empirical vegetation reflectance results could indeed serve as an alternative to the modelling component of the LVIN procedure. Further investigations are recommended to assess the surface reflectance retrievals, and to compare the results with the conventional and modelled-approaches described in previous sections.

Comments on the Observed Offsets

Whilst t -tests showed that offsets observed in the analysis of grass spectra and normalised image reflectances were statistically significant, there is no physically-based argument

as to why there should be an offset at all. In a personal communication with Dr. Kaufman it was suggested that the offset observed may be an artefact of the range of reflectances used in the analysis. In order to do atmospheric correction (for which the relationships were initially intended) not only is good correlation required between the VIS band and band 7, but the targets used need to be sufficiently dark. The results of Kaufman et al. (1997c) were based on data from atmospherically corrected Landsat TM and AVIRIS images, such as dense forest areas and some crops, where band 7 reflectances were typically < 0.15 . Furthermore, they demonstrated that relationships derived could retrieve ρ_{s1} and ρ_{s3} to within ± 0.006 reflectance units (and aerosol optical thickness with ± 0.06).

The band 7 reflectances used in the analysis with Mt. Barker image data were less than 0.15. The estimate of slope for band 1 in this work (Image-derived method) was 0.28, compared with 0.25 (Kaufman et al., 1997c); the intercepts in both analyses were the same (i.e. 0.005; see (Kaufman et al., 1997c), Table 1.). Relationships for band 3 were similarly comparable in slope; 0.42 in this work compared with 0.5. However, in Mt. Barker analysis, an offset of 0.01 was obtained that is 5 times larger than the average observed by Kaufman et al. (1997c), yet still within the range of values they obtained (-0.014 — 0.025). It was concluded by Kaufman and others that the offsets they observed were due to residual atmospheric effects. This may very well be the case in this work, since the reference image constructed for Mt. Barker was based on assumptions regarding aerosol optical thickness, not to mention all the other potential sources of error mentioned in the Section 4.3.7 (pp. 158–166).

Atmospheric effects cannot be used to explain the observed offsets in the McGillivray Oval grass spectra analysis since the spectra were collected at the Earth's surface. For the grass spectra, $0.1 \leq \rho_{s7} \leq 0.30$ which often constitutes a considerable range of the reflectances in band 7 (see histograms in Appendix G, for example). Restricting analysis to spectra $\rho_{s7} < 0.15$ would leave too few data points to establish a relationship with sufficiently high inter-band correlation.

What about Band 4?

The empirical vegetation reflectance relationships determined in this work provide estimates of surface reflectance in bands 1, 2, 3 and 5. The consistently poor correlation

observed between band 4 reflectances and those in band 7 for vegetated targets meant that no meaningful relationship could be established to relate ρ_{s4} to ρ_{s7} . It, therefore, remains that band 4 image data be normalised to surface reflectances using the conventional free-intercept LVIN procedure. A constrained LVIN procedure using a modelled value of path DN for band 4 may be considered, but one has to make assumptions about the various model parameters (particularly atmospheric inputs).

An alternative approach—not explored here because it is beyond the scope of the thesis—may be to use the Kaufman relationships for the purpose that they were initially intended: the estimation of aerosol optical thickness. For each vegetated pixel, the at-sensor reflectance can be determined from image data and the radiometric scaling factors, and the surface reflectance can be estimated using the relationships for band 1-3 and 5. With these two quantities, the RTE can be inverted and give an estimate of aerosol optical thickness for these band, namely τ_{M1} to τ_{M3} and τ_{M5} . Then, by employing the Ångström relationship

$$\tau_{M\lambda} = A\lambda^{-B},$$

coefficients A and B may be estimated in a 4-point regression with the aforementioned estimates of aerosol optical thickness, and thus provide an estimate of τ_{M4} . Given the estimate of aerosol optical thickness in band 4, radiative transfer code, such as 6S, may be employed to either correct the image data, or to model the path DN for use in the constrained regression implementation of the LVIN procedure for that band only.

4.6 Chapter Summary

- A like-value image normalisation (LVIN) procedure was applied to two multitemporal sequences of Landsat-5 TM and Landsat-7 ETM+ imagery with the aim of estimating surface reflectances and obtaining a normalised/standardised sequence of imagery for change detection studies.
- The LVIN procedure assumes that within a satellite image there exists features on the Earth's surface that have reasonably invariant reflectance properties through time. Employing robust regression on data extracted from an unprocessed (overpass) image and a reference image for these pseudo-invariant targets (PITs), a normalisation equation (linear gain and offset) is obtained to transform unprocessed

data, and give it the appearance that it was acquired under the same conditions as the reference images.

- The difference between the LVIN procedure described here and the method of Furby and Campbell (2001) was the use of reference images that have been corrected for atmospheric effects and converted into surface reflectances. The option of incorporating the theoretically darkest pixel in an image—known as the path *DN*—is also proposed in this thesis as a further modification of the method of Furby and Campbell (2001). It is suggested as a useful means of *tying down* the regression at the low reflectance end of the normalisation plots when no suitably dark PITs (or too few) can be found.
- A comparison of the modelled path *DN*s and the estimates from the free-intercept approach showed agreement to within the level of statistical uncertainty in the data, suggesting that the normalisation line is not seriously biased by constraining the regression. The constrained approach is, however, not recommended if there is uncertainty in the level of image product (and thus radiometric scaling factors) used.
- Visual inspection of the histograms of the reflectances retrieved via the LVIN procedure showed that, if overpass and reference images were acquired with the same sensor (say, both TM or both ETM+) then the LVIN procedure appeared to correct for atmospheric effects. This finding was supported in comparisons with the 6S-corrected image data. If the overpass and reference images were acquired with different sensors, then not only did the LVIN procedure correct for atmospheric effects, but appeared also to compensate for between-sensor differences.
- The lack of validation data meant that only a qualitative evaluation of the LVIN procedures (by comparing retrieved reflectances to those from the reference image) was possible. The scatter of points about the normalisation lines was a limiting factor in assessing the precision of the reflectance retrievals. Nevertheless, the LVIN procedure obtained results that were adequate for most practical applications.
- It was further demonstrated that NDVI images computed from LVIN-corrected reflectances had greater dynamic range than those based on at-sensor reflectances;

a finding consistent with the expected results of atmospheric correction for red and NIR bands. More importantly, the LVIN procedure was seen to correct for uncertainty in radiometric scaling factors and produce a standardised set of data with which vegetation change could be monitored.

- Finally, the preliminary results of an investigation into the use of empirical vegetation reflectance relationships in the LVIN procedure was presented.

CHAPTER 5

Conclusions

Images acquired for a given scene over time can appear quite different irrespective of what changes have occurred on the Earth's surface. These differences are due to (i) changes in satellite sensor systems, (ii) seasonal variations in solar position, or (iii) atmospheric effects. Radiometric processing aims to minimise, or eliminate, the contribution of these three factors to changes observed in sequences of imagery. The radiometric processing investigated in this thesis is known as image normalisation.

Image normalisation procedures achieve a level of standardisation by transforming satellite image data into common units, and give images the appearance that they were acquired under the same solar and view geometries, atmospheric condition, and with the same satellite sensor as that of a *reference* image. Furthermore, it is claimed (Hall et al., 1991; Furby and Campbell, 2001) that if a reference image is accurately calibrated and corrected for atmospheric effects, then normalisation procedures may be used to estimate surface reflectances for the other images in a multitemporal sequence. Such procedures have the advantage of being able to provide estimates of surface reflectance for scenes where no *in situ* observations of surface reflectance and/or atmospheric parameters—required knowledge for the more physically-based radiometric processing procedures—are available; a typical situation for the majority of places on Earth.

In this thesis, a like-value image normalisation (LVIN) procedure was described that is based on the procedure of Furby and Campbell (2001). The LVIN procedure uses the *DN*s from unprocessed *overpass* images and surface reflectances from a reference image for a set of pseudo-invariant targets (PITs), common to all images in a sequence. From these data, linear relationships are obtained that transform *DN*s into surface reflectances for a given image. The thesis also explored the use of the darkest pixel *DN*, referred to as the *modelled path DN*, as an alternative to finding suitably dark PITs. Conclusions from the investigation and recommendations for future work are given in the following.

5.1 Image and Model Data

The Reference Images

The LVIN procedure was applied to two multitemporal sequences of Landsat TM and ETM+ imagery. The first, known as the Hay scene, was composed of two TM and two ETM+ images acquired over a rural area of New South Wales, Australia. The second, known as the Mt. Barker scene, was composed of five TM and two ETM+ images on the southwest coast of Western Australia, Australia.

The Hay reference was an ETM+ image (March 27, 2000) that had coincident ground-measured surface reflectances for four targets. The reference image *DN*s were converted to surface reflectances via an empirical line procedure, called the hybrid empirical line (HEL) procedure. An independent set of surface reflectance measurements was not available to assess the performance of the procedure. However, it was concluded that the HEL procedure had produced a reference image of sufficient accuracy because of RMS errors calculated on the 4 measured targets ranged from 0.002 in band 1 to 0.022 in band 7.

As there were no *in situ* measurements of surface reflectance for any date in the Mt. Barker sequence, 6S was used to convert the *DN*s of an ETM+ image (February 6, 2000; chosen because its *DN* had the highest dynamic range of all the images in the sequence) into reflectances. The choice of model inputs was guided by radiosonde profiles, TOMS estimates of ozone column amount, and a knowledge of the terrain throughout the scene.

Both methods employed in the production of the reference images assume that atmospheric conditions are uniform across a scene. Often this is not the case, and a detailed analysis of the errors that this assumption introduces is recommended. A comparison of the results from the two approaches above to a correction procedure that operates on a pixel-by-pixel basis may provide some insight, but an ideal study would involve comparisons with ground-based measurements of surface reflectance for a large number of targets spread throughout the scene.

Modelled Path DN

The LVIN procedure requires a number of bright, mid-range and dark PITs to obtain an estimate for the image normalisation line. If too few PITs are sufficiently dark, then

scatter in PITs of higher reflectance in the LVIN plots would tend to dominate the regression and result in an image normalisation lines that incorrectly adjusts the lower reflectance pixels. In this thesis, the DN for a target with zero surface reflectance was modelled from the image's radiometric scaling factors, solar and sensor geometries at the time of the image was acquired, and estimates (or knowledge) of some key atmospheric parameters.

The Mt. Barker scene had an abundance of dark PITs (because of the scene's proximity to the Southern Ocean) in comparison to the Hay scene. Agreement of dark PITs' DN to the modeled path DN s was better for Mt. Barker than for Hay. The expectation is that if Hay had more dark PITs, one would observe better agreement in that scene too.

Constraining the regression fit to pass through the modelled path DN was investigated as a possible means for tying down the LVIN line at the dark end of the normalisation plots. A consideration for future work may be the development of a weighted regression scenario, in which the modelled path DN s are attributed weights that indicate the reliability of the modelled point. The weights could consider uncertainties in the radiometric scaling factors and the parameters that contribute to modelling the path radiance (such as aerosol type and optical thickness, water vapour concentrations, terrain elevation etc). This would require a more extensive analysis of the sensitivity of the LVIN procedure than that presented in this thesis.

Preliminary investigations presented in this thesis have shown that an alternative to modelling the path DN may be the use of vegetated targets and empirically-based inter-band reflectance relationships. The relationships derived in this thesis were found to be consistent with those of other researchers. If the relationships are to be incorporated into the LVIN procedure, then it may be useful to investigate the impact of seasonal effects on the empirical vegetation reflectance relationships and on the subsequent surface reflectance retrievals.

5.2 Addressing the Research Aim

Atmospheric, Solar Position and Sensor System Effects

In an examination of image histograms pre- and post-normalisation, it was revealed that the LVIN procedure adjusted image data in the manner expected of an atmospheric correction procedure; namely, the removal of the additive path effect, due to scattering by molecules and aerosols in the visible bands, and compensation for the multiplicative effects of extinction and gaseous absorption which are the dominant mechanisms affecting the near- and shortwave infrared bands.

This finding was based on comparisons of the LVIN surface retrievals with those from the 6S code for the situation where both reference and overpass images were acquired with the same sensor (ETM+). In this instance, changes due to sensor system differences were assumed to be negligible, and the close agreement between the LVIN procedure and 6S code supported the claim.

The results also imply that differences in sun angle and Earth-Sun distance are adjusted by the LVIN procedure, since these pieces of information are used by 6S.

When the reference and overpass images were acquired with different sensors, the LVIN procedure appeared to modify the image histograms in ways that were consistent with adjustments for differences in the dynamic ranges of data from the TM and ETM+ sensors.

The LVIN procedure's ability to remove atmospheric effects was again demonstrated in comparisons of the retrieved and at-sensor reflectances for vegetated targets in the Mt. Barker scene. Reflectances in visible bands were reduced while those in the near- and shortwave infrared bands increased after the application of the LVIN procedure.

Data Consistency through Time

The temporal consistency of the imagery after the application of the LVIN procedure was assessed by examining retrieved reflectances for a subset of the PITs common to all dates in both multitemporal sequences. The absolute accuracy of the retrievals could not be assessed because of a lack of validation data. Nevertheless, the procedure demonstrated a high level of precision by retrieving surface reflectances, for most bands, to within ± 0.01 – 0.02 reflectance units of the value for the same PIT in the reference image.

Time series of the normalised difference vegetation index (NDVI), calculated with at-sensor and LVIN retrieved reflectances, were constructed for selected locations throughout the Mt. Barker scene. These served as a useful graphical illustration of the vegetation change for specific locations through time.

The NDVI calculated from at-sensor reflectances for one of the dates in the Mt. Barker sequence (1992 TM image) was consistently lower in value than neighbouring points in the time series, even when there was no observed vegetation change between dates. This was attributed to the use of incorrect radiometric scaling factors as a consequence of uncertainty in the level of image product for the particular date. Nevertheless, the LVIN procedure was seen to compensate for this uncertainty and produced a consistent set of NDVI; supporting the notion that the procedure compensates for changes in satellite sensor systems.

5.3 Final Remarks

From the findings above, it may be concluded that the LVIN procedure certainly appeared to correct images in multitemporal sequences for effects due to the atmosphere, solar positions, and the sensor systems, but a thorough assessment was hampered by a lack of validation data. When the reference image has been processed to surface reflectances, the LVIN procedure can be used to retrieve surface reflectances in the other images in the sequence and produce a consistent set of image data for multitemporal analyses. The absolute accuracy of the retrievals is limited to the accuracy of the reference image corrections.

Finally, it is emphasised that constraining the LVIN normalisation line to pass through the modelled value of path DN is only recommended when the level of TM or ETM+ product—and thus the radiometric scaling factors—is known. There have been a number of changes to the on-ground processing of the TM imagery throughout the sensors lifetime (Markham and Barker, 1986; ACRES, 1999), and the application of the incorrect coefficients will result in dramatically different values for path DN . Ultimately, it is investigations such as those of Teillet et al. (2001) into the temporal change of TM's responsivity that will lead to an updated set of radiometric scaling factors for the historical archives of TM image products (Teillet, 2002).

References

- ACRES, 1999. Acres (ccrs) landsat Thematic Mapper digital data format description. Tech. Rep. Revised Edition – January 1999, Australian Centre for Remote Sensing, PO Box 28, Belconnen ACT 2617, Australia.
- Anderson, G., Berk, A., Acharya, P., Matthew, M., Bernstein, L., Chetwynd, J., Dothe, H., Alder-Golden, S., Ratkowski, A., Felde, G., Gardner, J., Hoke, M., Richtsmeier, S., Pukall, B., Mello, J., Jeong, L., 2000. MODTRAN4: Radiative transfer modeling for remote sensing. *Proceedings of SPIE* 4049, 176–183.
- Aranuvachapun, S., 1983. Variation of atmospheric optical depth for remote sensing radiance calculations. *Remote Sensing of Environment* 13, 131–147.
- Arvesen, J., Griffin, R., Pearson, B., 1969. Determination of extraterrestrial solar spectral irradiance from a research aircraft. *Applied Optics* 8, 2215–2232.
- Asrar, G., 2002. Associate Administrator, Office of Earth Science, NASA Headquarters. Plenary address to SPIE's Third International Asia-Pacific Environmental Remote Sensing Symposium: Remote Sensing of the Atmosphere, Ocean, Environment and Space. Hangzhou, China, 23-27 October 2002.
- Barron, E. J., Hartman, D. L., King, M. D., Schimel, D. S., Schoeberl, M. R., 1999. EOS Science Plan: The state of science in the EOS program. NASA Earth Observing System, NASA/Goddard Space Flight Center, Code 900 Greenbelt, Maryland 20771, USA, pp. 5–38.
- Behn, G., McKinnell, F. H., Caccetta, P., Vernes, T., 2000. Mapping forest cover, Kimberly region of Western Australia. *Australian Forestry* 64 (2), 80–87.
- Besag, J., 1986. On the statistical analysis of dirty pictures (with discussion). *Journal of the Royal Statistical Society, Series B* 48 (3), 259–302.

- Box, M. A., Box, G. P., 2001. Climate forcing by atmospheric aerosol particles. *The Physicist* 38, 91–95.
- Brion, J., Chakir, A., Charbonnier, J., Daumont, D., Parisse, C., Malicet, J., 1998. Absorption spectra measurements for the Ozone molecule in the 350–830nm region. *Journal of Atmospheric Chemistry* 30, 291–299.
- Browell, E., 1989. Differential absorption lidar sensing of ozone. *Proceedings of the IEEE* 77, 419–432.
- Caccetta, P., Allen, A., Watson, I., Beetson, B., Behn, G., Campbell, N., Eddy, P., Evans, F., Furby, S., Kiiveri, H., Mauger, G., McFarlane, D., Smith, R., Wallace, J., Wallis, R., 2000a. The Land Monitor project. *Proceedings of the 10th Australasian Remote Sensing and Photogrammetry Conference Adelaide*, 97–107.
- Caccetta, P. A., Campbell, N. A., Evans, F., Furby, S. L., Kiiveri, H. T., Wallace, J. F., 2000b. Mapping and monitoring land use and condition change in the south-west of Western Australia using remote sensing and other data. *Proceedings of the Europa 2000 Conference Barcelona*.
- Campbell, N. A., Atchley, W. R., 1981. The geometry of canonical variate analysis. *Systematic Zoology* 30 (3), 268–280.
- Campbell, N. A., Kiiveri, H. T., 1993. Canonical variate analysis with spatially-correlated data. *Australian Journal of Statistics* 35 (3), 333–344.
- Caselles, V., López-García, M. J., 1989. An alternative simple approach to estimate atmospheric correction in multitemporal studies. *International Journal of Remote Sensing* 10 (6), 1127–1134.
- Chandrasekhar, S., 1960. *Radiative Transfer*. Dover Publishers, New York, USA.
- Chavez, P. S., 1996. Image-based atmospheric corrections-revisited and improved. *Photogrammetric Engineering and Remote Sensing* 62 (9), 1025–1036.
- Cracknell, A. P., 1997. *The Advanced Very High Resolution Radiometer*. Taylor and Francis, London, England.

- d'Almeida, G. A., Koepke, P., Shettle, E. P., 1991. *Atmospheric Aerosols Global Climatology and Radiative Characteristics*. A. Deepak Publishing, Hampton, Virginia, USA.
- Danaher, T., Wu, X., Campbell, N., 2001. Bi-directional reflectance distribution function approach to radiometric calibration of landsat ETM+ imagery. In: *IEEE International Geoscience and Remote Sensing Symposium*. Vol. 6. pp. 2654–2657.
- Dingirard, M., Slater, P. N., 1999. Calibration of space-multispectral imaging sensors: A review. *Remote Sensing of Environment* 68, 194–205.
- Dubovik, O., Holben, B., Eck, T. F., Smirnov, A., Kaufman, Y. J., King, M. D., Tanré, D., Slutsker, I., 2002. Variability of absorption and optical properties of key aerosol types observed in worldwide locations. *Journal of the Atmospheric Sciences* 59, 590–608.
- Eckstein, B. A., Simpson, J. J., 1991. Aerosol and Rayleigh radiance contributions to coastal zone color scanner images. *International Journal of Remote Sensing* 12 (1), 135–168.
- Fligge, M., Solanki, S., Pap, J., Fröhlich, C., Wehrli, C., 2001. Variations of solar spectral irradiance from near UV to the infrared—measurements and results. *Journal of Atmospheric and Solar-Terrestrial Physics* 63, 1479–1487.
- Formenti, P., Winkler, H., Fourie, P., Piketh, S., Makgopa, B., Helas, G., Andreae, M., 2002. Aerosol optical depth over a remote semi-arid region of South Africa from spectral measurements of the daytime solar extinction and nighttime stellar extinction. *Atmospheric Research* 62, 11–32.
- Fraser, R. S., Kaufman, Y. J., 1985. The relative importance of aerosol scattering and absorption in remote sensing. *IEEE Transactions on Geoscience and Remote Sensing* GE-23 (5), 625–633.
- Fröhlich, C., Shaw, G., 1980. New determination of Rayleigh scattering in the terrestrial atmosphere. *Applied Optics* 19 (11), 1773–1775.
- Fung, T., LeDrew, E., 1987. Application of principal components analysis to change detection. *Photogrammetric Engineering and Remote Sensing* 53 (12), 1649–1658.

- Furby, S., 2000. Registration, calibration and thresholding training course. Tech. Rep. Course Notes, Australian Greenhouse Office Land Clearing and Vegetation Regrowth Consultancy, CSIRO Mathematical and Information Sciences, Floreat WA, 6014.
- Furby, S., Campbell, N., 2001. Calibrating images from different dates to 'like-value' digital counts. *Remote Sensing of Environment* 77, 186–196.
- Gao, B.-C., Kaufman, Y., 1999. The MODIS near-IR water vapor algorithm. Tech. Rep. MOD05 - Total Precipitable Water, Algorithm Technical Background Document.
- Gatebe, C. K., King, M. D., Tsay, S.-C., Ji, Q., Arnold, T., Li, J. Y., 2001. Sensitivity of off-nadir zenith angles to correlation between visible and near-infrared reflectance for use in remote sensing of aerosol over land. *IEEE Transactions in Geoscience and Remote Sensing* 39 (4), 805–819.
- Gilabert, M. A., Conese, C., Maselli, F., 1994. An atmospheric correction method for the automatic retrieval of surface reflectances from TM images. *International Journal of Remote Sensing* 15 (10), 2065–2086.
- Goetz, A. F. H., Vane, G., Solomon, J. E., Rock, B. N., 1985. Imaging spectrometry for Earth remote sensing. *Science* 228, 1147–1153.
- Gong, P., 1993. Change detection using principal component analysis and fuzzy set theory. *Canadian Journal of Remote Sensing* 19 (1), 22–29.
- Goward, S. N., Masek, J., 2001. Landsat—30 years and counting. *Remote Sensing of Environment* 78, 1–2.
- Graetz, R. D., Fisher, R. P., Wilson, M. A., 1992. Looking Back: The Changing Face of The Australian Continent, 1972–1992. COSSA Publication No. 029, CSIRO Office of Space Science and Application, GPO Box 3023, Canberra ACT, Australia.
- Hall, F., Strebel, D., Nickeson, J., Goetz, S., 1991. Radiometric rectification: Towards a common radiometric response among multirate, multisensor images. *Remote Sensing of Environment* 35, 11–27.
- Harrison, L., Michalsky, J., 1994. Objective algorithm for the retrieval of optical depths from ground-based measurements. *Applied Optics* 33 (22), 5126–5132.

- Hill, J., Sturm, B., 1988. Image-based atmospheric correction of multi-temporal thematic mapper data for agricultural land cover classification. *Proceedings of IGARSS'88 Symposium*, Edinburgh, Scotland, 13-16 Sept. 1988 , 895–899.
- Holben, B. N., Eck, T. F., Slutsker, I., Tanré, D., Buis, J. P., Setzer, A., Vermote, E., Reagan, J. A., Kaufman, Y. J., Nakajima, T., Lavenu, F., Jankowiak, I., Smirnov, A., 1998. AERONET - A federated instrument network and data archive for aerosol characterization. *Remote Sensing of Environment* 66, 1–16.
- Huete, A. R., 1988. A soil-adjusted vegetation index (SAVI). *Remote Sensing of Environment* 25, 295–309.
- Huete, A. R., Liu, H. Q., Batchily, K., van Leeuwen, W., 1997. A comparison of vegetation indices over a global set of TM images for EOS-MODIS. *Remote Sensing of Environment* 59, 440–451.
- Jensen, J. R., 1996. *Introductory Digital Image Processing: A Remote Sensing Perspective*. Prentice-Hall, Inc., New Jersey, USA.
- Joseph, J., Wiscombe, W., Weinman, J., 1976. The delta-eddington approximation for radiative flux transfer. *Journal of Atmospheric Sciences* 33, 2452–2459.
- Junge, C., 1963. *Air Chemistry and Radioactivity*. Academic Press, New York, USA.
- Karnieli, A., Kaufman, Y., Remer, L., Wald, A., 2001. AFRI – aerosol free vegetation index. *Remote Sensing of Environment* 77, 10–21.
- Kaufman, Y. J., 1984. Atmospheric effects on remote sensing of surface reflectance. *SPIE* 475, 20–633.
- Kaufman, Y. J., Brakke, T. W., 1986. Field experiment for measurement of the radiative characteristics of a hazy atmosphere. *Journal of the Atmospheric Sciences* 43 (11), 1135–1151.
- Kaufman, Y. J., Holben, B. N., 1993. Calibration of the AVHRR visible and near-ir bands by atmospheric scattering, ocean glint and desert reflection. *International Journal of Remote Sensing* 14 (1), 21–52.

- Kaufman, Y. J., Remer, L., 1994. Detection of forests using the mid-IR reflectance: An application for aerosol studies. *IEEE Transactions on Geoscience and Remote Sensing* 32 (3), 672–683.
- Kaufman, Y. J., Tanré, D., 1992. Atmospherically resistant vegetation index (ARVI) for EOS-MODIS. *IEEE Transactions on Geoscience and Remote Sensing* 30 (2), 261–270.
- Kaufman, Y. J., Tanré, D., 1996a. Strategy for direct and indirect methods for correcting the aerosol effect on remote sensing: from AVHRR to EOS-MODIS. *Remote Sensing of Environment* 55, 65–79.
- Kaufman, Y. J., Tanré, D., 1996b. Strategy for direct and indirect methods for correcting the aerosol effect on remote sensing: From AVHRR to EOS-MODIS. *Remote Sensing of Environment* 55, 65–79.
- Kaufman, Y. J., Tanré, D., Gordon, H. R., Nakajima, T., Lenoble, J., Frouin, R., Grassl, H., Herman, B. M., King, M. D., Teillet, P. M., 1997a. Passive remote sensing of tropospheric aerosol and atmospheric correction for aerosol effect. *Journal of Geophysical Research* 102 (D14), 16815–16830.
- Kaufman, Y. J., Tanré, D., Remer, L. A., Vermote, E. F., Chu, A., Holben, B. N., 1997b. Operational remote sensing of tropospheric aerosol over land from EOS moderate resolution imaging spectrometer. *Journal of Geophysical Research* 102 (D14), 17051–17067.
- Kaufman, Y. J., Wald, A., Remer, L., Gao, B.-C., Li, R.-R., Flynn, L., 1997c. The MODIS 2.1 μ m channel – correlation with visible reflectance for use in remote sensing of aerosol. *IEEE Transactions on Geoscience and Remote Sensing* 35 (5), 1286–1298.
- Kiiveri, H. T., Caccetta, P., 1996. Some statistical models for remotely sensed data. in ‘SISC96 Imaging Interface Workshop Proceedings’, Sydney , 35–42.
- Kiiveri, H. T., Caccetta, P., 1998. Data fusion, uncertainty and causal probabilistic networks for monitoring the salinisation of farmland. *Digital Signal Processing* 8, 225–230.
- Kiiveri, H. T., Caccetta, P., Evans, F., 2001. Use of conditional probability networks for environmental monitoring. *International Journal of Remote Sensing* 22 (7), 1173–1190.

- Kiiveri, H. T., Campbell, N. A., 1992. Allocation of remotely sensed data using Markov models for image data and pixel labels. *Australian Journal of Statistics* 34 (3), 361–374.
- King, M., Byrne, D., 1976. A method for inferring total ozone content from the spectral variation of total optical depth obtained with a solar radiometer. *Journal of Atmospheric Sciences* 33, 2242–2251.
- King, M. D., Herring, D. D., 2000. Monitoring Earth's vital signs. *Scientific American* April, 72–77.
- King, M. D., Kaufman, Y. J., Menzel, W. P., Tanré, D., 1992. Remote sensing of cloud, aerosol, and water vapour properties from the Moderate Resolution Imaging Spectrometer (MODIS). *IEEE Transactions on Geoscience and Remote Sensing* 30 (1), 2–27.
- King, M. D., Kaufman, Y. J., Tanré, D., Nakajima, T., 1999. Remote sensing of tropospheric aerosols from space: past present and future. *Bulletin of the American Meteorological Society* 80 (11), 2229–2259.
- Kumar, L., Schmidt, K., Dury, S., Skidmore, A., 2001. Imaging Spectrometry and Vegetation Science. in *Imaging Spectrometry*, F.D. van der Meer and S.M. de Jong (eds). Kluwer Academic Publishers, Netherlands, pp. 111–155.
- Liang, S., Fallah-Adl, H., Kalluri, S., JáJá, J., Kaufman, Y. J., Townshend, J. R. G., 1997. An atmospheric correction algorithm for Landsat thematic mapper imagery over land. *Journal of Geophysical Research* 102 (D14), 17173–17186.
- List, R. J., 1949. *Smithsonian Meteorological Tables*, 6th Edition. Smithsonian Institution Press, publication 4014.
- Loudon, R., 1983. *The Quantum Theory of Light*. Oxford University Press Inc., New York, USA.
- Marcar, N., Crawford, D., Leppert, P., Javanovic, T., Floyd, R., Farrow, R., 1995. *Trees for Saltland: a guide to selecting native species for Australia*. CSIRO Press, PO Box 89, 314 Albert St., East Melbourne, Victoria 3002, Australia.

- Markham, B. L., Barker, J. L., 1986. Landsat MSS and TM post-calibration dynamic ranges, exoatmospheric reflectances and at-satellite temperatures. Tech. Rep. 1, EOSAT Landsat Technical Notes – New Look-Up Tables.
- Mather, P. M., 1987. Computer Processing of Remotely-sensed Images: An Introduction. John Wiley, Chichester.
- Mather, P. M., 1999. Computer Processing of Remotely-sensed Images: An Introduction, 2nd Ed. John Wiley, Chichester.
- McPeters, R., Bhartia, P., Krueger, A., Herman, J., Wellemeyer, C., Seftor, C., Jaross, G., Torres, O., Moy, L., Labow, G., Byerly, W., Taylor, S., Swissler, T., Chebula, R., 1998. Earth probe total ozone mapping spectrometer TOMS data products users guide. Tech. Rep. 1998-206895, National Aeronautics and Space Administration, NASA Goddard Space Flight Center, Greenbelt, Maryland 20771 USA.
- Miura, T., Huete, A. R., Yoshioka, H., Holben, B. N., 2001. An error and sensitivity analysis of atmospheric resistant vegetation indices derived from dark target-based atmospheric correction. *Remote Sensing of Environment* 78, 284–298.
- Moran, M. S., Bryant, R., Thome, K., Ni, W., Nouvellon, Y., Gonzalez-Dugo, M. P., Qi, J., Clarke, T., 2001. A refined empirical line approach for reflectance factor retrieval from Landsat-5 TM and Landsat ETM+. *Remote Sensing of Environment* 78, 71–82.
- Moran, M. S., Jackson, R. D., Clarke, T. R., Qi, J., Cabot, F., Thome, K. J., Markham, B. L., 1995. Reflectance factor retrieval from landsat TM and SPOT HRV data for bright and dark targets. *Remote Sensing of Environment* 52, 218–230.
- Moran, M. S., Jackson, R. D., Slater, P. N., Teillet, P. M., 1992. Evaluation of simplified procedures for retrieval of land surface reflectance factors from satellite sensor output. *Remote Sensing of Environment* 41, 169–184.
- Neckel, H., Labs, D., 1984. The solar radiation between 3300 and 12500 Å. *Solar Physics* 90, 205–258.
- Nielsen, A. A., Conradsen, K., Simpson, J. J., 1998. Multivariate alteration detection (MAD) and MAF postprocessing in multitemporal, bispectral image data: New approaches to change detection studies. *Remote Sensing of Environment* 64, 1–19.

- Niemelä, S., Räisänen, P., Savijärvi, H., 2001. Comparison of surface radiative flux parameterizations Part II. Shortwave radiation. *Atmospheric Research* 58, 141–154.
- Ouaidrari, H., Vermote, E., 1999. Operational atmospheric correction of Landsat TM data. *Remote Sensing of Environment* 70, 4–15.
- Palmer, M., 1995. Calibration of a TM image to absolute reflectance. Tech. Rep. Technical Report, CSIRO Division of Mathematics and Statistics, Private Bag P.O. Wembley WA, 6014.
- Paltridge, G. W., Mitchell, R. M., 1990. Atmospheric and view angle correction of vegetation indices and grassland fuel moisture content derived from NOAA/AVHRR. *Remote Sensing of Environment* 31, 121–135.
- Peck, E., Reeder, K., 1972. Dispersion of air. *Journal of the Optical Society of America* 62 (8), 958–962.
- Prata, A., 1996. A new long-wave formula for estimating downward clear-sky radiation at the surface. *Quarterly Journal of the Royal Meteorological Society* 122, 1127–1151.
- Prata, A., 2000. Precipitable water retrieval from multi-filter rotating shadowband radiometer measurements. Tech. Rep. 47, CSIRO Atmospheric Research, CSIRO Atmospheric Research, PB 1, Aspendale, Victoria 3195, Australia.
- Prata, A., Rutter, G., 2001. Cal/val activities at the CIGSN Uardry field site, NSW: Australia in support of the EO-1 mission. unpublished .
- Prata, A. J., Cechet, R. P., Grant, I. F., Barton, I. J., 1997. Investigation of land surface radiation budgets using ATSR/ATSR-2 data. In: *Proc. 3rd ERS Symp. on Space at the service of our Environment*. Vol. 3 Vols of ESA SP-414. pp. 1795–1807.
- Remer, L. A., Wald, A. E., Kaufman, Y. J., 2001. Angular and seasonal variations of spectral surface reflectance ratios: Implications for remotes sensing of aerosol over land. *IEEE Transactions in Geoscience and Remote Sensing* 39 (2), 275–283.
- Richards, G., Furby, S., 2002. Sub-hectare land cover monitoring; developing a national scale time-series program. in *proceedings of the 11th Australasian Remote Sensing and Photogrammetry Conference*, Brisbane, Sept. 2–6, 2002 , 16–24.

- Richards, J. A., Jia, X., 1999. *Remote Sensing Digital Image Analysis: An introduction*, 3rd edn. Springer-Verlag, Berlin, Germany.
- Ridd, M. K., Liu, J., 1998. A comparison of four algorithms for change detection in an urban environment. *Remote Sensing of Environment* 63, 95–100.
- Roberts, D., Green, R., Adams, J., 1997. Temporal and spatial patterns in vegetation and atmospheric properties from AVIRIS. *Remote Sensing of Environment* 62, 223–240.
- Roderick, M., Smith, R., Lodwick, G., 1996. Calibrating long-term AVHRR-derived NDVI imagery. *Remote Sensing of Environment* 58, 1–12.
- Roderick, M. L., 1994. Satellite derived vegetation indices for monitoring seasonal vegetation conditions in Western Australia. Ph.D. thesis, School of Surveying and Land Information, Curtin University of Technology, Perth, W.A., Australia.
- Roujean, J.-L., Leroy, M., Deschamps, P.-Y., 1992. A bidirectional reflectance model of the earth's surface for the correction of remote sensing data. *Journal of Geophysical Research* 97 (D18), 20455–20468.
- Rousseeuw, P. J., Leroy, A. M., 1987. *Robust Regression and Outlier Detection*. Wiley Series in Probability and Mathematical Statistics, New York, USA.
- Schott, J., Salvaggio, C., Volchok, W., 1988. Radiometric scene normalisation using pseudoinvariant features. *Remote Sensing of Environment* 26, 1–16.
- Sing, A., 1989. Digital change detection techniques using remotely sensed data. *International Journal of Remote Sensing* 10 (6), 989–1003.
- Slater, P. N., Biggar, S. F., Holm, R. G., Jackson, R. D., Mao, Y., Moran, M., Palmer, J. M., Yuan, B., 1987. Reflectance- and radiance-based methods for the in-flight absolute calibration of multispectral sensors. *Remote Sensing of Environment* 22, 11–37.
- Slater, P. N., Biggar, S. F., Palmer, J. M., Thome, K. J., 2001. Unified approach to absolute radiometric calibration in the solar-reflective range. *Remote Sensing of Environment* 77, 293–303.

- Small, C., 2002. Multitemporal analysis of urban reflectance. *Remote Sensing of Environment* 81, 427–442.
- Stephens, G. L., 1994. *Remote Sensing of the Lower Atmosphere: An Introduction*. Oxford University Press, New York, USA.
- Switzer, P., Green, A., 1984. Min/max autocorrelation factors for multivariate spatial imagery. Tech. Rep. Technical Report, No. 6, Department of Statistics, Stanford University, Stanford, USA.
- Tanré, D., Deroo, C., Duhaui, P., Herman, M., Morcrette, J. J., Perbos, J., Deschamps, P. Y., 1986. Simulation of the satellite signal in the solar spectrum. Tech. Rep. User's Manual, Laboratoire d'Optique Atmosphérique. Université des Sciences et Techniques de Lille, 59655 Villeneuve d'Ascq Cédex, France.
- Tanré, D., Herman, M., Deschamps, P., 1981. Influence of the background contribution upon space measurements of ground reflectance. *Applied Optics* 20 (20), 3676–3686.
- Tanré, D., Herman, M., Deschamps, P., 1983. Influence of the atmosphere on space measurements of directional properties. *Applied Optics* 22 (5), 733–741.
- Tanré, D., Herman, M., Deschamps, P., A. de Lefte, 1979. Atmospheric modeling for space measurements of ground reflectance, including bidirectional properties. *Applied Optics* 18 (21), 3587–3594.
- Teillet, P., 1990. Rayleigh optical depth comparisons from various sources. *Applied Optics* 29 (13), 1897–1900.
- Teillet, P. M., 2002. Email correspondence – TM/ETM+ responsivities – pers. comm.
- Teillet, P. M., Barker, J. L., Markham, B. L., Irish, R. R., Fedosejevs, G., Storey, J. C., 2001. Radiometric cross-calibration of the Landsat-7 ETM+ and Landsat-5 TM sensors based on tandem data sets. *Remote Sensing of Environment* 78, 39–54.
- Teillet, P. M., Fedosejevs, G., 1995. On the dark target approach to atmospheric correction of remotely sensed data. *Canadian Journal of Remote Sensing* 21 (4), 374–387.
- Thome, K., Markham, B., Barker, J., Slater, P., Biggar, S., 1997. Radiometric calibration of Landsat. *Photogrammetric Engineering and Remote Sensing* 63 (7), 853–858.

- Thome, K. J., 2001. Absolute radiometric calibration of Landsat 5 ETM+ using the reflectance-based method. *Remote Sensing of Environment* 78, 27–38.
- Thome, K. J., Gellman, D. I., Parada, R. J., Biggar, S. F., Slater, P. N., Moran, M. S., 1993. In-flight radiometric calibration of Landsat-5 thematic mapper from 1984 to present. in *Proceedings of SPIE Conference* 1938.
- Tucker, C. J., 1979. Red and photographic infrared linear combinations for monitoring vegetation. *Remote Sensing of Environment* 8, 127–150.
- Twomey, S., 1977. *Atmospheric Aerosols. Developments in Atmospheric Science, Vol. 7.* Elsevier Scientific Publishing Co., Amsterdam, The Netherlands.
- Venables, W. N., Ripley, B. D., 1999. *Modern Applied Statistics with S-PLUS, Third Ed.* Springer-Verlag, New York, USA.
- Vermote, E., 2002. Email correspondence – correction in 6S output (absorbant) – pers. comm.
- Vermote, E., Tanré, D., Deuzé, J. L., Herman, M., Morcrette, J.-J., 1997a. Second simulation of the satellite signal in the solar spectrum, 6S: An overview. Tech. Rep. User Guide, Version 2, NASA Goddard Space Flight Center-Code 923.
- Vermote, E. F., Tanré, D., Deuzé, J. L., Herman, M., Morcrette, J.-J., 1997b. Second simulation of the satellite signal in the solar spectrum, 6S: An overview. *IEEE Transactions on Geoscience and Remote Sensing* 35 (3), 675–686.
- Wallace, J., Hobbs, P., 1977. *Atmospheric Science: An Introductory Survey.* Academic Press Inc., Florida, USA.
- Walthall, C. L., Norman, J. M., Welles, J. M., Campbell, G., Blad, B. L., 1985. Simple equation to approximate the bidirectional reflectance from the vegetative canopies and bare soil surfaces. *Applied Optics* 24 (3), 383–387.
- Wehr, T., Paulsen, T., Popescu, A., Snoeji, P., d'Andon, O. F., Barrot, G., 2002. Calibration and first results of stellar occultation measurements with GOMOS on Envisat. In: *IEEE International Geoscience and Remote Sensing Symposium and the 24th Canadian Symposium on Remote Sensing. Vol. 1.* pp. 605–607.

- Wu, X., Danaher, T., Wallace, J., Campbell, N., 2001. A BRDF-corrected Landsat 7 mosaic of the Australian continent. In: IEEE International Geoscience and Remote Sensing Symposium. Vol. 7. pp. 3274–3275.
- Yankee Environmental Systems, 1997. MFR-7 rotating shadowband radiometer, installation and user guide. Tech. Rep. Version 2.0, Yankee Environmental Systems, Inc., Airport Industrial Park, 101 Industrial Blvd, Turner Falls, MA 01376, USA.
- Young, A., 1980. Revised depolarization corrections for atmospheric extinction. *Applied Optics* 20 (19), 3427–3428.
- Young, A., 1981. On Rayleigh-scattering optical depth of the atmosphere. *Journal of Applied Meteorology* 20, 328–330.
- Zhao, W., Tamura, M., Takahashi, H., 2001. Atmospheric and spectral corrections for estimating surface albedo from satellite data using 6S code. *Remote Sensing of Environment* 76, 202–212.

APPENDIX A

Equation of State of Water Vapour and Other Useful Formulae

The equation of state for an ideal gas is given by

$$PV = nRT \quad (\text{A.1})$$

where P and T are the pressure and temperature of the gas respectively, V is the volume (in m^3) occupied by the gas, R is the universal gas constant ($8.314 \text{ J K}^{-1} \text{ mol}^{-1}$), and the number of moles of the gas, n , is given as:

$$n = \frac{m_{gas}}{M_{gas}},$$

where m_{gas} denotes the mass of gas (g) contained in the volume and M_{gas} the molecular weight of the gas (g/mol). For one mole of an ideal gas at standard temperature and pressure (STP)

$$P_0 V_0 = RT_0 \quad (\text{A.2})$$

where $P_0 = 1013.25 \text{ hPa}$, $T_0 = 273.16 \text{ K}$, and $V_0 = 22.4 \text{ L} = 2.24 \times 10^{-2} \text{ m}^3$. The density of the gas ρ_{gas} is defined as

$$\rho_{gas} = \frac{m_{gas}}{V} \implies m_{gas} = \rho_{gas} V,$$

thus Eq. (A.1) can be rewritten as

$$PV = \frac{\rho_{gas} V}{M_{gas}} RT$$

which, after manipulation with Eq. (A.2) gives the density of the gas

$$\rho_{gas} = \left(\frac{M_{gas}}{V_0}\right) \left(\frac{T_0}{T}\right) \left(\frac{P}{P_0}\right). \quad (\text{A.3})$$

In the case of dry air, composed of 78.08% N_2 (molecular weight 28.1 g/mol), 20.95% O_2 (molecular weight 32 g/mol) and 0.93% Ar (molecular weight 39.9 g/mol), and also

noting that at STP, 1 mole of the gas occupies $2.24 \times 10^{-2} \text{ m}^3$, Eq. (A.3) calculates the density of dry air as,

$$\rho_{da} = 1.292 \times 10^{-3} \left(\frac{T_0}{T} \right) \left(\frac{P}{P_0} \right). \quad (\text{A.4})$$

The equation of state for water vapour takes on a form similar to Eq. (A.1) and is given by

$$e = \rho_{wv} \frac{R}{M_{wv}} T, \quad (\text{A.5})$$

where R and T have been defined previously, e is the water vapour pressure (hPa), ρ_{wv} is the density of water vapour and M_{wv} is the molecular weight of water vapour. The water vapour pressure represents the contribution that water vapour makes to the total atmospheric pressure. Given estimates of pressure, temperature and relative humidity (RH), the vapour pressure can be calculated with the following expression:

$$e = e_s f_w RH, \quad (\text{A.6})$$

where e_s is the saturation vapour pressure, representing the total amount of moisture that air can hold at a given temperature, and f_w is a non-ideal gas scaling factor calculated as

$$f_w = 1 + 0.005 \left(\frac{P}{P_0} \right).$$

The saturation vapour pressure can be determined using the expression given in List (1949, p. 350)

$$\begin{aligned} \log_{10}(e_s) = A_1 \left(\frac{T_s}{T} - 1 \right) &+ A_2 \log_{10} \left(\frac{T_s}{T} \right) + A_3 \left(10^{E_1(1-T/T_s)} - 1 \right) \\ &+ A_4 \left(10^{E_1(T_s/T-1)} \right) + \log_{10}(P_0), \end{aligned} \quad (\text{A.7})$$

where $A_1 = -7.90298$, $A_2 = 5.02808$, $A_3 = -1.3816 \times 10^{-7}$, $A_4 = 8.1328 \times 10^{-3}$, $E_1 = 11.344$, $E_2 = -3.49149$ and T_s is the steam-point temperature ($= 373.16\text{K}$).

APPENDIX B

Ozone Absorption Coefficients for the Uardry MFRSR

The Uardry MFRSR has six narrow bands. The first five bands are positioned in such a way so as to avoid atmospheric water vapour absorption; the sixth band however is located in a prominent water vapour absorption feature around 940 nm (see Figure B.1). The bands centred around 500.6, 615 and 672.8 nm are located in the Chappuis band and are thus the most significantly affected by atmospheric ozone. For these bands, it is important to know the ozone optical thickness if one is to retrieve an estimate of aerosol optical thickness from the MFRSR measurements.

Recall from Eq. (2.15, p. 27) that, given an estimate of the ozone concentration (DU or atms-cm), τ_{O_3} can be computed at any wavelength if the ozone absorption coefficients, α_{O_3} , are known. Using the ozone transmittances modelled with MODTRAN4 for five standard atmospheric profiles, and the filter response functions of the Uardry MFRSR, ozone absorption coefficients were computed. They are given in Table B.1.

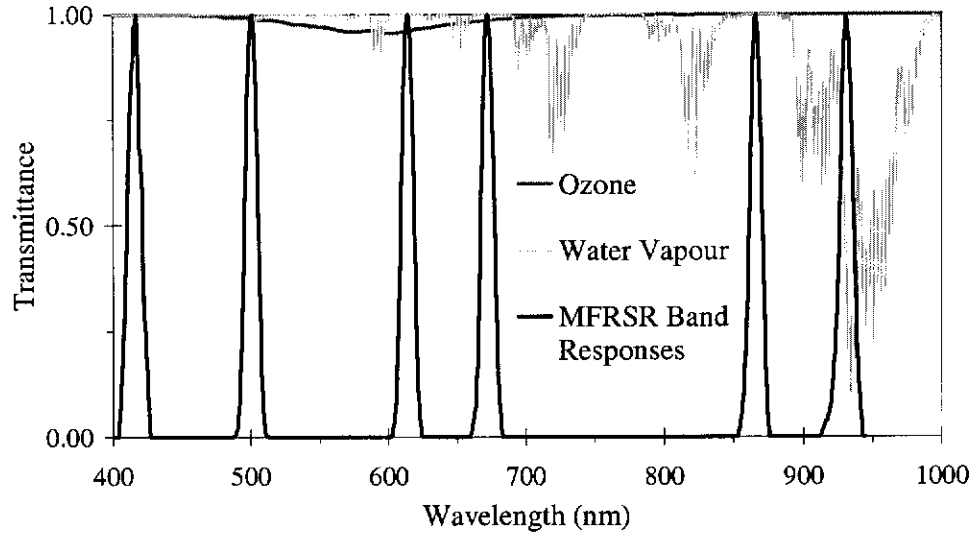


Figure B.1: The Uardry MFRSRS' spectral response curves, superimposed on MODTRAN4 simulations of mid-latitude summer ozone and water vapour transmittances.

Table B.1: Ozone absorption coefficients $\alpha_{O_3\lambda}$ (cm^{-1}) derived from MODTRAN4 ozone data for the 5 standard model profiles. The profiles are: mid-latitude summer (MLS); mid-latitude winter (MLW); sub-arctic summer (SubS); sub-arctic winter (SubW); and tropical (TROP).

Model Profile	500.6 nm	615.0 nm	672.8 nm
MLS	3.263×10^{-2}	1.191×10^{-1}	4.264×10^{-2}
MLW	3.241×10^{-2}	1.189×10^{-1}	4.249×10^{-2}
SubS	3.268×10^{-2}	1.191×10^{-1}	4.266×10^{-2}
SubW	3.237×10^{-2}	1.189×10^{-1}	4.248×10^{-2}
TROP	3.256×10^{-2}	1.189×10^{-1}	4.261×10^{-2}

APPENDIX C

Some radiosonde data for Western Australia, February 6, 2000

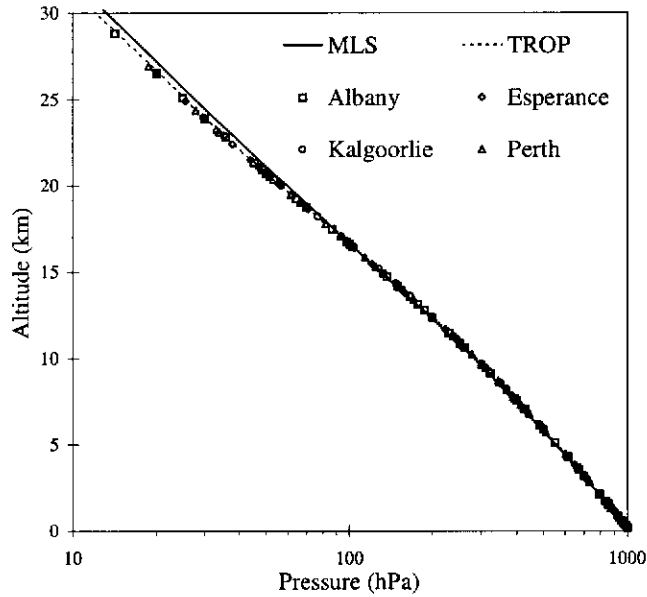
Radiosondes are launched from Australian Bureau of Meteorology (ABoM) stations located around Western Australia. Four locations used in this thesis were Albany, Esperance, Kalgoorlie-Boulder and Perth (Figure C.1). Figures C.2(a) and (b) contain the pressures and temperatures measured respectively by the radiosondes launched from the 4 locations at 0900 hours local time on February 6, 2000. Whilst these data belong to the ABoM, they were made accessible via a website maintained by the Univeristy of Wyoming, Department of Atmospheric Science

<http://weather.uwyo.edu/upperair/sounding.html>.

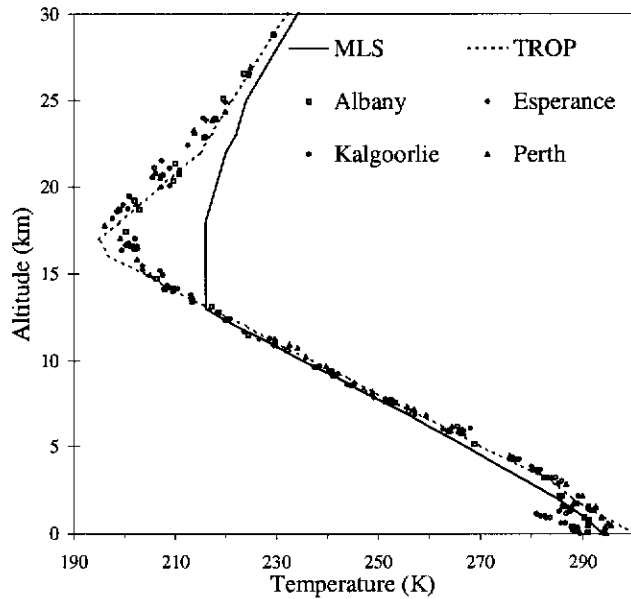
For comparison purposes, the model mid-latitude summer and tropical pressure and temperature profiles are also displayed.



Figure C.1: A map of Western Australia highlighting the location of the Australian Bureau of Meteorology radiosonde launch sites. Also illustrated is the location of the Mt. Barker scene, WRS 111/84.



(a)



(b)

Figure C.2: Plots of (a) pressure and (b) temperature profiles recorded by the radiosondes launched from Albany, Esperance, Kalgoorlie and Perth at 0900 hours on February 6, 2000. Model profiles of pressure and temperature for simulated mid-latitude summer (MLS) and tropical (TROP) conditions are also presented.

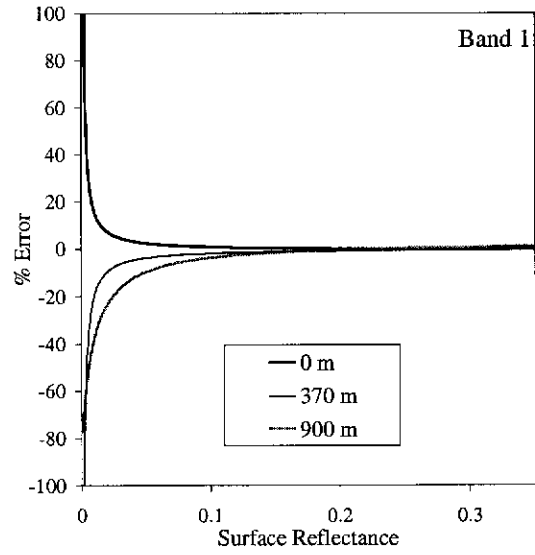
APPENDIX D

Effect of Variation in Elevation in the Reference Image for Mt. Barker

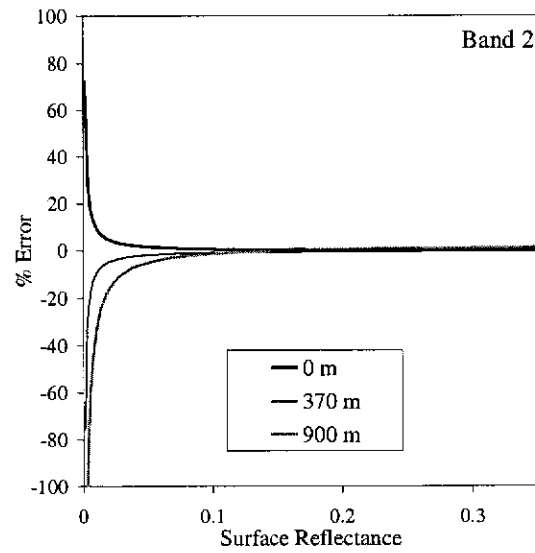
The elevation of terrain in the Mt. Barker scene ranges from $z = 0$ m (sea level) to $z \sim 900$ m. The 6S code was used to compute the image correction coefficients to produce the Mt. Barker reference image from the ETM+ image acquired on February 6, 2000. The code was executed with a median value of terrain elevation of $z = 200$ m. The error that this assumption introduces to surface reflectance estimation over the range of elevations in the Mt. Barker scene are considered below. The error described in the following figures and table is interpreted as the error in surface reflectance estimation if the elevation is assumed to be $z = 200$ m when the true elevation is h , where $h = 0, 370$ or 900 m.

Table D.1: The surface reflectance values, $\rho_{s\lambda}$, above which the error due to the assumption that $z = 200$ m, is less than 5% and 1%.

Band	Lower Limit for $\rho_{s\lambda}$	
	Error < 5%	Error < 1%
1	0.04	0.10
2	0.02	0.07
3	0.01	0.03
4	0.005	0.01
5	0	0
7	0	0

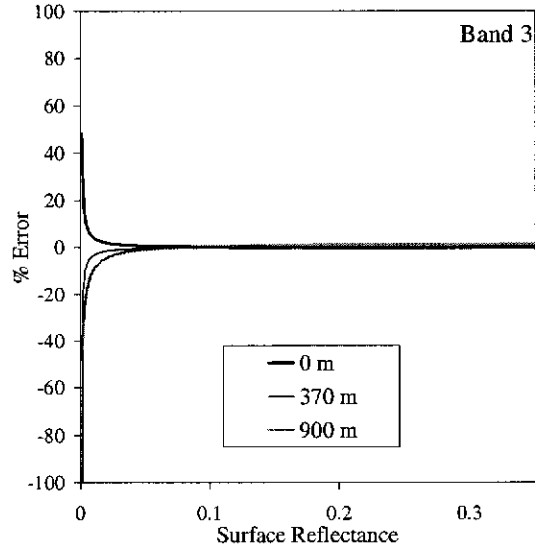


(a)

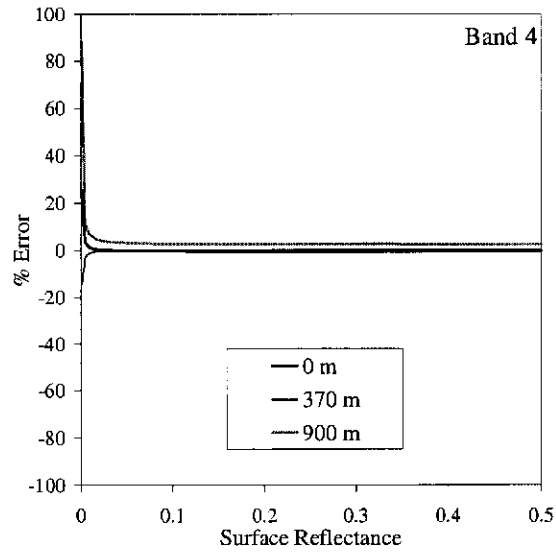


(b)

Figure D.1: Error (%) in the estimate of $\rho_{s\lambda}$ for ETM+ bands (a) 1 and (b) 2 if the elevation $z = 200$ m is used when the true elevation is either 0, 370 or 900 m.

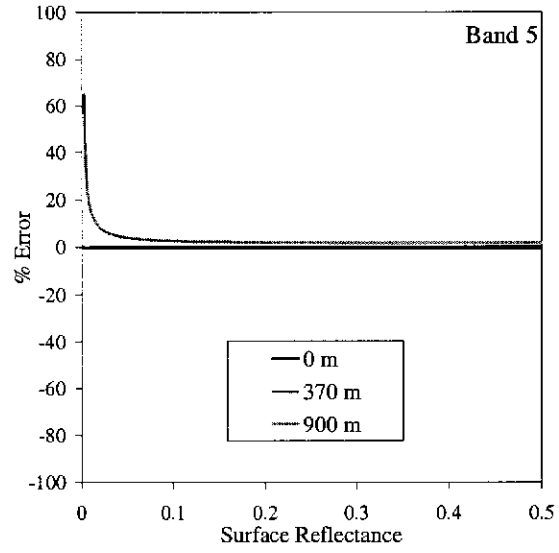


(a)

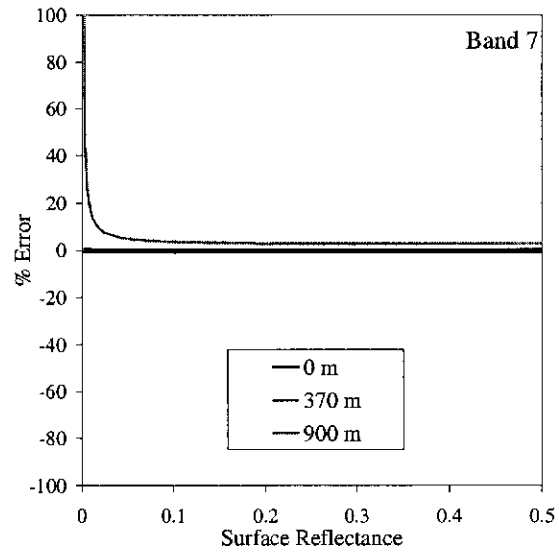


(b)

Figure D.2: Error (%) in the estimate of $\rho_{s\lambda}$ for ETM+ bands (a) 3 and (b) 4 if the elevation $z = 200$ m is used when the true elevation is either 0, 370 or 900 m.



(a)



(b)

Figure D.3: Error (%) in the estimate of $\rho_{s\lambda}$ for ETM+ bands (a) 5 and (b) 7 if the elevation $z = 200$ m is used when the true elevation is either 0, 370 or 900 m.

APPENDIX E

Overpass Like-value Image Normalisation Plots for Hay and Mt. Barker

The following figures contain the like-value image normalisation (LVIN) plots for the overpass images in both the Hay and Mt. Barker sequences. Recall from Section 4.3.4 (p. 147) that Black diamonds represent the data pair $(X_\lambda, \rho_{s\lambda})$ for each pixel associated with a PIT, whilst the modelled path DN for each band is illustrated by a white diamond. Also, each plot contains two fitted lines: A *free-intercept* line (solid), which represents the usual implementation of the like-value procedure described by Furby and Campbell (2001); and a *constrained* (dashed) regression line where the line of best fit is forced to pass through the modelled path DN . Confidence limits about the free-intercept regression line are displayed in grey. For the Hay overpass images (Figures E.1, E.2 and E.3) a 6S calibration line was calculated from atmospheric inputs and is displayed in the figures as a dotted line.

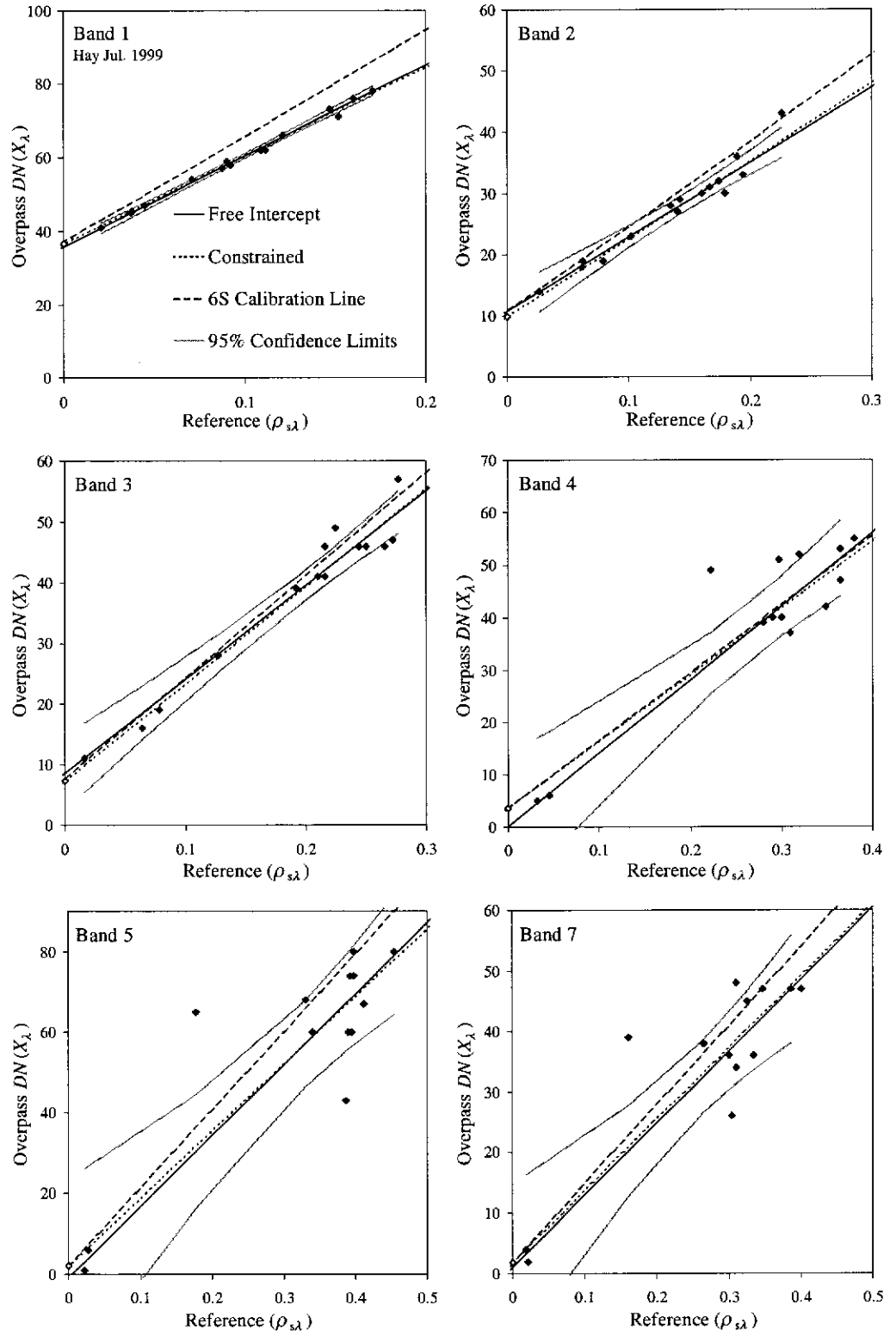


Figure E.1: Landsat-5 TM image for Hay acquired on July 22, 1999.

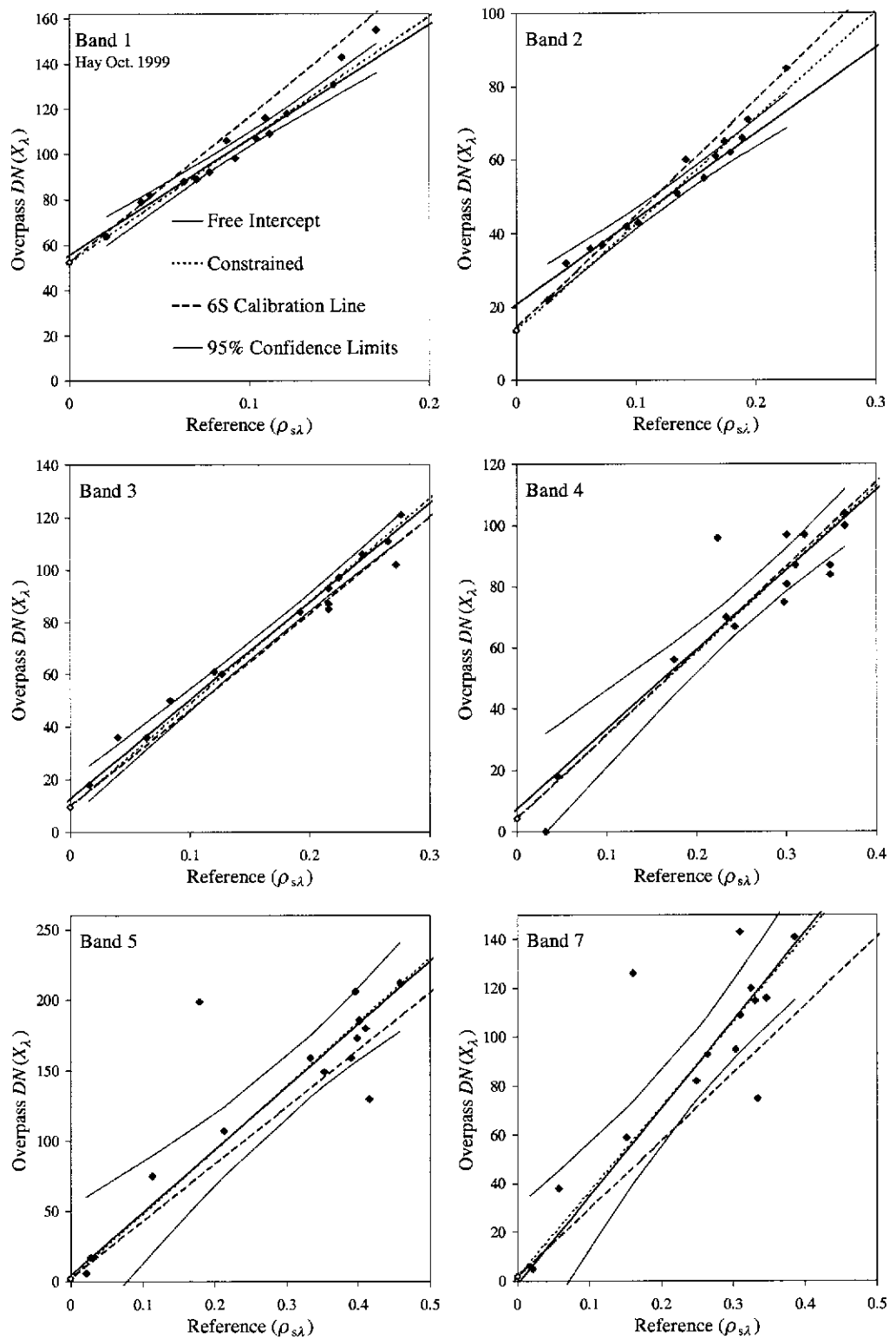


Figure E.2: Landsat-5 TM image for Hay acquired on October 26, 1999.

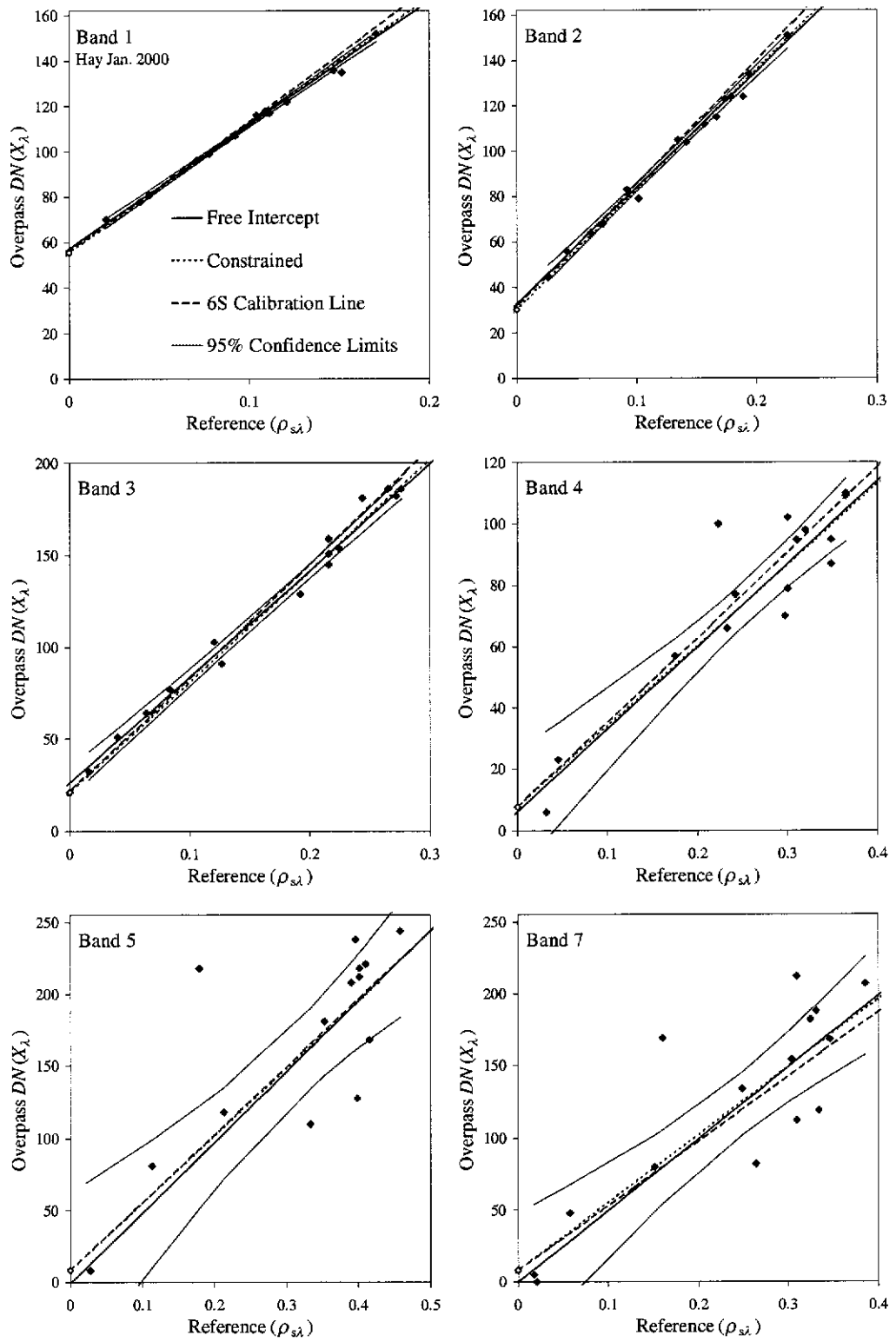


Figure E.3: Landsat-7 ETM+ image for Hay acquired on January 7, 2000.

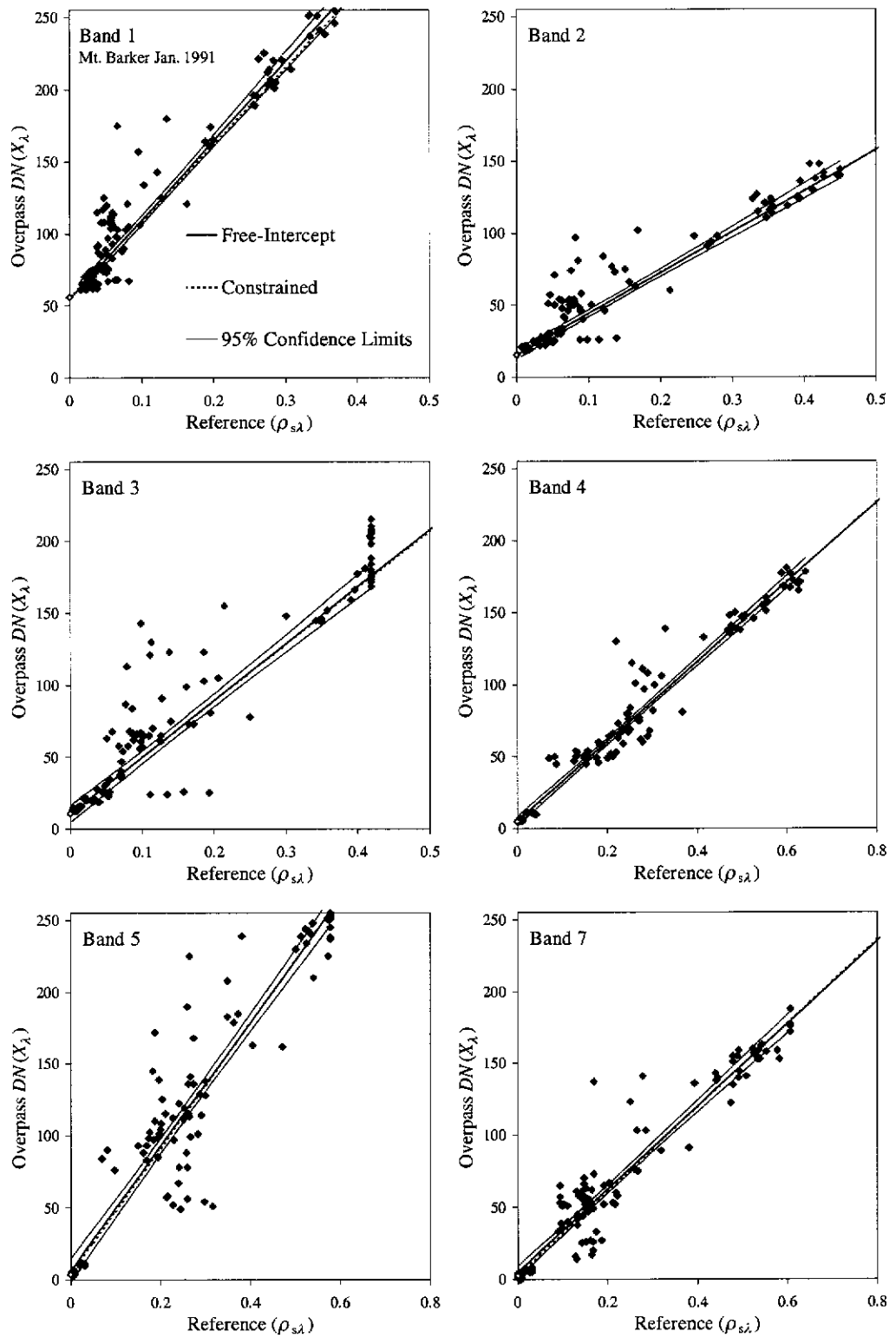


Figure E.4: Landsat-5 TM image for Mt. Barker acquired on January 20, 1991.

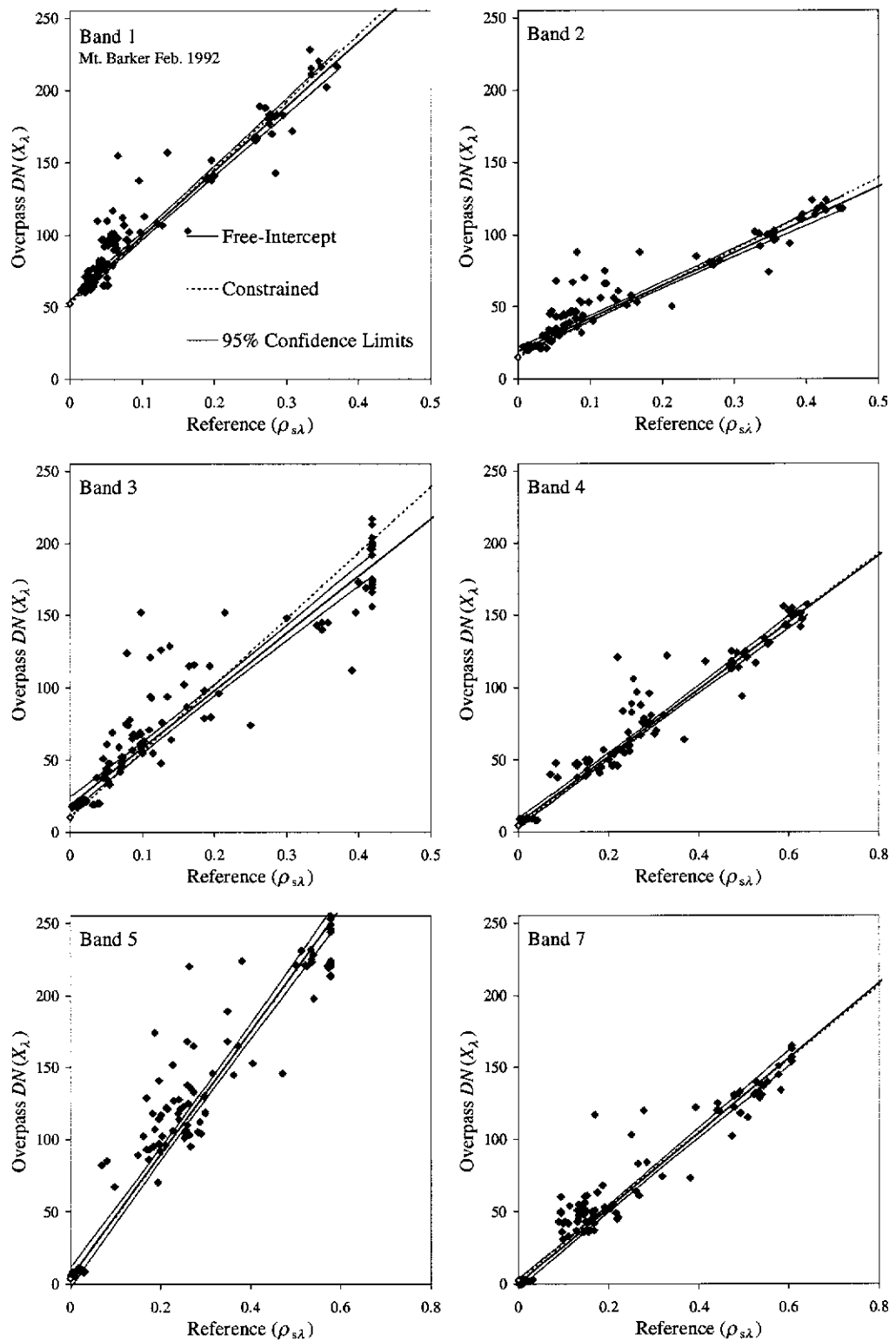


Figure E.5: Landsat-5 TM image for Mt. Barker acquired on February 24, 1992.

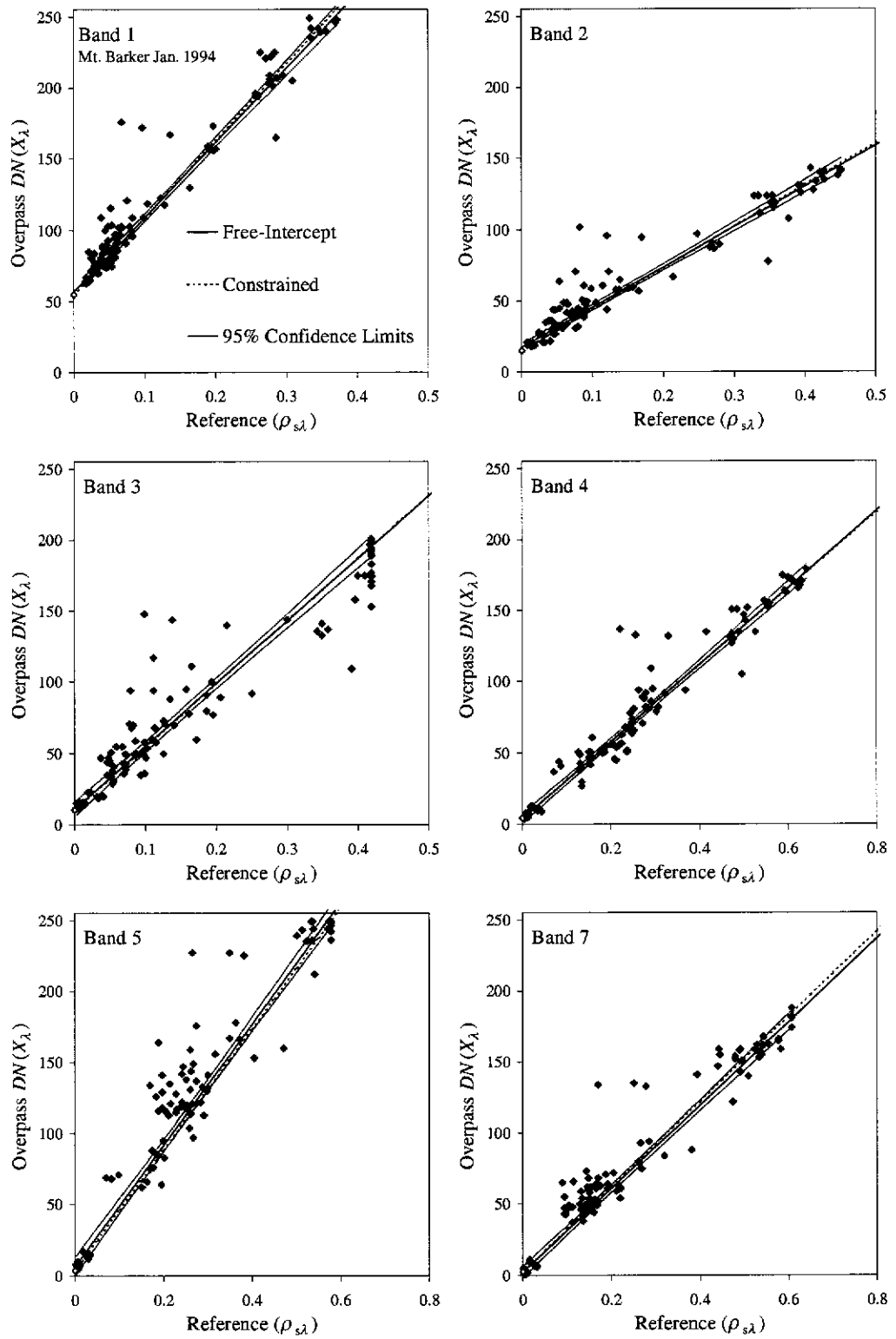


Figure E.6: Landsat-5 TM image for Mt. Barker acquired on January 28, 1994.

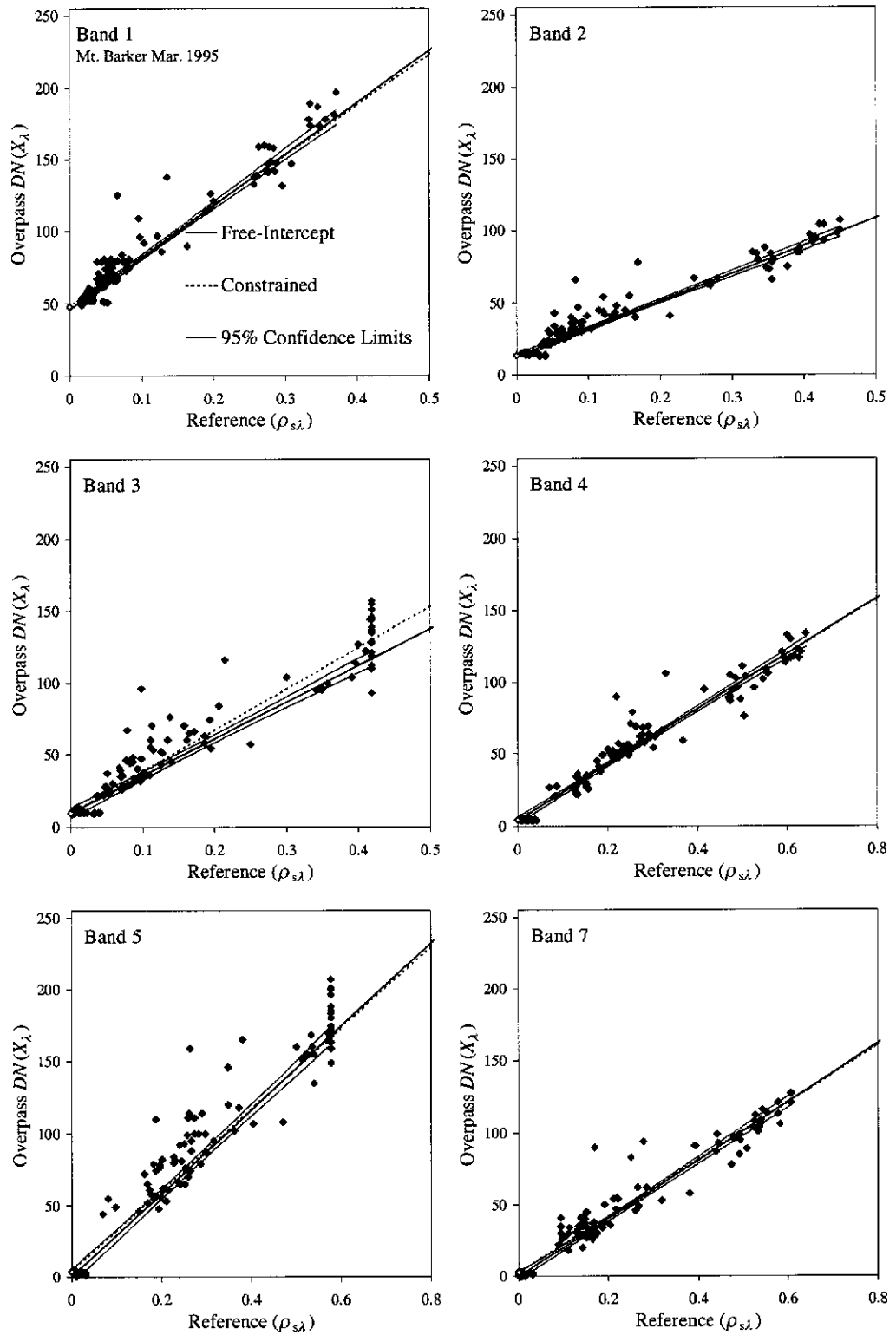


Figure E.7: Landsat-5 TM image for Mt. Barker acquired on March 20, 1995.

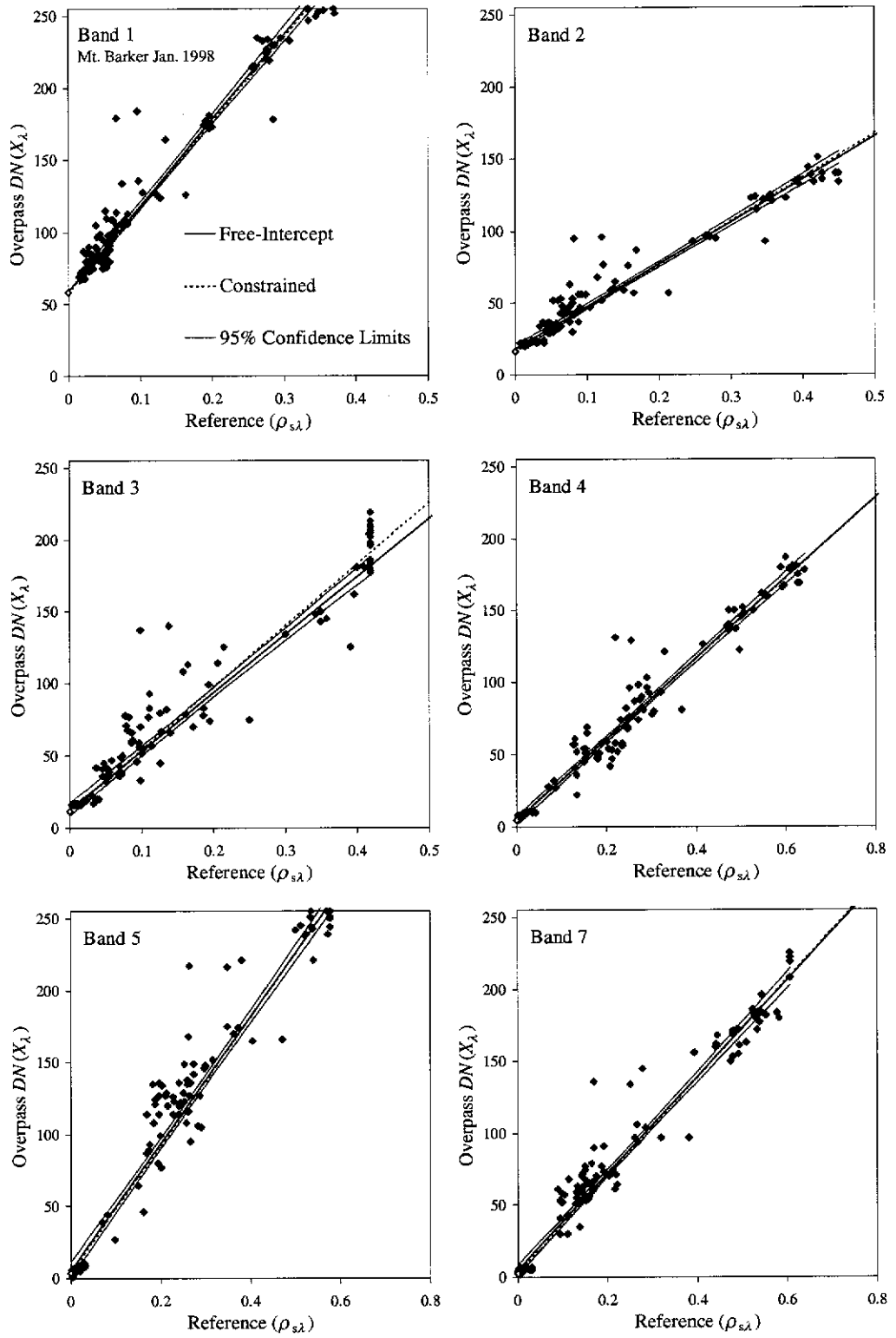


Figure E.8: Landsat-5 TM image for Mt. Barker acquired on January 7, 1998.

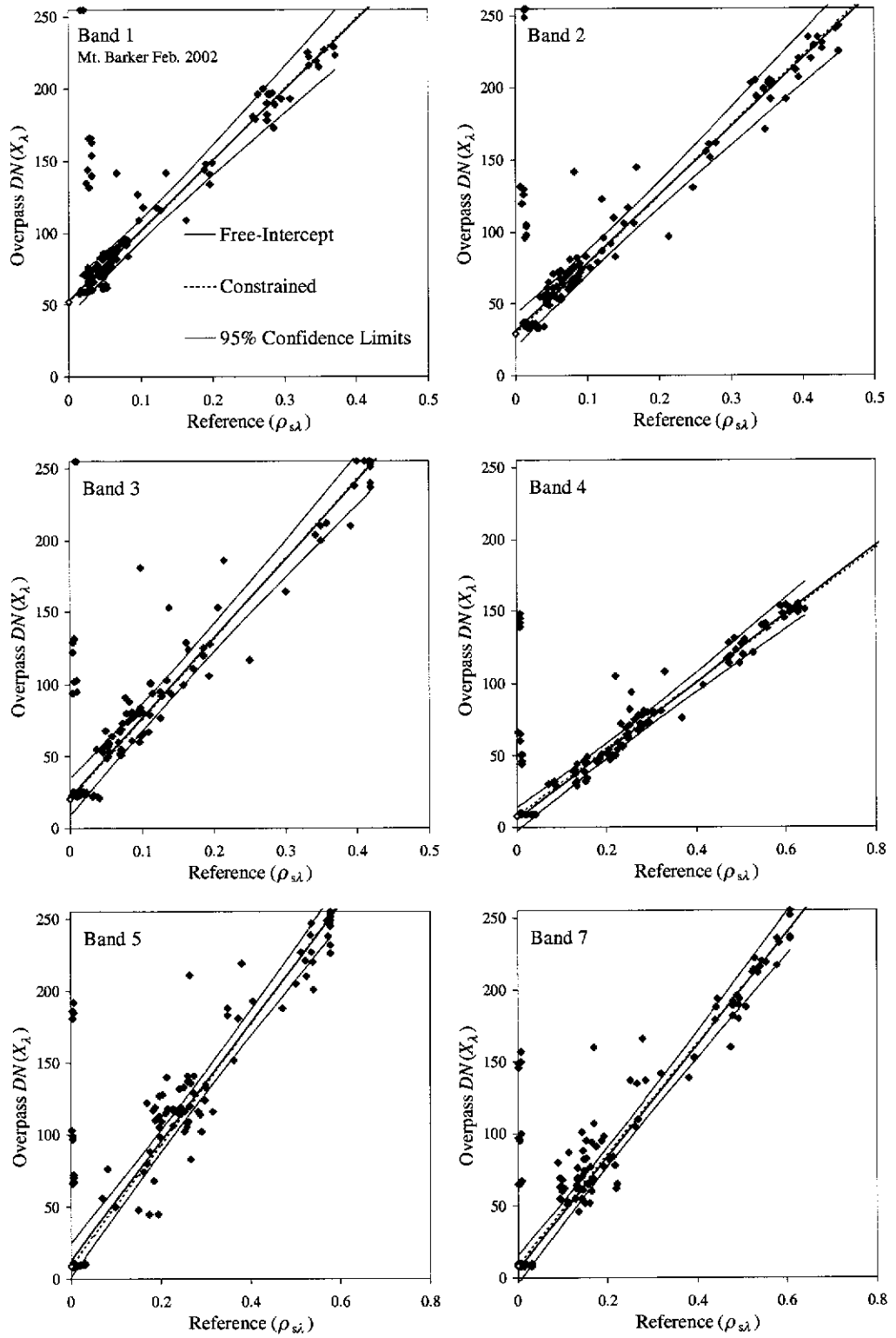


Figure E.9: Landsat-7 ETM+ image for Mt. Barker acquired on February 11, 2002.

APPENDIX F

Comparison of Free-Intercept and Constrained Regression Approaches

In both the Hay and Mt. Barker sequences, a surface reflectance was calculated for each PIT using the free-intercept and constrained regression correction lines, $\rho_{\text{corr}\lambda}^{(FREE)}$ and $\rho_{\text{corr}\lambda}^{(CONS)}$ respectively. To compare the results of the two approaches, a linear relationship was obtained by regressing $\rho_{\text{corr}\lambda}^{(FREE)}$ against $\rho_{\text{corr}\lambda}^{(CONS)}$ for each overpass image. The resulting slopes and intercepts are given in Tables F.1–F.3. Note, that perfect agreement between the two methods would yield a slope of 1 and an intercept of 0.

Furthermore, a relative difference (%) between the free-intercept and constrained approaches was calculated as

$$\text{Relative Difference(\%)} = 100 \times \frac{\rho_{\text{corr}\lambda}^{(FREE)} - \rho_{\text{corr}\lambda}^{(CONS)}}{\rho_{\text{corr}\lambda}^{(CONS)}} \quad (\text{F.1})$$

for a range of surface reflectance values. The resulting differences, for each overpass image, are displayed in the following Figures F.1–F.3.

Table F.1: Comparison of the free-intercept and constrained regression results for the Hay overpass images.

Band	July 22, 1999		October 26, 1999		January 7, 2000	
	Slope	Intercept	Slope	Intercept	Slope	Intercept
1	0.97	0.00	1.07	-0.01	1.03	-0.01
2	1.04	-0.01	1.24	-0.03	1.03	-0.03
3	1.04	-0.01	1.04	-0.01	1.04	-0.01
4	0.91	0.03	1.04	-0.01	0.98	-0.01
5	0.95	0.02	1.02	0.00	0.95	0.00
7	1.00	0.01	0.97	0.01	0.95	0.01

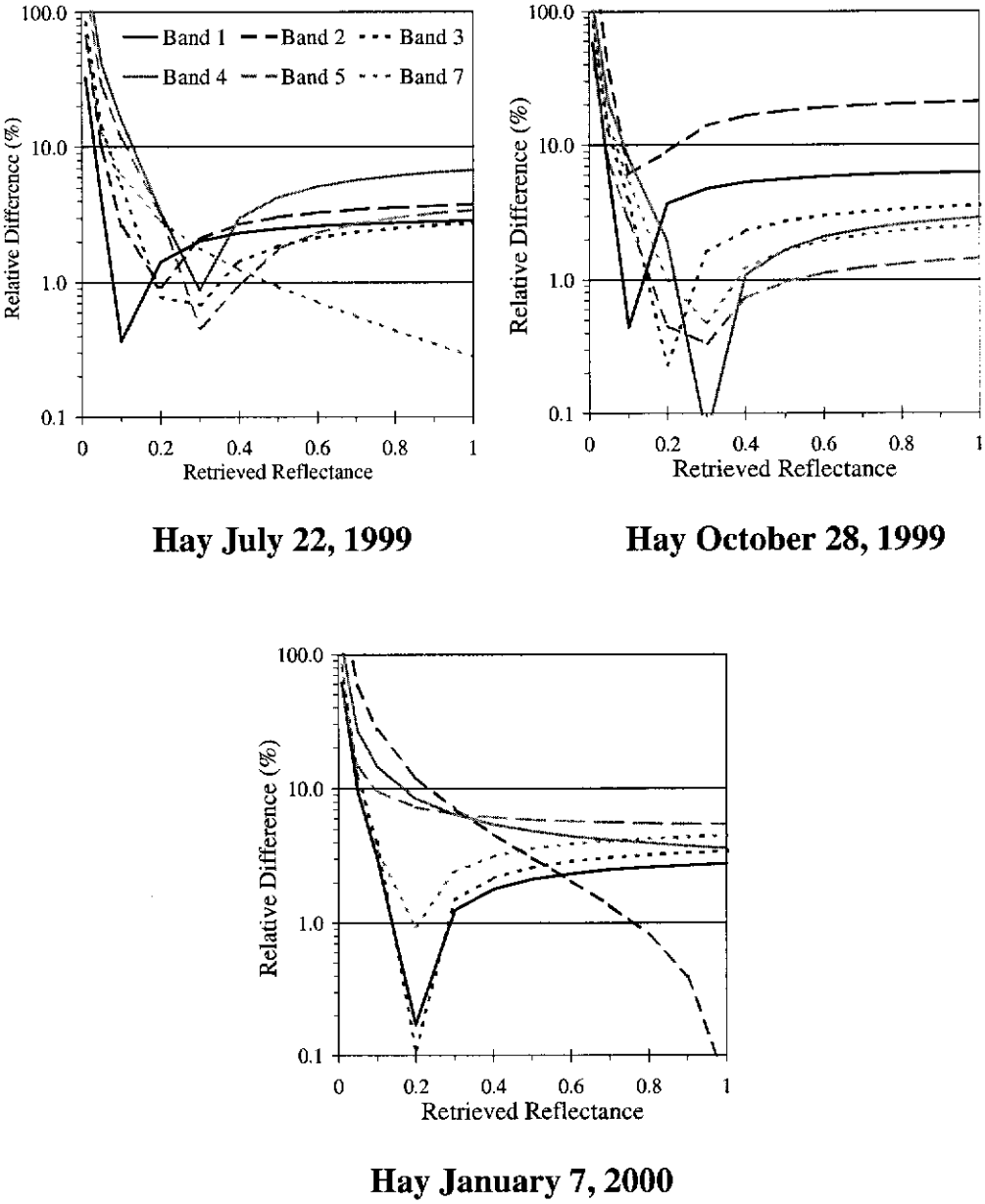
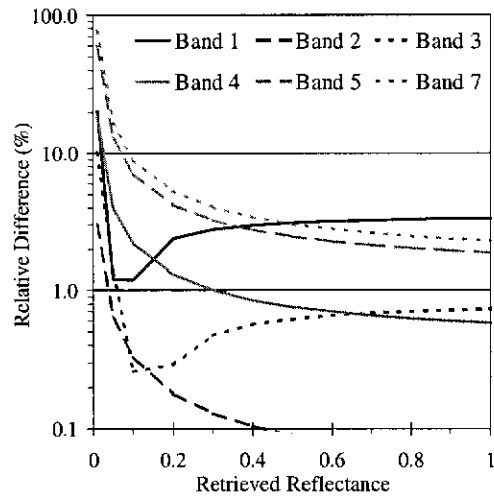


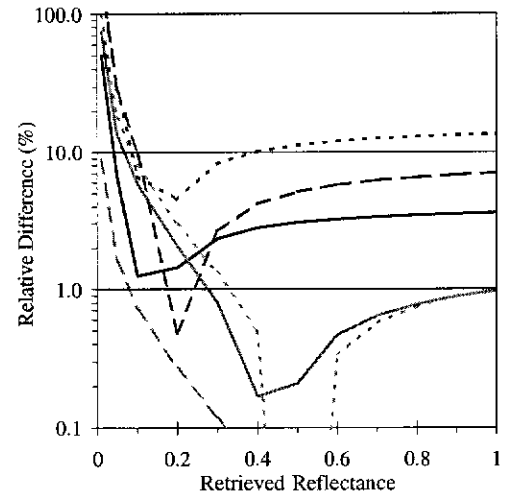
Figure F.1: The magnitude of the relative differences (%) between the free-intercept and constrained regression LVIN lines for all bands in the Hay overpass images.

Table F.2: Comparison of the free-intercept and constrained regression results for the Mt. Barker overpass images: 1991–1994.

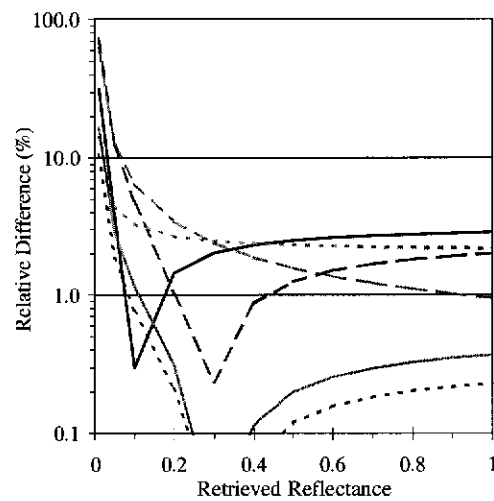
Band	January 20, 1991		February 24, 1992		January 28, 1994	
	Slope	Intercept	Slope	Intercept	Slope	Intercept
1	0.96	0.00	1.04	-0.01	1.03	0.00
2	1.00	0.00	1.09	-0.02	1.03	-0.01
3	0.99	0.00	1.16	-0.02	1.00	0.00
4	1.00	0.00	1.02	-0.01	0.99	0.00
5	1.01	0.01	1.00	0.00	1.00	-0.01
7	1.02	0.01	0.98	0.01	1.02	0.00



Mt. Barker January 20, 1991



Mt. Barker February 24, 1992

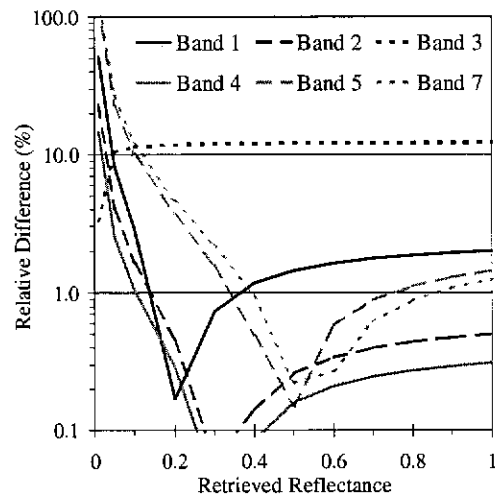


Mt. Barker January 28, 1994

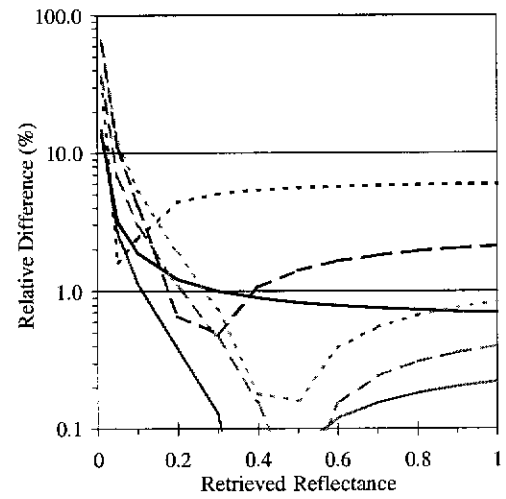
Figure F.2: The magnitude of the relative differences (%) between the free-intercept and constrained regression LVIN lines for all bands in the Mt. Barker overpass images January 20, 1991 to January 28, 1994.

Table F.3: Comparison of the free-intercept and constrained regression results for the Mt. Barker overpass images: 1995–2002.

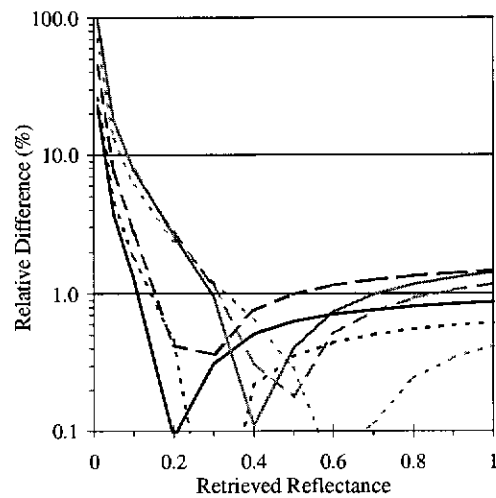
Band	March 20, 1995		January 7, 1998		February 11, 2002	
	Slope	Intercept	Slope	Intercept	Slope	Intercept
1	0.97	0.01	0.99	0.00	1.01	0.00
2	0.99	0.00	1.03	-0.01	1.02	0.00
3	1.12	0.00	1.06	0.00	1.01	0.00
4	1.00	0.00	1.00	0.00	0.98	0.01
5	0.97	0.01	1.01	0.00	1.02	-0.01
7	0.97	0.01	1.02	-0.01	0.99	0.01



Mt. Barker March 20, 1995



Mt. Barker January 7, 1998



Mt. Barker February 11, 2002

Figure F.3: The magnitude of the relative differences (%) between the free-intercept and constrained regression LVIN lines for all bands in the Mt. Barker overpass images March 20, 1995 to February 11, 2002.

Pre- and Post-normalisation Image Histograms

In the following figures, the histograms corresponding to overpass image data for both Hay and Mt. Barker sequences, processed in the fashion described in Chapter 4 (pp. 154–156), are presented. The reflectances in the pre-normalisation, or *Before*, histograms refer to the at-sensor reflectance (Eq. (3.3), p. 57), uncorrected for atmospheric effects. The histograms corresponding to post-normalisation (labelled *LVIN*) retrieved reflectances were obtained using the LVIN procedure (constrained approach) described in Chapter 4. For comparison, histograms for surface reflectances calculated with the 6S code (labelled *6S*) are also displayed.

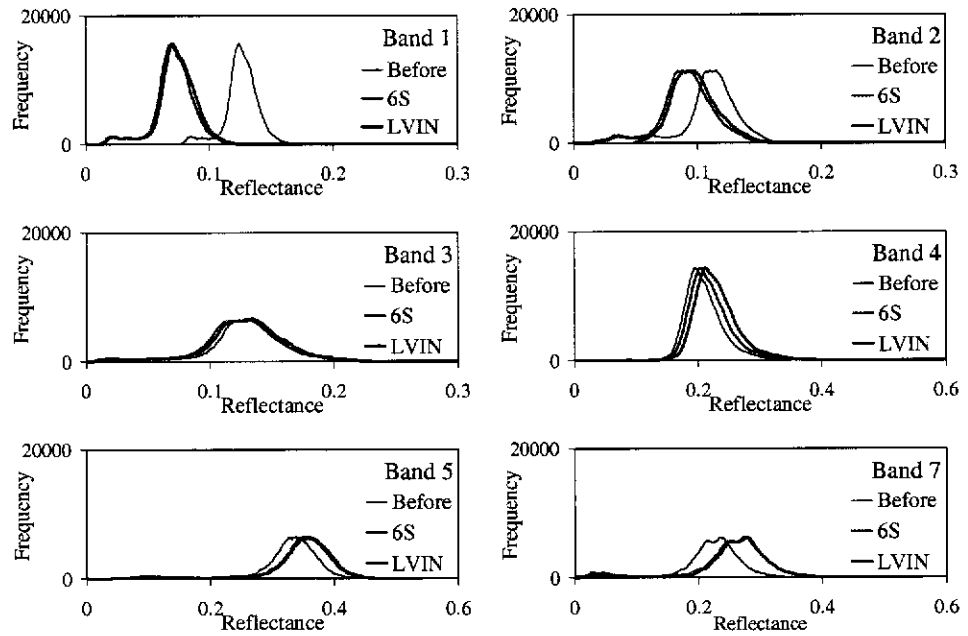


Figure G.1: Histograms of image data for Hay January 7, 2000.

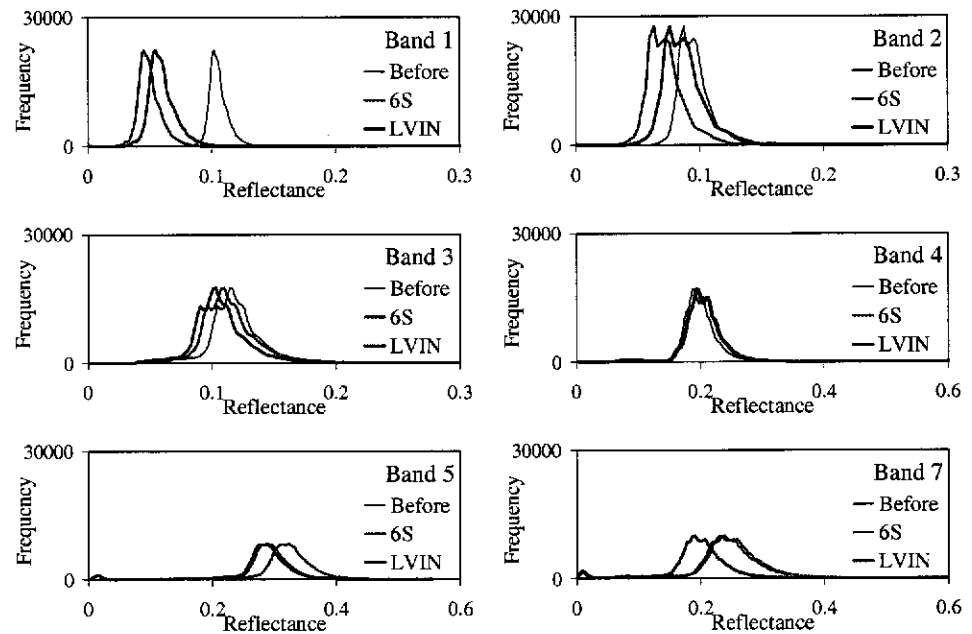


Figure G.2: Histograms of image data for Hay October 26, 1999.

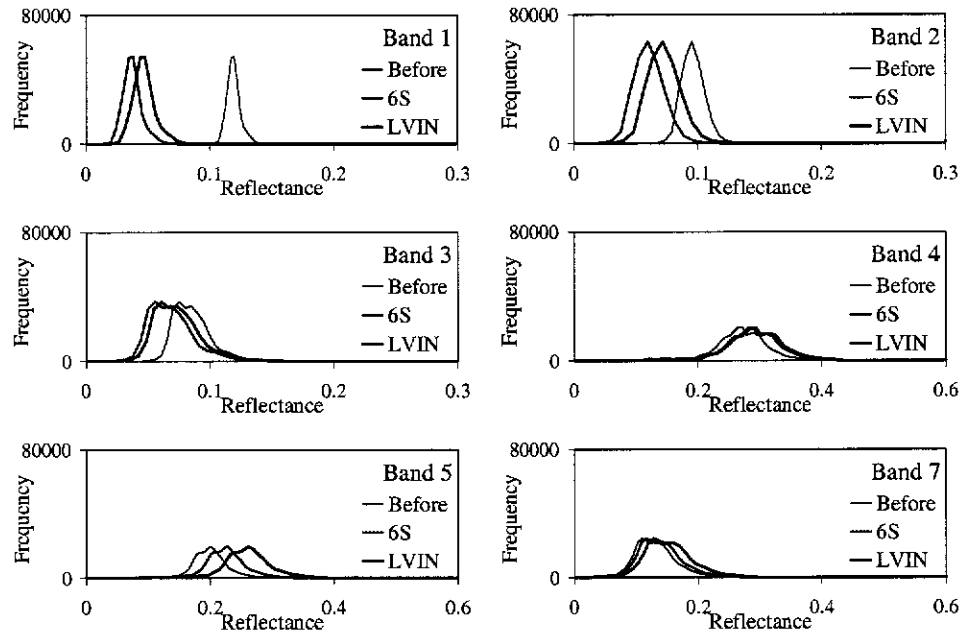


Figure G.3: Histograms of image data for Hay July 22, 1999.

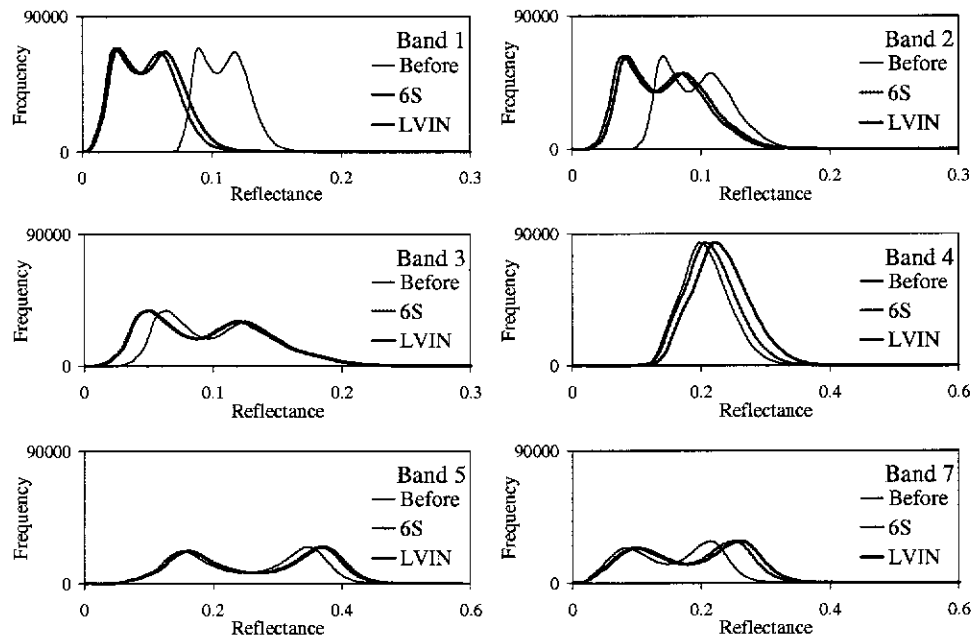


Figure G.4: Histograms of image data for Mt. Barker February 11, 2002.

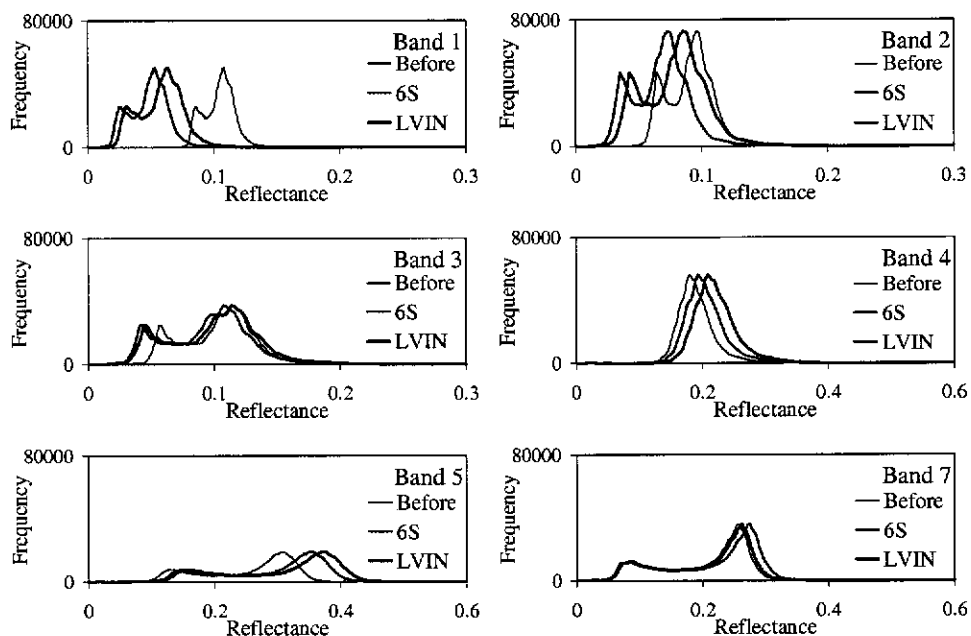


Figure G.5: Histograms of image data for Mt. Barker January 7, 1998.

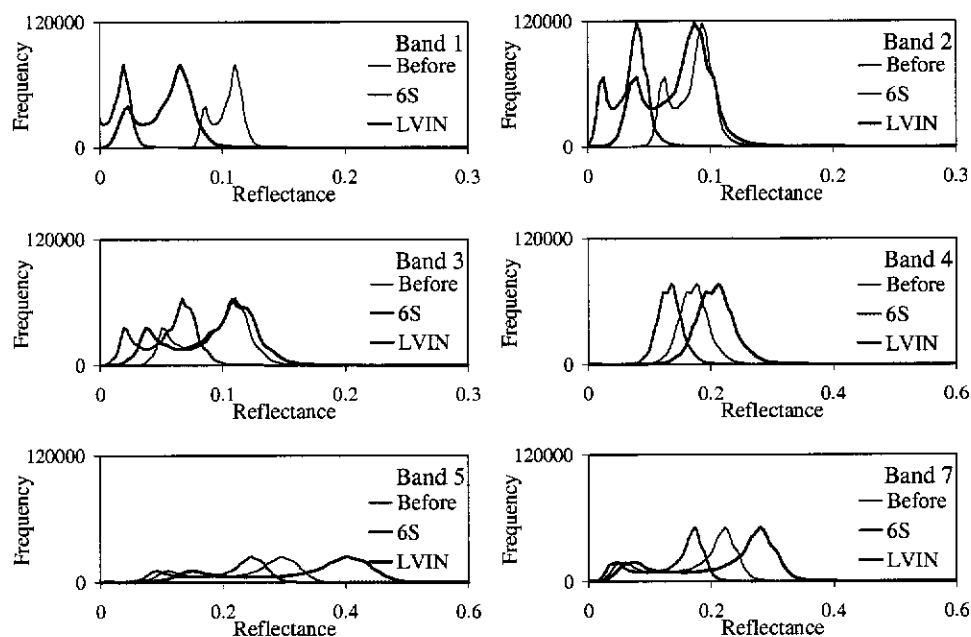


Figure G.6: Histograms of image data for Mt. Barker March 20, 1995.

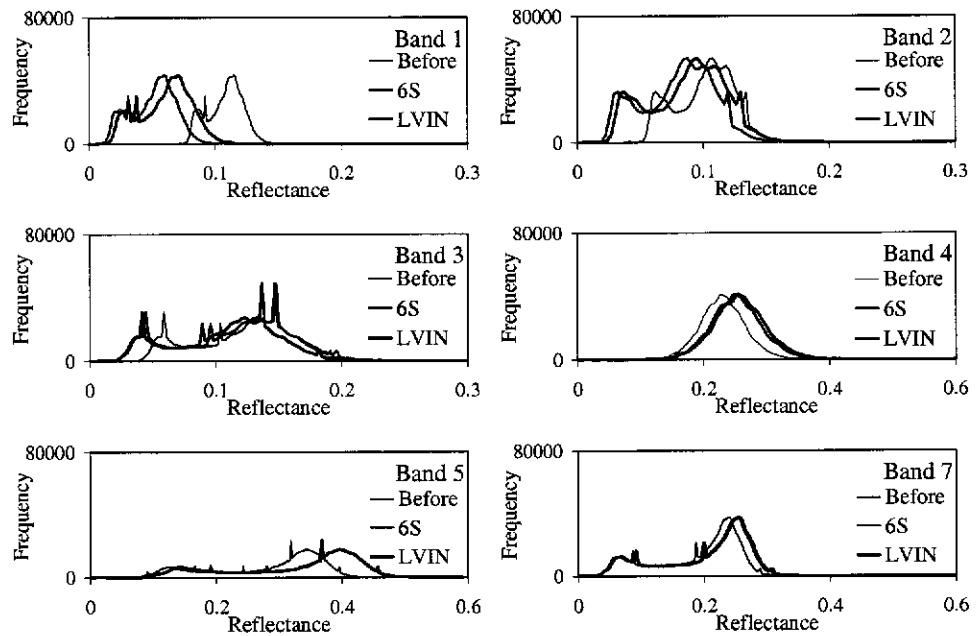


Figure G.7: Histograms of image data for Mt. Barker January 28, 1994.

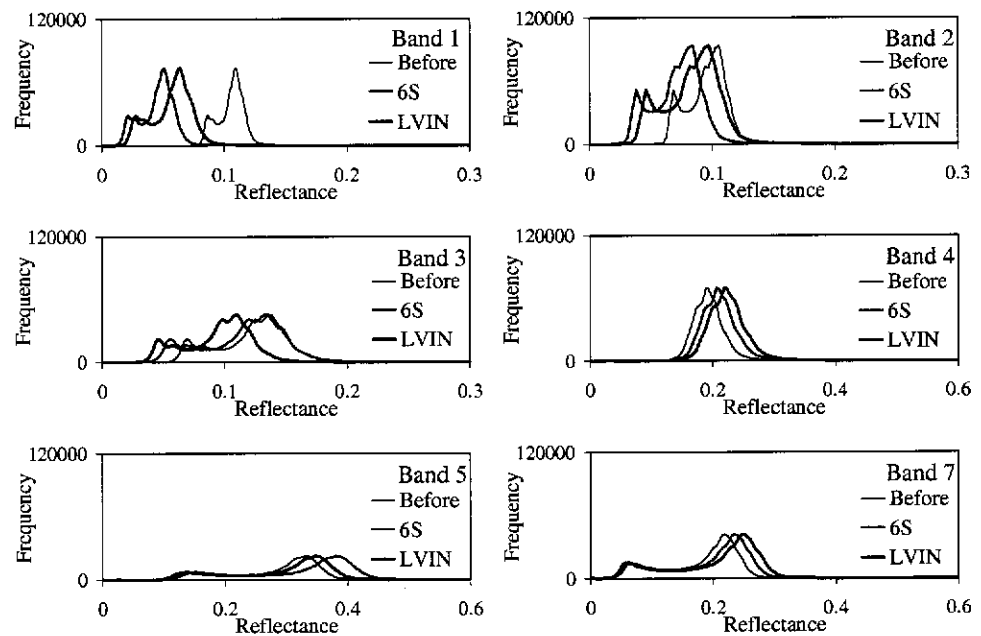


Figure G.8: Histograms of image data for Mt. Barker February 24, 1992.

APPENDIX H

Inter-band Correlation for Some Vegetation Targets

Kaufman et al. (1997c) established empirically-derived relationships (known here as the Kaufman relationships) that relate surface reflectances in some VIS bands to those in the SWIR band (2.2- μm band) for vegetated targets. The Kaufman relationships were investigated because they may be used to obtain image-derived estimates of path DN in the LVIN procedure (Section 4.5, p. 186). To test the validity of the Kaufman relationships, inter-band correlations were calculated between TM and ETM+ bands for a number of vegetated targets. These data and their respective correlation matrices are presented in the following for (a) ground-based spectroradiometer measurements (Section H.1) and (b) satellite imagery (Section H.2). Section H.3 demonstrates how one might incorporate the Kaufman relationships into the LVIN procedure by using the LVIN plots for the Mt. Barker image sequence (Appendix E, pp. 237–242).

H.1 Spectroradiometer Measurements

A GER Iris spectroradiometer (Iris) acquired ground-based reflectance measurements of grass on the McGillivray football oval (E 115°47', S 31°57') in Floreat, Western Australia, over the period January 1994 to February 1995 (see Section 4.5.1, p. 187). On each date, spectroradiometer readings were performed at various locations around the oval in an attempt to obtain an area mean reflectance. These spectra were convolved with the Landsat-5 TM and Landsat-7 ETM+ response curves and are given in Figures H.1 to H.11. Correlation matrices illustrating the inter-band correlation of these data are given in Tables H.1 to H.11.

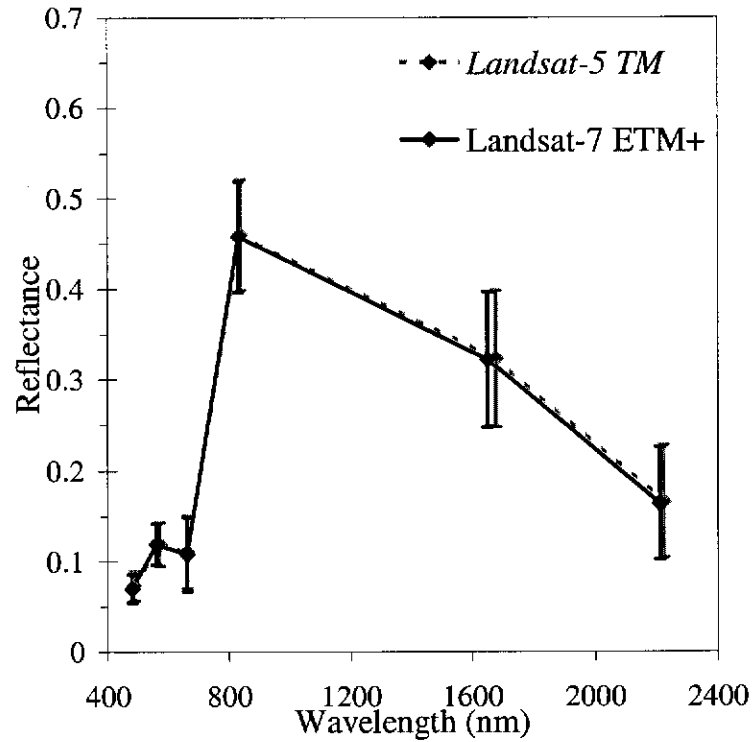


Figure H.1: The convolved Iris spectra (35 in total) of the McGillivray Oval grass acquired on January 19, 1994: Grey diamonds correspond to the mean value of spectra convolved with the Landsat-5 TM response curves; black diamonds correspond to the mean value of spectra convolved with the Landsat-7 ETM+ response curves. Error bars mark $2\times$ standard deviations about the mean value.

Table H.1: The inter-band correlation of 35 convolved grass spectra for January 1994: Iris data convolved with *Landsat-5 TM* response curves, lower triangle; convolved with Landsat-7 ETM+ response curves, upper triangle.

	1	2	3	4	5	7
1	1.000	0.927	0.944	-0.248	0.895	0.889
2	0.945	1.000	0.874	-0.121	0.795	0.807
3	0.951	0.906	1.000	-0.301	0.889	0.923
4	-0.236	-0.137	-0.287	1.000	-0.372	-0.455
5	0.891	0.814	0.889	-0.369	1.000	0.969
7	0.889	0.830	0.921	-0.447	0.971	1.000

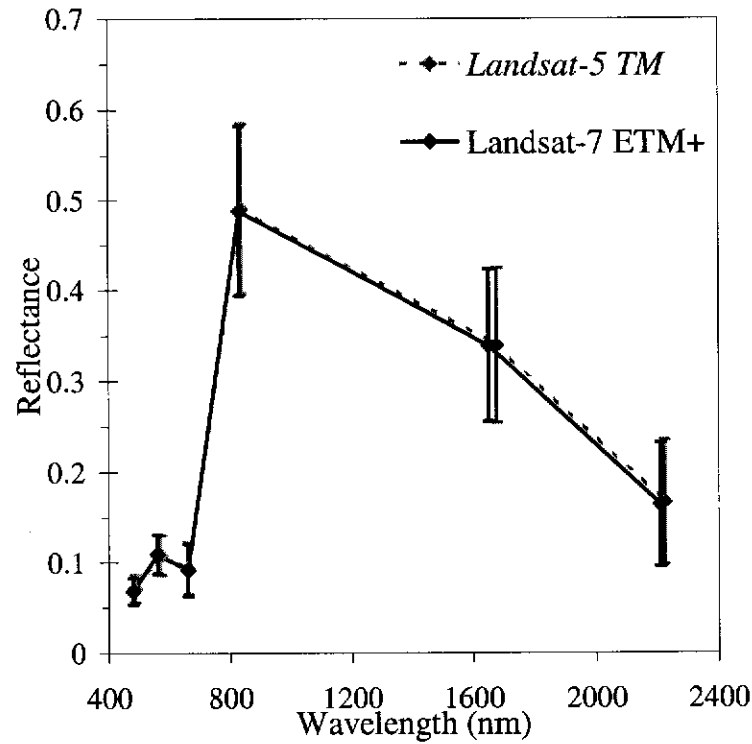


Figure H.2: The convolved Iris spectra (17 in total) of the McGillivray Oval grass acquired on February 18, 1994: Grey diamonds correspond to the mean value of spectra convolved with the Landsat-5 TM response curves; black diamonds correspond to the mean value of spectra convolved with the Landsat-7 ETM+ response curves. Error bars mark 2× standard deviations about the mean value.

Table H.2: The inter-band correlation of 17 convolved grass spectra for February 1994: Iris data convolved with *Landsat-5 TM* response curves, lower triangle; convolved with Landsat-7 ETM+ response curves, upper triangle.

	1	2	3	4	5	7
1	1.000	0.929	0.915	-0.074	0.538	0.542
2	0.942	1.000	0.842	0.078	0.622	0.599
3	0.922	0.878	1.000	-0.361	0.584	0.654
4	-0.068	0.037	-0.345	1.000	0.106	0.000
5	0.538	0.623	0.587	0.107	1.000	0.962
7	0.544	0.611	0.649	0.011	0.966	1.000

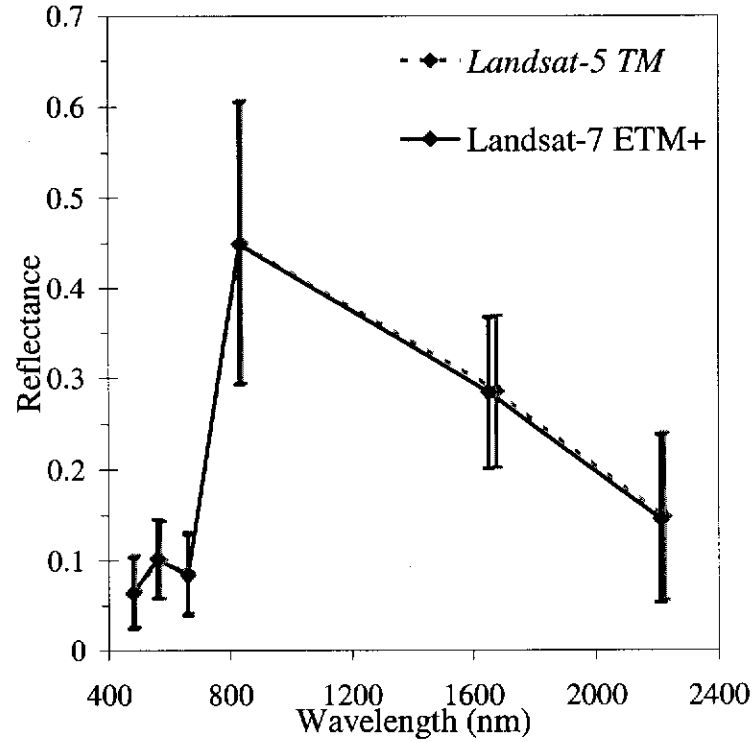


Figure H.3: The convolved Iris spectra (14 in total) of the McGillivray Oval grass acquired on March 30, 1994: Grey diamonds correspond to the mean value of spectra convolved with the Landsat-5 TM response curves; black diamonds correspond to the mean value of spectra convolved with the Landsat-7 ETM+ response curves. Error bars mark 2× standard deviations about the mean value.

Table H.3: The inter-band correlation of 14 convolved grass spectra for March 1994: Iris data convolved with *Landsat-5 TM* response curves, lower triangle; convolved with Landsat-7 ETM+ response curves, upper triangle.

	1	2	3	4	5	7
1	1.000	0.917	0.930	0.276	0.795	0.917
2	0.932	1.000	0.956	0.582	0.919	0.779
3	0.936	0.969	1.000	0.372	0.890	0.856
4	0.301	0.566	0.392	1.000	0.556	0.041
5	0.813	0.919	0.895	0.553	1.000	0.778
7	0.913	0.790	0.850	0.048	0.787	1.000

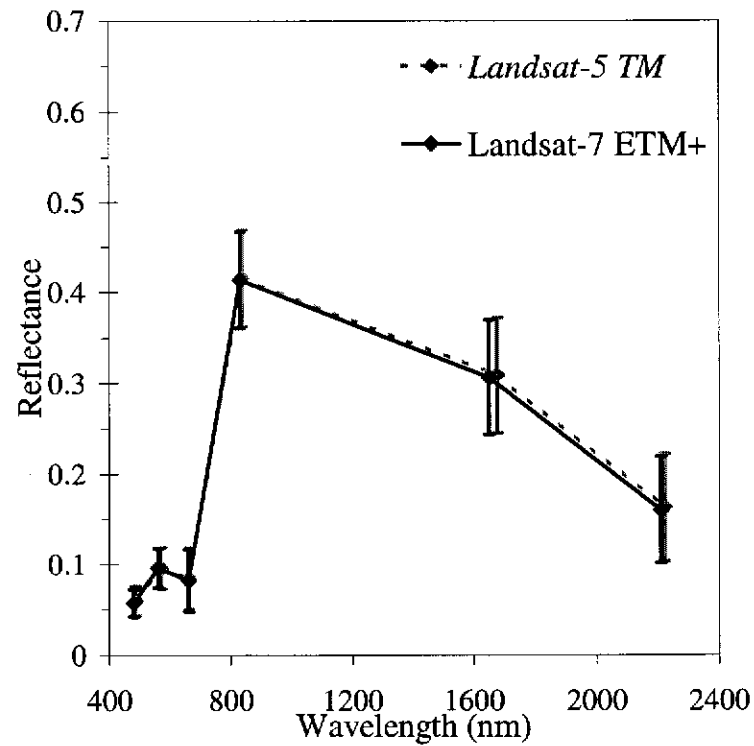


Figure H.4: The convolved Iris spectra (20 in total) of the McGillivray Oval grass acquired on April 27, 1994: Grey diamonds correspond to the mean value of spectra convolved with the Landsat-5 TM response curves; black diamonds correspond to the mean value of spectra convolved with the Landsat-7 ETM+ response curves. Error bars mark $2\times$ standard deviations about the mean value.

Table H.4: The inter-band correlation of 20 convolved grass spectra for April 1994: Iris data convolved with *Landsat-5 TM* response curves, lower triangle; convolved with Landsat-7 ETM+ response curves, upper triangle.

	1	2	3	4	5	7
1	1.000	0.957	0.981	-0.154	0.884	0.785
2	0.971	1.000	0.929	-0.053	0.837	0.710
3	0.983	0.949	1.000	-0.277	0.918	0.817
4	-0.145	-0.076	-0.265	1.000	-0.192	-0.129
5	0.882	0.855	0.916	-0.179	1.000	0.884
7	0.781	0.730	0.815	-0.119	0.893	1.000

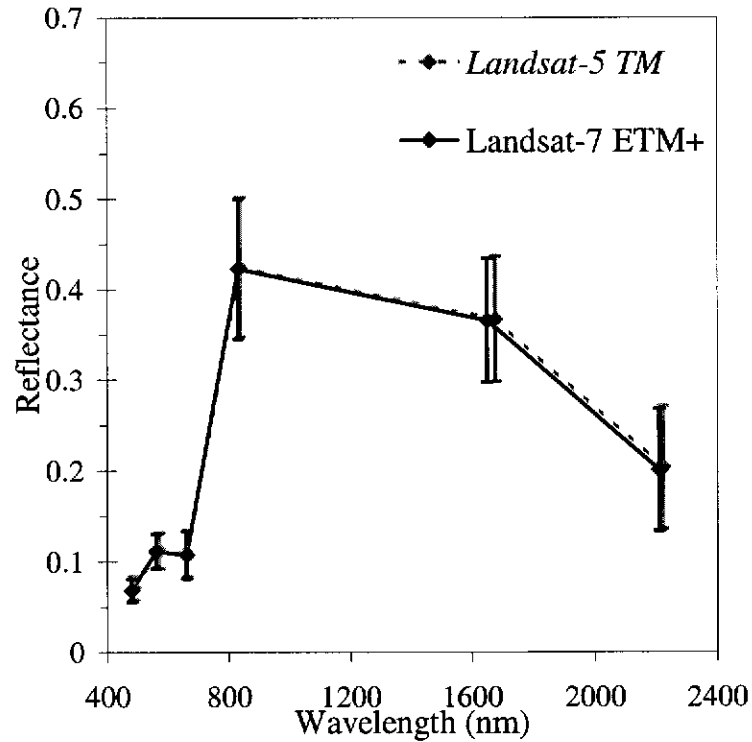


Figure H.5: The convolved Iris spectra (18 in total) of the McGillivray Oval grass acquired on May 27, 1994: Grey diamonds correspond to the mean value of spectra convolved with the Landsat-5 TM response curves; black diamonds correspond to the mean value of spectra convolved with the Landsat-7 ETM+ response curves. Error bars mark $2\times$ standard deviations about the mean value.

Table H.5: The inter-band correlation of 18 convolved grass spectra for May 1994: Iris data convolved with *Landsat-5 TM* response curves, lower triangle; convolved with Landsat-7 ETM+ response curves, upper triangle.

	1	2	3	4	5	7
1	1.000	0.845	0.973	0.046	0.769	0.809
2	0.884	1.000	0.842	0.472	0.896	0.817
3	0.976	0.882	1.000	-0.026	0.779	0.862
4	0.076	0.431	0.003	1.000	0.471	0.151
5	0.789	0.899	0.796	0.472	1.000	0.875
7	0.816	0.835	0.866	0.163	0.884	1.000

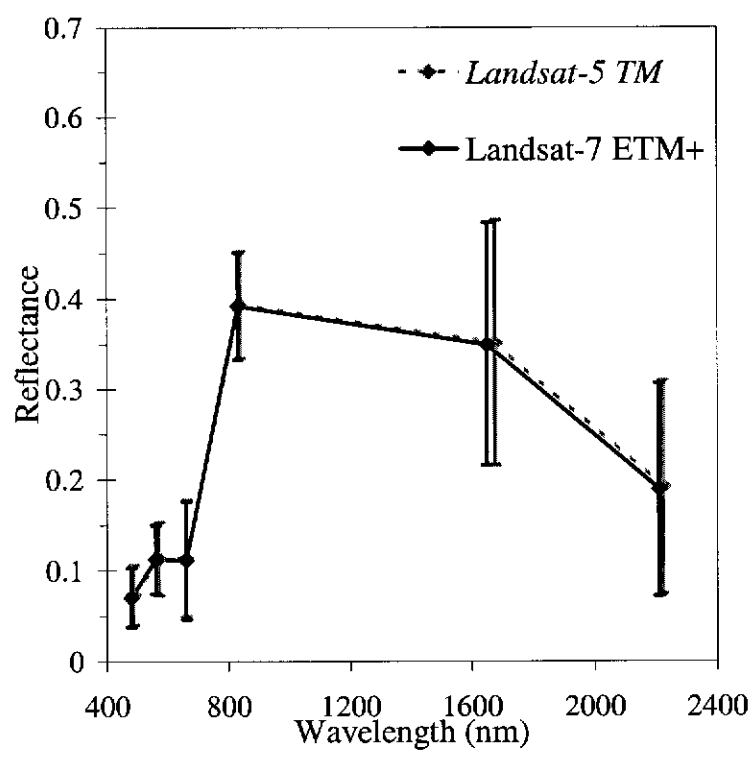


Figure H.6: The convolved Iris spectra (20 in total) of the McGillivray Oval grass acquired on July 28, 1994: Grey diamonds correspond to the mean value of spectra convolved with the Landsat-5 TM response curves; black diamonds correspond to the mean value of spectra convolved with the Landsat-7 ETM+ response curves. Error bars mark $2\times$ standard deviations about the mean value.

Table H.6: The inter-band correlation of 20 convolved grass spectra for July 1994: Iris data convolved with *Landsat-5 TM* response curves, lower triangle; convolved with Landsat-7 ETM+ response curves, upper triangle.

	1	2	3	4	5	7
1	1.000	0.954	0.995	0.328	0.945	0.919
2	0.971	1.000	0.944	0.479	0.885	0.863
3	0.995	0.960	1.000	0.269	0.936	0.926
4	0.348	0.462	0.286	1.000	0.432	0.193
5	0.944	0.897	0.937	0.437	1.000	0.921
7	0.916	0.876	0.925	0.203	0.922	1.000

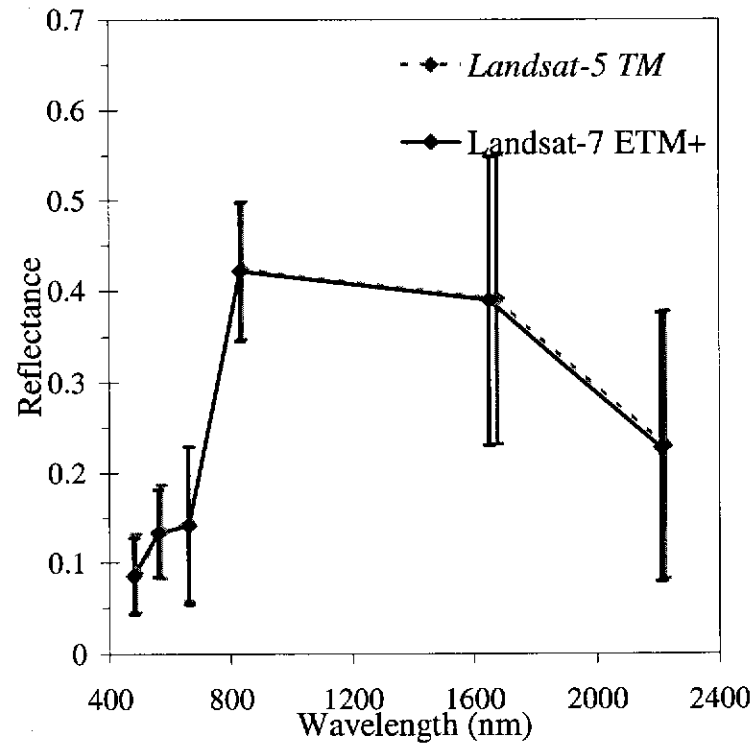


Figure H.7: The convolved Iris spectra (20 in total) of the McGillivray Oval grass acquired on September 6, 1994: Grey diamonds correspond to the mean value of spectra convolved with the Landsat-5 TM response curves; black diamonds correspond to the mean value of spectra convolved with the Landsat-7 ETM+ response curves. Error bars mark $2\times$ standard deviations about the mean value.

Table H.7: The inter-band correlation of 20 convolved grass spectra for Septemeber 1994: Iris data convolved with *Landsat-5 TM* response curves, lower triangle; convolved with Landsat-7 ETM+ response curves, upper triangle.

	1	2	3	4	5	7
1	1.000	0.969	0.995	-0.594	0.963	0.945
2	0.977	1.000	0.968	-0.525	0.899	0.869
3	0.996	0.976	1.000	-0.637	0.958	0.948
4	-0.586	-0.535	-0.627	1.000	-0.591	-0.670
5	0.960	0.906	0.956	-0.588	1.000	0.985
7	0.942	0.879	0.945	-0.662	0.987	1.000

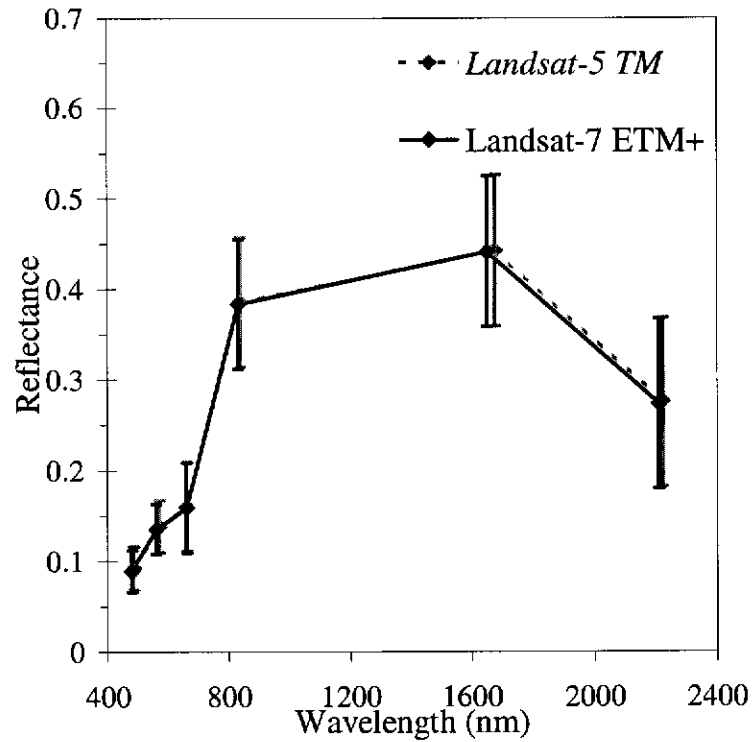


Figure H.8: The convolved Iris spectra (20 in total) of the McGillivray Oval grass acquired on October 11, 1994: Grey diamonds correspond to the mean value of spectra convolved with the Landsat-5 TM response curves; black diamonds correspond to the mean value of spectra convolved with the Landsat-7 ETM+ response curves. Error bars mark $2\times$ standard deviations about the mean value.

Table H.8: The inter-band correlation of 20 convolved grass spectra for October 1994: Iris data convolved with *Landsat-5 TM* response curves, lower triangle; convolved with Landsat-7 ETM+ response curves, upper triangle.

	1	2	3	4	5	7
1	1.000	0.938	0.956	-0.088	0.834	0.800
2	0.949	1.000	0.910	0.185	0.685	0.612
3	0.959	0.934	1.000	-0.212	0.831	0.851
4	-0.074	0.149	-0.193	1.000	-0.373	-0.598
5	0.826	0.695	0.824	-0.378	1.000	0.931
7	0.797	0.641	0.844	-0.592	0.932	1.000

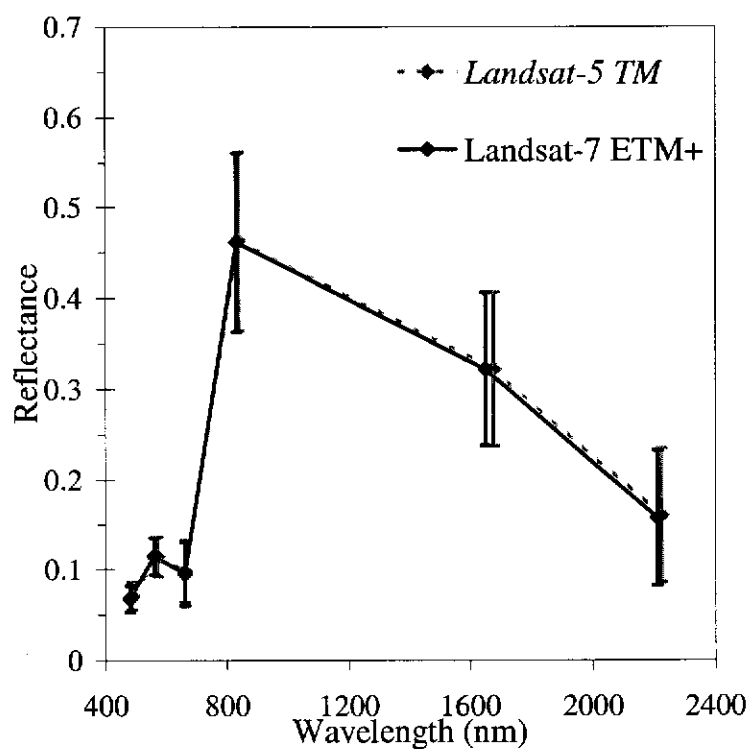


Figure H.9: The convolved Iris spectra (20 in total) of the McGillivray Oval grass acquired on December 6, 1994: Grey diamonds correspond to the mean value of spectra convolved with the Landsat-5 TM response curves; black diamonds correspond to the mean value of spectra convolved with the Landsat-7 ETM+ response curves. Error bars mark $2\times$ standard deviations about the mean value.

Table H.9: The inter-band correlation of 20 convolved grass spectra for December 1994: Iris data convolved with *Landsat-5 TM* response curves, lower triangle; convolved with Landsat-7 ETM+ response curves, upper triangle.

	1	2	3	4	5	7
1	1.000	0.880	0.937	-0.136	0.803	0.699
2	0.922	1.000	0.754	0.073	0.648	0.505
3	0.940	0.825	1.000	-0.374	0.888	0.854
4	-0.118	0.011	-0.354	1.000	-0.489	-0.645
5	0.791	0.699	0.884	-0.489	1.000	0.946
7	0.691	0.572	0.848	-0.640	0.950	1.000

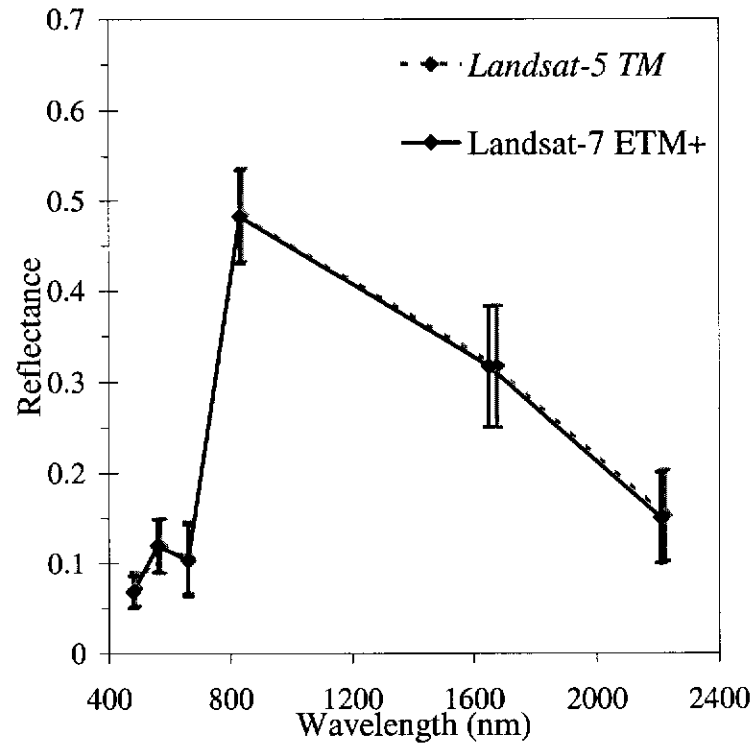


Figure H.10: The convolved Iris spectra (20 in total) of the McGillivray Oval grass acquired on January 6, 1995: Grey diamonds correspond to the mean value of spectra convolved with the Landsat-5 TM response curves; black diamonds correspond to the mean value of spectra convolved with the Landsat-7 ETM+ response curves. Error bars mark $2 \times$ standard deviations about the mean value.

Table H.10: The inter-band correlation of 20 convolved grass spectra for January 1995: Iris data convolved with *Landsat-5 TM* response curves, lower triangle; convolved with Landsat-7 ETM+ response curves, upper triangle.

	1	2	3	4	5	7
1	1.000	0.949	0.951	0.367	0.891	0.792
2	0.959	1.000	0.905	0.410	0.792	0.670
3	0.955	0.928	1.000	0.249	0.908	0.829
4	0.377	0.393	0.264	1.000	0.087	-0.089
5	0.886	0.806	0.905	0.090	1.000	0.959
7	0.787	0.694	0.825	-0.078	0.963	1.000

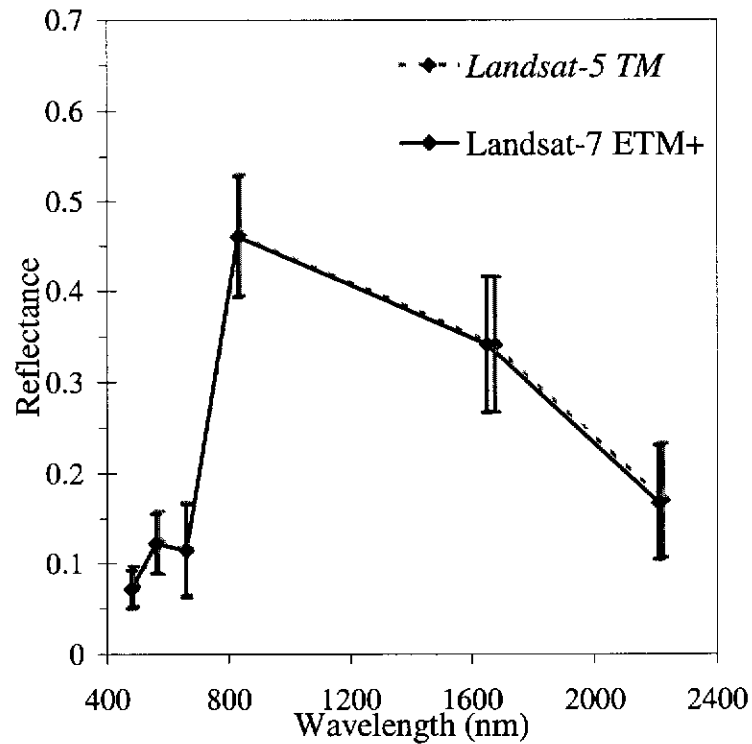


Figure H.11: The convolved Iris spectra (20 in total) of the McGillivray Oval grass acquired on February 7, 1995: Grey diamonds correspond to the mean value of spectra convolved with the Landsat-5 TM response curves; black diamonds correspond to the mean value of spectra convolved with the Landsat-7 ETM+ response curves. Error bars mark $2\times$ standard deviations about the mean value.

Table H.11: The inter-band correlation of 20 convolved grass spectra for February 1995: Iris data convolved with *Landsat-5 TM* response curves, lower triangle; convolved with Landsat-7 ETM+ response curves, upper triangle.

	1	2	3	4	5	7
1	1.000	0.957	0.978	0.307	0.859	0.914
2	0.967	1.000	0.927	0.391	0.850	0.897
3	0.980	0.944	1.000	0.266	0.848	0.931
4	0.308	0.382	0.274	1.000	0.350	0.211
5	0.860	0.856	0.852	0.349	1.000	0.948
7	0.916	0.906	0.932	0.215	0.951	1.000

H.2 Image Data

Reflectance spectra were extracted from 64 vegetated targets in the Mt. Barker scene for each date of corrected TM and ETM+ imagery (Section 4.5.1, p. 192). The inter-band correlation matrices for these data are given for each date in Tables H.12 to H.18.

Table H.12: Correlation matrix for vegetation targets January 20, 1991.

	1	2	3	4	5	7
1	1.000	0.962	0.973	-0.203	0.939	0.949
2		1.000	0.959	-0.055	0.896	0.888
3			1.000	-0.152	0.930	0.916
4				1.000	-0.170	-0.316
5					1.000	0.959
7						1.000

Table H.13: Correlation matrix for vegetation targets February 24, 1992.

	1	2	3	4	5	7
1	1.000	0.948	0.974	-0.122	0.940	0.946
2		1.000	0.945	0.071	0.915	0.906
3			1.000	-0.096	0.950	0.948
4				1.000	0.001	-0.195
5					1.000	0.954
7						1.000

Table H.14: Correlation matrix for vegetation targets January 28, 1994.

	1	2	3	4	5	7
1	1.000	0.938	0.974	0.030	0.941	0.933
2		1.000	0.949	0.228	0.899	0.867
3			1.000	0.093	0.948	0.926
4				1.000	0.030	-0.144
5					1.000	0.972
7						1.000

Table H.15: Correlation matrix for vegetation targets March 20, 1995.

	1	2	3	4	5	7
1	1.000	0.888	0.952	0.032	0.923	0.931
2		1.000	0.930	0.363	0.920	0.849
3			1.000	0.112	0.945	0.934
4				1.000	0.221	-0.010
5					1.000	0.952
7						1.000

Table H.16: Correlation matrix for vegetation targets January 7, 1998.

	1	2	3	4	5	7
1	1.000	0.942	0.979	-0.141	0.942	0.947
2		1.000	0.951	0.044	0.886	0.900
3			1.000	-0.101	0.952	0.941
4				1.000	-0.124	-0.248
5					1.000	0.965
7						1.000

Table H.17: Correlation matrix for vegetation targets February 6, 2000.

	1	2	3	4	5	7
1	1.000	0.881	0.968	-0.263	0.927	0.952
2		1.000	0.902	0.148	0.869	0.832
3			1.000	-0.154	0.943	0.933
4				1.000	-0.148	-0.321
5					1.000	0.964
7						1.000

Table H.18: Correlation matrix for vegetation targets February 11, 2002.

	1	2	3	4	5	7
1	1.000	0.870	0.959	-0.206	0.915	0.932
2		1.000	0.911	0.246	0.865	0.803
3			1.000	-0.071	0.913	0.892
4				1.000	-0.030	-0.248
5					1.000	0.949
7						1.000

H.3 LVIN plots and the Kaufman Relationships

As a demonstration of how the Kaufman relationships (Section 4.5.2, p. 195) may be incorporated into a LVIN procedure, the Mt. Barker sequence of imagery was once again employed. Specifically, the normalisation (LVIN) plots for the overpass images in the Mt. Barker sequence given in Appendix E (pp. 237–242) were used.

Figures (H.12–H.17) in the following contain an enlargement of the LVIN plots for bands 1, 2, 3 and 5 for each date of overpass imagery in the Mt. Barker sequence. Recall that the black diamonds are the pixel *DN*s for the PITs in the LVIN plots, and the black lines are the free-intercept LVIN lines with corresponding 95% confidence limits delineated in grey.

Twenty vegetated targets were chosen to which the empirical vegetation relationships (Table H.19) have been applied to form new data pairs: namely, those derived by Kaufman et al. (Kaufman, red squares), and the two sets of relationships derived in this work (Image-derived, green triangles; and Grass spectra, blue circles).

Table H.19: The empirical vegetation reflectance relationships of Kaufman et al. (Kaufman) and the relationships derived in this work using retrieved reflectance for vegetation in Mt. Barker sequence (Image-derived) and McGillivray Oval grass spectra (Grass Spectra). Further details of their derivation is given in Section 4.5, pp. 186–195.

	Kaufman	Image-derived	Grass Spectra
Band 1	$\rho_{s1} = 0.25 \rho_{s7}$	$\rho_{s1} = 0.005 + 0.28 \rho_{s7}$	$\rho_{s1} = 0.03 + 0.25 \rho_{s7}$
Band 2		$\rho_{s2} = 0.02 + 0.26 \rho_{s7}$	$\rho_{s2} = 0.06 + 0.29 \rho_{s7}$
Band 3	$\rho_{s3} = 0.50 \rho_{s7}$	$\rho_{s3} = 0.01 + 0.42 \rho_{s7}$	$\rho_{s3} = 0.02 + 0.54 \rho_{s7}$
Band 5		$\rho_{s5} = 0.05 + 1.28 \rho_{s7}$	$\rho_{s5} = 0.14 + 1.09 \rho_{s7}$

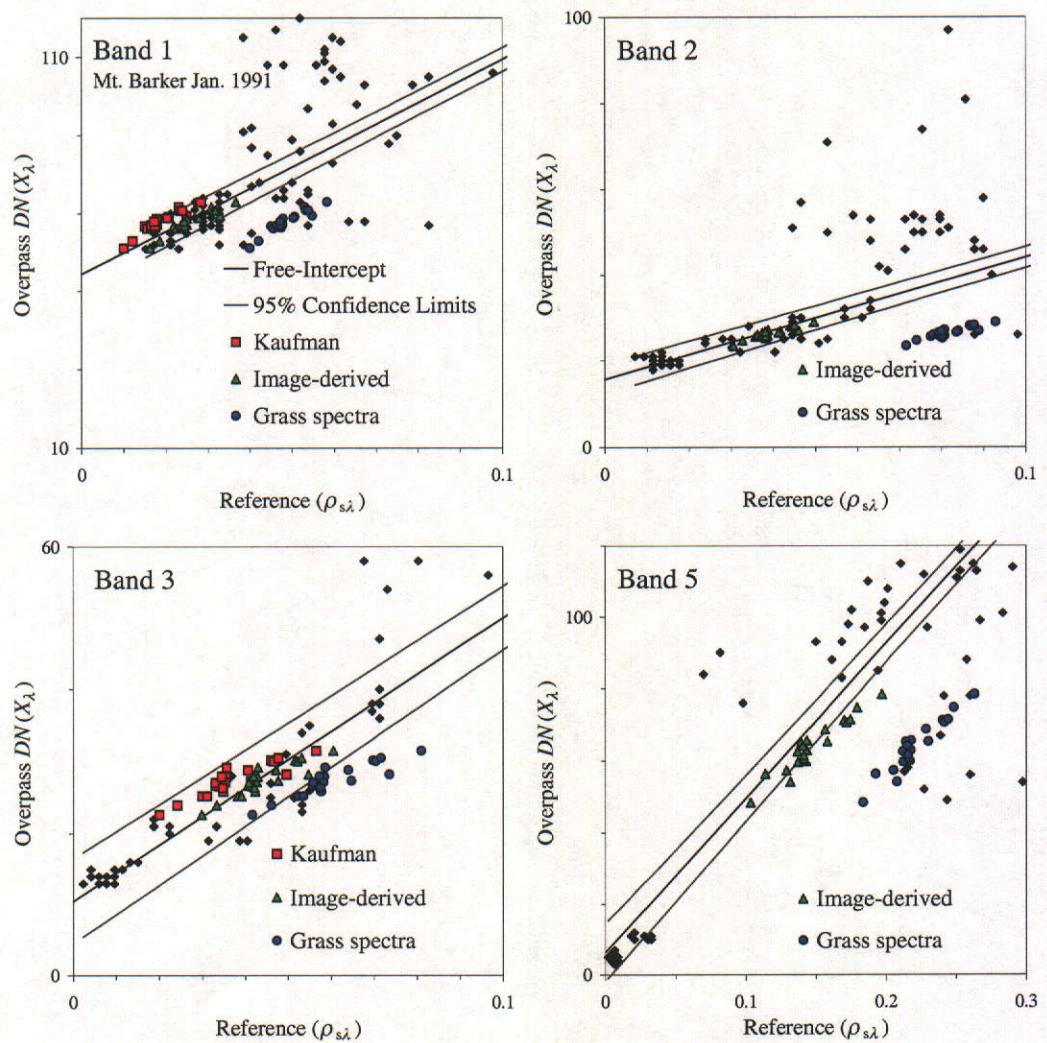


Figure H.12: Enlargements of the LVIN plots for bands 1, 2, 3 and 5 for the Mt. Barker TM imagery acquired on January 20, 1991. Twenty new data pairs corresponding to vegetated targets to which three vegetation reflectance relationships (Table H.19) were applied are illustrated as red squares (Kaufman), green triangles (Image-derived), and blue circles (Grass).

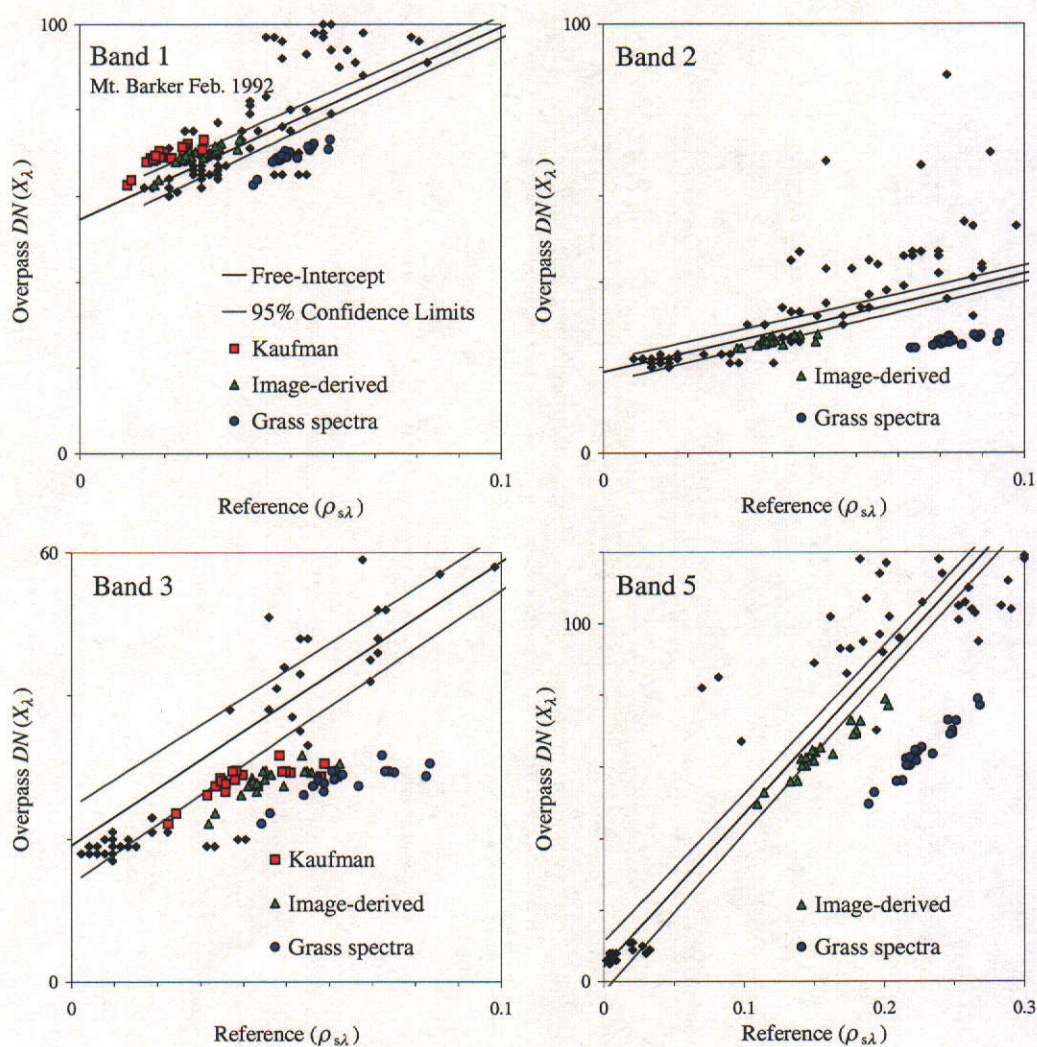


Figure H.13: Enlargements of the LVIN plots for bands 1, 2, 3 and 5 for the Mt. Barker TM imagery acquired on February 24, 1992. Twenty new data pairs corresponding to vegetated targets to which three vegetation reflectance relationships (Table H.19) were applied are illustrated as red squares (Kaufman), green triangles (Image-derived), and blue circles (Grass).

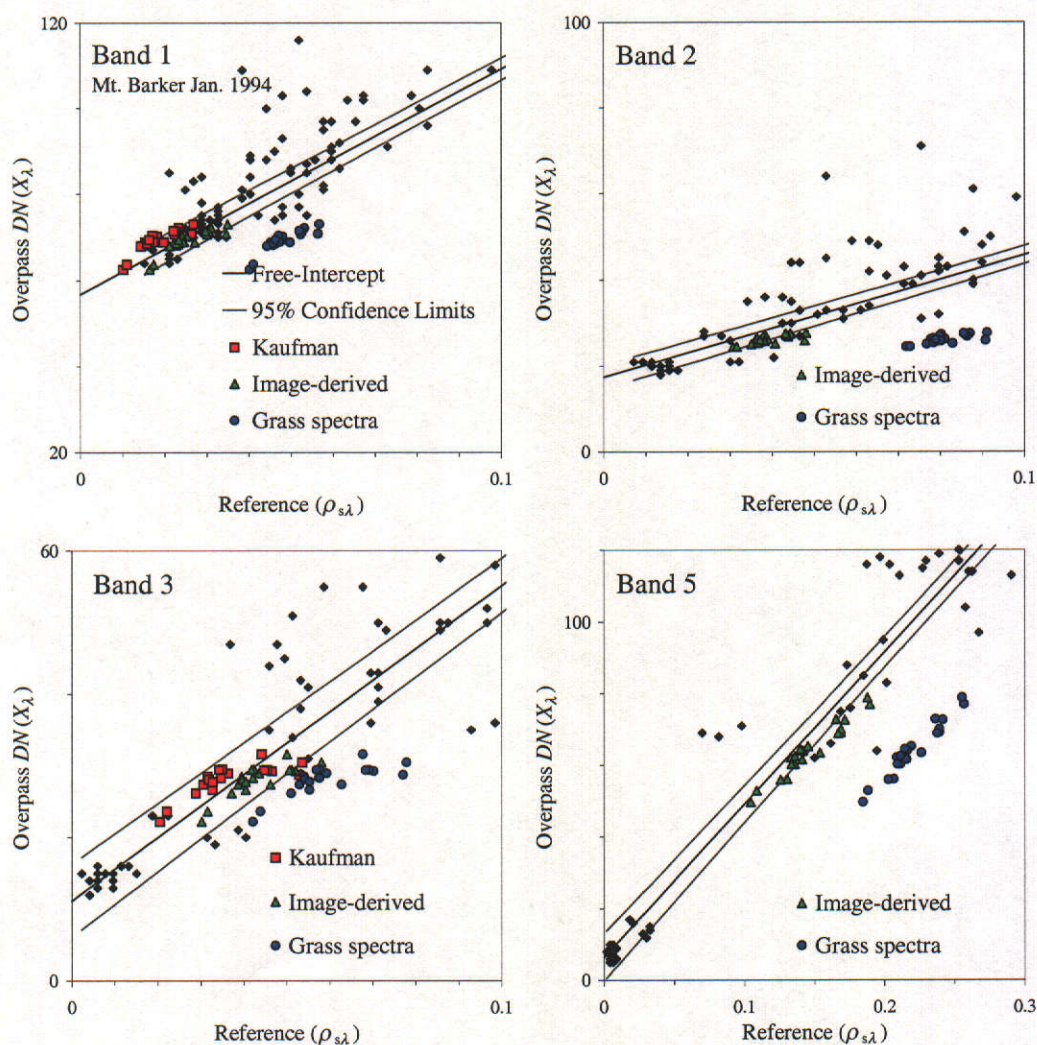


Figure H.14: Enlargements of the LVIN plots for bands 1, 2, 3 and 5 for the Mt. Barker TM imagery acquired on January 28, 1994. Twenty new data pairs corresponding to vegetated targets to which three vegetation reflectance relationships (Table H.19) were applied are illustrated as red squares (Kaufman), green triangles (Image-derived), and blue circles (Grass).

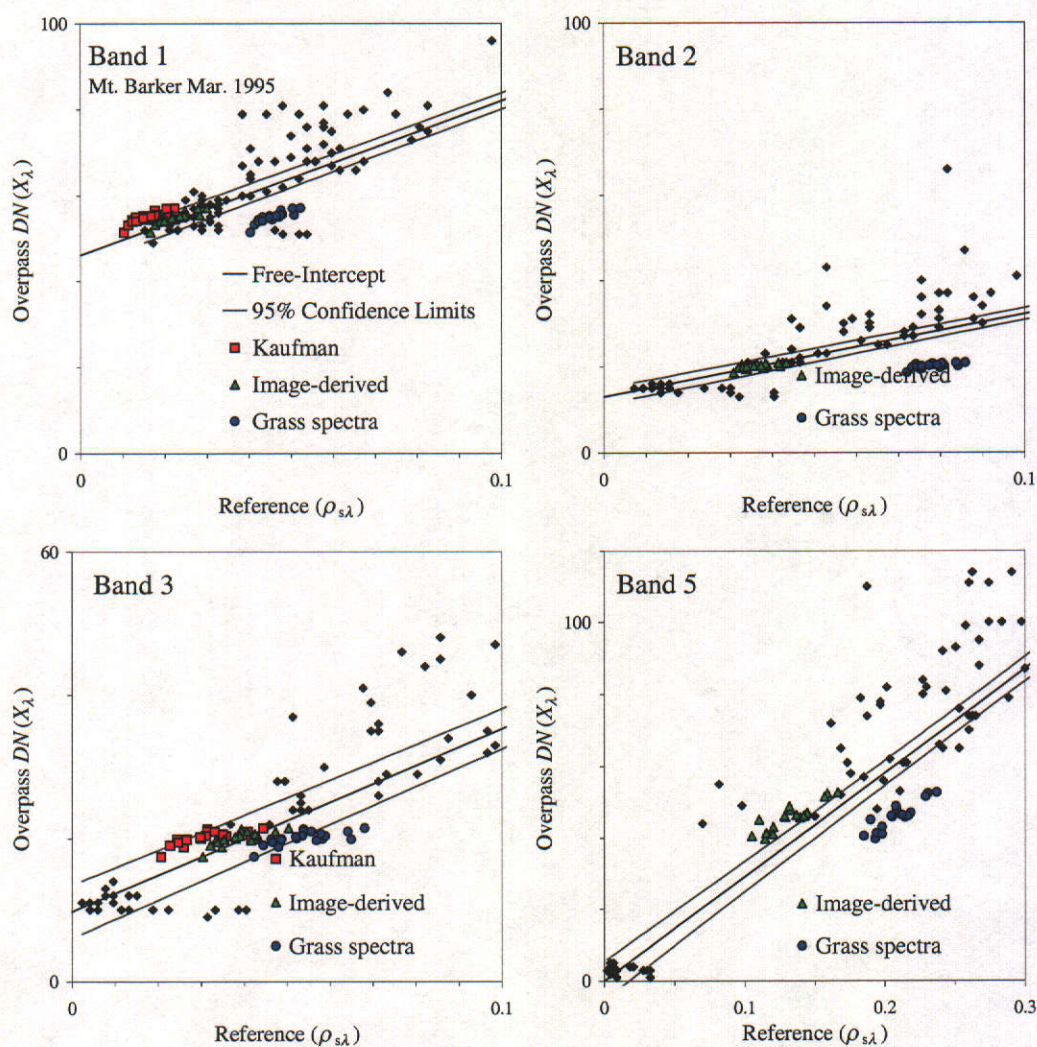


Figure H.15: Enlargements of the LVIN plots for bands 1, 2, 3 and 5 for the Mt. Barker TM imagery acquired on March 20, 1995. Twenty new data pairs corresponding to vegetated targets to which three vegetation reflectance relationships (Table H.19) were applied are illustrated as red squares (Kaufman), green triangles (Image-derived), and blue circles (Grass).

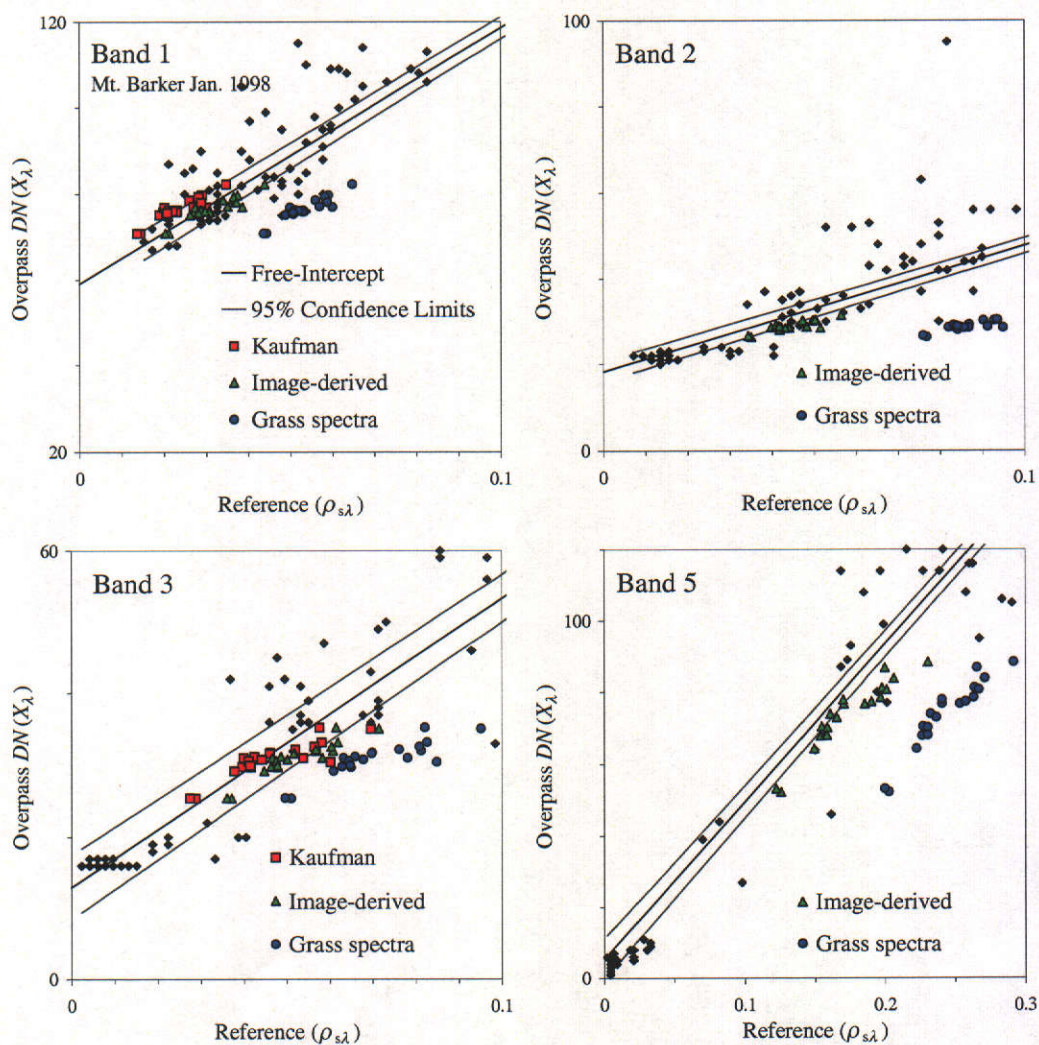


Figure H.16: Enlargements of the LVIN plots for bands 1, 2, 3 and 5 for the Mt. Barker TM imagery acquired on January 7, 1998. Twenty new data pairs corresponding to vegetated targets to which three vegetation reflectance relationships (Table H.19) were applied are illustrated as red squares (Kaufman), green triangles (Image-derived), and blue circles (Grass).

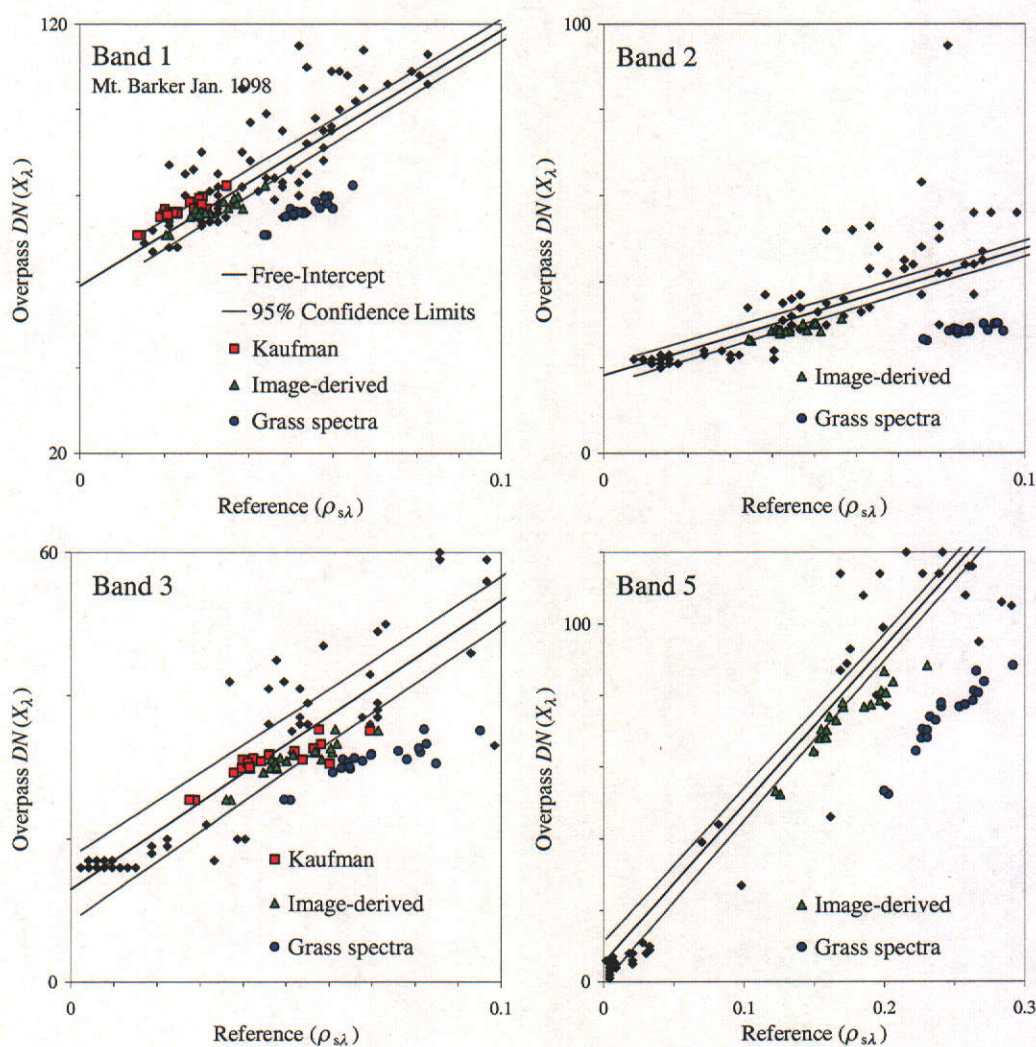


Figure H.17: Enlargements of the LVIN plots for bands 1, 2, 3 and 5 for the Mt. Barker ETM+ imagery acquired on February 11, 2002. Twenty new data pairs corresponding to vegetated targets to which three vegetation reflectance relationships (Table H.19) were applied are illustrated as red squares (Kaufman), green triangles (Image-derived), and blue circles (Grass).